Understanding the functional implications of differential integrin expression in cardiomyocytes

Hawkes, Will

Awarding institution:
King's College London

UNDERSTANDING THE FUNCTIONAL IMPLICATIONS OF DIFFERENTIAL INTEGRIN EXPRESSION IN CARDIOMYOCYTES

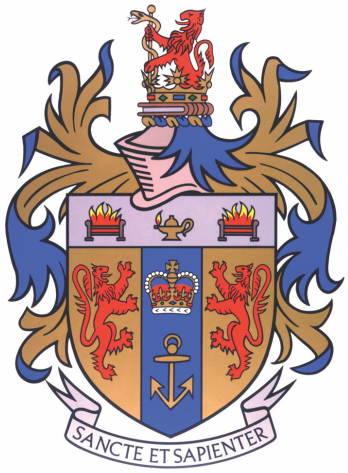

King's College London

William Hawkes

Randall Division of Cell and Molecular Biophysics

Faculty of Life Sciences & Medicine

King's College London

This thesis is submitted for the degree of Doctor of Philosophy

May 2020

I dedicate this thesis to my wife Hayley White and my parents Richard & Teresa Hawkes. Without their support, I would not be where I am today.

"Oh, the Places You'll Go"

DECLARATION

This dissertation is the result of my own work and includes nothing, which is the outcome of work done in collaboration except where specifically indicated in the text. It has not been previously submitted, in part or whole, to any university of institution for any degree, diploma, or other qualification.

Signed:_____

Date:_____22/11/2019_____

William Hawkes

ABSTRACT

Integrins are one of the major proteins that cells utilise to adhere to their extracellular matrix (ECM). Although integrins do not possess any catalytic capacity themselves, they facilitate and orchestrate the assembly of mechanically sensitive signalling hubs which provide essential cues to guide and inform cell behaviour. Within the heart, integrins are found in specialised adhesion structures called costameres which provide a physical link between the contractile sarcomere and the ECM. Via proteins such as vinculin and talin, integrin signalling has been reported to play a key role in developmental and diseased processes such as rigidity sensing and hypertrophy. Importantly, cardiomyocyte integrin expression is tightly regulated during development and diseased states where fibronectin binding integrin subtypes become dominant, whereas laminin binding subtypes are predominant in the healthy adult heart. Currently, the implications of this dynamic integrin expression profile for integrin signalling and cardiomyocyte behaviour is not well understood. Thus the aim of this thesis was to conduct a comparative investigation of cardiomyocyte spreading, morphology and contractility when cultured on fibronectin or laminin ligands. Initial investigations utilising PDMS substrates, nanopillar arrays and ligand micropatterning revealed that cardiomyocyte cultured on fibronectin exhibit greater spreading, contractility and vinculin enrichment than cells cultured on laminin. From these results, it was hypothesised that changes in integrin subtype expression may result in differential integrin signalling pathways. To understand the underpinning molecular mechanisms of these observations, we sought to investigate integrin clustering via the implementation of a DNA origami ligand nanopatterning platform. The results revealed key differences in the integrin clustering dynamics of fibronectin and laminin binding subtypes. This data provide new insights into the molecular mechanisms of integrin signalling in cardiomyocytes and advances our understanding of their role in development and disease.

ACKNOWLEDGEMENTS

I would like to thank the following people for their help and support throughout my studies. Thank you to my primary supervisor Dr Thomas Iskratsch for his invaluable contributions, commitment and dedication to my project throughout my PhD, without his help this project would not have been possible. Thanks also to my secondary supervisor Dr Matteo Palma for all his help and contributions towads the ligand nanopatterning and DNA origami work. The entire Iskratsch and Palma groups have provided invaluable contributions to this project over the last 3 years. Specifically, Pragati Pandey for all of his kindness and friendship in helping me learn most of my laboratory skills, Brian Sit for his helpful discussions and help in the lab, Matt Ward for his help with NRC prep and al his efforts in the lab. Dr Da Huang and Dr Keitel Cervantes-Salguero for their help in teaching me the relevant DNA origami techniques, Dr Mark Freeley for his help with AFM and HPLC. Thank you to Nikolaj Gadegaard and Paul Reynolds for contributing the EBL substrates, without their help this project would not have been possible. Thanks also to Roberto Buccafusca for all his help with the analytical chemistry. Thank you to all previoius and current members of the Ehler and Gautel Labs for all their helpful suggestions and discussion in lab meetings. Thank you to all members of the 2015/2016 membrs of the BBSRC LIDo cohort for their help and support over the years. Thank you also to Nadine Mogford for all of her help, compassion and dedication to all students on the LIDo programme. Thank you to the BBSRC for their support and funding.

Thank you to my family for their unwaivering support in helping me throughout my studies. Without my parents Richard and Teresa Hawkes as well as my parents in-law Gary and Nicola White, I would certainly not be where I am today.

Thank you to my wife and personal psychologist, Hayley White. Your contributions towards this thesis extends beyond meaasure and without your love, compassion and patience, I would not have been able to finshish this journey.

CONTENTS

LIST OF TABLES

LIST OF FIGURES

LIST OF ABBREVIATIONS AND ACRONYMS

AFM – Atomic Force Microscopy

AKT – Protein Kinase 2

Arp2/3 - Actin related proteins2/3

DCM- Dilated Cardiomyopathy

DGC – Dystrophin-associated Glycoprotein Complex

DLC1 – Deleted in Liver Cancer 1 protein

DNA – Deoxyribonucleic acid

ECM – Extracellular Matrix

ERK – Extracellular signal related kinase

FA – Focal Adhesion

FAK – Focal Adhesion Kinase

FERM – 4.1 Protein, Ezrin, Radixin, and Moesin

FHOD1 – formin homology domain-containing protein 1

FRET – Forster Resonance Energy Transfer

FRNK – FAK Related Non-Kinase

GEF – Guanin nucleotide exchange factor

HCM- Hypertrophic Cardiomyopathy

Hsp90 - heat shock protein 90

IDC – Intercalated Disc

ILK – Integrin Linked Kinase

IPP – Integrin-Linked Kinase, Pinch, Parvin

IQGAP1 - IQ Motif Containing GTPase Activating Protein 1

JNK – c-Jun N-terminal Kinase

KO – Knock Out

MAPK – Mitogen Activated Protein Kinases

MI – Myocardial Infarction

MtVcl – Metavinculin

NFκB - nuclear factor kappa-light-chain-enhancer of activated B cells

NRCs – Neonatal Rat Cardiomyocytes

PBS – Phosphate Buffered Saline

PDMS – poly(dimethylsiloxane)

PINCH - particularly interesting new cysteine-histidine–rich protein.

PIP2 - Phosphatidylinositol 4,5-bisphosphate

PIPKIγ - Type I gamma phosphatidylinositol phosphate kinase

PKC – Protein Kinase C

PO – Pressure Overload

PP1a – Protein phosphatase 1a

Pyk2 – Protein tyrosine kinase 2beta

RhoA – Ras homologue family member A.

RIAM - Rap1-GTP-interactin adapter molecule

RIE – Reactive Ion Etching

ROI – Region of Interest

RP-HPLC – Reverse Phase High Performance Liquid Chromatography

RT – Room temperature

Src – Proto-oncogene tyrosine protein kinase

ssDNA – single strand Deoxyribonucleic acid

TIAM1 - T-lymphoma invasion and metastasis-inducing protein 1

Tln - Talin

VASP – Vasodilator-Stimulated Phosphoprotein

Vcl – Vinculin

List of Appendices

PUBLICATIONS WHICH HAVE BEEN INCLUDED AS PART OF THIS THESIS:

1. PANDEY, P., HAWKES, W., HU, J., MEGONE, W. V., GAUTROT, J., ANILKUMAR, N., ZHANG, M., HIRVONEN, L., COX, S., EHLER, E., HONE, J., SHEETZ, M. & ISKRATSCH, T. 2018. Cardiomyocytes Sense Matrix Rigidity through a Combination of Muscle and Non-muscle Myosin Contractions. Dev Cell, 44, 326-336.
2. HAWKES, W., HUANG, D., REYNOLDS, P., HAMMOND, L., WARD, M., GADEGAARD, N., MARSHALL, J. F., ISKRATSCH, T. & PALMA, M. 2019. Probing the nanoscale organisation and multivalency of cell surface receptors: DNA origami nanoarrays for cellular studies with single-molecule control. *Faraday Discussions,* 219, 203-219.

1 INTRODUCTION

1.1 The Heart

The heart is the first functional organ to form in the developing embryo. As the size of the embryo increases, diffusion of oxygen to the cells at the centre becomes increasingly difficult and the heart is required to deliver oxygen. With continued development, the heart increases in size as cardiomyocytes proliferate and become increasingly organised to support oxygen demands. Throughout development, the cytoskeleton of cardiomyocytes becomes increasingly organised via cell-cell contacts, called intercalated discs (ICD), and cell-extracellular matrix (ECM) contacts at rib-like structures called costameres. These cell-cell and cell-ECM linkages play a major role in mechanically coupling cardiomyocytes with their environment as they respond to increases in haemodynamic load and changes in ECM composition during development and disease (Ward and Iskratsch, 2019).

The study of how cells physically interact with their mechanical environment to direct and inform behaviour is called mechanobiology. Cells exert forces upon their environment via specialist adhesion structures which "sense" the compliance of the ECM. Mechanically sensitive proteins at adhesion sites translate the corresponding forces into chemical signals, in a process called mechanotransduction (Iskratsch et al., 2014). Owing to their contractile nature, cardiomyocytes have a unique mechanotransduction regime, whereby cells are exposed to the regular forces from cellular tractions, in addition to cyclical forces from muscle contraction and haemodynamic filling of the chambers (Pandey et al., 2018, Ward and Iskratsch, 2019).

The primary contractile unit of cardiomyocytes is the sarcomere. This highly organised structure is formed of parallel filamentous actin (F-actin) and actin associated proteins, anchored to the z-discs at the lateral aspect of the sarcomere, interdigitated by antiparallel myosin filaments and associated proteins, anchored at the centre of the sarcomere (M-band). Upon electrical excitation and a corresponding release of calcium, myosin filaments engage with the actin and initiate a contraction, as described by the sliding filament theory (Huxley and Niedergerke, 1954, Huxley and Hanson, 1954). The sarcomere is repeated in series throughout the length of cardiomyocytes to form myofibrils that contract together in unison. In addition to coupling between cells, the sarcomere is also coupled to the ECM at the z-discs via the costameres, where transverse forces regulate mechanotransduction (Pardo et al., 1983, Ervasti, 2003).

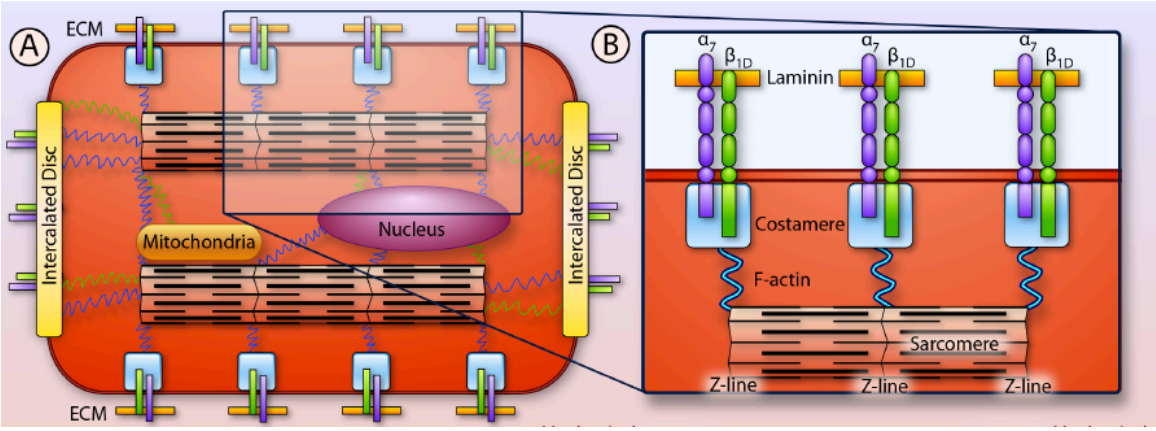

Figure 1.1. A) Schematic representation of the cytoskeletal structure of cardiomyocytes. B) Integrin heterodimers (green and purple) represent a fundamental link between the ECM and sarcomere. ECM = extracellular matrix, F-actin = filamentous actin. Figure from Israeli-Rosenberg et al., 2014.

1.2 Intercalated Discs, Costameres as Focal Adhesions

Cardiomyocytes have physical links both to their ECM and the surrounding cardiomyocytes. These physical links provide cardiomyocytes to opportunity for registration and integration of their contractile sarcomeres with the sarcomeres of surrounding cells for improved contraction efficiency (Lyon et al., 2015). Furthermore, integration of the sarcomere with cell-ECM structures affords cardiomyocyte the ability to "sense" the biomechanical and biochemical properties of their micro- and nano-environment to inform cell behaviours such as hypertrophy and survival (Hawkes et al.,

2019, Pandey et al., 2018, Israeli-Rosenberg et al., 2014). Intercellular binding is regulated by specialist cell-cell adhesion structures called intercalated discs, while bonds between the cell and the ECM are mediated via specialist cell-ECM adhesion structures called costameres (as depicted in Figure 1.1).

The ICD is the primary structure that facilitates transmission of contractile forces, electrical conduction and sequential alignment of sarcomeres between connected cardiomyocytes. Primarily, the ICD is formed of three structures, each with highly specific roles: namely, Desmosomes, Gap Junctions and Fascia Adherens (Figure 1.2). Desmosomes are specially designed for resisting the shear forces associated with coordinated contraction of the heart during systole, as mediated by inter-cellular junctions by desmocollin/desmoglen, which integrate with the desmin cytoskeleton and non-sarcomeric actin filaments (Estigoy et al., 2009, Garrod et al., 2005). Gap junctions are specialist electrical conduction sites due to the tightly packed intra-cellular connexin bonds and as such, play essential roles in conduction pathology such as atrial fibrillation (van der Velden and Jongsma, 2002). The fascia adherens are essential intra-cellular adhesion sites for cytoskeletal integration of adjoining cells, facilitating coordinated contraction and mechanotransduction and are thus, highly important in cardiomyocytes (Estigoy et al., 2009). Both N-Cadherins and E-cadherins are essential for myofibrillar organisation via integration with catenins and actin filaments. E-cadherins have also been suggested to stimulate the cell cycle pathway (Ferreira-Cornwell et al., 2002). More recent work has demonstrated that ICDs are involved in intra-cellular signalling and actin assembly/maintenance via associated with many proteins, such as vinculin, α-actinin and formin homology domain-containing protein 1 (Estigoy et al., 2009, Dwyer et al., 2014, Ehler, 2018)

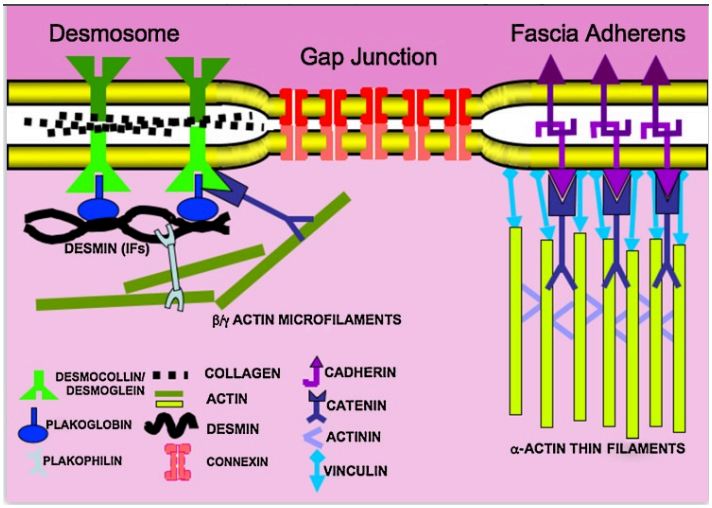

Figure 1.2. Schematic representation of the intercalated disc. The ICD is composed of three main structures, desmosomes, gap junctions and fascia adherens. In additional to providing structure support for cell-cell contacts, ICDs also facilitate the conduction of action potentials from one cell to another via the gap junction. Both muscle and non-muscle forms of actin are associated with the ICD and as such, many actin associated proteins are found at these sites. Common proteins include desmin, α-actinin, vinculin, catenin and cadherin. Ifs = intermediate filaments. (Estigoy et al., 2009).

Costameres are specialised structures that act to couple the sarcomere laterally, via the z-disc, to the ECM (Figure 1.1B & Figure 1.3). The integrin adhesion complex and the dystrophin-associated glycoprotein complex (DGC) form the two major components of the costamere (Ward and Iskratsch, 2019) and have both been established as mechanosensitive (Engler et al., 2008, Hersch et al., 2013, Lyon et al., 2015, Morikawa et al., 2017, Pandey et al., 2018). Although the dystroglycan complex is important for cardiomyocyte function, the integrin adhesion complex has received far more attention due to its dynamic responses to changes in the composition and mechanical properties of the ECM(Israeli-Rosenberg et al., 2014, Ward and Iskratsch, 2019).

The costameric integrin adhesion complex is often considered to be a specialised version of the focal adhesion (FA) found in adherent cells (Iskratsch et al., 2014, Israeli-Rosenberg et al., 2014, Sit et al., 2019). Actin associated proteins such as talin (Manso et al., 2013, Bogatan et al., 2015, Manso et al., 2017, Pandey et al., 2018), vinculin (Pardo et al., 1983, Mondello et al., 1996, Zemljic-Harpf et al., 2007) and α-actinin act to tether the sarcomere to the ECM by binding integrins to the z-disc (Figure 1.1C). Furthermore, many costameric proteins have been identified to activate signalling pathways associated with development and disease (Samarel, 2005, Israeli-Rosenberg et al., 2014, Sit et al., 2019, Ward and Iskratsch, 2019).

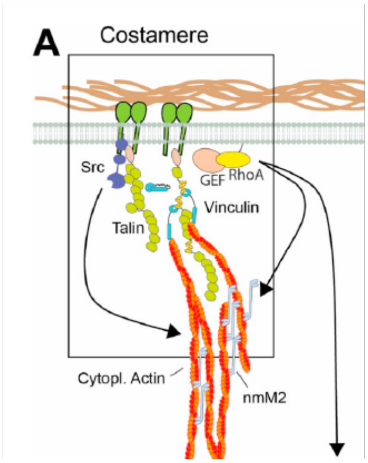

Figure 1.3. Key proteins found at the cardiomyocyte costamere. Transmembranous integrins (dark green) bind to the ECM and recruit key signalling proteins such as Src, GEF, RhoA in addition to structural protein such as talin and vinculin, which act as adaptors to facilitate integration of the actin cytoskeleton with cell-ECM binding sites. Src = Proto-oncogene tyrosine protein kinase, GEF = Guanine nucleotide exchange factor, RhoA = Ras homologue family member A. Adapted from Ward & Iskratsch, 2019.

1.3 Structure and Function of Integrins

Integrins are transmembranous proteins, consisting of α and β subunits that non-covalently associate with one another to form a heterodimer. There are 18 α and 8 β subunits, that combine to form 24 different subtypes that recognise specific components of the ECM, such as collagen, fibronectin and laminin. The majority of the integrin structure is situated outside of the cell membrane, where they bind ECM ligands. The extra-cellular components consist of the membrane-proximal calf domains, a flexible knee domain, the thigh domain and the head domain (Figure 1.4). Conformational changes occur at the knee and head domains to regulate the affinity for ECM ligands (Gahmberg et al., 2009). The relatively short cytoplasmic domain consists of 40-60 amino acids which contain binding sites for numerous proteins.

The extra-cellular domain can exist in a number of conformations that regulate the binding affinity to ECM ligands (Figure 1.4). In their state of lowest affinity, integrins adopt a closed confirmation where the head domains are closely packed together and the knee domain is bent, positioning the heads close the membrane. In their state of medium ligand affinity, the integrin thigh and knee domains are fully extended but the head

domains remain closely packed and closed. Upon full activation, integrins are fully extended with the heads in an open confirmation where they are most likely to bind to ECM ligands. The activation of integrins from closed to open states can be regulated by intracellular signals (termed inside-out signalling) and extracellular signals (termed outside-in signalling). The high affinity between α5β1 integrins and the RGD domain of fibronectin (Li and Springer, 2017) can result in integrin activation via proximity alone and is a good example of outside-in signalling. The binding of proteins such as talin to β-integrin tails is a good example of inside-out signalling, where this interaction separates the α and β tails, causing the extracellular domain to extend into the open conformation (Calderwood et al., 2003, Kim et al., 2012).

The β integrin subtype is considered to be responsible for providing bindings sites for proteins at the cytoplasmic tail (Legate and Fassler, 2009) although a number of protein binding sites have also been identified on the tail of α subunits (Bachmann et al., 2019). Integrins themselves do not have any intracellular signalling capacity but are able to

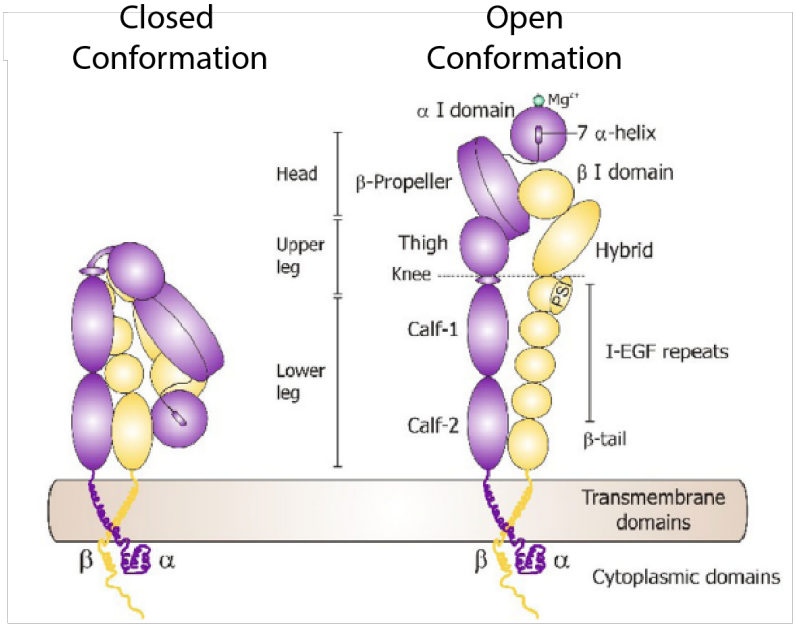

Figure 1.4. Conformation and structure of integrin heterodimers. In the closed conformation, the head domain is closed and located close to the cell membrane. Conformational changes occur primarily around the knee joint between the thigh and calf domains. Integrin-ECM interactions occur at the head domain where protein interaction can occur on either of the head domains or via combination of the two. Taken from Ghamberg et al., 2009.

recruit a number of proteins capable of initiating signalling cascades. The occurs

primarily via two highly conserved domains on the integrin tails, the NPxY and NxxY domains (Humphries et al., 2006, Gahmberg et al., 2009, Legate and Fassler, 2009). As a result, many proteins compete for a limited number of binding sites on integrin tails. The regulation of adaptor binding to integrin tails occurs via changes in integrin confirmation and affinity modification of proteins, via phosphorylation of the serine threonine rich tail domain (Calderwood et al., 2003, Bachmann et al., 2019).

Proteins that bind integrin tails are often termed adaptor proteins due to the way in which they recruit and bind to other proteins. Adaptors can be classified into three groups depending on their major functions; 1) structural adaptors bind directly to integrin tails and provide a physical link to the actin cytoskeleton, 2) scaffolding proteins recruit other proteins for structural or signalling roles and 3) catalytic proteins regulate signalling pathways from the site of the integrin adhesion. The clustering of integrins at adhesion sites acts to assemble of a complex array of adaptor proteins to form FAs, which then participate in mechanotransduction (Iskratsch et al., 2014).

Costameric integrin adhesion sites represent a structural link to the ECM for essential functions that regulate cardiomyocyte behaviour. In-vivo studies have identified a clear role of costameric proteins such as talin (Manso et al., 2013, Manso et al., 2017), vinculin (Vasile et al., 2006, Zemljic-Harpf et al., 2007), focal adhesion kinase (FAK, (Peng et al., 2006)), paxillin (Hirth et al., 2016) and Kindlin (Dowling et al., 2008) in regulating the physiological and pathological behaviours. Furthermore, in-vitro studies have begun to unravel the costameric mechanisms of integrin mediated mechanotransduction, and their importance in normal cardiomyocyte function (Torsoni et al., 2003, Engler et al., 2008, Tangney et al., 2013, Pandey et al., 2018). Thus, the following section will discuss the field of cell spreading and its importance in understanding the role of integrin adhesion at the costamere.

1.4 The Cardiomyocyte Focal Adhesion In-Vitro vs the Costamere In-Vivo

The field of in-vitro cell spreading and integrin mediated mechanotransduction is vast and has been seminal in understanding how cell-ECM interactions are fundamental to cell behaviour and survival (Iskratsch et al., 2014, Wolfenson et al., 2019). Research on the role of costameric integrin adhesion is no exception and in-vitro studies have become increasingly prevalent since the discovery that integrin adhesions in culture contain many of the same components found in the costamere in-vivo (Ervasti, 2003, Samarel, 2005).

Furthermore, technological development in the field of induced pluripotent stem cell derived cardiomyocytes has led to a surge in in-vitro cardiomyocyte research (Mummery, 2018).

In culture, neonatal cardiomyocytes (particularly neonatal rat cardiomyocytes (Samarel, 2005)) disassemble their cytoskeleton, including IDC and costameric structures, to remodel their adhesive structures and adapt to the two dimension culture environment. In order to achieve this, cardiomyocytes adhere and spread over their environment via the assembly of adhesive structure that resemble those found in the traditional FA (Samarel, 2014, Sit et al., 2019, Ward and Iskratsch, 2019). Isolated neonatal cardiomyocytes also form mechanically sensitive costamere-like structures that resemble the lateral transmission of force from the z-disc to the ECM (Danowski et al., 1992). However, cardiomyocyte spreading in-vitro is highly reliant upon integrin adhesion structures for cell morphology and cytoskeletal organisation. The resulting dominance of integrin mediated mechanotransduction and resulting cell behaviour is likely to differ to that observed in-vivo where the role of ICDs is highly important.

In light of the dominant nature of integrin adhesions in-vitro, it is highly important that the structure and function of adhesion plaques resemble their costameric counterparts. Indeed, many of the important structural and signalling costameric proteins such as talin (Manso et al., 2013, Pandey et al., 2018), vinculin (Rudiger et al., 1998), focal adhesion kinase (Torsoni et al., 2003, Lal et al., 2007), kindlin (Qi et al., 2015), protocol-oncogene tyrosine-protein kinase Src (Src, (Pandey et al., 2018)) are found at cardiomyocyte FAs. Consequently, important costameric signalling cascades such as the hypertrophic pathways can be easily recapitulated in vitro (Johnston et al., 2009, Pandey et al., 2018, Manso et al., 2013, Ogawa et al., 2000). As a result, in-vitro cardiomyocyte research has led to a wealth of research in the role of the costamere/integrin adhesion complex in cardiomyopathy. In particular, in-vitro culturing of cardiomyocytes benefits from the ability to engineer the chemical and mechanical properties of culture surfaces and mimic the highly dynamic nature of the cardiac ECM.

1.5 The Changing Cardiac ECM: Dynamic Chemical and Mechanical Properties of the Heart

The cardiac ECM is composed of a complex meshwork of proteoglycans, glycosaminoglycans and glycoproteins which primarily contains collagens, fibronectin and laminin (Lockhart et al., 2011, Rienks et al., 2014, Hughes and Jacobs, 2017). While

providing a scaffold, it also functions to deliver extra-cellular chemical cues to inform cell behaviour. During development, the fibrillar collagens (types I, III, IV & VI) are highly expressed and are essential for embryonic development (Lockhart et al., 2011, Williams et al., 2014). Fibronectin (especially EIIIA and EIIIB splice variants) is also highly expressed during development up until birth, when expression steadily declines during postnatal development and into adulthood (Kim et al., 1999, Lockhart et al., 2011). Laminin (with alpha chains 1-5) is expressed at low levels during embryonic development and becomes upregulated during post-natal development, in an opposite trend to fibronectin (Kim et al., 1999, Ringelmann et al., 1999, Oliviéro et al., 2000). During ageing and in diseased states, the cardiac ECM undergoes a transition back to a more a developmental ECM phenotype, where fibronectin becomes upregulated (Mamuya and Brecher, 1992, Burgess et al., 2001).

In parallel with changes to ECM composition and deposition, cardiomyocytes alter their integrin expression to match the major ECM components. Cardiomyocytes predominantly express $\alpha1\beta1$, $\alpha3\beta1$, $\alpha5\beta1$, $\alpha6\beta1$ and $\alpha7\beta1$ integrins (Figure 1.5) which preferentially bind to collagen ($\alpha1\beta1$), fibronectin ($\alpha5\beta1$, $\alpha6\beta$) and laminin ($\alpha3\beta1$, $\alpha7\beta1$). Expression of different integrin subtypes mirrors the expression of ECM proteins. Collagen is upregulated during development where it provides a key structural role and a network of highways for migration of cardiac fibroblasts as the heart develops. Collagen expression also remains relatively stable into adulthood and becomes upregulated at sites of cardiac damage when cardiac fibroblasts increase collagen deposition during fibrosis and scar formation (Rog-Zielinska et al., 2016). Fibronectin and laminin ligands, however, exhibit more dynamic expression during development and disease, suggesting a more active role in cardiomyocyte outside-in signalling (Ward and Iskratsch, 2019). As a result, cardiomyocytes predominantly express the fibronectin binding $\alpha v\beta1$ and $\alpha5\beta1$ integrin subtypes during development which become downregulated after birth, when the laminin binding $\alpha7\beta1$ subtype becomes the predominant subtype (Brancaccio et al., 1998). Likewise, during disease, cardiomyocyte integrin expression switches back to the developmental phenotype where fibronectin binding integrin subtypes become dominant (Babbitt et al., 2002, Balasubramanian and Kuppuswamy, 2003, Johnston et al., 2009, Suryakumar et al., 2010). The $\beta1$ integrin is the dominant beta-subtype in the heart throughout the lifespan (Israeli-Rosenberg et al., 2014, Ward and Iskratsch, 2019).

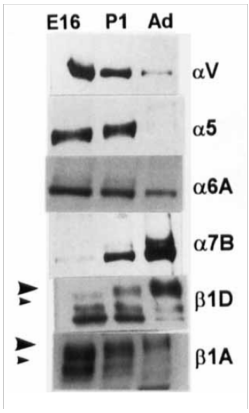

Figure 1.5. Cardiomyocyte integrin subtype expression during development and into adulthood in the mouse heart. Samples were collected at embryonic day 16 (E16), post-natal day 1(P1) and in adult (Ad) mice. Data indicates that the fibronectin binding αv and α5 and α6 subtypes are dominant during development. During post-natal development, fibronectin binding subtypes become down regulated and replaced by dominant expression of the laminin binding α7 subtypes. The β1 subtypes is dominant in the heart but exhibits dynamic expression of the β1A and β1D splice variants. Figure adapted from Brancaccio et al., 1998.

Variations in both the ligand and integrin subtype via alternative splicing further complicate matters, providing cardiomyocytes with an additional means to distinguish different ligands within the ECM. Numerous fibronectin splice variants are known to exist, of which, the EIIIA and EIIIB alternative splice variants play essential roles in development of the heart (Lockhart et al., 2011). During adulthood, alternative splicing of fibronectin is less frequent, but is associated with injury and pathology (White et al., 2008). However, little is known about the affinity of α5β1 for fibronectin variants. Laminins are comprised of α, β and γ chains which form numerous combinations. Integrins bind directly to the α chain, which has 5 different isoforms (α1-5). During development, the α1 and α2 isoforms are predominantly expressed which switches to α5 in the adult heart (Miner et al., 1997, Ringelmann et al., 1999, Oliviéro et al., 2000). The laminin binding α7X2β1 integrin (an alternative splice variant of α7β1) bind most strongly to the α1 laminin chain, while the α7Xβ1 integrin splice variant binds most strongly to α5 laminin chains. The laminin binding α6β1 and α3β1integrins bind α1, 3 and 5 chains and α2, 3 and 5 chains, respectively (Nishiuchi et al., 2006). Finally, although the β1 integrin is stably expressed in cardiomyocytes, splice variants exists and

differ during development. The β1A splice variant is strongly expressed during development and plays a key role in early myogenesis and maturation. The β1D splice variant then becomes expressed in late development and is the dominant isoform in adult cardiomyocytes (Brancaccio et al., 1998, Maitra et al., 2000). Importantly, these β1 variants have non-interchangeable roles and their coordinated expression is essential for myogenesis (Cachaco et al., 2003). Therefore, via different integrin subtypes and splice variants, cardiomyocytes have an extensive repertoire of tools to detect changes in ECM composition that occur during development and disease.

In addition to recognising specific chemical components, cells also utilise integrin adhesions to test the mechanical properties of the ECM, via rigidity sensing (Iskratsch et al., 2014, Wolfenson et al., 2019). The dynamic nature of the cardiac ECM during development and disease also results in changes to its mechanical properties and therefore, rigidity sensing dynamics. During development, the stiffness of the heart is thought to range between 1-10 kPa, which increases to 10-20 kPa in the adult left ventricle, which further increases in excess of 50 kPa during diseased fibrotic states (Ward and Iskratsch, 2019). While, the range of measurements was shown by Ward & Iskratsch (2019) to vary significantly by method and model organism, all studies are in agreement that the heart undergoes gradual stiffening during development, with further stiffening during diseased states such as hypertrophic cardiomyopathy (HCM) and fibrosis. Thus, via a dynamic physical, chemical and mechanical environment, the cardiac ECM stimulates significant changes to integrin mediated mechanotransduction during development and disease.

Being positioned at the cell membrane-ECM interface makes integrins one of the first responders to chemical and mechanical cues. Furthermore, by providing a physical link between the ECM, mechanosensitive proteins and the contractile sarcomere, cardiomyocytes have the ability to detect and respond to chemical and mechanical signals in a highly complex manner. The following section with focus on this link at the costamere and aims to discuss what is known about key mechanosensitive proteins.

1.6 Mechanotransduction at the Costamere

Mechanotransduction in cardiomyocytes is a unique and complex process, owing to the combination of passive (ECM remodelling, stiffness and haemodynamic loading) and

active (myofibrillar and non-myofibrillar contractility) forces/stimuli present within the heart. Costameres have been regarded as important mechanotransducers since observations that they directly transmit contractile forces to the surrounding ECM (Danowski et al., 1992). Others have also demonstrated that via the mechanical linkage of myofibrils to the ECM, stretching (e.g. stretching of the ventricle during haemodynamic loading) is detected across the entire cell, resulting in a highly complex mechanotransduction response (Mansour et al., 2004). Integrins play an essential role in mediating this response. For example, β1 integrins are required to activate the hypertrophic response after both pharmacological treatment (Ross et al., 1998) and mechanical stretching (Lal et al., 2007), via phosphorylation of mitogen-activated protein kinases (MAPK) p38, protein kinase 2(AKT) and Extra-cellular signal Related Kinase 1/2 (ERK ½) and c-Jun N-terminal Kinase (JNK), as seen in Figure 1.6. Many downstream consequences of cardiomyocyte mechanotransduction have been well defined and strong links have been reported with gene expression and cardiomyocyte behaviours such as hypertrophy (Samarel, 2005, Buyandelger et al., 2011, Samarel, 2014, Israeli-Rosenberg et al., 2014, Jaka et al., 2015, Sit et al., 2019, Ward and Iskratsch, 2019). However, the molecular mechanisms (i.e. mechanical stretching/unfolding, ligand affinity/avidity, molecular clutches, protein binding partners) that regulate integrin mediated signalling responses at the costamere are less well understood. The following section will present and discuss the major costameric players in mechanotransduction.

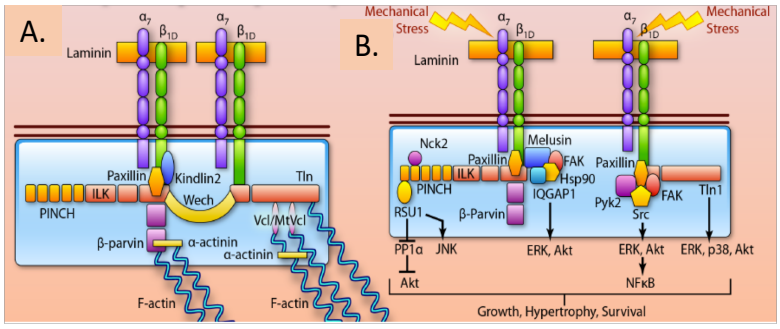

Figure 1.6. Schematic depiction of known adaptor proteins present at the intercalated disc. A) Many scaffolding proteins such as paxillin, kindlin, talin and α-actinin have essential structural roles in bridging the connection between the cytoskeleton and the ECM bound integrins. B) Stimulation of the costameric structure,s and associated signalling proteins, with mechanical stress initiates signalling pathways important for growth, hypertrophy and survival. Tln – talin, FAK – focal adhesion kinase, Src – Proto-

oncogene tyrosine protein kinase, ERK – Extracellular signal related kinase, Akt – Protein kinase 2, NFκB - nuclear factor kappa-light-chain-enhancer of activated B cells, PP1a – Protein phosphatase 1a, Pyk2 – Protein tyrosine kinase 2beta, Vcl – Vinculin, MtVcl – Metavinculin, IQGAP1 - IQ Motif Containing GTPase Activating Protein 1, Hsp90 - heat shock protein 90, ILK – Integrin linked kinase, PINCH - particularly interesting new cysteine-histidine–rich protein.

1.6.1 Talin

The large protein talin is ubiquitously expressed in cells and has received a lot of attention for its essential role in FA dynamics (Klapholz and Brown, 2017). Within the cardiomyocyte, talin is strongly enriched at the costameres and intercalated discs (Manso et al., 2013, Wu et al., 2015, Manso et al., 2017) where it is known to provide a structural role by providing a biomechanical link between integrins and F-actin (Samarel, 2005, del Rio et al., 2009, Manso et al., 2017). Consistent with its structural role in adhesion reinforcement, talin unfolds under tension to reveal cryptic binding sites that act to reinforce the talin-actin bond via the recruitment of additional vinculin (del Rio et al., 2009). Talin is also a potent activator of integrins: via disruption of the bond between the α and β integrin tails, they can switch integrins to their high affinity conformation (Calderwood et al., 1999, Kim et al., 2012, Klapholz and Brown, 2017), thereby regulating integrin adhesion dynamics.

Talin is a 260 kDa protein consisting of an N-terminal head domain and a C-terminal rod domain (Figure 1.7). The N-terminal region contains ~ 400 amino acids that form the FERM (protein 4.1, ezrin, radixin, moesin) domain which contains the F1, F2, F3 and F0 subdomains. The F3 subdomain bind β integrin tails with high affinity, which can be traced to a single residue depending on the talin isoform (Elliott et al., 2010, Qi et al., 2016). Talin contains binding sites for many other proteins, as shown in Figure 1.7.

Vertebrates have two talin isoforms, talin 1 and 2, which exhibit differential expression during cardiac development and disease. Talin 1 is strongly expressed during embryonic development, which becomes down regulated after birth, when talin 2 is upregulated (Manso et al., 2013). This likely reflects the change in integrin expression due to stronger affinity of talin 1 and 2 for β1A and β1D integrins, respectively (Anthis et al., 2010). The binding affinity of talin 2 for β1D is highly important for mediating cellular traction

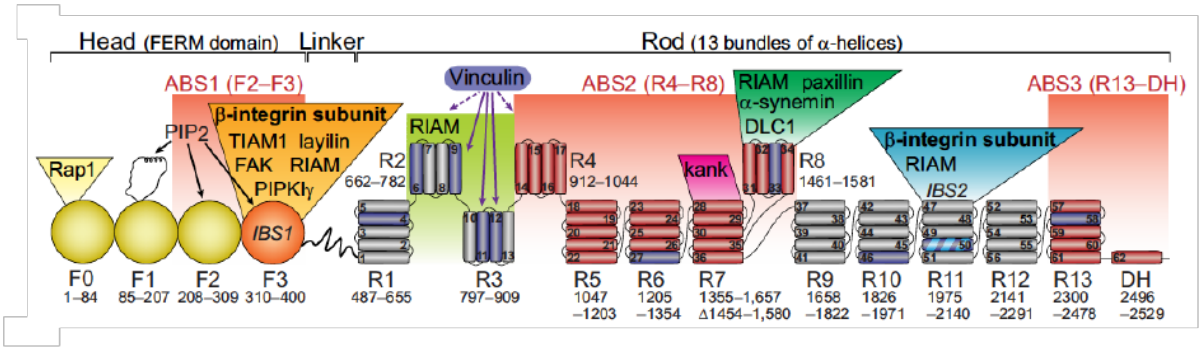

Figure 1.7. Talin as a complex adapter protein. The N-terminal head (FERM) domain contains four subdomains (F0-3) which contains actin binding cites on F2 & F3 and an integrin binding site on F3. The integrin binding site on F3 competes with other adaptor proteins such as FAK (focal adhesion kinase), laylin, TIAM1 (T-lymphoma invasion and metastasis-inducing protein 1), RIAM (Rap1-GTP-interactin adapter molecule) and PIPKIγ (Type I gamma phosphatidylinositol phosphate kinase). The rod domain is connected to the head domain via an ~80 amino acid linker between F3 and R1. The rod domain contains 61 α-helices, organised into 13 bundles (R1-13). Cryptic vinculin binding sites are also indicated for R2, R3 & R4. The numerous actin binding sites on the rod domain are also indicated for R4-R8 and R13-DH. Protein binding sites are indicated. IBS – Integrin binding site, ABS – actin binding site. Domain numbering is consistent with Talin 1. Image from Klapholz & Brown, 2017.

forces (Anthis et al., 2010, Qi et al., 2016, Pandey et al., 2018). However, talin 1 is able to compensate for loss of talin 2 in cardiomyocytes during normal development and basal functioning, suggesting a level of redundancy between the two isoforms (Manso et al., 2017).

Talin also plays a key role in development and basal functioning of the heart. Loss of talin is embryonic lethal in drosophila (Bogatan et al., 2015) and zebra fish (Wu et al., 2015), with cardiomyocytes exhibiting severe structural deformities and failure to proliferate. Cre mediated Talin 1 and 2 knock out (KO) mice are born with

morphologically normal hearts, suggesting that talin could be essential during early developmental stages (in this study, Cre is only expressed from E10.5). However, these mice develop severe dilated cardiomyopathy 4 weeks post birth, with 0% survival after 8 weeks (Manso et al., 2017). Evaluation of cardiomyocyte structural integrity revealed severely disorganised costameric and sarcomeric structures, due to downregulation of β1 integrins (Manso et al., 2017).

Recent work from the Iskratsch lab has revealed an important role for talin in cardiomyocyte rigidity sensing (Pandey et al., 2018). The use of FRET tension sensors revealed that talin undergoes specific stretching regimes depending on substrate rigidity; with no stretching on soft, cyclic stretching at physiological and constant stretching on stiff substrates. Furthermore, activation of the non-receptor tyrosine kinase Src was also upregulated according to substrate stiffness. From this finding, it was hypothesised that talin signalling may form a feedback loop, via Src and the actin assembly protein FHOD1, to facilitate rigidity sensing (Figure 1.8). Others have also demonstrated that talin 1 is responsible for mediation of a hypertrophic response in cardiomyocytes, via β-adrenergic signalling, which talin 2 cannot do on its own (Manso et al., 2013). Recent observations

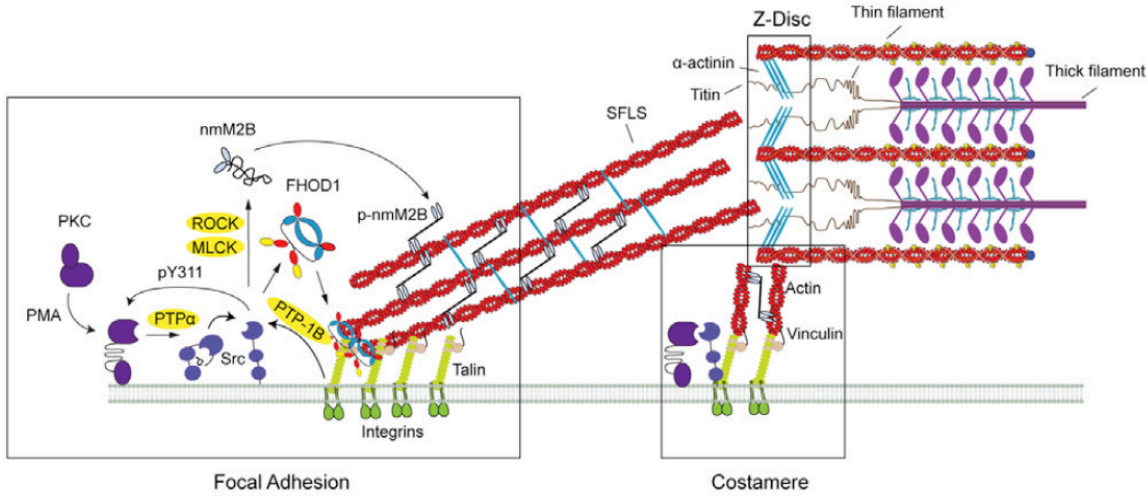

Figure 1.8. Talin participates in in a rigidity sensing feedback loop in cardiomyocytes. Talin stretching and mechanotransduction on different stiffnesses occurs alongside stiffness dependent feedback loop. The proposed feedback loop starts with talin stretching, resulting in activation of Src and downstream activation of the actin assembly protein FHOD1 and non-muscle myosin 2B (p-nmM2B) which in turn increases cytoskeletal contractility, stimulating/maintaining talin stretching, restarting the feedback loop. Model presented by Pandey et al., 2018.

have also revealed that complete unfolding of talin may facilitate the recruitment of other proteins, such as Deleted in Liver Cancer 1 (DLC1), that play a key role in heart development and disease (Ward and Iskratsch, 2019). The findings discussed above present talin as a key hub of mechanotransduction in cardiomyocytes. Thus, talin represents an exciting target for future investigations to further understand the molecular regulation of mechanotransduction.

1.6.2 Vinculin

Vinculin is a 116 kDa adaptor protein that localises to FAs, costameres and the ICDs. At the costamere, vinculin primarily acts as a structural adapter protein by reinforcing the talin-actin bond. Vinculin possesses a number of binding sites for costameric adaptors, including α-actinin, vasodilator-stimulated phosphoprotein (VASP), paxillin and protein kinase C α (PKCα), demonstrating its role as a structural adaptor (Ziegler et al., 2006). Figure 1.9 displays the structure of vinculin and illustrates the multiple protein binding sites. Vinculin exists in a closed, auto-inhibited state which can be released via binding

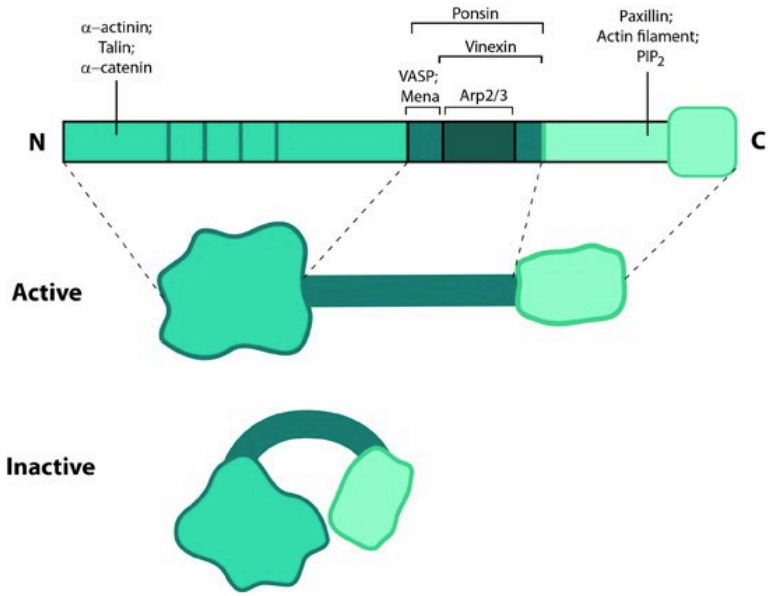

Figure 1.9. Structure of vinculin as a scaffolding adaptor protein. Vinculin exists in an auto-inhibited state which is released upon talin binding to the N terminal domain. Numerous protein binding sites are located along the protein, including talin, α-actinin, α-catenin, Ponsin, Vinexin, VASP (vasodilator stimulated phosphoprotein), Mena, Arp2/3 (actin related proteins2/3), paxillin, actin and PIP2 (Phosphatidylinositol 4,5-bisphosphate). Source: MBInfo, mechanobio.info.

to talin in the cytosol, or upon recruitment to talin when under tension (del Rio et al., 2009, Austen et al., 2015, Atherton et al., Preprint). Upon recruitment to FAs, vinculin mediates the transmission of forces between the contractile cytoskeleton and the ECM by reinforcing the talin-actin bond (del Rio et al., 2009, Pasapera et al., 2010, Yao et al., 2016), framing vinculin as a key mechanotransducer. However, recent observations that vinculin forms a complex with talin within the cytosol, which then goes on to promote FA assembly in a force independent process, suggest that vinculin may play a more complex and activate role in FA mechanotransduction than previously thought (Atherton et al., Preprint).

Skeletal and cardiac muscle expresses an alternative spliced variant of vinculin, called metavinculin, which contains a 68-amino acid insert within the vinculin tail domain (Belkin et al., 1988, Rudiger et al., 1998). The metavinculin insert domain contains a unique α-helix insert which causes a differential actin bundling phenotype, resulting in thinner F-actin structures (Rudiger et al., 1998, Rangarajan et al., 2010). Within the metavinculin insert, three point mutations have been associated with cardiomyopathy through disruption to actin bundling, disorganisation of IDC structure and loss of costameric localisation (Olson et al., 2002, Vasile et al., 2006).

Within the heart, loss of function and knockout studies have begun to highlight the role of vinculin in cardiomyocytes. Cre recombinase ablation of vinculin in mouse cardiomyocytes (homozygous KO from E10.5 onwards), resulted in phenotypically normal mice being born with preserved cardiac function. From 6 weeks of age, ventricular tachycardia resulted in sudden death due to poor electrical conduction and severe disruption to ICD structure (Zemljic-Harpf et al., 2007). Disruption to the costameric and z-disc structure was observed but the authors were unable to differentiate between the role of vinculin at the ICD or costamere. This was later achieved using atomic force microscopy (AFM) to evaluate the membrane stiffness and costamere mechanics of isolated vinculin-null cardiomyocytes (Tangney et al., 2013). Compared to wild type controls, vinculin-null hearts had 55% lower transverse cortical stiffness, which was hypothesised to be the result of decreased cytoskeletal tension between neighbouring costameres. Furthermore, vinculin null cardiomyocytes were 40% less likely to bind to fibronectin coated AFM probes, which was likely due to decreased integrin expression in these cardiomyocytes (Zemljic-Harpf et al., 2007). These results suggest that vinculin has a key role in regulating the structural integrity of cardiomyocytes, via maintenance of the mechanical link between the z-disc and the ECM. Thus, via its interaction with talin,

vinculin represents a core component of the costamere as a structural adaptor and would thus participate strongly in mechanotransduction.

1.6.3 Focal Adhesion Kinase (FAK)

FAK is a nonreceptor tyrosine kinase that localises to the costamere and plays a key role in regulating hypertrophic signalling pathways (Israeli-Rosenberg et al., 2014, Samarel, 2014). Localisation of FAK to costameres occurs via coordinated interactions with paxillin, talin and Src (Frame et al., 2010, Israeli-Rosenberg et al., 2014). FAK also has an alternative splice variant, FAK-related nonkinase (FRNK) which acts as a dominant negative mutant of FAK activity (DiMichele et al., 2009). Similar to talin, FAK contains a FERM domain, which can release other FAK molecules from their autoinhibited state, resulting in auto-phosphorylation of Y397, enabling binding to the non-receptor tyrosine kinase Src (Frame et al., 2010).

Genetic ablation studies have demonstrated a clear role for FAK in development and disease. Embryonic deletion of FAK in mice is lethal by E18.5, with hearts exhibiting ventricular wall defects (Peng et al., 2006). However, perinatal deletion of heart specific FAK in mice and investigation of heart development in their offspring, resulted in phenotypically normal mice, suggesting that FAK is not required for basal heart function (DiMichele et al., 2006). A much stronger role for FAK is established upon exposure of FAK KO hearts to pressure overload (PO) via aortic constriction. Compared to control littermates, FAK-KO mouse hearts exhibited a blunted hypertrophic response, suggesting that FAK plays a key role in the compensatory response to hypertrophic stimuli (Peng et al., 2006, DiMichele et al., 2006, Peng et al., 2008).

In cardiomyocytes, mechanical stretching of cells cultured on flexible polymer substrates, results in rapid phosphorylation of FAK Y-397, Y-681 and Y-295 in a β1D integrin dependent manner (Torsoni et al., 2003, Lal et al., 2007). Furthermore, β1D integrin dependent FAK phosphorylation was found to cooperate with angiotensin II receptor activity, another regulator of hypertrophic signalling (Kagiyama et al., 2002, Zhou et al., 2016). Furthermore, FAK/angiontensin II hypertrophy was also strongly affected by the presence of FRNK (Lal et al., 2007), suggesting a complex mechanosignalling network. Upon stretch induced activation, FAK translocates from the perinuclear region to the costameres, where it participates in hypertrophic signalling via activation of the MAPKs ERK, p38 and JNK (Torsoni et al., 2003, Lal et al., 2007). Additional studies in non-

cardiomyocytes have also revealed a role for FAK in activation of Rho-family GTPases, suggesting a potential additional role in regulation of cytoskeletal dynamics (Mitra et al., 2005). The key to the underlying regulation and activity of FAK may be due to an important interaction with Src (Frame et al., 2010). Upon release from its auto-inhibited state, FAK is able to phosphorylate itself at Y-397, permitting Src bidning which activates FAK to its fully catalytic state via phosphorylation of Y-576 and Y-577, which cannot then be deactivated (Mitra et al., 2005, Frame et al., 2010). Consequent formation of a complex with Src may play an important role in costamere localisation and activation of Src mediated signalling cascades.

A more recent study in zebra fish embryos has further demonstrated the complexity of FAK activity and regulation at the costamere. The results reported that paxillin acts to stabilise FAK activity and that together, the two proteins are required for vinculin activation and costameric localisation (Hirth et al., 2016). While the mechanism of how FAK and paxillin regulate vinculin recruitment is unknown, it is intriguing to hypothesise that by acting as a scaffolding adaptor for Src, FAK may facilitate rigidity sensing via a recently proposed Src feedback loop (Pandey et al., 2018).

1.6.4 Other Integrin Associated Proteins in Cardiomyocytes.

Although talin, vinculin and FAK have received much attention as costameric mechanosensors, there are a number of other, less well understood, proteins that also localise to the costamere. Among these is the IPP complex, containing the proteins integrin-linked kinase (ILK), PINCH and PARVIN , which assemble within the cytosol before binding to β1 integrin tails. Although initially thought to possess a catalytic capacity, ILK is a pseudo kinase, which primarily functions as a scaffolding adaptor protein (Legate et al., 2006, Wickstrom et al., 2010). In this effect, the IPP complex has been identified to bind a number of costameric proteins, such as vinculin and paxillin in addition to F-actin (Legate et al., 2006, Israeli-Rosenberg et al., 2014). Furthermore, knock out of ILK or PINCH results in postnatal lethality and cardiomyopathy due to the induction of dilated cardiomyopathy (DCM) and reduced contractility, establishing the role of the IPP complex as an important structural adaptor (Liang et al., 2009, Meder et al., 2011). Outside of the heart, the IPP complex has been shown to provide structural stability to integrin adhesion sites in a force-dependent manner, by decreasing integrin turnover and permitting mechanotransduction (Vakaloglou et al., 2016). However, the

mechanosensitive role of the IPP within muscle is not so clear and further research is required (Vakaloglou et al., 2012).

Kindlin is another scaffolding adaptor protein which can activate β1 integrin via localisation to costameres and direct binding to the integrin cytoplasmic tail (Israeli-Rosenberg et al., 2014, Li et al., 2017). Similar to vinculin, genetic ablation studies have revealed significant disruption of the sarcomeric-costamere interaction and highly irregular IDC structures, with difficulty in differentiating the two effects. Importantly, Kindlin negative mice died during early embryogenesis suggesting a key role for Kindlin in heart development (Dowling et al., 2008). Uncovering the crystal structure of Kindlin-2 (expressed within the heart) revealed that Kindlins control integrin activation by switching from a monomeric to dimeric state, in a manner different to that of talin (Li et al., 2017). Furthermore, Kindlin mediated integrin activation has also been found to enhance integrin-talin interactions, and may function as a synergistic adaptor protein within the mechanotransduction process (Montanez et al., 2008). However, knowledge and understanding of Kindlin protein binding partners remains elusive and the exact role of Kindlin as a costameric structural adaptor is not well understood. More recent work in immortalised kidney fibroblasts negative for Kindlin-2, demonstrated that during nascent adhesion formation, Kindlin-2 recruits paxillin which together forms a complex with FAK, activating signalling pathways involved in rigidity sensing (Theodosiou et al., 2016). However, this was not the case in mature focal adhesions and it is, therefore, difficult to relate these findings to the potential function of Kindlin-2 at the costamere.

1.7 Regulation of the Actin Cytoskeleton

The assembly of a contractile cytoskeleton is essential for the function of cardiomyocytes and, as a result, proteins that regulate polymerisation and maintenance of actin filaments are highly important for heart function. The nucleation and polymerisation of actin filaments is an energetically unfavourable process that requires actin assembly proteins. These can be classified into three groups; (1) The Arp2/3 complex which promoted the formation of branched actin filaments, (2) WH2 domain containing proteins such as spire and leiomodin and (3) the formin family of proteins which both nucleate actin to form linear actin filaments (Randall and Ehler, 2014). The WH2 containing protein leiomodin binds actin filament at the slow growing, pointed end and play an essential role in myofibrillogenesis (Chereau et al., 2008). Formins bind to the fast growing, barbed end

of actin filaments, where they work in a processive way by moving along filaments as they grow (Randall and Ehler, 2014). Recent data in cardiomyocytes demonstrates that the formin FHOD1 can be recruited and activated downstream of integrin signalling (Pandey et al., 2018). Furthermore, additional studies in non-muscle cells have also identified FHOD1 as an important member of the integrin mechanosensing machinery (Iskratsch et al., 2013, Changede et al., 2015). Therefore, formins represent an exciting area for future research into cardiomyocyte rigidity sensing.

The formin family of proteins are characterised by the presence of formin-homology domains 1 and 2, which recruit and nucleate actin, respectively. Inactive formins adopt an auto-inhibited state which is released upon binding of a Rho GTPase to the N-terminal GTPase binding domain (GBD). This enables dimerisation of the FH2 domain with other formins, resulting in the formation of a donut shaped heterodimer (Figure 1.10). There are several members of the formin family that have been divided into serval classes; mouse diaphanous related formins (mDia), formin like proteins (FRL), formin homology 2 domain containing proteins (FHOD), dishevelled-associated activator of

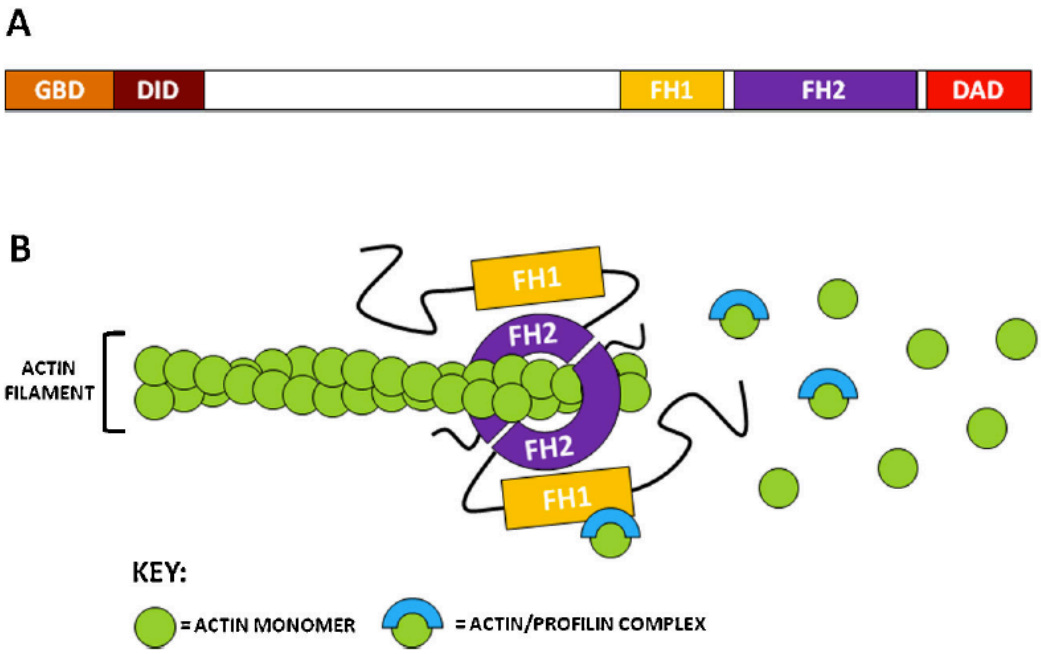

Figure 1.10. Schematic of key components of the formin family of proteins and their association with actin filaments. A) Domain structure of single formins. GBD, GTPase Binding Domain, DID, Diaphanous Inhibitory Domain, FH1, Formin Homology Domain 1, FH2, Formin Homology Domain 2, DAD, Diaphanous Autoregulatory Domain. B) Active formins dimerise and nucleate actin into linear filaments. Figure adapted from Randall & Ehler, 2014.

morphogenesis (DAAM), inverted formins (INF), formin 1 (FMN1) and formin 2 (FMN2). Within the heart, several formins have been found to play important roles in regulation of the actin cytoskeleton; Daam1, Daam2, FHOD3 and FHOD1.

FHOD1 is a prominent formin in cardiomyocytes which, unlike other formins (e.g. FHOD3), does not act at the sarcomere. FHOD1 is not capable of nucleating cardiac actin and instead, participates in the polymerisation of cytoplasmic actin filaments, which are present at the ICDs and costameres (Schonichen and Geyer, 2010, Patel et al., 2018, Grimes et al., 2019). Consistent with this hypothesised role for polymerising cytoplasmic actin, FHOD1 localisation is prominent at the ICD and FA/costamere in healthy and diseased models (Ehler et al., 2004, Dwyer et al., 2014, Al Haj et al., 2015, Pandey et al., 2018). Furthermore, a recent study by the Iskratsch lab demonstrated that FHOD1 plays a critical role in non-myofibrillar force generation in neonatal rat cardiomyocytes, which is activated downstream of PKC and Src activation during hypertrophic signalling (Pandey et al., 2018). These results are also in agreement with observations that FHOD1 is a potent regulator of directed traction forces at integrin mediated adhesions (Iskratsch et al., 2013). However, a recent study has reported that FHOD1 knock out mice are born with phenotypically normal hearts, proposing that FHOD1 is dispensable for cardiac development. Furthermore, the same study also investigated FHOD1 activity in a dilated cardiomyopathy (DCM) mouse model (Myosin binding protein C3 null mice) and reported no change in FHOD1 expression or subcellular enrichment (Sanematsu et al., 2019). The reason for these inconsistent results has been suggested due to the use of different FHOD1 antibodies (Sanematsu et al., 2019) but clearly, further work is required to understand the role of FHOD1 in cardiomyocytes.

1.8 Integrins as Mechanoreceptors: Ahead of the Focal Adhesion

From a broad range of experiments carried out *in vitro* and *in vivo*, the importance of the costamere for development, basal functioning and responses to pathology in cardiomyocytes is well established, as discussed above. However, the way in which integrin mediated signalling at the costamere changes in response to dynamic integrin expression and cardiac tissue stiffness is less well understood. The majority of cytoplasmic integrin-protein interactions occur via the β1 integrin tail, although the number of interactions identified at α integrin tails are increasing (Legate and Fassler, 2009, Morse et al., 2014, Bachmann et al., 2019). As expression of the β1 integrin subunit

is stable, it could be hypothesised that protein interactions at the costamere may also remain relatively consistent. However, integrin subtypes differ dramatically in their bond kinetics and cells exploit this to fine tune their rigidity sensing behaviours (Elosegui-Artola et al., 2014, Bharadwaj et al., 2017, Lerche et al., Preprint). At the level of the integrin-ligand bond, vast differences in activation energy (Li and Springer, 2017), clustering (Elosegui-Artola et al., 2014, Schaufler et al., 2016, Lerche et al., Preprint) have been reported between different integrin subtypes. Furthermore, tissue stiffness is a central factor in determining the integrin-ligand bond dynamics (Elosegui-Artola et al., 2014, Oria et al., 2017, Lerche et al., Preprint). It is therefore important to understand how changes in the integrin-ECM interface (such as tissue stiffness and integrin expression) alter mechanotransduction. Investigations within cardiomyocytes have remained limited to date, so the following section will present recent insights on the role of integrins in mechanotransduction from cell lines and computational models.

1.8.1 The Molecular Clutch Model

The molecular clutch model has been developed to understand the intra-molecular interactions that occur within adhesion structures and has provided experimental evidence that cells utilise integrins to modulate rigidity sensing. The model consists of four basic elements that form the adhesion structure: 1) Cytoskeletal tractions from myosin motors pulling on actin filaments as well as actin retrograde flow from the assembly of actin filaments, 2) Adaptor proteins connecting actin to integrins (talin, vinculin, paxillin, FAK, kindlin etc.), 3) Integrins connecting actin to the ECM and 4) ECM ligands. The resulting model describes three basic regimes of rigidity sensing by predicting the association/dissociation rates of intramolecular bonds during loading: 1) The application of optimal force, maintains bond lifetimes to balance association/disassociation rates, permitting force transmission long enough to enable a mechanotransduction event, such as talin unfolding and vinculin reinforcement. 2) Excessive force or rapid loading above bond thresholds results in excessive dissociation (dissociation > association) and an unstable adhesion. 3) Sub-optimal loading reduces bond dissociation (dissociation < association) but mechanosensitive proteins do not experience sufficient tension to initiate

signalling

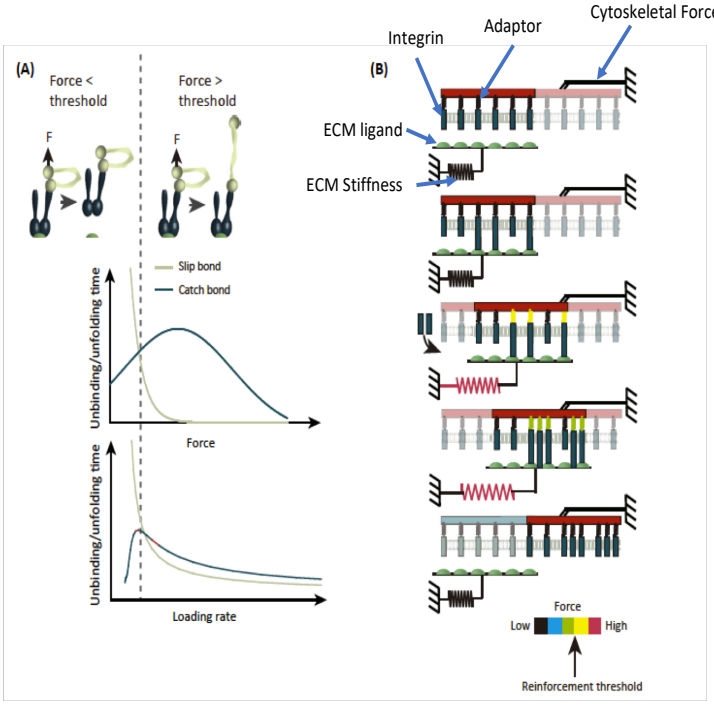

Figure 1.11. Integrin mediated mechanotransduction, as described by the molecular clutch model. A) The effect of force and loading rate on mechanotransduction events (protein unfolding or unbinding). Typical bond/unfolding lifetimes are shown for catch and slip bonds . Below an optimum force threshold, proteins such as integrins unbind before mechanotransduction can occur. At an optimum force and loading threshold, lifetimes of integrin catch bonds are prolonged long enough for protein unfolding to occur (such as talin unfolding), initiating a mechanotransduction event. B) Load-fail cycles predicted by the molecular clutch model. Top to bottom: Top frame illustrates the components of the molecular clutch model. Second frame shows engagement of integrins with ligands prior to loading, only a subset of integrins engage. Third frame shows that upon loading from cytoskeletal contraction, integrin adaptors experience loading. The stress felt by adaptors is dependent upon ECM stiffness, ligand density and protein bond types. Adaptors experience sufficient force to surpass the mechanotransduction threshold, resulting in prolonged bond lifetime, a mechanotransduction event such as protein unfolding and adhesion reinforcement via increased integrin recruitment (frame 4). The bottom frame demonstrate disassembly of the adhesion after a sufficient time or excessive loading. C) The importance of substrate rigidity on reacting the force threshold

and its effect on cell tractions, actin flow and integrin density. Reinforcement of the adhesion (via integrin clustering) prevents a decline in cell tractions and actin flow.

pathways (Elosegui-Artola et al., 2018).

Figure 1.11 describes the components of the molecular clutch model. Upon the application of force to the adhesion, the model utilises known data of adhesion bond lifetimes to predict the loading regime as a function of loading rate, the magnitude of force and substrate rigidity. Importantly, intramolecular bond lifetimes of different elements within the model are dependent on the types of bond: Slip bonds decrease their lifetime with increasing force, while catch bonds increase their lifetime with increasing force, up to a certain point. Thus, loading of catch bonds can act to stabilise the adhesome by decreasing protein dissociation, while loading of slip bonds results in a more dynamic system by increasing the dissociation rate (Elosegui-Artola et al., 2018). Catch bond behaviour has been described for integrin-ECM interactions for both α5β1 and αvβ3 integrins (Kong et al., 2009), suggesting that loading certain integrin adhesions acts to stabilise the adhesome (e.g. providing sufficient time for additional integrins to bind). On the other hand, slip bond behaviour has been described for talin1-αvβ3 integrin bonds (Jiang et al., 2003), suggesting that stabilisation of integrins can facilitate more dynamic talin-integrin interactions. A recent study has identified that adhesion loading and dynamic bond lifetimes can be regulated by integrin clustering, which is essential for controlling mechanotransduction in response to changing substrate rigidity and traction forces (Oria et al., 2017).

1.8.2 The Nanoarchetecture of Integrin Adhesions- The Importance of Integrin Clustering

The importance of integrin clustering in cell spreading and adhesion has been well known since the discovery that fibroblasts will only form adhesions and stress fibres when 3 or more integrins are clustered < ~60 nm of each other (Arnold et al., 2004, Schvartzman et al., 2011). Follow up investigations also revealed that above this 60 nm threshold, turnover of FA proteins such as zyxin, paxillin and vinculin is greatly increased, and cells were unable to form stable adhesions that permit spreading (Cavalcanti-Adam et al., 2007). Furthermore, this clustering requirement was found to be highly sensitive to

changes in ligand positioning of just a few tens of nanometres, suggesting that integrin clustering may be a specific mechanism to sense the geometry of the ECM (Huang et al., 2009, Schvartzman et al., 2011). By combining ligand nanopatterning techniques with molecular force probes, it was revealed that cells were only able to generate traction forces upon their environment, when inter-ligand spacing was < 60 nm (Liu et al., 2014). Thus, integrin clustering was found to directly regulate spreading through the stabilisation of adhesions to facilitate mechanotransduction. However, the underlying mechanisms that make integrin clustering such an important element for mechanotransduction remained unclear.

The result that integrin clustering stabilises adhesions for force transmission, suggests that the requirement for clustering may depend upon the forces that adhesions experience. To provide further clarity on this question, Oria and colleagues (2017) evaluated cell adhesion formation, using ligand nanopatterning experiments at different substrate rigidities. Firstly, the results demonstrated that the requirement for integrin clustering is dependent upon substrate rigidity. On softer substrate stiffnesses of 1 – 30 kPa, cells required integrin spacing of 200 - 100 nm and the 60 nm threshold was only observed on stiff substrates of >150 kPa. Importantly, integrin spacing of 60 nm on soft substrates, prevented adhesion formation and cell spreading. These results were fed into the molecular clutch model which was able to predict cellular traction forces with remarkable accuracy, when compared to experimental results. In line with previous predictions from the model (Elosegui-Artola et al., 2014), these results suggest that integrin clustering acts to stabilise adhesions by modulating molecular tension experienced within the adhesion. This was further verified by the observation that increasing cytoskeletal contractility (i.e. increasing molecular tension within adhesions) at lower rigidities resulted in a decrease in the clustering requirement (i.e. more force requires more integrins) and vice versa. Thus, on stiff substrates, the ECM doesn't yield, resulting in adhesion proteins bearing the majority of the traction forces and a high degree of clustering is required to distribute the load and prevent overloading. At low rigidities, the ECM yields and bears the majority of the traction forces and fewer integrins are required to ensure adhesion proteins are subject to sufficient loading to facilitate mechanotransduction.

These findings demonstrate that changes and cellular contractility and in tissue stiffness can result in dramatic changes in the composition of adhesion structures. This has important implications for the heart which undergoes dynamic changes in stiffness during development and disease. Importantly, whether the integrin clustering requirement

changes between different integrin subtypes, is not well understood, especially in the case of cardiomyocytes. We therefore look to work carried out in other systems.

1.8.3 Is there Evidence For Differential Mechanotransduction Between Integrin Subtypes?

The expression of different integrin subtypes within the same cell provides a mechanism to recognise different components of the ECM. In binding to the ECM, integrin subtypes demonstrate a large degree of overlap in their ligand affinities, such as the binding of α5β1 and αvβ3 integrins to the RGD motif (Humphries et al., 2006, Bharadwaj et al., 2017, Schaufler et al., 2016). However, little evidence exists of overlapping or redundant functions of different integrin subtypes from a signalling perspective. Different subtypes have been reported to exhibit unique spatial and mechanical properties during adhesion assembly and maturation. Upon initial adhesion, α3-class integrins outcompete α5β1 by forming stronger adhesions, more rapidly, which has a knock-on effect for the spatial distribution of subtypes within (Bharadwaj et al., 2017) and between individual adhesions (Schaufler et al., 2016). In cancer cells, αvβ6 integrins also outcompete α5β1 to favour stronger traction forces in response to increasing substrate stiffness (Elosegui-Artola et al., 2014). Furthermore, recent work has also reported preferential integrin subtype expresion for adhesion formation on very soft surfcaes (Lerche et al., Preprint). Therefore, this data suggest that the expression different integrin subtypes may function, in part, to adapt to changes in substrate rigidity. However, these experiments did not control for the spatial distribution of integrin clustering, which is key for mediating rigidity sensing (Oria et al., 2017). Under comparable integrin clustering and substrate rigidity conditions, α5β1 integrins promote greater cell spreading while αvβ3 subtypes form larger adhesions and are essential for adhesion maturation (Schaufler et al., 2016). These findings suggest that the underlying clustering properties of different integrin subtypes may direct the rigidity sensing of cells. In contrast to the cell lines used to investigate the molecular clutch model, cardiomyocytes have a unique rigidity sensing mechanism that utilises a combination of muscle and non-muscle myosin contractility (Pandey et al., 2018). It is therefore important to investigate the integrin clustering properties of different integrin subtypes in cardiomyocytes to understand how integrin signalling changes during development, healthy functioning and disease of the heart.

1.9 Summary

The cardiac extracellular matrix undergoes dramatic changes in tissue composition and stiffness during development and disease. Fibronectin and laminin ligands exhibit a dynamic expression profile during development and disease, suggesting that they have important, yet independent roles and consequences for cardiomyocytes behaviour. The costamere represents an important mechanosignalling hub for detection of dynamic extracellular cues, via the assembly of highly complex adhesome structures. Costameric mechanosignalling is well known to detect and respond to mechanical changes in the ECM. However, little is known about how integrin mechanosignalling is altered upon the expression of different integrin isoforms. Recent work has identified key differences in the ligation and clustering dynamics of different integrin subtypes in non-cardiac cells and highlights a large gap in the literature on cardiac integrin signalling. From these findings, the aim of the current thesis was to further investigate cardiomyocyte integrin signalling dynamics when adhering to fibronectin and laminin.

1.10 Hypothesis

Recent developments have outlined the importance of integrin clustering in the facilitating mechanotransduction. Furthermore, important differences have been discovered in the rigidity sensing properties of different integrin subtypes. Therefore, it is hypothesised that within cardiomyocytes, a change in the integrin expression observed during development and disease will result in a corresponding change in the rigidity sensing behaviours such as cell spreading, traction forces and adhesion formation. Furthermore, it is also hypothesised that differences in rigidity sensing behaviour will also manifest as differences in the integrin clustering properties of fibronectin and laminin binding subtypes.

1.11 Aims and Objectives

Integrin mediated mechanotransduction plays a kay role in the basal and pathological functioning of cardiomyocytes. Recent findings in other cell types has demonstrated that integrin expression can be utilised to exploit a range of subtypes with unique rigidity sensing properties, depending on the required cellular function. Cardiomyocytes utilise integrins to respond to changes in the chemical and mechanical landscape of their

environment but how different integrin subtypes differ in their mechanosignalling properties, in this cellular context, is not well understood. In light of this knowledge, further research into the consequences of culturing cardiomyocytes on engineered surfaces, with tuneable chemical and mechanical properties, would be of great interest and benefit in understanding cardiomyocyte behaviours during development and disease. Thus, the central question of this project was "how do the physical, chemical and geometric properties of the ECM affect cell spreading, integrin signalling and rigidity sensing behaviours of cardiomyocytes?". The role of collagen will not be addressed in the current investigation. Specifically, this investigation will focus on the role of fibronectin or laminin ligands on cardiomyocyte behaviours, due to their dynamic expression during development and disease. To answer this research question, this thesis will present novel data on cardiomyocyte spreading and rigidity sensing on fibronectin and laminin substrates. Furthermore, novel data will also be presented on the development and implementation of a ligand nanopatterning platform to begin to investigate the differences or similarities of ligand dependent, cardiomyocyte adhesion nanoarchitecture.

2 MATERIALS & MATERIALS

2.1 Materials

2.1.1 DNA Origami Materials

ssDNA:

M13mp18 ssDNA	Tilibit
DNA backbone and strands	Integrated DNA Technology (IDT)
Acrydite ssDNA	IDT
Amino Anchors	IDT
Alexa 647 labelled ssDNA	IDT

Peptides:

RGDfC – Cyclo(- Arg - Gly - Asp - D - Phe - Cys)	Anaspec
IKVAV (laminin A Chain, 2091-2108) - Cys-Ser-Arg-Ala-Arg-Lys-Gln-Ala-Ala-Ser-Ile-Lys-Val-Ala-Val-Ser-Ala-Asp-Arg	Alfa Aesar

Buffers:

TAE Buffer	40 mM Tris, 20 mM Acetic Acid, 1 mM EDTA, 12.5 mM MgCl
Tris buffer	5 mM Tris, 30 mM MgCl, pH 8.3
MOPS buffer	10 mM MOPS, 30 mM MgCl, pH 8.1
TEAA Buffer	100 mM Triethyl amine, 100 mM Acetic acid, pH 7

Reagents:

Sulfo NHS (N-hydroxysulfosuccinimide)	Thermo Fisher
EDC (1-Ethyl-3-(3′-dimethylaminopropyl)carbodiimide)	Sigma
CTES (Carboxyethylsilantriol)	Gelest

AFM tips:

Scan Assyst Air (silicon tip on Nitride lever, f_0: 70 kHz, k: 0.4 N/m)	Bruker
Scan Assyst Fluid + (silicon tip on Nitride lever, f_0: 150 kHz, k: 0.7 N/m)	Bruker

Spin filters:

100 kDa Spin Column	Amicon
3 kDa Spin Column	Amicon

HPLC Column:

C18 column, 2.5 μm, 4.6 mm x 50 mm	Xbridge, Waters

2.1.2 Substrate nanofabrication

Chemicals:

99% Ethanol	Sigma
Propanol-2	VWR
Acetone (HPLC Grade)	VWR
NMP (1-Methyl-2-pyrrolidinone)	VWR
MFCD26	Microposit

Methyl Isobutyl Ketone (MIBK)	Emplura
950K PMMA (Poly(Methylmethacrylate))	Sigma
HMDS (Hexamethyldisilazane)	Sigma

2.1.3 Tissue culture

Buffers:

ADS Buffer	116mM NaCl, 20mM Hepes, 0.8mM NaH2PO4, 5.6mM Glucose, 5.4 mM KCL, 0.8 mM MgSO4 at pH 7.4
Enzyme solution	246U Collagenase and 0.6 mg Pancreatin / ml at pH 7.4
Immunostaining Buffer	20 mM Tris, 155 mM NaCl, 2 mM EGTA, 2mM $MgCl_2$, 1% BSA at pH 7.4
Phosphate Buffered Saline	Sigma

Tissue Culture Media:

NRC Plating Media	65% DMEM, 17% M199, 10% Horse Serum, 5% FCS, 2% Glutamax, 1% Penecillin/Streptamycin
NRC Maintenance Media	77% DMEM, 18% M199, 2% Horse Serum, 2% Glutamax, 1% Penecillin/Streptamycin
MEF Media	87% DMEM, 10% FBS, 2% Glutamax, 1% Penecillin/Streptamycin

Transfections:

Lipofectamine LTX with Plus	Thermo Fisher
Optimem	Gibco

Drugs:

PP2 (10 μM)	Cambridge Bioscience
smiFH2 (5 μM)	Sigma
Verapamil Hydrochloride (10 μM)	Santa Cruz Biotechnology
Omecamtiv Mercabil (500 nM)	AdooQ Bioscience
Y27632 (10 μM)	Tocris
Blebbistatin (50 μM)	Calbiochem
Calyculin A (100 nM)	Sigma

Ligands:

Fibronectin (Human)	Roche
Laminin (Engelbreth-Holm-Swarm, Murine)	Sigma – L2020

2.1.4 PDMS

Sylgard 184	Dow Corning
Sylgard 527	Dow Corning
HMS 301 ((25-35% Methylhydrosiloxane)–Dimethylsiloxane Copolymer)	Gelest
VDT 731 (Vinylmethylsiloxane-Dimethylsiloxane)	Gelest

Modulator (2,4,6,8-Tetramethyl-2,4,6,8-tetravinylcyclotetrasiloxane)	Sigma
Platimun Catalyst (Platinum(0)-2,4,6,8-tetramethyl-2,4,6,8-tetravinylcyclotetrasiloxane complex solution)	Thermo Fisher

2.1.5 Antibodies

Primary Antibodies:

Anti-α– actinin (Mouse, IF: 1:500)	Sigma (#A7811)
Anti-Vinculin (Mouse, IF: 1:200)	Sigma (#V9131)
Anti-phospho-Src Family (Tyr416, Rabbit, 1:200)	Cell Signalling Technology (#2101)
Anti-phospho FHOD1 (Thr1141, Rabbit, 1:200)	ECM Biosciences (#FP3481)

Secondary Antibodies:

Cy2 Goat anti-mouse (1:200)	Jackson Immuno Research (#115-225-146)
Cy3 Goat anti-mouse (1:200)	Jackson Immuno Research (#115-165-146)
Cy5 Goat anti-mouse (1:200)	Jackson Immuno Research (#115-175-146)
Cy2 Goat anti-Rabbit (1:200)	Jackson Immuno Research (#111-165-144)
Cy3 Goat anti-Rabbit (1:200)	Jackson Immuno Research (#111-165-144)

Cy5 Goat anti-Rabbit (1:200)	Jackson Immuno Research (#111-175-144)

2.2 Methods

2.2.1 DNA Origami and Nanopatterning

2.2.1.1 Synthesis of DNA Origami.

DNA origami designs and protocols were initially implemented from the protocols developed and published by Paul Rothemund and Ashwin Gopinath (Gopinath and Rothemund, 2014, Gopinath et al., 2016, Rothemund, 2006, Woo and Rothemund, 2014) DNA origami was assembled by combining M13mp18 (40 nM) and staple strands (200 nM) in 50 µL of 10 mM TAE buffer with 12.5 mM Mg^{2+}. M13mp18 is a bacteria phage vector strand 7249 bases in length. An appropriate quantity of ions, such as magnesium (here), or sodium, are required for efficient DNA hybridization. This acts to equilibrate electrostatic repulsion between highly negatively charged DNA molecules. A concentration of 12.5 mM Mg^{2+} was sufficient to achieve a high yield of DNA origami and limit any aggregation effects. DNA origami are synthesised by annealing from an initial temperature of 94 °C to completely melt all dsDNA. Temperature step-controlled annealing was carried out in a PCR machine. Samples were cooled from 94 to 65 °C at a rate of ~0.3 °C per minute. A cooling rate of 0.1 °C per minute is employed from 65 °C to room temperature. The self-assembled DNA origami were then purified using Millipore Amicon Ultra 100 kDa spin columns in a centrifuge at 2000 rcf for 6 min, three times, removing excess staple strands. DNA origami were adjusted to a concentration ~40 nM and stored in Lo-Bind Eppendorf tubes at 4 ºC. A NanoDrop spectrophotometer was used to detect the approximate concentration of DNA origami products based on the constant of a molecular weight of 330 g/mol per base and an extinction coefficient = 33 mg/mL for A260 = the actual result is close to the estimated numbers. To ensure efficient assembly and labelling of DNA origami with peptide conjugates, unmodified staple strands and amino anchors were added at a 5 X excess to the M13mp18 backbone and peptide conjugates were added at a 10 X excess to amount of available sticky-ends, as validated in chapter 4.5.2. Full sequences of all modified oligonucleotides utilised in the design of the functionalised DNA origami can be found in the appendix.

2.2.1.2 AFM Characterisation of DNA Origami

Initial AFM parameters were guided by protocol published by Ashwin Gopinath (Gopinath and Rothemund, 2014) and were adapted as necessary to achieve high image quality. AFM (Bruker, Dimension Icon) was used to image the DNA origami structures. DNA origami were cast on either glass, or mica surfaces for imaging. The DNA origami solution is diluted by TAE buffer with 30 mM $MgCl_2$ to around 1 nM in order to get a good separation of the DNA nanostructures once immobilized on surface. Magnesium is required in the procedure as an ion charged bridge, immobilizing DNA origami to the substrate surfaces. Mica samples were cleaved twice by solid scotch tape immediately prior to casting. 5 μL of diluted DNA origami solution was directly deposited on freshly cleaved mica and left to adsorb on the surface for 2 min. Subsequently, the substrate was washed by distilled water to remove non-adsorbed DNA origami and then blown dry with compressed air. Silicon nitride ScanAsyst-Air tips with 0.4 N/m spring constant were used to scan the sample by AFM under ScanAsyst Mode. A resolution of 512 pixels per line (for scan sizes of 1-5μm) with 1 Hz scan rate was chosen for appropriate imaging of the DNA nanostructure.

For DNA origami cast randomly on glass substrates. All AFM imaging was carried out in air using peak force quantitative nanomechanical mapping (QNM) mode. The advantages of this mode is that by measuring the mechanical features of the sample, it permits the user more methods by which to view and analyse the sample. This is particularly important after extensive treatment of the substrate to help identify what is present on the substrate and to help verify the success of the experiment. Every scan was optimised in live scanning mode by altering the amplitude set point (how hard the tip presses against the surface) and gain levels. After identifying the best settings for each scan, a full scan was repeated.

For the nanopatterned substrates, imaging the PMMA layer (during development and etching experiments) was carried out in air using peak force QNM mode. After lift-off, however, the highly hydrophobic hexamethyldisilazane (HMDS) layer on EBL patterned surfaces made it very difficult to accurately track the surface when scanning in air. Therefore, to characterise DNA origami on the EBL nanopattern, AFM characterisation was carried out in fluid soft tapping mode. All samples were imaged in imaging buffer (5mM Tris, pH 8.3, 40mM $MgCl_2$). This buffer was used to ensure that DNA origami were strongly bound, flat against the surface by the elevated pH and magnesium concentration, facilitating a clearer image acquisition. Silicon nitride ScanAsyst-Fluid+

with 0.7 N/m spring constant were used at a resolution of 512 pixels per line and a 1Hz scan rate. Amplitude setpoint and gain were optimised for each sample and tip. Further difficulties were experienced when imaging e-Beam patterned DNA origami after an overnight incubation in PBS. Mild hydrolysis of the HMDS background resulted in physisorption of salts to the background which resulted in frequent contamination of the AFM tip and imaging artefacts such as shadows and feature duplication. As a result, samples were washed in 0.1% Tween 20 in 10 mM Tris pH 8.3 40 mM $MgCl_2$ (v/v) for 20 minutes and before being switched back to imaging buffer. This improved the cleanliness of the surface, although image acquisition remained problematic.

2.2.1.3 Peptide-DNA Conjugation

For cRGDfC and IKVAV peptides, conjugation to ssDNA was performed through a UV mediated thiol-ene reaction, via a sulfhydryl (thiol) group on the peptides and a ene-group on acrydite modified ssDNA (Integrated DNA Technologies). Peptides were diluted to 100 µM in H_2O containing 100 X TCEP, to reduce any disulfide bonds and present the cysteine groups for conjugation. 8µl of peptides were then mixed with 8 µl of acrydite modified ssDNA at a final concentration of 20 µM and 200 µM, respectively. A reaction buffer was made containing 120 mM Tris (pH 6.8) and 35 mM of the photoinitiator 2-hydroxy-4′-(2-hydroxyethoxy)-2-methylpropiophenone. 2.5 µl of the reaction buffer then was added to the peptide/ssDNA mix. When exposed to UV light, the photoinitiator is degraded, releasing free radicals which catalyse the reaction between the sulfhydryl group on the peptide and the ene residue on the acrydite, completing the conjugation (Torres-Kolbus et al., 2014). Samples were exposed to 260 nm UV light for 1 hour and purified using Amicon ultra 3kDa spin columns (Merck Millipore) to remove any unconjugated peptides and the photoinitiator, and samples were resuspended in 0.1 M TEAA buffer (0.1 M Triethyl Amine, 0.1 M Acetic Acid, pH 7.0).

2.2.1.4 Conjugate Verification and Purification: Reversed Phase High Performance Liquid Chromatography (HPLC)

After spin filtration, samples were resuspended in 0.1 M TEAA buffer and samples were injected into a c18 column (XBridge, 2.5 µm, 4.6 mm x 50 mm) in a 95:5 solution of TEAA:acetonitrile (ACN), as published by (Huang et al., 2019). Between 0 and 28 minutes, the proportion of TEAA:ACN was changed, in a linear manner, to 50:50. This gradient time was chosen to achieve a sufficient gap between elution time of the conjugate and the unconjugated DNA. Unconjugated peptides were removed in the spin filtration stage. The conjugated products were obtained by collecting the eluted product between

3.4 and 4.6 minutes, before the unconjugated ssDNA eluted at 5.6 minutes. Conjugates were then frozen in liquid nitrogen and freeze dried overnight to remove the solvent. Successful purification was confirmed using RP-HPLC, by observing the absence of the ssDNA peak, and samples were stored in H_2O at -20 ^oC.

2.2.2 Fabrication of Nanopatterned Substrates with Electron Beam Lithography (EBL).

All work in this section was carried out by Paul Reynolds (Nikolaj Gaadegard Lab, University of Glasgow) in the James Watt NanoFab Centre. Substrates were produced by direct write EBL on coverslips. Coverslips were solvent cleaned in an ultrasonic bath (acetone followed by methanol, IPA, and water) and dehydrated in a 180 ^oC oven overnight. Design and fabrication of EBL patterned substrates was based on protocols published by Gopinath and Rothemund (2014). An oxygen plasma treatment for 60s at 100W power prepared the surface for silane deposition, which was done from HMDS vapour in a closed container at 150 ^oC. A 950k molecular weight poly(methyl methacrylate) (PMMA) film was spin coated on the coverslips at 5k rpm, followed by a short solvent bake on a 180 ^oC hotplate for 30s. A 10 nm aluminium charge conduction layer was evaporated on the coverslips, and they were mounted on a 4-inch silicon wafer for EBL processing using crystalbond 555 adhesive. Samples were loaded into the EBL chamber (Vistec VB6 2006) to define arrays of 200 nm and 300 nm pitch holes, 150 nm in diameter in the PMMA layer. After exposure, the aluminium charge conduction layer was removed in a 2.6% TMAH solution (MF-CD26) for 60s followed by water rinse. The surface roughness for both kind of patterned surfaces was calculated from AFM topographical heights (Z) by measuring the root mean square:

$$Rq = \sqrt{\frac{\sum Z_i^2}{N}}$$

2.2.3 Positioning and Cross-linking of DNA Origami to E-Beam Patterned Substrates

The following protocol for the positioning and washing of substrates during the positioning of DNA origami was adapted from Gopinath and Rothemund (2014). Substrates were first developed in a 2:1 solution of propanol-2:methyl isobutyl ketone for 60 seconds at 23 °C, followed by a 30 seconds wash in 100 % propanol-2. DNA origami binding sites were then etched using oxygen plasma treatment (100W, 70 seconds, room air) followed by silanisation with 0.1% CTES in Tris buffer (5 mM, pH 8.0) for 30

minutes at room temperature. The PMMA resist was then removed by immersion in NMP at 50 °C for 2 minutes followed by sonication for 10 minutes. DNA Origami were incubated for 1 hour at room temperature at a concentration of 500 pM in placement buffer (5 mM Tris, pH 8.3, 50 mM MgCl2). Due to the hydrophobic nature of the HMDS layer and the size of the patterned area, 100 µL of DNA origami solution was required to cover the surface sufficiently. The tris buffer was then exchanged with MOPS buffer (10 mM, pH 8.1, 50 mM MgCl2) to remove primary amines, followed by an additional wash with MOPS buffer (10 mM, pH 8.1, 50 mM MgCl2) containing 100 mM EDC and 50 mM sulfo-NHS. Finally, samples were then washed with the MOPS buffer (10mM, pH 8.1) containing 50 mM NaCl and incubated in DPBS containing 50 mM NaCl. Before AFM characterisation, samples were placed into placement buffer. A pH of 8.1 or higher has been demonstrated to increase the changes of DNA origami binding to the silanised surface (Gopinath & Rothemund, 2014). This is due to the elevated ionisation state of the silane at higher pH, generating more [-OH] groups at the binding sites, thus increasing the chances the DNA origami binding. However, long durations at elevated pH result in hydrolysis of the HMDS background and loss of the passivation layer essential to reduce nonspecific adhesion between cells and the substrate. The buffer pH chosen here reflects what has been reported to be effective within the literature (Gopinath and Rothemund, 2014, Gopinath et al., 2016, Shen et al., 2018b).

2.2.4 Photobleaching Assays

To evaluate the efficiency of DNA origami labelling and functionalised via the sticky-end strands, photobleaching assays were employed. DNA origami were fabricated with 6, 12 or 18 Alexa-647 fluorophores. 35mm glass bottomed dishes were plasma treated for 5 minutes at 18W to generate surface silanols for the physisorption or DNA origami. DNA origami were cast into the dish at a concentration of 200pM (200 µl) in 10mM Tris buffer (pH 8.3) containing 20mM MgCl and were incubated at room temperature for 1 hour. The substrate was very gently washed with tris buffer once to reduce the background noise from DNA origami still in solution and the dish was loaded into a confocal microscope (Zeiss LSM710 Confocal). Samples were imaged at a sampling rate of 143Hz with a 100X objective. This frame rate was chosen to detect rapid single bleaching events, which has also been demonstrated to be sufficient in previous work (Cox et al., 2011).

Upon image acquisition, the focus was adjusted and the stage moved to an adjacent area to ensure all bleaching events were captured. A total of 10,000 frames (70 seconds) were

acquired which was sufficient to totally bleach the sample and obtain a good signal from the background. The magnitude of a single bleaching event was quantified by manually calculating the average drop in signal from 50 individual bleaching events. Individual signalling events were counted manually (as can be seen in Figure 4.17) by observing the number of "stepping events" and the number of observed bleaching events were divided by the total signal drop from the start to the end of photobleaching (Chen et al., 2014). To calculate the total number of fluorophores on a single DNA origami, the absolute difference between the starting signal intensity and the final signal intensity (the background signal) after the sample had been fully photobleached was divided by the average magnitude of a single bleaching or "stepping event" (Chen et al., 2014).

2.2.5 Cell Isolation and Tissue Culture

2.2.5.1 Cardiomyocyte Isolation and Culture

Neonatal rat cardiomyocytes were isolated and harvested as published in (Pandey et al., 2018) New born (Postnatal day 0-3) rat hearts were dissected into ice-cold ADS buffer (116 mM NaCl, 20mM Hepes, 0.8 mM NaH_2PO_4, 5.6 mM glucose, 5.4 mM KCL, 0.8 mM $MgSO_4$) and washed again with ADS buffer. The ADS buffer was then removed and hearts were incubated with of 5ml enzyme solution in ADS buffer (ES, 246U collagenase and 0.6 mg pancreatin/mL), for 5 min, at 37 °C under vigorous shaking (Ehler et al., 2013). Tissues were then triturated by pipetting up and down 30 times and the supernatant was discarded. This step was followed by 6 digests further digests. After each digest and trituration, the supernatant was collected and transferred into plating medium (65 % DMEM, 17 % M199, 10 % Horse Serum, 5 % FCS, 2 % Glutamax, 1 % Penecillin/Streptamycin (P/S)) and 5 ml of fresh enzyme solution was added to the hearts. Every two digests, the supernatant was combined in one tube with 20 ml plating medium, then passed through a 100 μm cell strainer, spun down at 1200 rpm for 5 min at room temperature, resuspended in 10 ml plating medium and pre-plated in 10 cm tissues culture dishes for a minimum of 90 minutes to allow the cardiac fibroblasts the adhere to the dish (Ehler et al., 2013). After all digests had been completed, and the final dish had at least 90 minutes pre-plating, the media was collected and the dishes were washed down once to collect the cardiomyocytes, leaving behind many of the fibroblasts. Cardiomyocytes were then plated onto the respective substrates either in plating medium or serum free medium (70 % DMEM, 22 % M199, 2 % Glutamax, 1 % Penicillin/ Streptamycin (P/S)). The medium was changed the next day to serum containing maintenance medium (78 %

DMEM, 17 % M199, 2 % horse serum, 2 % Glutamax, 1 % P/S) or serum free maintenance medium (78 % DMEM, 19 % M199, 2 % Glutamax, 1 % P/S).

2.2.5.2 Immortalised Mouse Embryonic Fibroblasts (MEFs)

Immortalised MEFs were chosen as a control cell line for carrying out validation experiments on DNA origami and optimisation experiments on the micropattern. These cells were cultured in a high glucose maintenance medium and incubated at 37 ^{o}C with 5 % CO_2. Cells became 70 – 80 % confluent every 2 – 3 days and were then passaged. After the cells had been passaged 20 times, the culture was discarded and a fresh batch of cells were thawed from liquid nitrogen.

2.2.6 Fabrication of PDMS Coated Coverslips and Ligand Micropatterning

2.2.6.1 PDMS Coated Glass Coverslips

PDMS coverslips were prepared as described in (Pandey et al., 2018). Sylgard 184 (1:10, base : cross-linker) and Sylgard 527 (1:1, parts A:B) were mixed at a ratio of 1:19, 1:9 and 1:4. Soft PDMS gels were pre-cured in 50 ml falcon tubes on a roller for 2 hours at room temperature until they had a similar viscosity as PDMS 184. Then, 150 ul of the PDMS mix was placed on plasma cleaned (5 minutes, 18W, ozone oxygen plasma, PDC-32G-2, Harrick Plasma) 22x22 glass coverslips (size no.1.5) and spin coated at 1000 rpm for 100 seconds and baked at 80 °C for 2 hours. Sample mechanisms of PDMS substrates were calculated using oscillatory using a TA Discovery HR-3 hybrid rheometer. The samples were cured in situ at 80°C for 2hrs and the gelation was monitored by an oscillating time sweep, with an oscillating frequency of 1Hz and an oscillating displacement of 1e-4rads. Once cured the samples were then kept at room temperature for 5 minutes to cool and were then characterised using an oscillating frequency and stress sweep, and by transient stress relaxation. The frequency sweeps were performed from 0.1-100Hz at an oscillating displacement of 1e-4rads and the stress sweeps were performed from 0.1-100Pa at a frequency of 1Hz. Finally stress relaxation was performed using a shear strain of 2%and a hold time of 300s. Rheology measurements (kindly carried out by Will Megone, QMUL) calculated the final stiffness of 1:19, 1:9 and 1:4 gels to be 6 kPa 20 kPa and 130 kPa (respectively).

2.2.6.2 Fabrication of Micropatterned Lines.

Ligands were micropatterned using PDMS stamps created via soft lithography, largely as described by (Qin et al., 2010). The micropattern consisted of parallel lines 1 μm in width

and a 5 µm centre-to-centre distance. To make the PDMS stamps, 3.4 g of VDT-731 (Gelest Inc.) was mixed with 1 g of HMS-301 before mixing 4 drops of modulator (Sigma, 2,4,6,8-Tetramethyl-2,4,6,8-tetravinylcyclotetrasiloxane) and then mixing in 4 droplets of a platinum catalyst (Platinum(0)-2,4,6,8-tetramethyl-2,4,6,8-tetravinylcyclotetrasiloxane complex solution). The hPDMS mixture was degassed by centrifugation and spread over a silicon wafer with the negative micropattern and cured at 60 ^{o}C for 40 minutes. 40 ml of PDMS (Sylgard 184) was poured over the cured hPDMS and backed for 2 hours at 80 ^{o}C. Micropattern stamps were cut into ~1 cm^2 cubes, washed with H_2O, to remove any PDMS dust and blow dried.

Fibronectin (Human, Roche #11051407001) or laminin (Engelbreth-Holm-Swarm, Murine, Sigma #L2020) were labelled (if required) at 100 mg / ml in bicarbonate buffer (10 mM, pH 8.3) with amine reactive Atto-405, Atto-488 and Atto-546 NHS-esters (Sigma – 10 µl per 100 µg of ligand). Labelling was carried out for 1 hour at room temperature with gentle agitation before dialysis against PBS to remove unconjugated fluorescent NHS-esters. For labelling the micropattern, labelled ligands were diluted 3x with unlabelled ligands.

Micropattern stamping surfaces were coated with 15 µl of the desired ligands and incubated at room temperature for 45 minutes. Even coating of the stamping surface was achieved by placing a 22 x 22 mm glass coverslip over each 15 µl droplet. Glass coverslips were prepared for stamping by plasma treatment for 5 minutes (Harrick Plasma, room air, 18 W) to generate charged surface silanols groups and facilitate transfer of the ligands from the micropattern to the culture surface. Exposure of PDMS to oxygen plasma can increase the surface stiffness of the gel (Glatz and Fery, 2019). Therefore, PDMS coated coverslips were plasma treated for 1 minute.

Ligand coated PDMS stamps were dipped in diH_2O 5 times, blow dried with N^2, inverted and placed on the plasma treated coverslips with light pressure for 10 seconds. Micropatterned surfaces were immediately placed in PBS containing 5% BSA (Cell Signalling Technology) for 1 hour to minimise nonspecific cell adhesion (Sweryda-Krawiec et al., 2004).

2.2.6.3 Tissue Culture on the Micropatterned Lines

Prior to any tissue culture, micropatterned ligands were blocked against nonspecific adhesion with 5 % BSA for 30 minutes. Blood serum products contain large amounts of fibronectin and other ECM components that could be laid down by the cells and skew the

results of the experiments. Therefore, all cells were plated and cultured in serum-free media for the duration of the experiment. RPTP cells were cultured for 1 hour and NRCs were cultured for 24 hours before fixation with 4 % PFA.

2.2.6.4 Image Analysis of Micropattern Data

All images were processed in ImageJ (Schneider et al., 2012). Images underwent a background subtraction (radius = 20 pixels), to minimise background noise. The filter parameters were optimised to achieve the highest signal to noise ratio while maintaining fine detail in the images.

Cell morphology and quantification of whole cell protein intensity were calculated by firstly outlining the cell by thresholding and measuring cell area, length and the integrated density of the fluorescent signal using ImageJ.

Adhesion density along the lines were calculated by measuring the pixel intensity along the length of the line for the desired channels. Enrichment of adhesion proteins was evaluated by calculating the signal intensity of the object channel over the lines only, relative to the signal intensity from the whole cell. ROI's for the whole cell were generated using thresholding. ROIs for the adaptor proteins along the lines were generated by the overlap between the ROI for the whole cell and ROIs for each line (generated from the lines image). Signal intensities were calculated using the integrated density feature of ImageJ and then normalised to the area of each ROI to obtain a measure of enrichment per unit area.

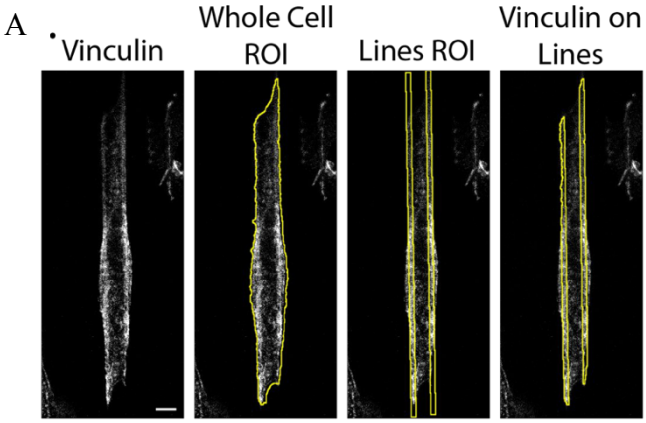

2.2.6.5 Drug Treatments of Cardiomyocytes on Randomly Positioned IKVAV and RGDfC DNA Origami Arrays

Randomly positioned DNA Origami arrays were fabricated as described above and NRCs were isolated and cultured overnight in serum free plating media to allow attachment and

spreading. The following morning, cells were given fresh serum free maintenance media. After 21 hours in culture, culture media was exchanged to serum free maintenance media containing Blebbistatin (50 μM), PP2 (10 μM), Y- Y27632 (10 μM), smiFH2 (5 μM), Verapamil Hydrochloride (10 μM), Calyculin A (100 nM) or Omecamtiv Mercabil (500 nM). Cells were fixed with 4% PFA after 3 hours of treatment.

2.2.7 Immunostaining

Immunostaining was performed as presented by Pandey et al. (2018). Cells were firstly fixed by removing culture media, washing with PBS and incubating cell in a solution of 4% paraformaldehyde for 10 minutes at room temperature (RT). Cells were washed with PBS and then permeabilised by incubation with a 0.2% solution of Triton-x (Sigma) for 5 minutes at RT. Samples were then briefly washed with PBS before being incubated with immunostaining buffer (20 mM Tris, 155 mM NaCl, 2 mM EGTA, 2 mM MgCl2 at pH 7.4) containing 1% BSA (CST) for blocking of non-specific binding of antibodies. Cells were then incubated with primary antibodies (see 2.1.5 for antibodies and concentrations) in immunostaining buffer at 4°C overnight. The following day, samples were washed at least 3 times with PBS (5 minute incubation at RT on a rocker) to remove primary antibodies that remained in solution. Samples were then incubated in secondary antibodies (see 2.1.5 for concentrations) in immunostaining buffer for 1 hour at room temperature. Samples were then washed 3 times with PBS (5 minute incubation at RT on a rocker) before being mounted on a coverslips with a drop of Mowiol (MOWIOL 4-88) to prevent fading of fluorophores. The antibodies used in this thesis are presented in section 2.1.5. However, a number of antibodies were also tested for use in this thesis but were not of sufficient quality to be included. These antibodies can be found in appendicies.

2.2.8 Nano-Pillar Arrays

2.2.8.1 Fabrication of the Nano-Pillars

Micro-Pillar arrays (1.7 μm height (Pandey et al., 2018), 500 nm diameter, 1 μm centre to centre, k=3.75nN / μm) were created by soft lithography from a negative master, using PDMS (Sylgard 184). The negative master chips were first spin coated with 10 μl of CdSeS/ZnS alloyed quantum dots (488 nm, Aldrich) at 500 rpm for 10 seconds clockwise then counter clockwise, followed by 30 seconds at 10,000 rpm both clockwise and counter

clockwise. ~80 µl of mixed Slygard 184 was then spin coated onto the master chip at 1500 rpm for 60 seconds. Coated chips were then degassed in a vacuum chamber for 5 minutes and glass bottomed 35mm dishes (No.0, Ibidi) were plasma treated (as above). Degassed coated master chips were placed face down in the treated dishes and cured in the oven for 2 hours at 80 °C or overnight at 60 °C. Pillars were coated with fibronectin (50 µg / ml) or laminin (50 µg / ml) in PBS for 1 hour at 37 °C. Cells were plated on pillars in serum free plating medium.

2.2.8.2 Live Cell Imaging of NRCs on the Nano-Pillars

NRCs were cultured on nano-pillar arrays for 24-48 hours prior to imaging to provide sufficient time for the cell to recover and begin spontaneous contraction. Prior to imaging, cells were given fresh media. Samples were loaded into a live cell imaging chamber and mounted on a Zeiss LSM710 Confocal microscope in widefield mode.

Cells were firstly imaged in their normal condition for a few contraction cycles (typically a 30 second window recorded 2-10 contractions). Without pacing, the number of contractions varied from cell to cell. Brightfield movies provided the outline of the cell and confirmed that the cell was spontaneously contracting. Movies were then taken of the pillars by exciting the 575 quantum dots using a 547 laser line to detect pillar displacements. Following this, cells were trypsinised with TryplE for 20 minutes to detach the cells form the pillars and obtain a reference of the pillars under zero stress. This final stage was essential to accurately calculate the pillar displacements in the proceeding data analysis step (see the following section).

2.2.8.3 Calculation of the Pillar Stiffness

Pillar stiffness was calculated as reported in Ghibaudo et al., 2008). Furthermore, the effects of substrate warping, as described by Schoen et al. (Schoen et al., 2010) was also taken into account.

$$k_{bend} = \frac{3}{64}\,\pi E\,\frac{D^4}{H^3};$$

$$corr = \frac{\frac{16}{3}\left(\frac{L}{D}\right)^3}{\left(\frac{16}{3}\left(\frac{L}{D}\right)^3 + \frac{7+6v}{3}\,\frac{L}{D} + 8\,T_{tilt}(v)\left(\frac{L}{D}\right)^2\right)};$$

$$T_{tilt}(v) = a\,\frac{(1+v)}{2\pi}\left\{2(1-v) + \left(1 - \frac{1}{4(1-v)}\right)\right\}$$

$$k = k_{bend} * corr;$$

$$E_{Eff} = \frac{9k}{4\pi a};$$

2.2.8.4 Analysis of Pillar Displacements to Calculate Traction Forces

ImageJ was used to process the pillar movie files and prepare them for analysis. This was necessary to increase the signal to noise ratio of the data from the quantum dots after photobleaching. Furthermore, it was necessary to align movies taken from the reference image and experimental images.

Data were first imported into ImageJ and processed with a bandpass filter to remove signals greater than 30 pixels (the size of the pillars) and less than 0 pixels. Images then underwent a background subtraction (radius = 20 pixels), Gaussian blur (radius = 1 pixels) and a Kalman stack filter. Regions of interest were defined and analysed using the Nano Tracking Plugin (MBI, Singapore). This plugin tracks the displacement of the pillars throughout the movie, relative to the reference frame, recoding the position of every pillar in each frame.

This data was then analysed using custom Matlab scripts to calculate the displacement of each pillar as a vector (magnitude and direction) and plots these vectors on the movie files. The level of noise was calculated by tracking any recorded displacements of pillars outside the cell. This was calculated for every cell analysed and an average noise level was calculated and pillar displacements greater than this level of noise were then included in the analysis. The data used for the statistical analysis was taken from whole cells and not individual pillars.

2.3 Statistical Analysis

All statistical calculations were carried out using Graphpad Prism (v 8.0). Analysis of differences between cardiomyocyte morphology on different stiffnesses and ligands were conducted using a two-way ANOVA to evaluate differences within and between conditions. To limit the degree of freedom, ANOVA calculations were restricted to

evaluate only the relevant conditions (i.e. differences between stiffnesses on the same ligand and not differences between ligands on different stiffnesses). Where appropriate, students t-tests were used to evaluate significant differences between two conditions. N numbers are given in figure legends. A single biological repeat is presented as observations from a single preparation and isolation of a litter of neonatal rats. Independent repeats/experiments refers to observations from different biological repeats using cells from different litters. The minimum N number of independent repeats used in this thesis is two. In cases where n numbers indicate single cells, data will have been pooled from 2 or more biological repeats and will be indicated where relevant. Technical repeats from the same passage are used for work with MEF cells.

3 CARDIOMYOCYTE RIGIDITY SENSING ON FIBRONECTIN & LAMININ

3.1 Integrin Expression in Neonatal Rat Cardiomyocytes

To investigate the different integrin signalling regimes occurring within cardiomyocytes, it was important to work with a model system which expresses the relevant integrin subtypes. Neonatal rat cardiomyocytes (NRCs) have been used extensively as an in-vitro model system within cardiac mechanobiology due to their ability to disassemble their myofibrils, spread on tissue culture surfaces and then reassemble their myofibrils in the presence of experimental stimuli. The ECM of the neonatal rat heart contains significant amounts of both fibronectin and laminin and, as a result, NRCs express integrin subtypes that bind to both fibronectin (predominantly $\alpha5\beta1$) and laminin (predominantly $\alpha7\beta1$) (Brancaccio et al., 1998, Maitra et al., 2000, Williams et al., 2014). Furthermore, in-vitro culture of NRCs has been routinely carried out on substrates coated with fibronectin or laminin, with studies reporting similar levels of cell attachment on both ligands (Borg et al., 1984, Taylor et al., 2000, Boateng et al., 2005, Williams et al., 2014). To compare and contrast the rigidity sensing behaviours of NRCs cultured on fibronectin or laminin, it was firstly important to verify that NRC express similar levels of $\alpha5\beta1$ and $\alpha7\beta1$ integrin subtypes.

To provide further verification of integrin expression in NRCs, a mini meta-analysis of integrin gene expression was carried out from online data repositories. Data was collected using Genevestigator, which collates data from numerous online microarray and mRNA-Sequence datasets. Genevestigator standardises all data in the database to the $\log^2$ format for comparison between different probes. An advantage of Genevestigator is the standardisation of expression data from thousands of experiments, enabling easy meta-analysis. For comparison, genevestigator to characterises expression data into three categories, low (0 – 7.5), medium (7.5 – 11.5) and high (> 11.5).

Inclusion criteria for the meta-analysis were as follows: 1) Whole heart lysates, 2) Cells were cultured in-vitro for 24-48 hours prior to lysis, 3) Cells were isolated from either Sprague Dawley or Wistar rats from P1 – 3) Studies must report data from at least three independent repeats. Data from control experiments such as treatment with DMSO were also included within the analysis. Searching the Genevestigator database returned 4 studies that met the inclusion criteria, reporting a total of 17 independent experiments. Within these 4 studies, the expression of α3, α5, α6, α7, α8, αv, β1 and β3 integrin subtypes, which have all been studies in cardiomyocytes, were analysed. In general, the level of mRNA expression for all subtypes was medium to high (Figure 3.1). Importantly, this data demonstrates that, at the level of transcription, NRCs express a range of fibronectin and laminin binding integrins at a medium to high level. This finding suggests

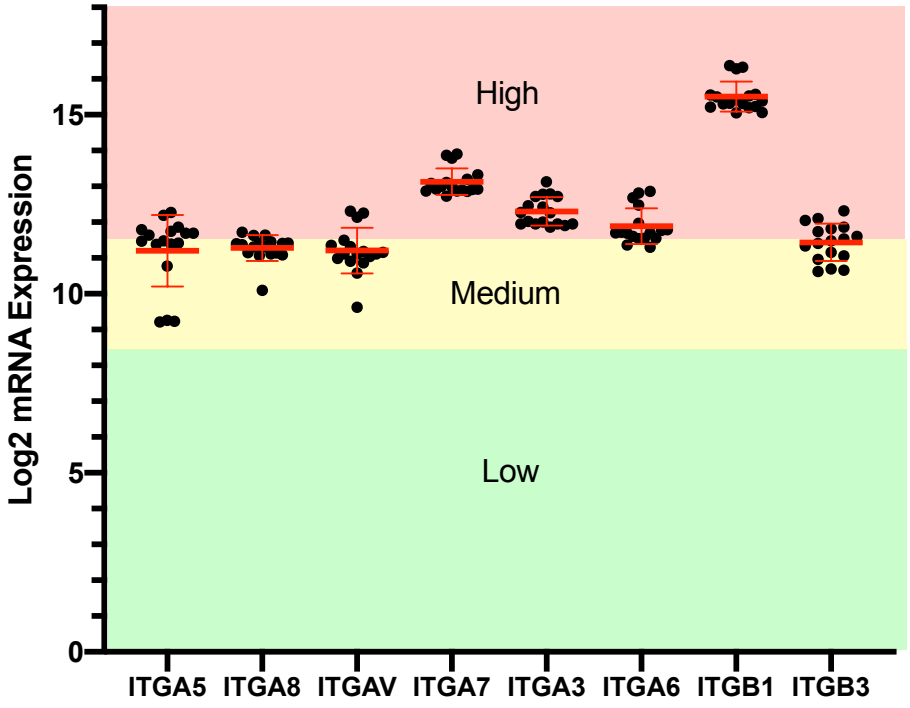

Figure 3.1. Summary of the mini-meta analysis of microarray and mRNA expression data from the Genevestigator database for the alpha subunits for the fibronectin/RGD binding ITGA5 (α5), ITGA8 (α8), ITGAV (αv) and laminin binding ITGA7 (α7), ITGA3 (α3) and ITGA6 (α6) subtypes. Expression also shown for the beta subtypes ITGB1 (β1) and ITGB3 (β3). All data has been normalised to the Log2 expression, which can be classified to three classes of expression; High (>11.5), Medium (8.5 – 11.5) and Low (<8.5). Bars indicate mean ± SD.

that NRCs represent a suitable model for investigating the integrin rigidity sensing behaviours of different integrin isoforms in cardiomyocytes.

3.2 Spreading and Rigidity Sensing of NRCs on Fibronectin and Laminin Coated Substrates

3.2.1 NRC Spreading on PDMS Substrates

During development and disease, cardiomyocytes are subject to dynamic changes in ECM composition and stiffness. Previous work has demonstrated a relationship between ECM stiffness and cell area, contractility, cytoskeletal architecture and morphology (Engler et al., 2008, Hersch et al., 2013, McCain et al., 2014, Pandey et al., 2018). Furthermore, recent work from the Iskratsch lab (Pandey et al., 2018) has demonstrated that cardiomyocytes sense changes in matrix rigidity via a combination of myofibrillar and non-myofibrillar contractions and that the costameric protein talin plays a key role in mediating the mechanotransduction response. While the effect and mechanisms by which cardiomyocytes detect changes in ECM rigidity are beginning to unfold, it is not clear whether these rigidity sensing strategies are consistent when occurring via different integrin isoforms.

PDMS substrates offer a highly tuneable platform for controlling substrate rigidity and therefore, provide a strong platform for investigating the rigidity sensing behaviours of NRCs. By mixing PDMS 184 and PDMS 527 at different ratios, we are able to produce substrates of different stiffnesses, representing Embroynic/neonatal (PDMS 184 : PDMS 527, 1:19), adult (1:9) and fibrotic (1:4) conditions of the heart. The stiffness of the different PDMS conditions was confirmed using oscillatory rheology, the results of which demonstrated the PDMS stiffness to be 6 kPa for neonatal, 20 kPa for adult and 130 kPa for fibrotic conditions (Figure 3.2). All rheology work was carried out together with William Valentine-Megone from the Gautrot group at Queen Mary University of London.

Previous work has shown that contractility is highly sensitive to substrate stiffness and that cardiomyocytes fine tune their contractile properties to match ECM elasticity (Engler et al., 2008, Hersch et al., 2013). To verify that PDMS substrates of various stiffness produce similar contractile responses to those observed on other polyacrylamide or other

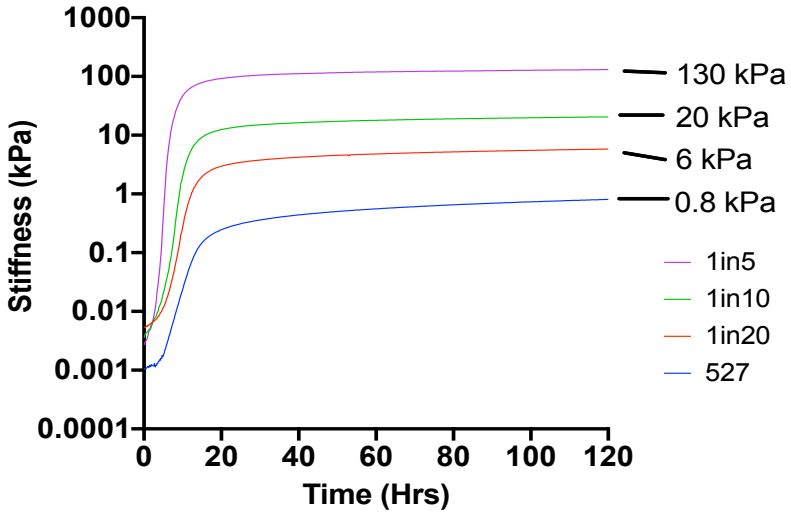

Figure 3.2. Rheometric measurements of PDMS stiffness by mixing 185 PDMS and 527 PDMS at different ratios. Data was collected in collaboration with William Valentine Megone (Galtrot lab, QMUL).

silicone based substrates, NRCs were plated on 1kPa, 6kPa, 20kPa and 130kPa substrates and visualised GFP α-actinin to measure sarcomeric shortening at the z-disc. This work was collected in collaboration with Liisa Hirvonen (Cox Lab, KCL). Consistent with the work of others, sarcomeric shortening and velocity was greater on soft compared to rigid substrates and confirms the suitability of PDMS substrates for investigating NRC rigidity sensing (Figure 3.3).

Cell spreading and morphology provide useful measures of the overarching mechanotransduction occurring within cells (Wolfenson et al., 2019). Therefore, NRCs were isolated and cultured for 24 – 72 hours on 6 kPa, 20kPa and 130kPa PDMS substrates coated with fibronectin or laminin. Cells were cultured in serum free media to remove any effect of serum components on NRC spreading. Cell area, morphology, was evaluated by visualising F-actin and α-actinin (Figure 3.4). After 24 hours, NRCs cultured on fibronectin had significantly greater cell area in 20kPa and 130 kPa conditions while cells in the 6kPa condition were spread to a similar extent. After 48 hours spreading, cells in all conditions had significantly increased in cell area compared to 24 hours. NRCs spreading on fibronectin again exhibited a larger cell area compared to those on laminin on the 6kPa and 20 kPa condition only. After 72 hours in culture, no significant differences in cell area were observed between fibronectin and laminin although there was a trend toward NRCs on fibronectin having greater cell area at 6 kPa. These results

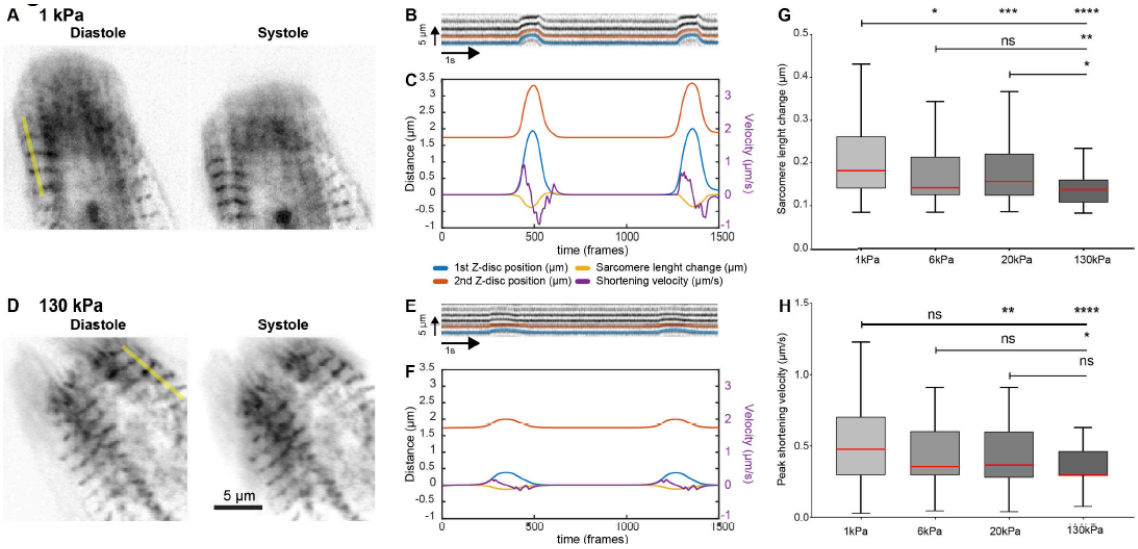

*Figure 3.3. Sarcomeric contraction velocity of NRCs on PDMS substrates of different stiffness. NRCs were infected with a GFP α-actinin adenovirus and sarcomeric contractions were recorded with high speed movies (209 fps). This data was collected in collaboration with Liisa Hirvonon (Cox lab, QMUL). A,D) Representative images of infected NRCs on soft (1 kPa) and stiff (20 kPa) PDMS. Yellow lines indicate areas of analysis with kymographs (B & E). Kymographs were used to monitor z-disc position during contraction on 1 kPa (C) and 130 kPa (D) PDMS. G, H) Quantification of sarcomere length change and shortening velocity in the four PDMS conditions. n = 11, 12, 11 & 13 cells for 1, 6, 20 & 130 kPa. * = $p < 0.05$, ** $p < 0.01$, *** = $p < 0.001$, $p < 0.0001$. P values from ANOVA and Tukey correction for multiple comparisons.*

demonstrate unique differences in the spreading of cardiomyocytes and that substrate rigidity and composition play in important roles in NRC rigidity sensing. Differences were ameliorated with increasing time in culture which could, in part, be due to cardiomyocyte depositing their own matrix over time. Therefore, to reduce the impact of

endogenous matrix deposition, and ensure confidence in our observations between

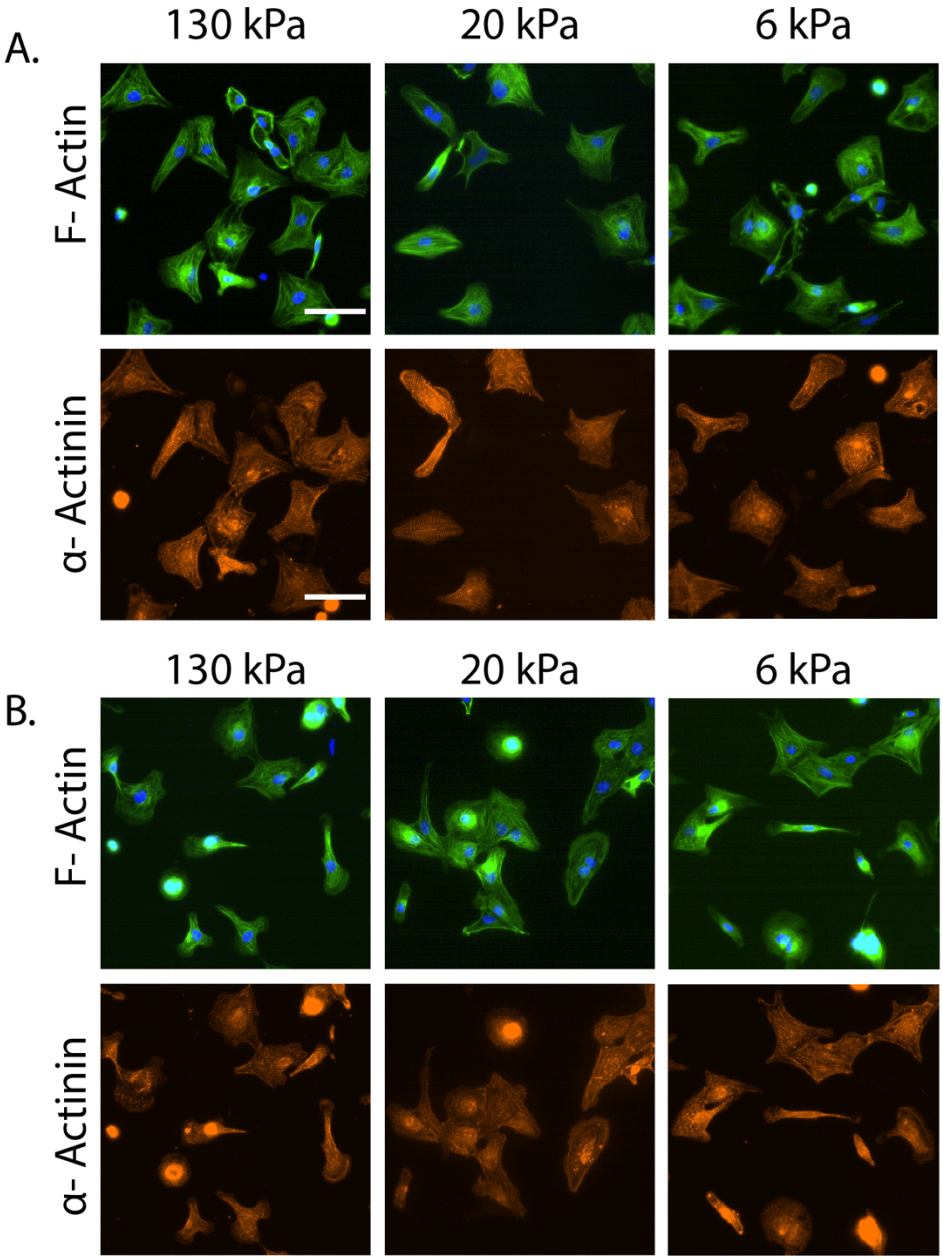

*Figure 3.4. NRC spreading on embryonic, adult and fibrotic PDMS substrates coated with Fibronectin (A) or Laminin (B). Quantified Cell Area after 24, 48 and 72 hours in culture. n = 3 independent experiments, > 400 cells per condition. * = p < 0.05, ** p < 0.01, *** = p < 0.001, p < 0.0001. P values from one-way (fibronectin vs laminin for each condition) ANOVA and Tukey correction for multiple comparisons. Scale bars = 50 μm.*

fibronectin and laminin, the rest of our analysis focussed on the 24 hour time point only.

At the 24 hour time point, significant differences in cell area were observed between stiffnesses, suggesting that NRCs are able to actively detect differences in substrate rigidity, even at this early time point. Analysis of cell morphology also provided further validation of the use of this early time point. Quantifying cell circularity revealed that 79 % of 1,741 cells could be characterised by an index of <0.4 and that NRCs adopt a more polygonal, rather than circular, shape (Figure 3.5C). Significant differences were also observed in cell morphology between cells spreading on fibronectin or laminin. At 6 kPa, NRCs on fibronectin were significantly more circular than cells on laminin. At 20 kPa, the opposite trend was observed where NRCs on laminin were significantly more circular than those on fibronectin.

To evaluate whether the differences in spreading observed between fibronectin and laminin could be attributed to differences in cytoskeletal assembly, the fluorescent intensity of F-actin and α-actinin was quantified (Figure 3.5 D & E). This measure is frequently utilised as an indication of cytoskeletal content. To ensure reliability, all samples were immunostained at the same time, from the same antibody solutions. NRCs cultured on fibronectin had significantly greater F-actin intensity in 6kPa and 20kPa conditions only. Interestingly, NRCs on laminin at 130 kPa had significantly greater F-actin intensity than those on fibronectin. For α-actinin content, only NRCs on 20kPa fibronectin substrates had significantly greater intensity compared to laminin. Between stiffnesses, subtle but significant differences were observed. On fibronectin, cells in the 20kPa condition had significantly greater F-actin and α-actinin intensity. Whereas on laminin, NRCs had significantly greater F-actin intensity in 130kPa conditions and significantly lower α-actinin in 20kPa conditions. These results suggests that NRC

rigidity sensing may have subtle but important differences when spreading on different ligands.

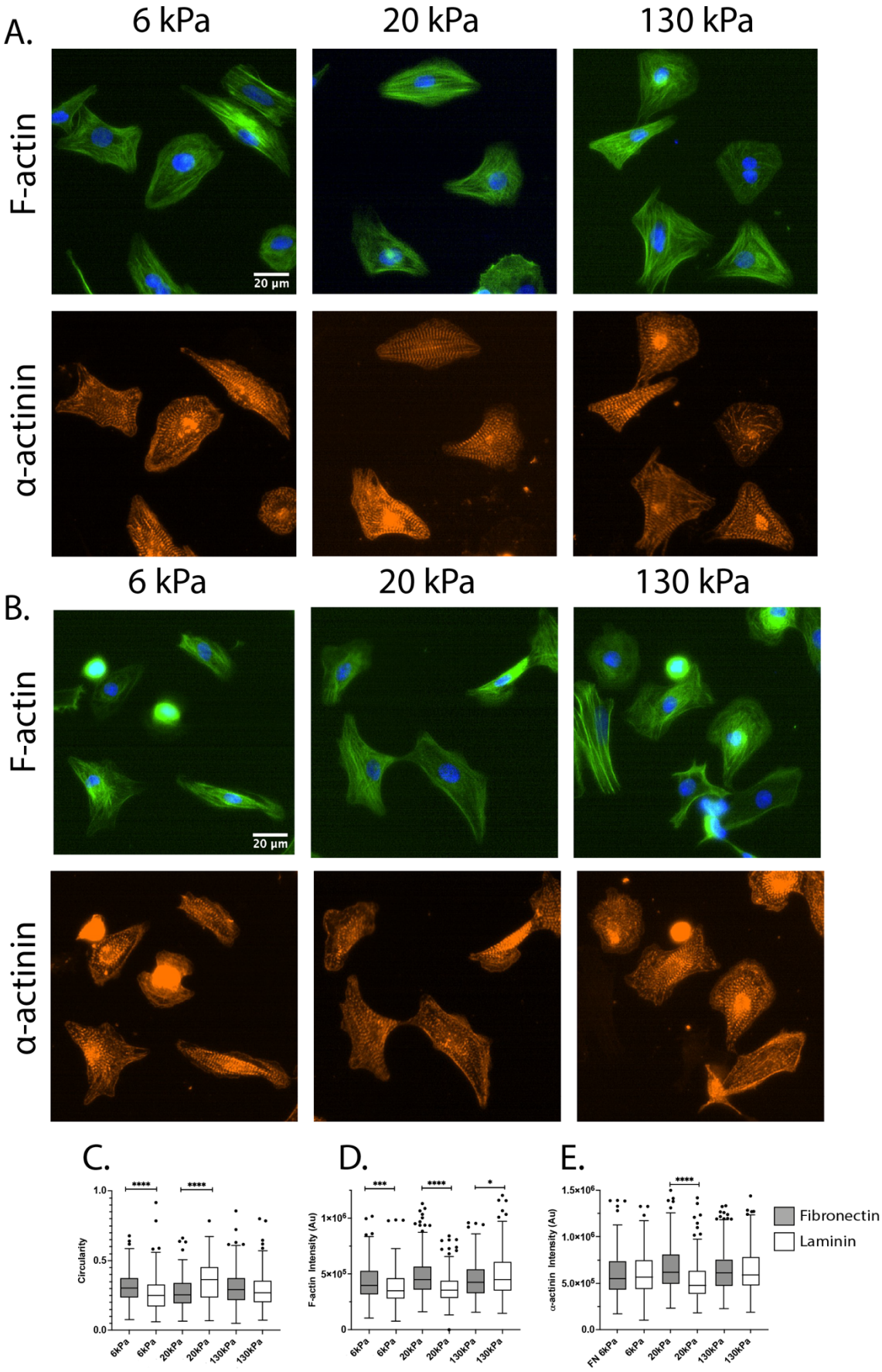

*Figure 3.5. Cytoskeletal morphology of NRCs cultured on fibronectin of laminin for 24 hours. Cells on fibronectin (A) and laminin (B) coated substrates were stained for F-actin and α-actinin and cell morphology (C), F-actin intensity (D) and α-actinin intensity were quantified. n = 2 independent experiments, > 300 cells per condition. * = $p < 0.05$, ** $p < 0.01$, *** = $p < 0.001$, $p < 0.0001$. P values from one-way (fibronectin vs laminin for each condition) ANOVA and Tukey correction for multiple comparisons.*

3.2.2 Cardiomyocyte Traction Forces: Differences between Fibronectin & Laminin

Previous work has demonstrated that cardiomyocytes employ a combination of myofibrillar and non-myofibrillar contractions for rigidity sensing (Pandey et al., 2018). Furthermore, cardiomyocyte contractility is closely related to sarcomeric content and cell morphology (Engler et al., 2008, Rodriguez et al., 2011, Hersch et al., 2013, McCain et al., 2014, Oyunbaatar et al., 2016). The differences observed between NRC spreading and morphology on fibronectin and laminin may be indicative of differences in the underlying traction forces.

In order to quantify fibronectin and laminin mediated traction forces, NRCs were cultured on nanopillar arrays. This platform has previously been successfully employed to measure the rigidity sensing behaviours of cardiomyocytes (Rodriguez et al., 2011, Hersch et al., 2013, Oyunbaatar et al., 2016, Pandey et al., 2018) and other non-muscle cells (Ghassemi et al., 2012, Iskratsch et al., 2013, Yang et al., 2016) . Furthermore, in collaboration with the Lappalainen lab (University of Helsinki), I have also demonstrated that nanopillars can be employed with high precision and sensitivity to detect cytoskeletal events such as stress fibre breakage(Ciuba et al., 2018). Therefore, nanopillar arrays (pillar diameter = 500 nm, spacing = 1000 nm, Stiffness = 3 pN / nm, calculated moduli of individual pillars = 10 kPa) were employed to compare the traction forces of NRCs cultured on fibronectin of laminin. This pillar dimension was chosen as previous work has identified cyclical stretching of the mechanosensitive protein Talin, within this stiffness range (Pandey et al., 2018). Pillar tops were firstly coated with quantum dots to enable accurate visualisation of pillar positions. Pillar displacements were measured with the cell *in situ*

and then compared to the position of the pillars after the cells had been removed by trypsinisation.

Freshly isolated NRCs were cultured for 24 hours before observing pillar displacements with live cell experiments. NRCs cast onto pillars without a fibronectin or laminin coating did not adhere and died before the start of experiments. After 24 hours, NRCs were spread on both fibronectin and laminin coated pillars but the extent of spreading was less (~50-75%) than that observed on flat PDMS substrates, suggesting that the nanotopography of the pillars is a more challenging environment for the NRCs to attach and spread. At this time point, cell traction forces were slightly larger on fibronectin than on laminin but this did not approach statistical significance (Figure 3.6). Measured pillar displacements in either condition ranged between 20 – 40 nm. Background noise from pillar displacements outside of the cell was calculated at 27 nm and so the traction forces detected in NRCs after 24 hours, especially on laminin were not sufficient high enough above the level of background noise. Therefore, NRCs were cultured on the nanopillars for an additional 24 hours to allow more time for cell adhesions and the cytoskeleton to mature.

After 48 hours, NRCs began to spontaneously twitch, suggesting a more mature cytoskeletal phenotype. Significant pillar placements were observed during the resting state (hereby referred to as the diastolic phase) with additional displacements of a subset of pillars occurring during twitches (hereby referred to as the systolic phase). Diastolic traction forces were significantly greater than those measured at 24 hours, and pillar displacements ranged from 58 – 100 nm on laminin and 87 – 241 nm on fibronectin . Noise levels were measured at ~ 30 nm on both fibronectin and laminin. On average, diastolic traction forces were 78 ± 21 % (mean ± SD) greater on fibronectin compared to laminin, with displacements measured at 79 ± 15 nm and 140 ± 49 nm for laminin and fibronectin, respectively. Systolic contractility (net maximum pillar displacements measured during systolic phase) was 46 ± 13 % greater in NRCs cultured on fibronectin compared to laminin, with displacements measured at 87 ± 23 nm and 127 ± 28 nm on laminin and fibronectin, respectively.

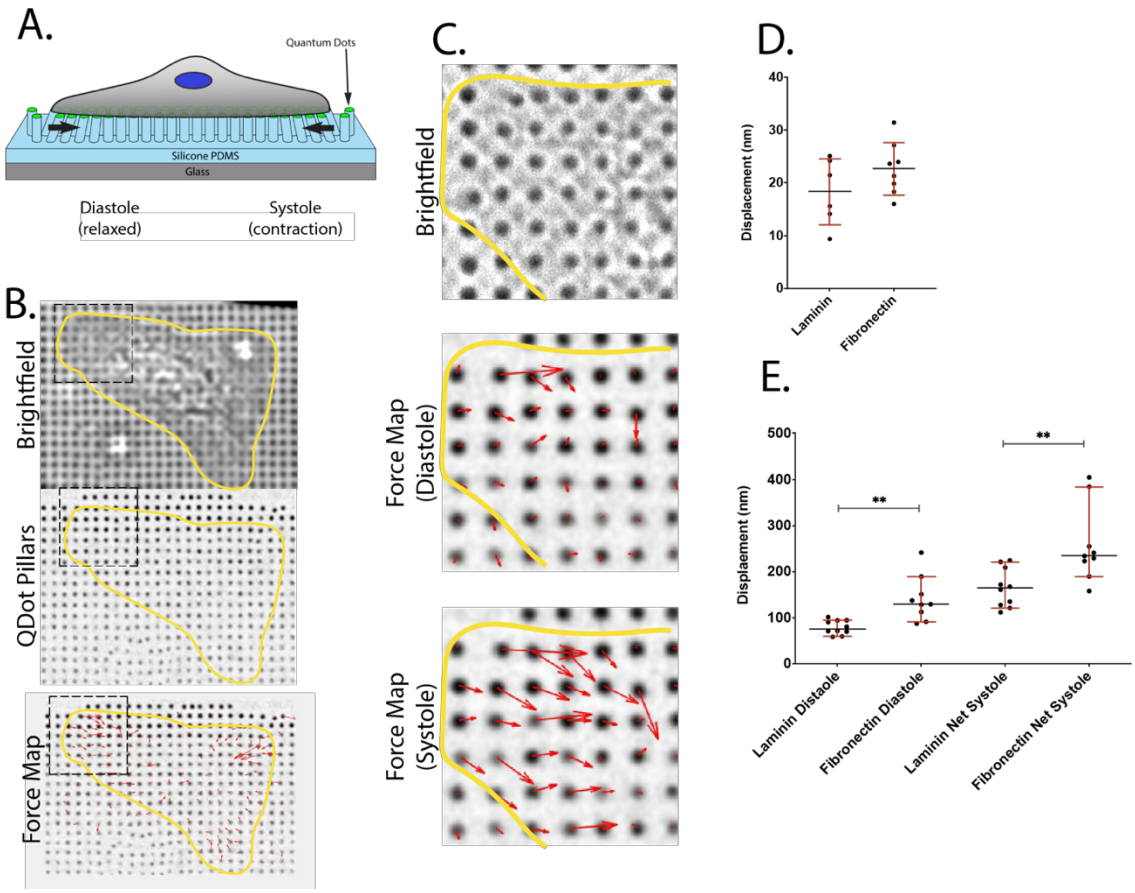

*Figure 3.6. A) NRC traction forces were analysed using PDMS nanopillars coated with quantum dots. B) Bright field images enabled confirmation of cell spreading and spontaneous twitching. C. Examples pillar displacements during diastole and systole. D) Analysis of pillar displacements after 24 hours in culture n = 7 & 9 cells for laminin and 9 fibronectin, respectively . E) Analysis of diastolic and systolic pillar displacements after 48 hours in culture. n = 10 & 9 cells for laminin and fibronectin respectively. * = $p < 0.05$, ** $p < 0.01$. P values from students t-test (fibronectin vs laminin). Figure adapted from Iskratsch, Wolfenson & Sheetz, 2014.*

To help characterise the contribution of myofibrillar (sarcomeric myosin) and non-myofibrillar (non-muscle myosin) forces to the displacements observed during the diastolic phase, NRCs were treated with verapamil, which inhibits myofibrillar tension by blocking L-type and T-type calcium channels. Verapamil treatment (15 minutes) resulted in inhibition of the systolic phase and an average decrease in diastolic pillar displacements of ~ 15% (Figure 3.7). Pillar by pillar analysis of displacements in the untreated diastolic phase relative to the displacements under verapamil treatment, revealed a log normal distribution, peaking at around 0.6 which suggests a 40 % reduction in tension in the absence of myofibrillar forces. However, the majority of the pillar

displacements were insensitive to verapamil treatment, especially at the edges of cells (Figure 3.7A, blue circles) suggesting a strong contribution of non-myofibrillar forces during the diastolic phase. Therefore, this data suggests that NRCs on fibronectin are capable of generating significantly greater myofibrillar and non-myofibrillar traction forces when cultured on fibronectin. Furthermore, this finding suggests that mechanosensitive elements at fibronectin adhesions experience greater tension and may promote more mechanosignalling events than laminin adhesions.

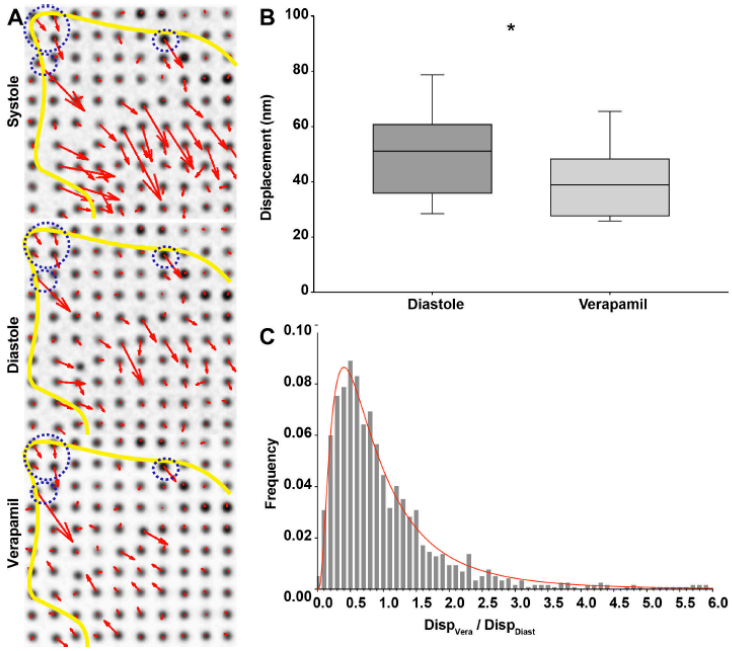

*Figure 3.7. Verapamil treatment of NRCs on fibronectin coated pillars. A) Representative force maps during systole, diastole and after verapamil treatment. Blue circles highlight pillars which were insensitive to verapamil treatment. B) Quantification of pillar displacements during diastole before and after verapamil treatment. C) Pillar by pillar analysis of displacement in diastole relative to displacement after verapamil treatment demonstrated a log normal distribution, peaking around 0.4, suggesting a 40% loss of tension. * = $p < 0.05$. P value from students t- test.*

3.3 Adhesion dependent Cardiomyocyte Rigidity Sensing Using Ligand Micropatterning

3.3.1 Micropatterning of Fibronectin and Laminin Lines

The data presented so far in this chapter has suggested that NRCs cultured on fibronectin and laminin have different rigidity sensing properties. On fibronectin, NRCs have significantly greater cell area, more cytoskeletal content and exhibit greater myofibrillar and non-myofibrillar traction forces. Furthermore, subtle rigidity dependent differences were observed in cytoskeletal content and spreading, suggesting an interplay between rigidity and composition of the ECM. It is therefore important to investigate these differences at the level of the focal adhesion, which appears to be mediating these observed differences. Ligand micropatterning offers a strong platform for controlling the composition and geometry of the ECM and has been utilised in previous work to investigate the effects of cardiomyocyte morphology on sarcomere assembly and contractility (Kuo et al., 2012, McCain et al., 2014, Yuan et al., 2017). Furthermore, micropatterning of fine features (1 – 4 μm in size) has been utilised by others to investigate focal adhesion and integrin signalling properties in other model systems such as T-cells and carcinoma cells (Tabdanov et al., 2015, Tabdanov et al., 2018, Rafiq et al., 2019). We therefore sought to combine micropatterning techniques with PDMS substrates to compare adhesion properties of NRCs spreading on micropatterned fibronectin or laminin, at different rigidities.

Micropatterned substrates were engineered by creating PDMS stamps presenting parallel lines, 1 μm thick at 5 μm spacings. To visualise the micropattern, fibronectin and laminin were labelled with a GFP NHS-ester. Stamps were coated with GFP-fibronectin or GFP-

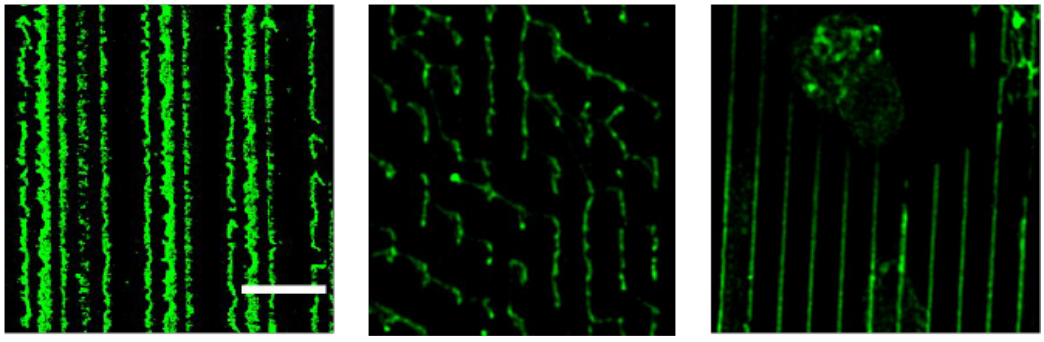

Figure 3.8. Common stamping errors on 6 kPa PDMS substrates. Common errors include background stamping where the PDMS has come into contact with the areas between the lines (left), streaking (middle) where the stickiness of the soft PDMS caused pattern streaks, and substrate yielding or topographical deformation of the PDMS (right). Scale bar = 10 μm.

laminin and patterns were transferred to PDMS substrates via manual contact printing (Figure 3.9A). Analysis of the stamped line features verified that micropatterns could be stamped consistently, with an average line width of 1.1 μm (range = 0.9 – 1.3 μm) on 130 kPa and 20 kPa and 6 kPa substrates.

Culturing of mouse embryonic fibroblasts on micropatterned fibronectin lines for 1 hour demonstrated that FAs (as evidenced by paxillin immunofluorescence Figure 3.9B) only form on the lines and not on the background. Culturing of NRCs on the micropattern for 24 hours also demonstrated strong paxillin staining to the micropatterned ligands (Figure 3.9C). Because the micropattern is non-covalently adsorbed to the PDMS, the NRCs may be able to reorganise and/or degrade the micropattern. For this reason, culture duration of NRCs on the micropattern was limited to 24 hours. This time point was also chosen to minimise artefact from NRCs depositing their own matrix over time. Furthermore, the softness of the 6 kPa PDMS substrates resulted in considerable variability in the quality of the stamp and patterning errors such as background stamping (the compliant substrate allowed contact with the background of the stamp, streaking and topographical

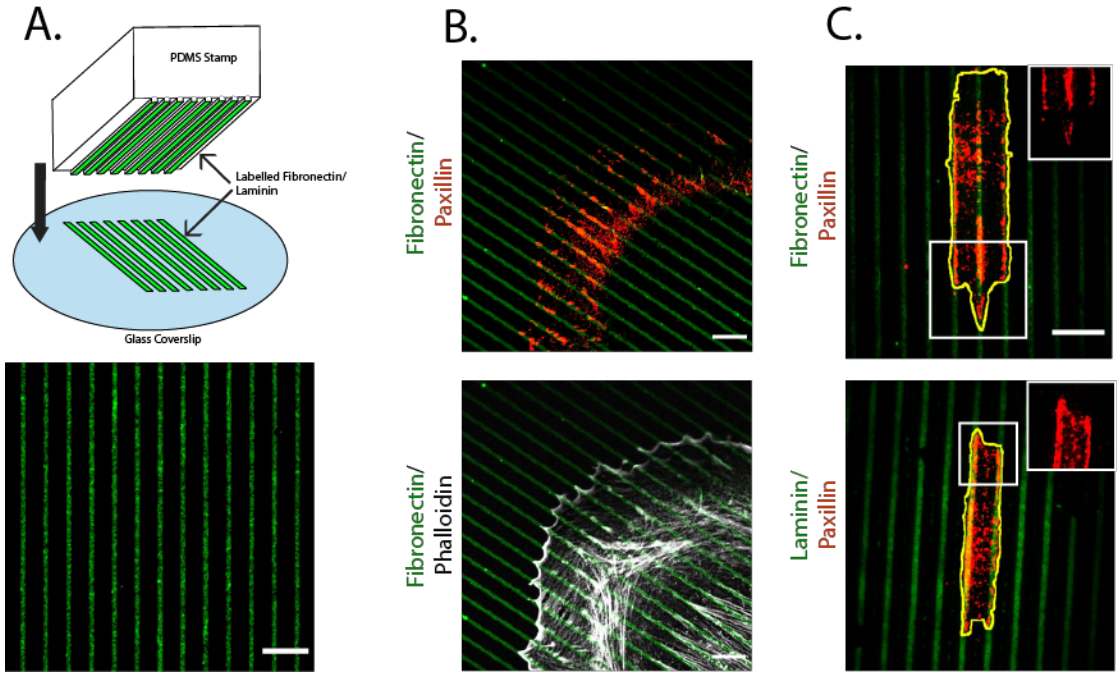

Figure 3.9. A) Schematic of stamping of atto 488-labelled fibronectin or laminin using PDMS stamps. B) MEFs were cultured on micropatterned atto 488 fibronectin for 1 hour and cell exhibited strong localisation of paxillin to the lines which also results in alignment of the cytoskeleton with the micropattern. C) NRCs cultured on fibronectin and laminin lines also exhibited strong paxillin localisation to the micropatterned lines. Scale bars = 10 μm.

deformation of the PDMS (Figure 3.8) were observed. Therefore, experiments were limited to 130 kPa and 20 kPa substrates.

3.3.2 NRC Morphology on Fibronectin and Laminin Lines

After 24 hours in culture, NRCs on 130 kPa and 20 kPa micropatterned substrates all cardiomyocytes adopted a rod like morphology, independent of stiffness and ligand type.

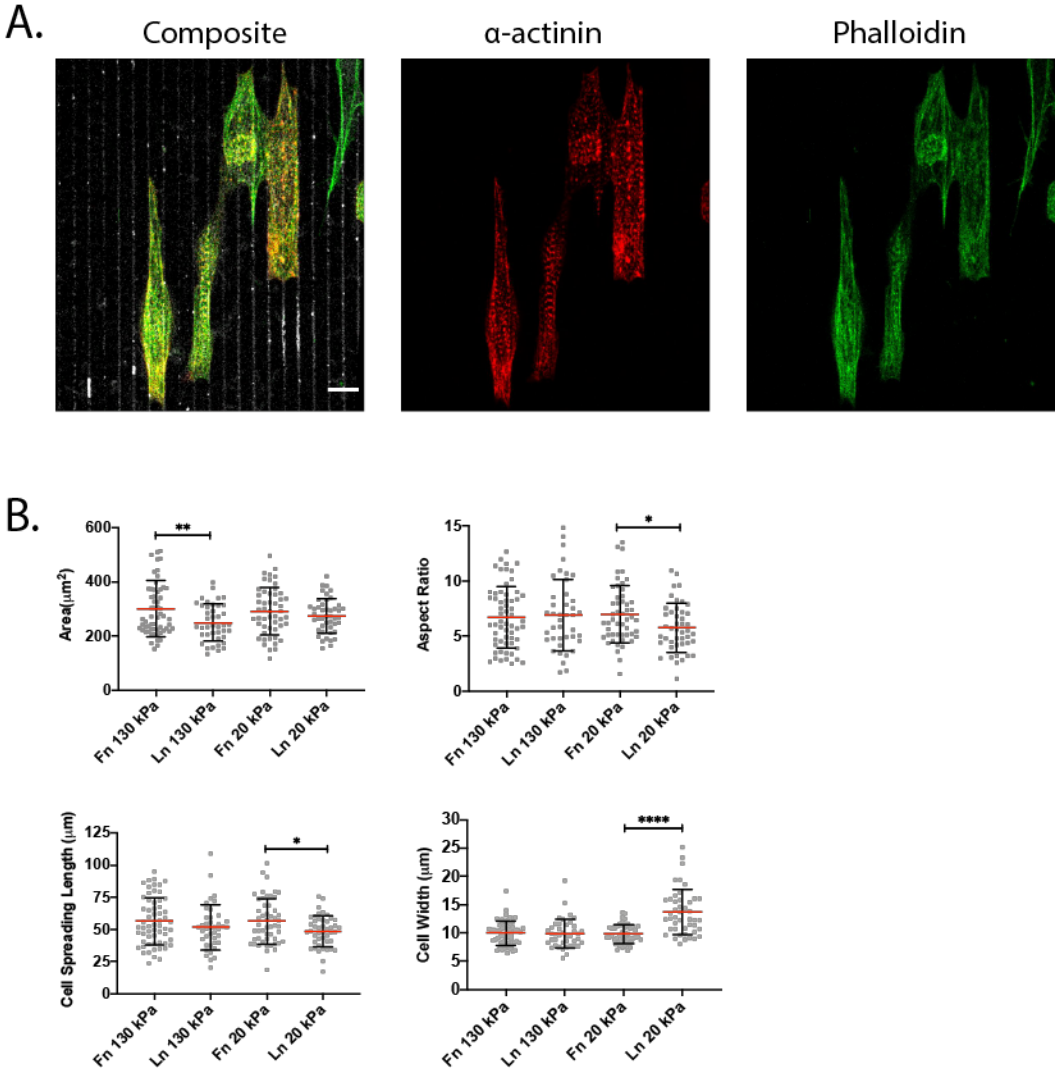

*Figure 3.10. Spreading of NRCs on micropatterned fibronectin or laminin lines. A) Representative images of typical cell morphology after 24 hours in culture on the micropatterned lines. B) Quantification of cell area, aspect ratio, cell spreading length along the lines and cell spreading width across the lines. n = 60, 41, 51 & 45 cells (from 3 biological repeats) for fibronectin 130 kPa, laminin 130 kPa, fibronectin 20 kPa and laminin 20 kPa. Data points (grey dots) indicate values for individual cells, red lines indicate the mean and error bars indicate 25th to 75th percentiles. * = $p < 0.05$, ** $p < 0.01$, *** = $p < 0.001$, $p < 0.0001$. P values from students t- test. Scale bar = 10 μm.*

NRCs exhibited a range of morphologies by spreading across just 1 - 3 lines, resulting in cells exhibiting narrow widths of 5-15 μm and long cell lengths of 30 – 100 μm (Figure 3.10) which appears to be consistent with previous observations on micropatterned line with similar dimensions (Clark et al., 1992). Statistical analysis revealed that at 130 kPa, NRCs on fibronectin had significantly greater adhesion area but similar cell length to NRCs cultured on laminin. At 20 kPa, NRCs on fibronectin had similar cell area but significantly greater cell length compared to laminin. Previous work has demonstrated that when NRCs adopt such a rod like morphology, subtle changes in cell aspect ratio (AR) can have significant effects on contractility, by modulating the stacking of myofibrils in serial (high AR) or in parallel (low AR) (Kuo et al., 2012, McCain et al., 2014). NRC ARs were thus quantified, revealing that NRCs exhibited ARs ranging from 1:3 – 1:9 (on average). At 130 kPa, cell ARs were similar between fibronectin (6.7 ± 2.8) and laminin (6.9 ± 3.2). At 20 kPa, NRCs on laminin micropatterns had significantly lower AR than those on fibronectin (6.9 ± 2.6 and 5.6 ± 2.2, respectively), suggesting possible differences in cytoskeletal arrangement.

3.3.3 Enrichment of Cytoskeletal Proteins on Micropatterned Fibronectin and Laminin Lines

Visualisation of the cytoskeleton (F-actin & α-actinin via immunofluorescence) and analysis of whole cell F-actin and α-actinin content (fluorescence intensity), revealed significantly greater F-actin enrichment and a trend towards greater α-actinin content on fibronectin at 130 kPa (Figure 3.11). At 20 kPa, no significant differences in whole-cell F-actin or α-actinin intensity were observed between the two ligands, although F-actin content demonstrated a trend towards being significantly lower on laminin. Finally, both F-actin and α-actinin appeared to be enriched at the cell edges, in proximity to the micropatterned lines. Analysis of F-actin or α-actinin enrichment to the lines compared to the whole cell, revealed that both F-actin and α-actinin were mildly enriched in proximity to the lines. Statistical analysis revealed significantly less F-actin on 20 kPa laminin lines compared to fibronectin, but not 130 kPa. α-actinin exhibited a trend towards significantly less enrichment on 20 kPa laminin lines. These results suggest a potential interplay between substrate rigidity and ECM composition, with NRCs exhibiting strong spreading phenotype with increased cytoskeletal content at fibrotic stiffnesses, with a more pronounced effect on fibronectin. However, analysis of cytoskeletal enrichment in proximity to integrin adhesions at the lines, revealed similar

behaviours between ligands at the fibrotic stiffness and significantly less activity on laminin at physiological stiffness, suggesting more pronounced differences in ECM sensing at 20 kPa.

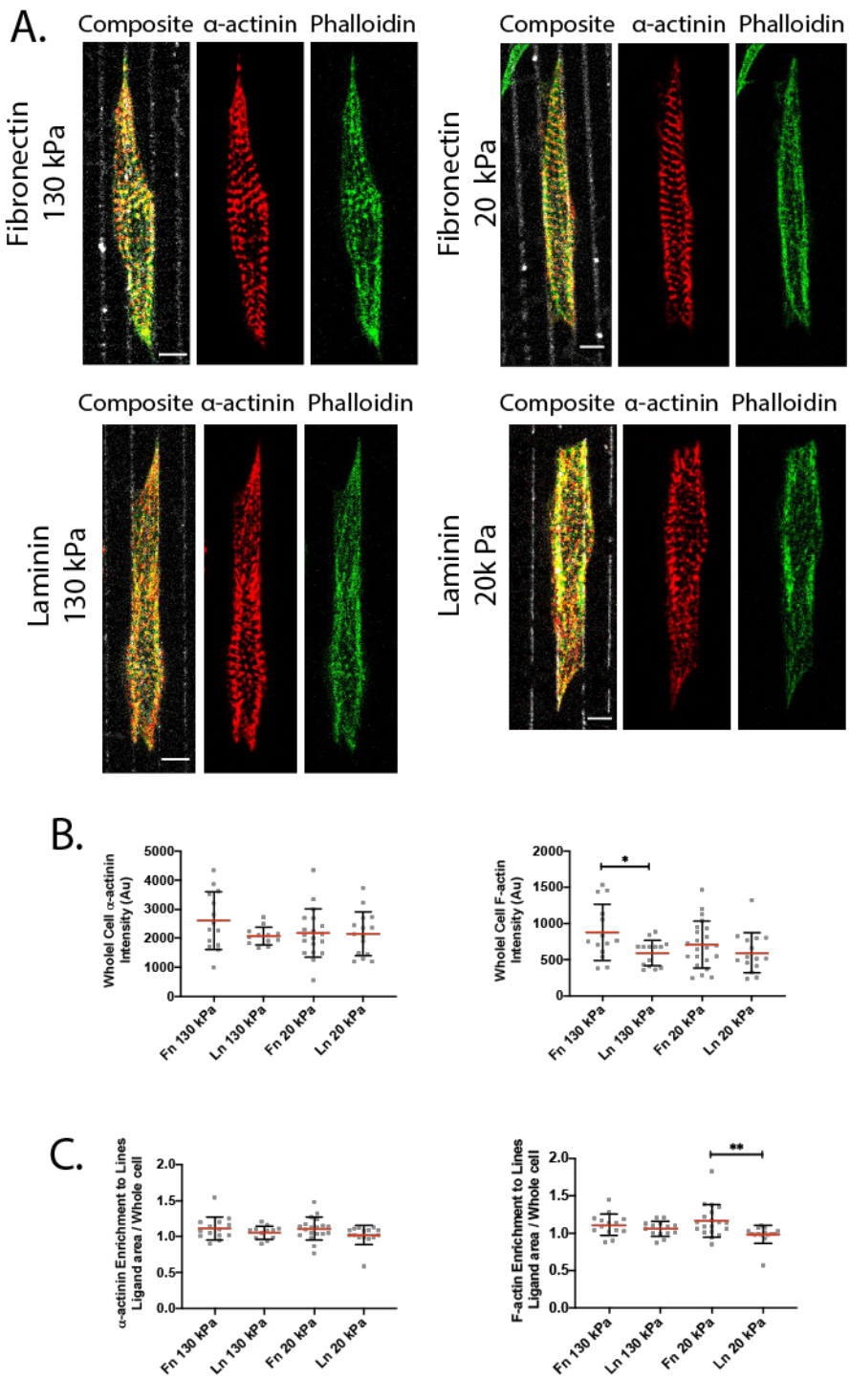

*Figure 3.11. Cytoskeletal and sarcomeric content on the different micropatterns and enrichment to fibronectin and laminin lines. A) Representative images from each condition. B) Quantification of Whole cell F- actin and α-actinin content. C) Quantification of F- actin and α-actinin enrichment to the lines relative to the whole cell. n = 14, 14, 22 & 15 cells (from 2 biological repeats) for fibronectin 130 kPa, laminin 130 kPa, fibronectin 20 kPa and laminin 20 kPa. * = $p < 0.05$, ** $p < 0.01$, *** = $p < 0.001$, $p < 0.0001$. for the Plots, data points (grey dots) indicate values for individual cells, red lines indicate the mean and error bars indicate 25th to 75th percentiles. P values from students t- test. Scale bar = 5 μm.*

3.3.4 Vinculin Enrichment to Fibronectin and Laminin Lines

In light of morphological and cytoskeletal differences between NRCs spreading on fibronectin and laminin lines, it was necessary to evaluate the effects of the different pattern dimensions at the level of the focal adhesion. Vinculin is a prominent adapter protein in cardiomyocyte focal adhesions and plays a key role in integrin mediated force transmission (Zemljic-Harpf et al., 2007, Tangney et al., 2013, Yao et al., 2016). Recent work from the Iskratsch lab using NRCs, has also demonstrated the localisation of vinculin at sites of high force transmission (Pandey et al., 2018). Following the observation that NRCs on fibronectin exert greater traction forces than cells on laminin (Figure 3.6). It was hypothesised that vinculin may be differentially enriched at fibronectin and laminin adhesions.

To test this hypothesis, the chosen vinculin antibody was validated by comparing its colocalization with transfected GFP-vinculin in MEFs (Figure 3.12A). After antibody validation, vinculin enrichment was quantified on the 130 kPa and 20 kPa micropatterns after 24 hours in culture (see Figure 3.12B for visual description of image segmentation). Enrichment was calculated by measuring the immunostaining density (total signal divided by area) from areas of the cell that overlapped with the lines, relative to the whole cell, minus the background (Tabdanov et al., 2015, Tabdanov et al., 2018). Therefore, a value of greater than 1 suggest enrichment to the lines, relative to the rest of the cell. Vinculin was enriched to adhesions along the micropatterned lines throughout the entire length of the cells. Analysis of vinculin enrichment on 130 kPa micropatterns revealed similar enrichment on both fibronectin and laminin (1.1 ± 0.12 and 1.08 ± 0.14, respectively). On 20 kPa substrates, however, NRCs on fibronectin lines exhibited significantly more vinculin enrichment than cells on laminin (1.13 ± 0.11 and 0.84 ± 0.09, respectively).

Coupled with the observation of reduced traction forces on nanopillars (10 kPa), reduced AR and cytoskeletal content, reduced vinculin enrichment to laminin lines at 20 kPa is suggestive of less molecular tension at laminin compared fibronectin adhesion.

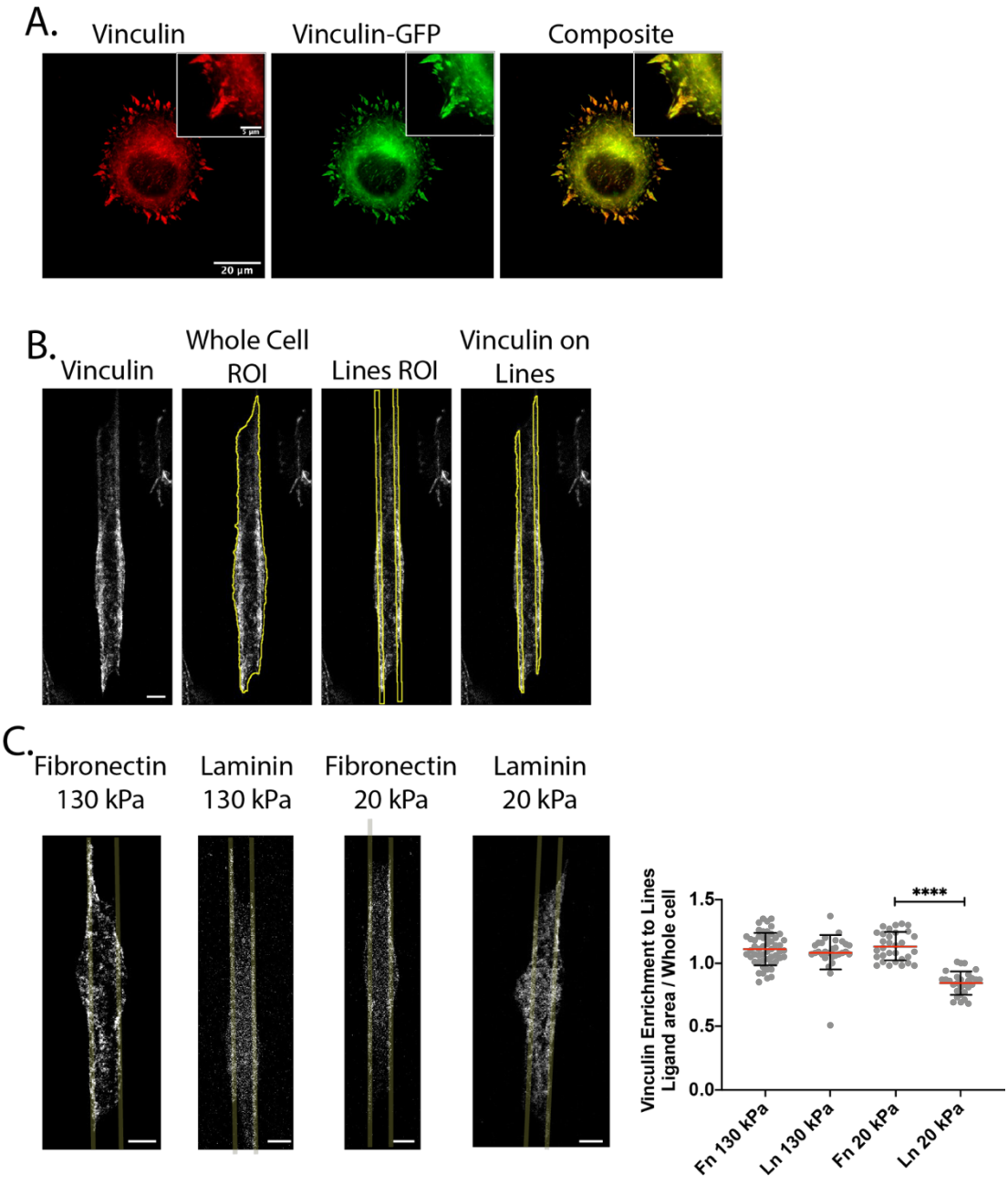

*Figure 3.12. Vinculin enrichment to micropatterned fibronectin and laminin lines. A) Validation of a vinculin antibody for immunofluorescence studies was confirmed by visualising co-localisation between the antibody and a transiently transfected GFP-vinculin plasmid in MEFs. B) Visual descriptions of analysis of vinculin enrichment to the lines. Regions of interest (ROI) are generated for the whole cell and the position of the lines. Then an ROI is generated of the overlapping area of the whole cell and lines ROI. Vinculin enrichment is calculated by dividing the signal intensity form the vinculin on the lines ROI by the signal intensity from the whole cell. Enrichment values greater than 1 = enrichment to the lines. C) Representative images and quantification of vinculin enrichment to fibronectin and laminin lines of fibrotic or physiological stiffness. n = 53, 29, 31 & 29 cells (from 2 biological repeats) for fibronectin 130 kPa, laminin 130 kPa, fibronectin 20 kPa and laminin 20 kPa. Plots, data points (grey dots) indicate values for individual cells, red lines indicate the mean and error bars indicate 25th to 75th percentiles. * = $p < 0.05$, ** $p < 0.01$, *** = $p < 0.001$, $p < 0.0001$. P values from students t- test. Scale bar = 5 μm.*

3.3.5 FHOD1 Enrichment to Fibronectin and Laminin Lines

So far, results from the micropatterned lines have suggested that NRCs cultured on laminin at physiological stiffness (20 kPa) have less vinculin and F-actin enrichment at adhesion sites, suggesting less tension through adhesions. To further investigate the different rigidity sensing regimes observed on fibronectin and laminin lines, it was important to evaluate the localisation of other proteins that participate in rigidity sensing. The actin polymerising protein Formin Homology Domain-containing protein 1 (FHOD1) has been shown to be a key regulator of integrin mediated traction forces and participate in cardiomyocyte rigidity sensing at focal adhesions (Iskratsch et al., 2013, Pandey et al., 2018). Therefore, activity and localisation of FHOD1 was evaluated on the micropatterned lines using a phospho-specific FHOD1 antibody (active FHOD1, phosphorylated at Thr1141, pFHOD1). The antibody was first validated for immunostaining by comparing localisation with a transiently transfected GFP-FHOD1 plasmid which exhibited colocalization at the cell edge, where FHOD1 is thought to be activated by ROCK (Hannemann et al., 2008). This observation is also in agreement with reports of this antibody localising close to sites of high traction forces at the cell edge

(Pandey et al., 2018). In NRCs cultured on micropattern, pFHOD1 exhibited a low level of localisation to the lines in addition to a diffuse cytoplasmic or cytoskeletal localisation (Figure 3.13). However, analysis of pFHOD1 enrichment to the lines vs the whole cell did not demonstrate significant enrichment to the lines (enrichment value < 1), due to moderate staining to cytoplasmic and cytoskeletal structures. While the conditions observed here may provide sufficient cues for cell spreading and morphology, the micropatterned lines do not appear to be a good platform to investigate enrichment of adhesion proteins in detail. The observed enrichment of vinculin and poor enrichment of pFHOD1 suggest that key adhesion proteins are not being recruited to adhesions using this platform. It was, therefore, necessary to continue investigations on substrates that are less restrictive to cell spreading and enable greater adaptor enrichment while also permitting comparison of adhesion to fibronectin and laminin.

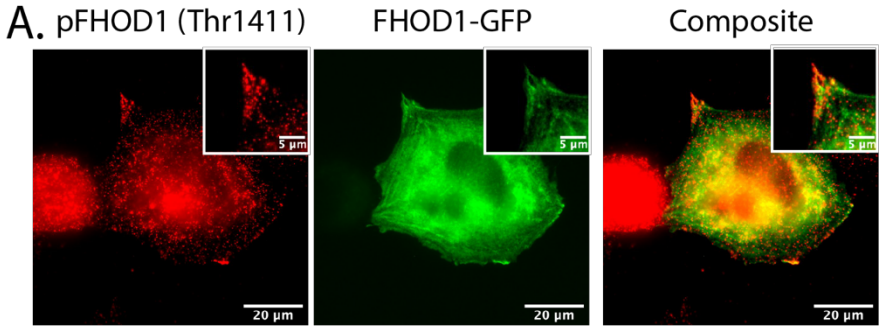

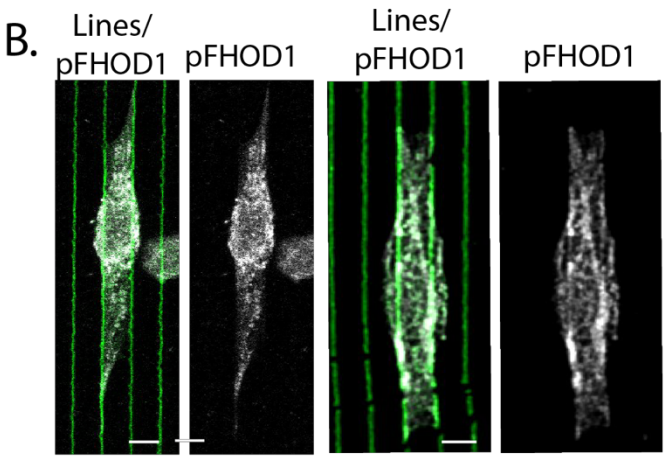

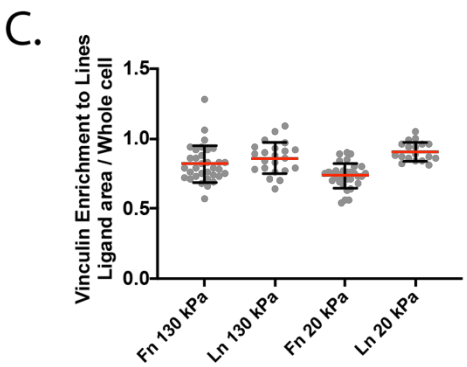

Figure 3.13. Analysis of pFHOD1 enrichment to micropatterned fibronectin and laminin lines. A & C) Validation of pFHOD1 antibody for immunofluorescence studies was confirmed by visualising co-localisation between the antibody and a transiently transfected GFP-FHOD1 plasmid in MEFs. B) Representative images of diffuse (Left) or cytoskeletal (right) pFHOD1 localisation, note mild enrichment to the lines. E) Quantification of pFHOD1 enrichment to the lines demonstrated poor enrichment. n = 33, 22, 32, 18 cells (from 2 biological repeats) for fibronectin 130 kPa, laminin 130 kPa, fibronectin 20 kPa and laminin 20 kPa. Plots, data points (grey dots) indicate values for individual cells, red lines indicate the mean and error bars indicate 25th to 75th percentiles. Unlabelled scale bars = 5 μm.

3.3.6 Investigating Vinculin and pFHOD1 Enrichment Using Micropatterned Grids

To further investigate the localisation of adaptor proteins to different ligands, micropatterned grids were engineered to present fibronectin and laminin lines in a perpendicular fashion, presenting a grid of ligands. Grids were produced in the same manner as the lines, with fibronectin lines being manually stamped on the PDMS followed immediately by manual perpendicular stamping of laminin lines. This approach offers the advantage of directly comparing fibronectin and laminin adhesion within the same cells. On micropatterned grids, cell area increased at both rigidities and cells still preferred to spread across 2-4 lines. Interestingly, NRC morphology and spreading along either ligand demonstrated rigidity dependent changes. At 130 kPa, NRCs invariably aligned their major axis along fibronectin lines, as demonstrated by dramatic differences in spreading length on fibronectin and laminin Figure 3.14. At 20 kPa, however, spreading along fibronectin or laminin lines was more variable, with decreased spreading along fibronectin and increased spreading along laminin, relative to 130 kPa. This stiffness dependent morphology change is further verified by the cell ARs which were significantly greater at 130 kPa (mean ± SD, 6.1 ± 2.9) compared to 20 kPa (4.2 ± 2.1). These results suggest that fibronectin adhesions may be stronger and more stable at fibrotic stiffnesses and that laminin adhesions may play a more important role in spreading and adhesion at physiological stiffnesses. To further investigate this, vinculin and pFHOD1 localisation were evaluated on the grids to evaluate how the morphological differences observed at each stiffness translate to the enrichment of adaptor proteins.

Vinculin enrichment on the grids demonstrated stark differences on fibronectin and laminin lines, which was also changed with substrate rigidity. At 130 kPa, vinculin was greatly enriched on fibronectin lines, with less enrichment on laminin lines. At 20 kPa, vinculin enrichment was still greater on fibronectin lines but, compared to 130 kPa, enrichment was generally lower on fibronectin and greater on laminin lines. To evaluate

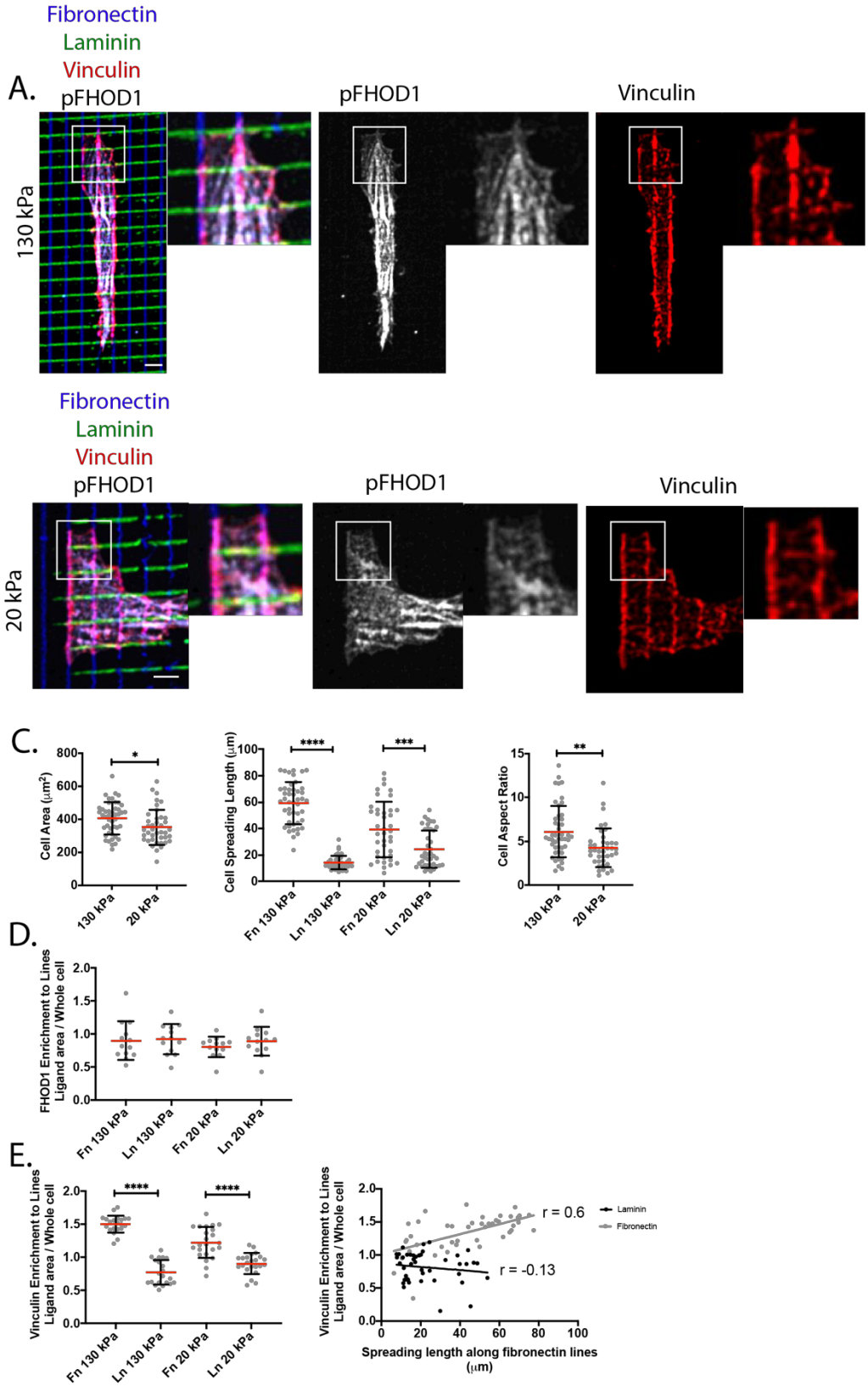

Figure 3.14. Vinculin and pFHOD1 enrichment to fibronectin/laminin grids. A & B) Representative images on pFHOD1 (A) and vinculin (B) localisation to the grids. C) Quantification of cell morphology on the grids. n = 46 and 40 cells (from 2 biological repeats) for 130 kPa and 20 kPa conditions. D) Analysis of pFHOD1 enrichment to the grids. n = 13 cells (from 2 biological repeats) in each condition. E) Analysis of vinculin enrichment to the grids and Persons correlation coefficient of vinculin enrichment vs spreading length . n = 21 & 23 cells (from 2 biological repeats) at 130 kPa and 20 kPa conditions. Plots, data points (grey dots) indicate values for individual cells, red lines indicate the mean and error bars indicate 25th to 75th percentiles. = $p < 0.05$, ** $p < 0.01$, *** = $p < 0.001$, $p < 0.0001$. P values from students t- test. Scale bar = 5 μm.*

whether vinculin enrichment was dependent upon the degree of spreading on either set of lines, vinculin enrichment against the spreading length. The results demonstrated a moderate positive correlation on fibronectin ($r = 0.6$, $p < 0.0001$) and no correlation on laminin ($r = -0.13$, $p > 0.05$), suggesting differential regulation of vinculin recruitment.

On the micropatterned grids, pFHOD1 exhibited a more distinct localisation to F-actin or cytoskeletal structures, resulting in little enrichment to the line (enrichment value < 1, Figure 3.13D). However, subcellular enrichment of pFHOD1 to adhesions was still observed (Figure 3.13A) consistent with its hypothesised role in cardiomyocyte rigidity sensing (Pandey et al., 2018). Adhesion enrichment of pFHOD1 was mostly observed in small protrusions along lines at the cell edge. These findings suggest that pFHOD1 is present at fibronectin and laminin adhesions and may participate in actin polymerisation downstream of integrin signalling, as suggested by others (Iskratsch et al., 2013, Pandey et al., 2018). However, this investigation was unable to further investigate this pathway due to the different subcellular localisations of pFHOD1.

3.4 Discussion

This investigation has shown that the spreading and adhesion behaviours of NRCs differ when cultured on fibronectin and laminin. NRCs cultured on fibronectin spread further, exhibit more cytoskeletal content and have greater myofibrillar and non-myofibrillar contractility, which likely results in the greater enrichment of force sensitive integrin adaptor proteins such as vinculin. Ligand micropatterning also revealed an important differences between substrates with physiological or fibrotic stiffness. At high stiffness,

NRCs exhibit a preference for fibronectin adhesions, which promote greater spreading, vinculin enrichment and cytoskeletal assembly, resulting in preferential adhesion and alignment. At physiological stiffness, fibronectin adhesions are still dominant but NRCs demonstrate increased spreading along laminin ligands compared to fibrotic stiffnesses. However, increased spreading along laminin at physiological stiffness did not result in strong vinculin enrichment to laminin adhesions, suggesting the NRCs preferentially spread along fibronectin due to increased adhesion stability.

Cardiomyocyte integrin expression is dynamic during development and disease. The fibronectin binding α5β1 integrins are upregulated when the heart is undergoing dynamic changes in ECM stiffness during embryonic development and disease states (Ward and Iskratsch, 2019). In the current investigation, NRCs cultured on fibronectin exhibited greater substrate interaction (cell area) as well as greater contractility (traction forces), cytoskeletal content (F-actin and α-actinin) and vinculin enrichment to adhesions. This phenotype could be more favourable for important behaviours during embryonic development (such as migration or proliferation) and disease (such cytoskeletal remodelling or rapid hypertrophy). Indeed, the fibronectin binding α5 integrin subtype is rapidly upregulated in cardiomyocytes during diseased states such as hypertension and ischaemia (Nawata et al., 1999, Babbitt et al., 2002). Furthermore, numerous studies have identified fibronectin binding integrins as key players in mediating cardiomyocyte hypertrophy (Ogawa et al., 2000, Babbitt et al., 2002, Balasubramanian and Kuppuswamy, 2003, Willey, 2003, Johnston et al., 2009). However, why fibronectin binding integrin subtypes play such a strong role in pathological hypertrophic signalling remains unclear. The results from the current investigation suggest that NRCs on fibronectin substrates have greater vinculin enrichment which suggest greater adhesion stability through reinforcement of the integrin/F-actin link (Humphries et al., 2007, del Rio et al., 2009). This would permit the greater spreading, cytoskeletal content and traction forces observed here.

This investigation directly compared the behaviour (morphology, forces) of cardiomyocytes cultured on fibronectin and laminin coated substrates. The nano-pillar arrays implemented here are advantageous for this approach as they permit the analysis of the traction forces occurring at multiple adhesion sites, providing superior resolution to micro-pillar arrays used by others (Rodriguez et al., 2011, Hersch et al., 2013, Oyunbaatar et al., 2016). Furthermore, the sub-micron dimensions of the pillars disrupt cell morphology less than micro-pillars by enabling cells to sit on top of, as opposed to

between, the pillars (Li et al., 2007). The results from the current investigation demonstrate that NRCs on fibronectin coated pillars produce greater traction forces during diastolic and systolic phases, than those on laminin coated pillars. The majority of diastolic pillar displacements at the cell edge were insensitive to muscle myosin inhibition, suggesting that both muscle and non-muscle myosin contribute towards the elevated traction forces on fibronectin. Recent work from the Iskratsch lab has demonstrated that both myofibrillar and non-myofibrillar contractility contribute towards rigidity sensing in NRCs (Pandey et al., 2018). Results from cell spreading and micropatterning suggest that differences in cytoskeletal content and adhesion stability may explain the observed differences in contractility. However, cytoskeletal content and vinculin enrichment was also found to vary dependent upon substrate rigidity. Previous work as demonstrated that cardiomyocyte contractility increases with substrate stiffness (Engler et al., 2008)}(Hersch et al., 2013, Pandey et al., 2018). Furthermore, how contractility changes between fibronectin and laminin remains unclear and further investigation with nanopillars of different stiffness will provide more information on the role of integrin signalling on cardiomyocyte traction forces. This is especially important in the light of previous work which clearly demonstrated a direct link between integrin subtype, adaptor protein enrichment and cellular contractility (Rahmouni et al., 2013).

Implementation of PDMS substrates and ligand micropatterning has revealed unique spreading, morphology and adhesion enrichment properties of NRCs on fibronectin and laminin. Micropatterning has several advantages including, control the adhesion area, cell morphology, ECM geometry and ligand composition, while enabling analysis of adhesion properties relative to the micropattern. Previous work has demonstrated that NRCs will align their myofibrils along the axis of maximal stress, which can be modulated by controlling cell morphology (Yuan et al., 2017). Culturing of NRCs on micropatterned fibronectin rectangles with defined ARs demonstrated that cardiomyocytes generate maximum traction forces at 13 kPa when cell have an AR of 7:1. Furthermore, at 90 kPa, cell morphology required an AR of 2:1 for maximum traction force (Kuo et al., 2012, McCain et al., 2014). All NRCs observed in the current investigation adopted a highly polarised rod-shaped morphology along micropatterned lines with average ARs ranging from 4:1 – 7:1 on all stiffnesses, suggesting that NRCs are adopting spreading morphologies for optimal contractility. However, no differences in morphology were observed between fibronectin lines at 130 kPa and 20 kPa (AR = ~1:7), while cells on laminin exhibited a less extreme aspect ratio in softer conditions only (AR = ~ 1:5). These

results may reflect differences in maturity of the contractile cytoskeleton due to differences in the culture time (24 hours vs 72 hours) between this study and McCain et al. (2014). Therefore, the behaviours observed here may represent early rigidity sensing strategies and perhaps reflects how NRCs initially sense changes in ECM stiffness and composition.

Rigidity sensing occurs via the coordinated assembly of contractile cytoskeletal elements at FAs (Iskratsch et al., 2014). Extensive data on the precise molecular regulation of rigidity sensing in cardiomyocytes is still missing from the literature, but recent work has identified protein kinase C (PKC) and Src as key regulators of non-myofibrillar rigidity sensing (Pandey et al., 2018). In non-myocytes, Src phosphorylation of FHOD1 results in localisation to the plasma membrane, where it is further activated by ROCK to direct rigidity sensing (Hannemann et al., 2008, Iskratsch et al., 2013). In cardiomyocytes, FHOD1 has been observed to localise to the intercalated disc (ICD) and the costamere where it is capable to nucleating the cytoplasmic actin found there (Al Haj et al., 2015, Patel et al., 2018). However, others have suggest that FHOD1 has more of an actin bundling and capping role and that it is disposable for heart development in mice (Schonichen et al., 2013, Sanematsu et al., 2019). The current investigation has observed localisation of active FHOD1 at both fibronectin and laminin adhesions. However, FHOD1 was also strongly localised to cytoplasmic or cytoskeletal structures. These findings are consistent with proposed roles of FHOD1 at integrin adhesions and at the cytoskeleton (Iskratsch et al., 2013, Schulze et al., 2014, Pandey et al., 2018). Future investigations could utilise the micropatterns to further investigate the mechanisms that regulate FHOD1 localisation and translocation to adhesions (such as PCK activation, Src activity or contractility).

Micro array and published (Miner et al., 1997, Brancaccio et al., 1998, Maitra et al., 2000) data suggests that adhesion to fibronectin is mediated by a combination of $\alpha5\beta1$, $\alpha v\beta3$ and $\alpha v\beta1$ integrins and that adhesion of cardiomyocytes to laminin occurs via a combination of $\alpha3\beta1$, $\alpha6\beta1$ and $\alpha7\beta1$ integrins. While different integrin subtypes have considerable overlap in their ligand affinity, little evidence exists of redundant sub-cellular functions between different integrin subtypes. Cancer cells utilise a combination of fibronectin binding integrins for rigidity sensing depending on substrate stiffness (Elosegui-Artola et al., 2014). It has been reported that carcinoma cells utilise $\alpha5\beta1$ integrins to exert greater traction forces on soft (~1 kPa) substrates, a combination of $\alpha5\beta1$ and $\alpha v\beta6$ integrins to generate traction forces at moderate rigidities (5-10 kPa) and

mostly αvβ6 integrins at high rigidities (Elosegui-Artola et al., 2014). Furthermore, cells that express the fibronectin binding α5β1 and αvβ3 integrins utilise the capabilities of α5β1 subtypes to exert greater traction forces for rapid cell spreading and adhesion stability, while αvβ3 provide a greater capacity for the recruitment of adaptor proteins and the activation of integrin signalling pathways such as ROCK and Arp2/3 (Schaufler et al., 2016, Bharadwaj et al., 2017). Results from the current study demonstrate that fibronectin mediated adhesions promote a stronger spreading phenotype, presumably owing to greater adhesion stability/strength, as evidenced by higher vinculin enrichment and traction forces. Fibronectin binding integrins are specifically upregulated during compensatory events, such as post-MI, where elevated contractility may be beneficial to recovery of cardiac function (Nawata et al., 1999, Burgess et al., 2001). However, the roles of different fibronectin and laminin binding integrin subtypes within the behaviours observed here remain unclear. Furthermore, this investigation has not presented data on NRC integrin expression. Microarray data suggest that within the first 24 hours of culture, NRCs express both fibronectin and laminin subtypes. Furthermore, preliminary Western Blot data (not shown) appears to confirm this data. However, future work should go on to verify integrin expression in NRCs in culture. This will provide further validity to the results presented here. Furthermore, future studies could then go on to utilise integrin specific ligand nanopatterning, integrin specific blocking antibodies, siRNAs and integrin transfection constructs to elucidate the roles of specific integrin subtypes in cardiomyocyte integrin signalling.

There are a number of limitations that should be taken into account when interpreting the results of the current investigation. Firstly, at the time of isolation (postnatal days 1-3) NRCs are not terminally differentiated and as a result, are able to disassemble their myofibrils, spread over tissue culture surface and reassemble their myofibrils de-novo. While this enables detailed investigation of the integrin mediated signalling properties of cardiomyocytes, the morphology and behaviours of integrin adhesions and myofibrils may not resemble those in-vivo. Finally, while the 24 hour culture duration time point used here was necessary to reduce the influence of endogenous matrix deposition, it should be noted that NRCs could still be adjusting to in-vitro culture conditions and results could be different with longer culture durations. Furthermore, cardiomyocyte cytoskeletal maturation has been reported to continue for at least 44 hours (Skwarek-Maruszewska et al., 2009) and the results obtained here may reflect a more immature phenotype.

This investigation has demonstrated that NRCs exhibit different rigidity sensing behaviours on fibronectin and laminin ligands, during early spreading. Both fibronectin and laminin are key components within the basal lamina of the cardiac ECM. Cardiomyocytes alter their integrin expression to favour fibronectin or laminin ligands according to the developmental stage, or diseased state of the heart. Previous work has suggested that matrix rigidity can be a direct regulator of integrin expression, depending on the desired function (Schiller et al., 2013, Elosegui-Artola et al., 2014), and differential expression of integrin subtypes can work in a competitive (Guasch et al., 2015, Bharadwaj et al., 2017) or complementary fashion (Elosegui-Artola et al., 2014, Schaufler et al., 2016). The findings from the current investigation suggest that laminin and fibronectin adhesion have different mechanical properties. Furthermore, results from micropatterned grids suggest that fibronectin and laminin integrins have mutually exclusive but complementary roles at physiological, but not at fibrotic stiffnesses. Recent work has demonstrated that the activity and function of different integrins is largely determined by their bond dynamics under force (Elosegui-Artola et al., 2014, Oria et al., 2017). Importantly, differential integrin bond dynamics and their functional implications for rigidity sensing, manifest at the FA through integrin clustering, which occurs at the nanoscale from a few tens to hundreds of nanometres, depending on substrate rigidity (Cavalcanti-Adam et al., 2007, Huang et al., 2009, Schaufler et al., 2016). Thus, to understand the functional roles of fibronectin and laminin binding integrins in cardiomyocytes, it is essential to understand the clustering of $\alpha5\beta1$ and $\alpha7\beta1$ integrin subtypes. The next chapter of this thesis will present the development and optimisation of a ligand nanopatterning platform for the investigation of integrin-ligand clustering dynamics in cardiomyocytes.

4 Implementation and Optimisation of a DNA Origami Ligand Nanopatterning Platform

4.1 Introduction

The previous chapter has presented importance differences in the spreading, traction forces and adhesion assembly in cardiomyocytes cultured on fibronectin or laminin. We hypothesised that the underlying clustering and signalling behaviours of different integrin subtypes could be underpinning these behaviours. To investigate the integrin clustering behaviour of fibronectin (predominantly $\alpha5\beta1$) or laminin (predominantly $\alpha7\beta1$) binding integrin subtypes, it was necessary to implement a platform capable of precisely controlling the composition, concentration and geometry of integrin binding ligands in the ECM.

Previous work to investigate integrin clustering in adherent cells has utilised micellular diblock copolymer self-assembly for single molecule nanopatterning of integrin ligands. This platform utilises gold nanoislands to tether single integrins at specific distances with a resolution of ~ 30 nm (Arnold et al., 2004). Notably, this approach offers the ability to control inter-ligand spacing, ligand geometry (hexagonal or triangular ligand clusters) and the global order/disorder of the nanopattern (Arnold et al., 2004, Cavalcanti-Adam et al., 2007, Huang et al., 2009, Schvartzman et al., 2011). However, recent developments in DNA nanotechnology have presented an additional ligand nanopatterning model in the form of DNA origami (Rothemund, 2006, Gopinath and Rothemund, 2014, Huang et al., 2017, Huang et al., 2019). Specifically, DNA origami nanostructures ~ 100 nm in size can be functionalised with integrin binding peptides with high resolution. Lithographic nanopatterning is then used to selectively position functionalised DNA origami, in desired

configurations, across tissue culture surfaces. While providing similar capabilities of micellular diblock copolymer self-assembly, DNA origami offers two key advantages. Firstly, the modifiable nature of DNA structures provides significant improvements in the resolution of single molecule positioning, with published designs offering 6 nm resolution (Rothemund, 2006). Furthermore, recent work from the Palma lab demonstrated the capacity of DNA origami for multivalent investigations, with the ability to control the positioning of 2 or more molecules with nanoscale resolution (Hawkes et al., 2019, Huang et al., 2019). Therefore, this investigation has sought to utilise the advantageous capabilities of DNA origami to investigate the integrin clustering and signalling behaviours of cardiomyocytes. While the multivalent capabilities of DNA origami are not explored in this thesis, this platform offers multiple meaningful options to build on the work presented.

Initial attempts to implement DNA origami nanopatterning technology and replicate previously published work (Gopinath and Rothemund, 2014) were unsuccessful. Furthermore, compared to previous work, different equipment was used to fabricate nanopatterned substrates in the current investigation which resulted in significant changes in the characteristics of substrates produced. This meant that published protocols were unsuitable for this investigation and considerable efforts were thus required to optimise the methodology for the current investigation. Therefore, this chapter will present the implementation and optimisation of a DNA origami nanopatterning platform for the investigation of integrin clustering dynamics in cardiomyocytes.

4.2 Design and modification of DNA origami

4.2.1 DNA Origami Design and Fabrication

DNA origami are highly customisable, nanoscale structures consisting of a long single strand of DNA (ssDNA) (termed the backbone), folded into defined shapes by hundreds of short strands (called staple strands) of ssDNA that are complimentary to multiple sites along the backbone (Figure 4.1). The use of computer assisted design of DNA origami has resulted in the systematic production of DNA nanostructures with high efficiency and few errors (Rothemund, 2006). Furthermore, the production of structures with precisely known parameters also enables easy and efficient modification of DNA origami designs. Previous work has reported successful modification of DNA origami for covalent attachment to silica (Gopinath and Rothemund, 2014), attachment of single quantum dots to individual DNA origami (Huang et al., 2017) and to present ligands for cell adhesion (Huang et al., 2019).

The pointed triangle DNA origami has proven to be one of the most reliable and repeatable designs for fabrication (Rothemund, 2006) and has been used successfully in

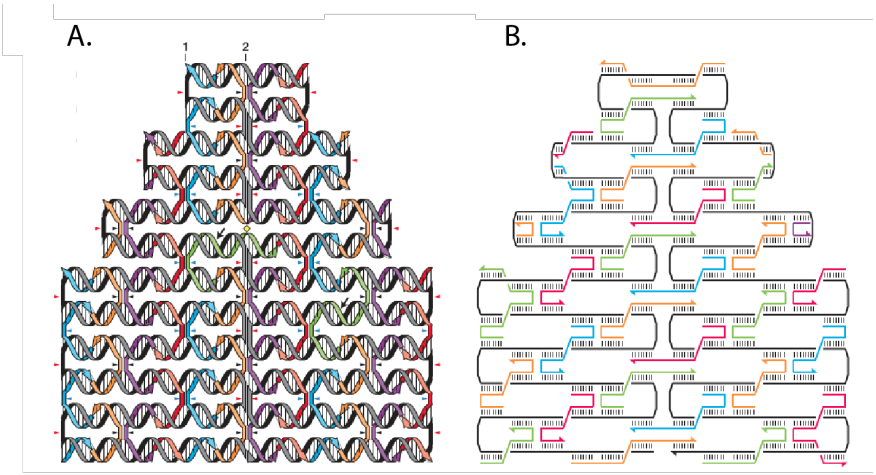

Figure 4.1. Example design of DNA origami nanostructures. A) Colour coded design of DNA origami. The backbone (black/grey) is folded to design the shape of the structure by short staple stands (blue, orange, purple, red & green). B) Depicts how staples bind to multiple points along the backbone to fold the structure into shape. Source: Rothemund, 2004.

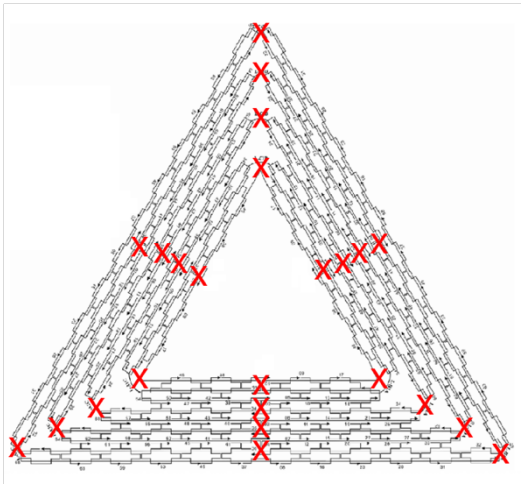

Figure 4.2. Schematic design of the Pointed Triangle DNA Origami. Red x indicates locations where the backbone is folded. Note that backbone folds do not occur along the outer edges. Modified from Rothemund, 2004.

patterning platforms in the past (Gopinath and Rothemund, 2014, Huang et al., 2017, Brassat et al., 2018, Shen et al., 2018a, Huang et al., 2019). Therefore, the pointed triangle DNA origami design was chosen for the current investigation. The three pointed triangle design utilises backbone 7,249 nucleotides in length, which is derived from the bacteriophage m13mp18. The backbone is folded into the pointed triangle shape by 206 staple strands with an average length of 35 nucleotides. This DNA origami design is particularly suitable for nanopatterning investigations due to the intrinsic design of the structure. DNA origami structures can aggregate at sites where folds in the backbone occur at the edge of the structure (Rothemund, 2006, Woo and Rothemund, 2014). The pointed triangle DNA origami is designed so that no folds in the backbone occur along the outer edges of the structure (Figure 4.2), preventing aggregation from blunt end

stacking (Rothemund, 2006). The sequences for the backbone and all staple strands used in the current investigation are reported in the appendix.

To verify the reliability of DNA origami assembly in our hands, triangular DNA origami were assembled and their physical dimensions were characterised using atomic force microscopy (AFM). Triangular DNA origami were fabricated by adding staple strands at a 5x excess to the backbone and then annealed from 90 °C to 20 °C over 3 hours, followed by spin column filtration to remove excess staples. Imaging was carried out in dry and fluidic conditions to verify DNA origami dimensions in different environments. High resolution scans confirmed that the triangular DNA origami were forming to the expected dimension of 127 ± 4 nm edge length in air and 128 ± 4 nm in fluid scanning (Figure 4.3). Furthermore, cross sections of the DNA origami height demonstrate the DNA origami to be 1.5 – 2 nm in height. This corresponds to the diameter of a single DNA helix and confirm the DNA origami design. Higher scale AFM scans then confirmed that from 250 DNA origamis, ~95% of the structures were fully assembled. The other 5%

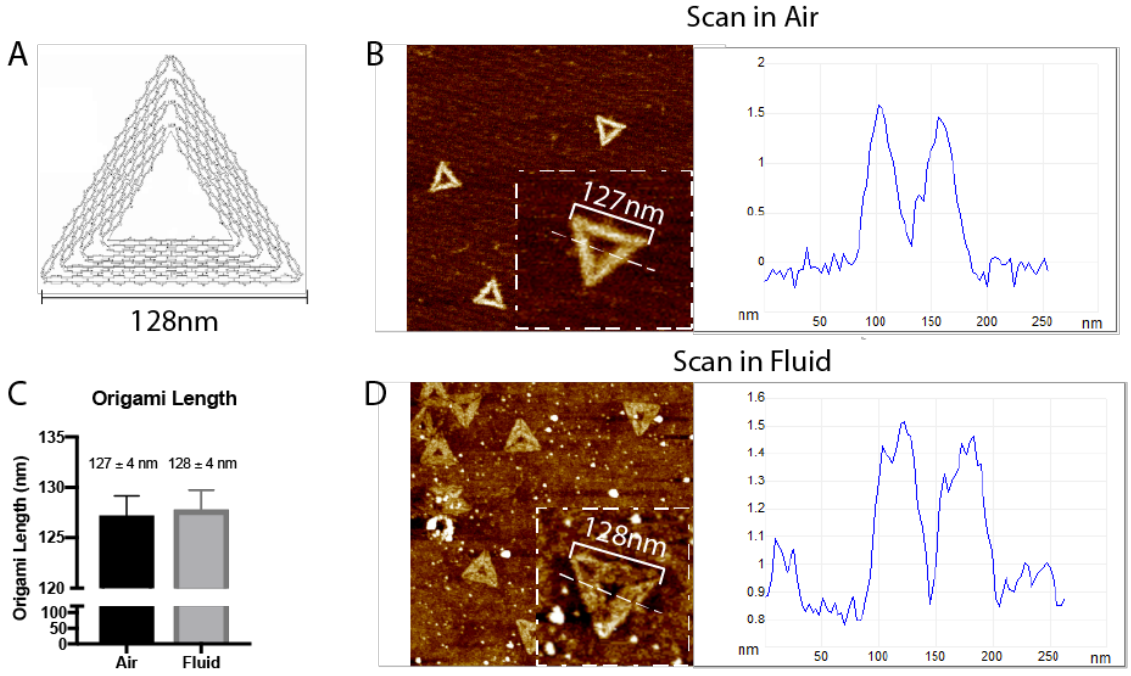

Figure 4.3. AFM characterisation of sharp pointed triangle DNA origami structures deposited on mica. A) Schematic of the DNA origami with the predicted size of 128 nm. DNA origami were characterised using AFM in air (B) and in liquid (D) which confirmed fabrication of DNA origami with the expected dimensions. Cross-sections also demonstrated the height of a single DNA origami to be ~1.5 nm, corresponding to the width of a single DNA helix and verifying the single helix structure.

displayed strand breakages, presumably due to damage from shear forces during pipetting. This data is in lines with the reported performance of the pointed triangle DNA origami design (Rothemund, 2006) confirmed the reliable assembly of the triangular DNA origami for this investigation.

4.2.2 Optimisation of DNA Origami Covalent Immobilisation: Amino Anchor Modification and Cross-Linking

This investigation aims to utilise DNA origami as a functional platform to precisely control the properties of the ECM. Therefore, the DNA origami are required to remain bound to tissue culture surfaces in a range of buffers. The adsorption of DNA origami to silicon based surfaces is commonly achieved by divalent ions (such as MgCl) which form a bridge between a negatively charged surface (commonly mica or silicon) and the negatively charged DNA origami. This approach has been utilised for the successful positioning of single DNA origami in previous work (Gopinath and Rothemund, 2014, Brassat et al., 2018). However, washing of physiosorbed DNA origami with commonly used buffers, such as PBS, releases DNA origami from the surface (Gopinath and Rothemund, 2014). Furthermore, for use on tissue culture surfaces, DNA is required to remain stably bound to the surface, in solution, for long periods of time. It was therefore necessary to modify the DNA origami to facilitate covalent immobilisation to silicon surfaces such as glass. All experiments were performed on borosilicate glass coverslips to allow optical microscopy in later experiments.

Covalent attachment of DNA origami to silicon substrates has previously been achieved through carbodiimide catalysis between amino residues on the DNA origami and a carboxyl silane (Gopinath and Rothemund, 2014). Therefore, DNA origami were modified to present 15 free adenine (poly-A) nucleotides at their 5' ends, which were complementary to staple strands containing 15 thymine (poly-T) nucleotides with an additional amino residue at the 5' end (hereby referred to as an amino anchor). This two-step "sticky-end" design was chosen over a one-step (addition of an amino anchor directly to the original staple strand) amino modification for ease of use in future investigations where the amino anchor may be substituted for another functional group such as biotin/streptavidin.

Modified strands were purchased from IDT and added to the backbone prior to annealing and the DNA origami were fabricated as described above. Glass coverslips were prepared by room air O_2 plasma treatment (Harrick Plasma, 18W 10 minutes) and the surface was

silanised with 0.01% carboxyethylsilanetriol (CTES). CTES treatment forms carboxyl groups on the surface through which the DNA origami can be covalently cross-linked to the surface via EDC/NHS catalysis of the amino anchor and carboxyl silane (Figure 4.4) (Gopinath and Rothemund, 2014). This cross-linking reaction forms amide bonds between the DNA origami and the silane which remain stable in PBS (Gopinath & Rothemund, 2014). After silanisation, 1 nM of DNA origami was cast on the glass coverslips, which were then cross-linked to the surface via EDC/NHS catalysis. AFM characterisation of non-covalently adsorbed and covalently attached DNA origami confirmed that only the EDC/NHS treated DNA origami remained bound to the surface after overnight incubation in PBS, confirming stable cross-linking (Figure 4.4).

The number of amino anchors required for efficient cross-linking to glass surfaces was initially unknown. Previous investigations have reported efficient cross-linking with 6

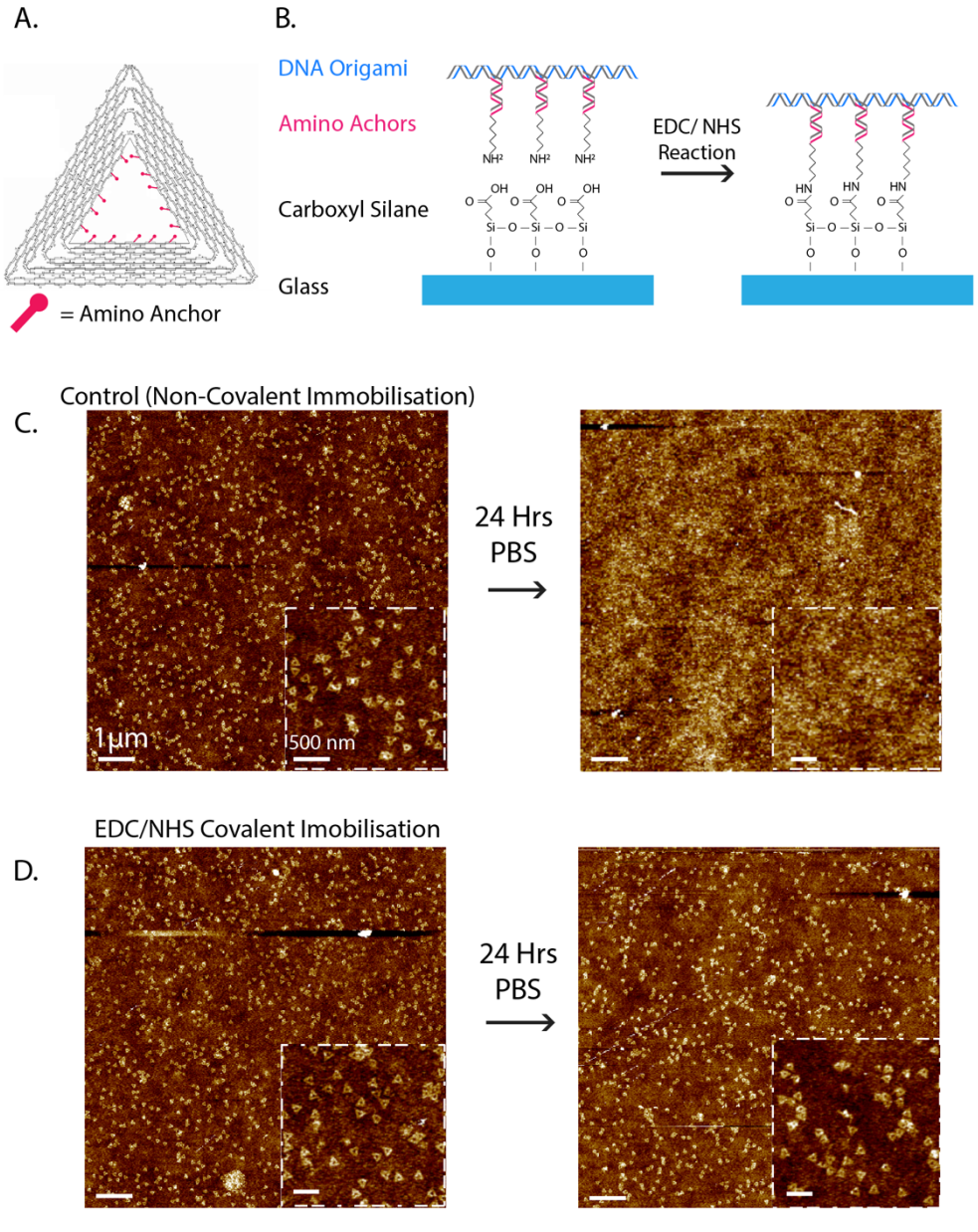

Figure 4.4. Modification of DNA origami for covalent attachment to glass substrates and stability in tissue culture buffers (PBS). A) Schematic of amino anchor modifications along the inner edges. B) Schematic of covalent attachment approach. Surfaces are first silanised with CTES before casting DNA origami which are then incubated with EDC & NHS, resulting in covalent bonding of DNA origami to the glass. C) AFM DNA Origami adsorbed to the glass surface via MgCl are stable in PBS, resulting in detachment of DNA origami from the surface. D) After EDC/NHS mediated covalent attachment to glass, DNA origami are stable and remain bound to the surface after 24 hours in PBS. Scale bars in large images = 1μm and 500 nm in

(Huang et al., 2017) and 15 amino anchors (Gopinath & Rothemund, 2014) but the effect of anchor number was not evaluated in either case. To test whether the number of amino anchors was important for cross-linking efficiency, DNA origami functionalised with 6 or 15 amino anchors were covalently bound to glass coverslips. To remove non-covalently attached DNA origami from the surface, samples were incubated in PBS overnight before being characterised with AFM. Increasing the number of amino anchors from 6 to 15 resulted in a significant increase in DNA origami density from 10 ± 3 / μm^2 to 16 ± 2 / μm^2 Figure 4.5.

Effective crosslinking of DNA origami to the glass surface would also be dependent upon the quality of surface silanisation with COOH groups, for strong adsorption to the surface followed by cross-linking. High quality silanisation could be achieved with longer plasma treatment, to generate more silanols for silanisation, of improved CTES silane treatment to generate sufficient COOH groups for cross-linking. The aim of this project is to combine DNA nanotechnology with surfaces patterned by e-beam lithography, which are sensitive to plasma treatment. Therefore, plasma treatment was kept the same (10 minutes, 18W) and cross-linking of DNA origami (1 nM) with 6 or 15 amino anchors was compared between surfaces treated with 0.01% or 0.1% CTES. AFM characterisation revealed significant differences between 6 and 15 amino anchors at 0.01% CTES but not at 0.1% CTES. This results suggests that the quality of DNA origami cross-linking is improved by silanisation with 0.1% CTES treatment and that, under this condition, the number of amino anchors is not important for short term cross-linking. However, the stability of covalently attached DNA origami over long periods in solution was not tested. Therefore, 15 amino anchors were chosen for future investigations to maximise the number of anchors (there are a maximum of 15 modifications available along the inner

edges of the DNA origami), under the assumption that more amide bonds to the surface results in more stable cross-linking.

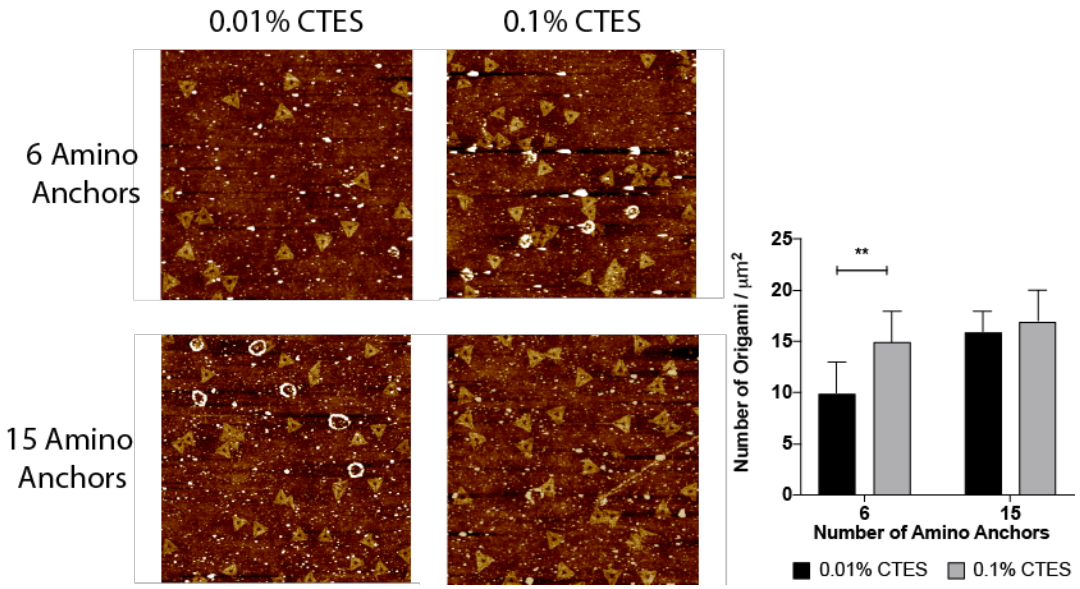

*Figure 4.5. Optimisation of surface silanisation results in higher cross-linking yield, independent of the number of amino anchors. Glass surfaces were silanised with 0.01% CTES or 0.1% CTES for 30 minutes. AFM was then used to image the DNA DNA origami presenting 6 or 15 amino anchors which had been cross-linked to the surface. The quantification displays mean ± SD DNA origami density per µm² over three independent repeats. Student's t-test, ** = p<0.01.*

4.3 Nanoscale Patterning of DNA Origami for Large Scale Investigations

For the investigation of integrin clustering on a biological level, the patterning of DNA origami was required on the scale of nanometres to micrometres which requires efficient placement of DNA origami. Lithographic techniques are often used for high precision patterning at the scale required for biological investigations. Here, electron-beam lithography (EBL) was employed to pattern silica surfaces of 1.5 mm x 1.5 mm in size to which the DNA origami were precisely immobilised in specific configurations.

4.3.1 Fabrication of E-Beam Nanopatterned Substrates**.**

To control the positioning of single DNA origami structures on tissue culture surfaces, EBL was employed due to its capacity for high precision surface patterning. All EBL work was carried out by Paul Reynolds (Gadegaard Lab, University of Glasgow). Circular holes (diameter = 150 nm) were patterned into a resist on a glass coverslip in 200 nm, 300 nm or 300 $\pm$ 50 nm intervals across 1.5 mm x 1.5 mm areas, resulting in 126.56 million or 56.25 million DNA origami bindings sites, respectively. These configurations were chosen to investigate the effect of ordered and disordered integrin cluster geometries in combination with the different peptide configurations discussed previously.

Glass coverslips were cleaned before evaporation coating of an Hexamethyldisilazane (HMDS) resist followed by spin coating of a Poly(methyl methacrylate) (PMMA) resist and were then loaded into an EBL system (Vistec VB6 2006) for patterning. The three pattern configurations were each written into the resists and three, 1.5 x 1.5 mm areas were patterned for the 200 nm and 300 nm resists while three, 0.75 x 0.75 mm areas were written with the disorganised pattern (Figure 4.6). Scanning electron microscopy (SEM) was used to verify the EBL pattern which confirmed the size of the holes to be 150nm in diameter. Patterned coverslips were then shipped to London for the proceeding steps.

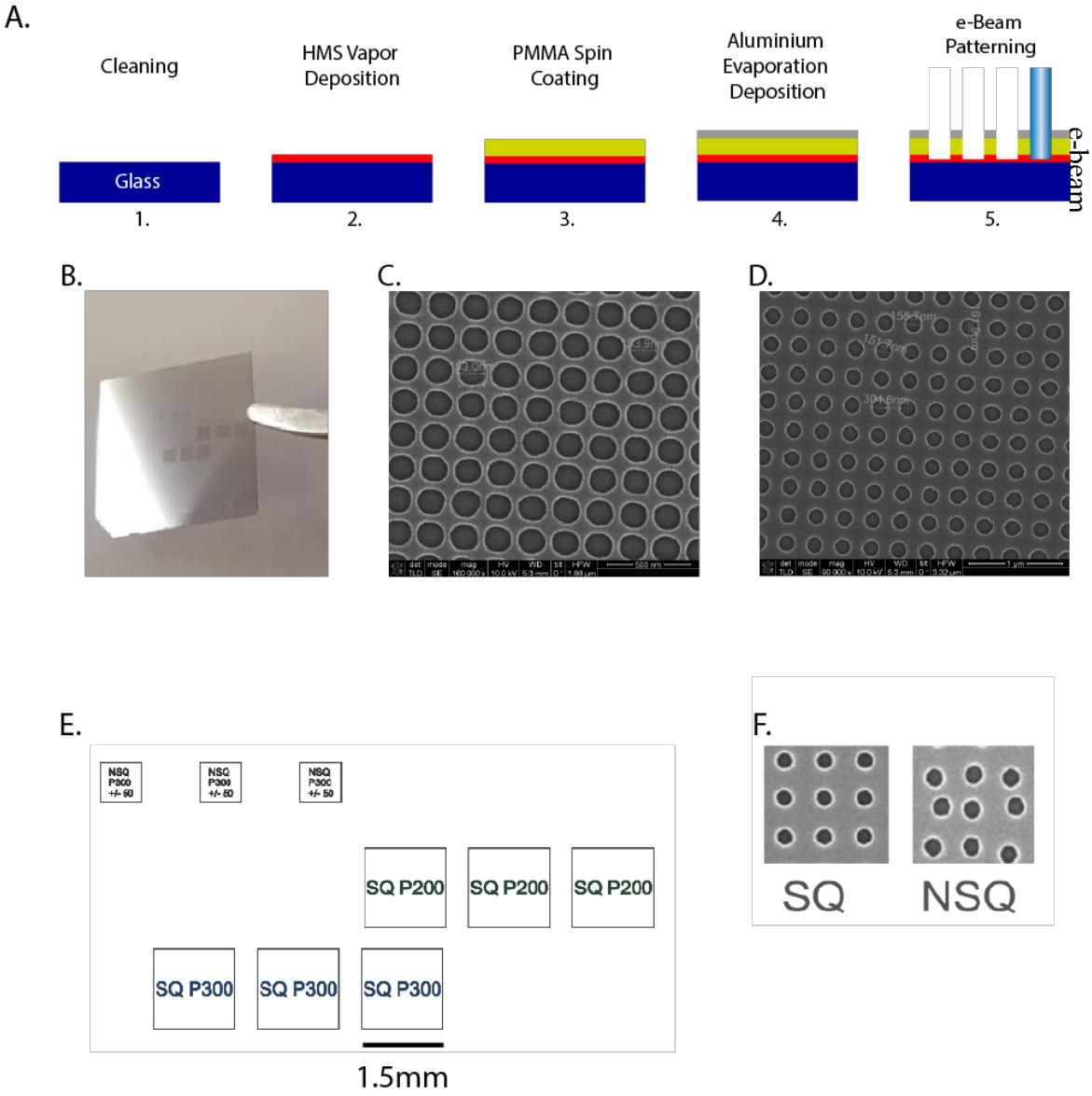

Figure 4.6. Fabrication of the e-beam nanopatterned substrates. This work was carried out by Paul Reynolds (Gadegaard Lab) at the University of Glasgow. A) Schematic of the surface preparation and e-beam patterning process. Samples were shipped as seen in B, after e-beam writing. C & D) Characterisation of the surface features using scanning electron microscopy (SEM) of the pattern confirmed the holes of be 150nm in diameter at the desired spacing of 200 (SQ P200) or 300 (SQ P300) nm. E) Nanopatterned chips consisted of 9 patterned areas. 300 nm and 200 nm arrays were patterned in 3 1.5 x 1.5 mm square (SQ) arrays and 300 ± 50 nm were patterned in 3 0.75 x 0.75 mm non-square (NSQ) arrays, as shown in SEM images in (F).

4.3.2 Optimisation Surface Activation Using O^2 Plasma Etching

To prepare the nanopatterned substrates for placement of DNA origami, the EBL pattern was developed using a 2:1 solution of propanol-2:methyl isobutyl ketone for 60 seconds at 23 °C (Gopinath and Rothemund, 2014). This removes un-crosslinked PMMA from the holes and exposes the underlying HMDS passivation layer. As previously stated, surface silanisation is critical for DNA origami cross-linking. The ideal tool for etching the HMDS from the bottom of the holes and generating silanol [OH-] groups for CTES silanisation would have been reactive ion etching (RIE) (Gopinath and Rothemund, 2014, Gopinath et al., 2016, Shen et al., 2018a). This generates a unidirectional flow of highly charged ions towards the surface of the pattern, at an angle perpendicular to the surface, etching the surface. Importantly, the HMDS would be etched from the bottom of the holes and silanols would be generated in a highly efficient way, without widening the holes themselves. However, RIE equipment was not available at King's College or QMUL. The London Centre for Nanotechnology own an RIE chamber but the time of investigation, the centre were not allowing the use of glass substrates. Therefore, the etching procedure was optimised using an O_2 plasma chamber (Henniker HPT-200). This generates an isotropic field of reactive ions which rapidly widens the holes while etching the surface at the bottom.

At a power of 100 W, O_2 plasma etching was optimised to achieve maximum etching of glass surfaces at the bottom of the nanopatterned holes without widening their diameter beyond 150nm. Etching time was critical to ensure sufficient silanol generation on the underlying glass and the extent of etching was evaluated using AFM by monitoring the width of the patterned holes. The results from etching experiments can be seen in Figure 4.7. As etching time increased, the bottom of the holes became flatter and wider and the three patterns were etched at different rates. After 70 seconds, the diameter of the holes on the 200 nm, 300 nm and 300 $\pm$ 50 nm configurations were (mean $\pm$SD) 153 $\pm$ 6 nm, 131 $\pm$ 7 nm and 70 $\pm$ 28 nm, respectively. On the ordered patterns, etching was faster and more homogenous compared to the disordered array where etching was highly variable, suggesting inconsistent silanol generation on the underlying glass.

While feature width was limited to a maximum of 150 nm and under the optimised conditions, the HMDS was cleared from the holes, the quality of silanol generation or silanisation cannot be directly measured. The quality of silanisation is believed to be key to the quality of DNA origami positioning on the nanopattern and as such, it is also believed to be the reason for differences in the DNA origami placement conditions

(described below) compared to those reported by others in the literature (Gopinath and Rothemund, 2014).

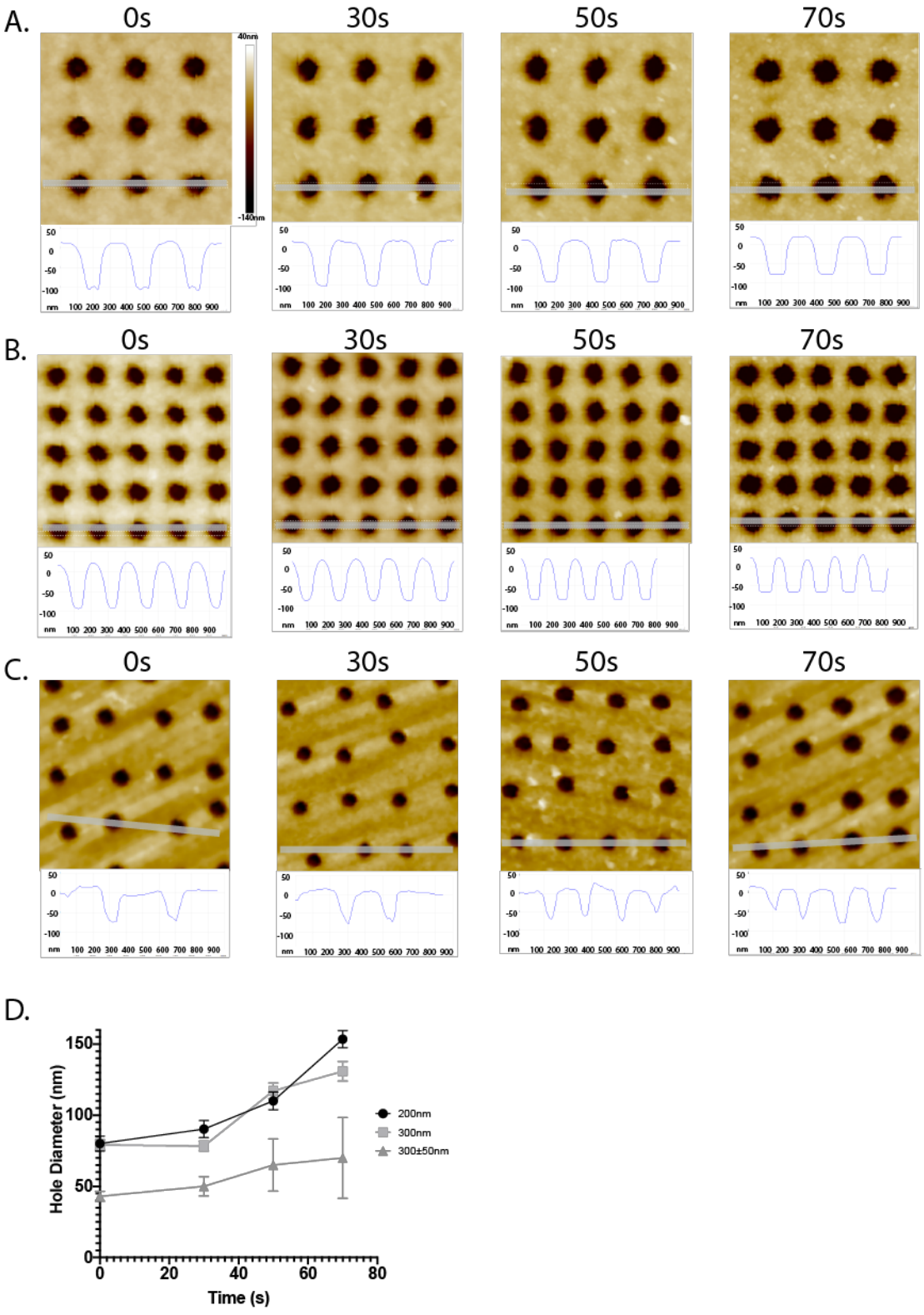

Figure 4.7. Optimisation of nanopattern O_2 plasma etching to achieve sufficient clearing of residual PMMA and HMDS form the bottom of the holes. 300 nm (A), 200 nm (B) and 300 ± 50 nm nanopatterns were etched with O2 plasma from room air (21 %) for 30 – 70 seconds. AFM characterisation of the nanopattern with progressive etching revealed that the PMMA was being etched in both the x, y and z directions as demonstrated by widening of features and decreasing thickness of the PMMA resist. Etching time was optimised to achieve maximum clearing of the holes to allow maximum silanol generation within. The maximum hole diameter was set at 150nm to ensure each hole could only fit a single DNA origami. After 70s etching time, the mean ± SD hole diameter was 153 ± 6 nm, 131 ± 7 nm and 70 ± 28 nm for 200 nm, 300 nm and 300 ± 50 nm arrays, respectively. Grey bars indicate the trace for the cross-section below each image. Measurements were taken from >50 holes for each condition.

4.3.3 Optimisation of Resist Lift-Off

To ensure a flat surface with no topological effects of the surface on cell adhesion, it was important to achieve sufficient lift-off of the PMMA resist, without damaging the underlying pattern in the HMDS passivation layer. The first approach to be tested was an overnight incubation in acetone at room temperature (Palma et al., 2011). Surface characterisation with AFM demonstrated that only a partial lift-off was achieved. Residues of PMMA and aluminium remained on the surface of the pattern, as shown by the large white (high) features in Figure 4.8. Lift-off was then attempted by a 20 minute soak in N-Methyl-2-pyrrolidone (NMP) at 50 ^{o}C (Gopinath and Rothemund, 2014) but again large residues of PMMA and aluminium remained on the surface. The best results were observed by soaking coverslips in NMP at 50 ^{o}C for 10 minutes followed by 10 minutes of sonication in NMP at 50 ^{o}C . The PMMA resist was fully removed while maintaining the HMDS pattern for DNA origami placement (Figure 4.8).

4.3.4 Optimisation of DNA Origami Placement on EBL Nanopatterns

This platform was implemented to fabricate ECM mimicking cell culture surfaces with precise ligand concentration, spacing and stoichiometry. To stably cross-link DNA origami to the surface, a two-step approach was used. Firstly, DNA origami were cast

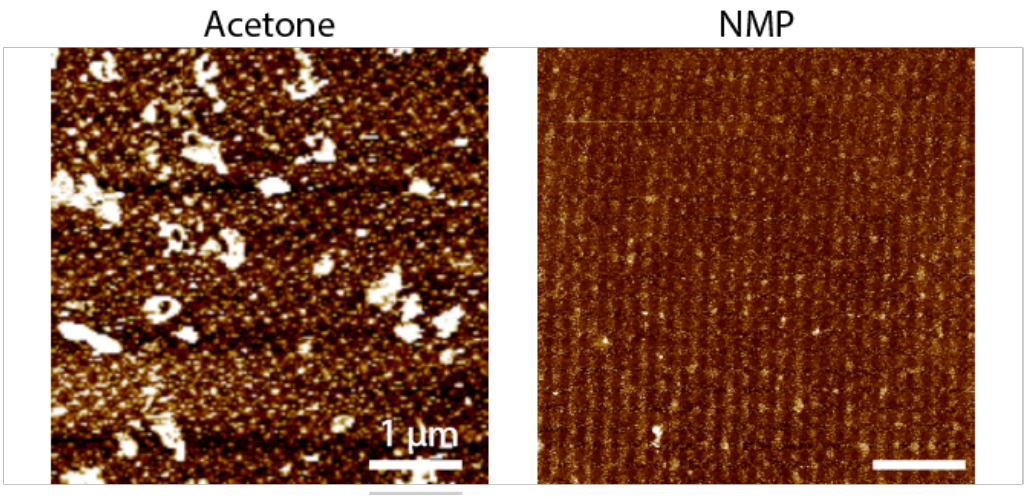

Figure 4.8. Examples of the poor resist lift-off achieved via an overnight soak in acetone compared to a good lift-off achieved by a 10 minutes soak in NMP followed by 10 minutes sonication in NMP at 50 °C.

onto the surface which was subsequently washed to remove excess DNA origami. Secondly, the DNA origami were incubated with EDC and NHS to form amide bonds between the amino anchors and the carboxyl silane (Gopinath and Rothemund, 2014). It was therefore essential to validate the casting conditions to the nanopattern. Substrates with 200nm and 300nm nanopatterns were fabricated, developed and etched via the optimised approach, described above, and DNA origami were cast onto the silinised surface. Previous reports (Gopinath and Rothemund, 2014) have reported the optimum placement conditions to be 110 pM DNA origami in 5 mM Tris and 12.5 mM MgCl at pH 8.3 and an incubation of 1 hour at room temperature, which was used as a starting point for comparative analysis. Results from the optimisation of placement conditions can be seen in Figure 4.9.

The initial placement conditions resulted in a yield of 15 % and 28 % for the 200 nm and 300 nm patterns (respectively) and therefore placement conditions were optimised for the current investigation. Both the DNA origami and MgCl concentration were optimised to achieve high pattern occupancy. Increasing DNA origami concentration results in an increased probability of DNA origami binding events while increased MgCl results in stronger binding of DNA origami to the pattern. Keeping the MgCl concentration at 12.5 mM but increasing the DNA origami concentration to 250 pM and 500 pM results in small increases in placement yield to 39 % and 44 % for 200 nm and 300 nm arrays, respectively. This data confirms that isotropic O_2 plasma etching results in poor surface activation and while DNA origami are binding to the pattern, higher concentration of

Mg^{2+} ions are required to prevent unbinding. Increases in both DNA origami and MgCl

concentration were required to achieve 100% binding site occupancy on both nanopattern

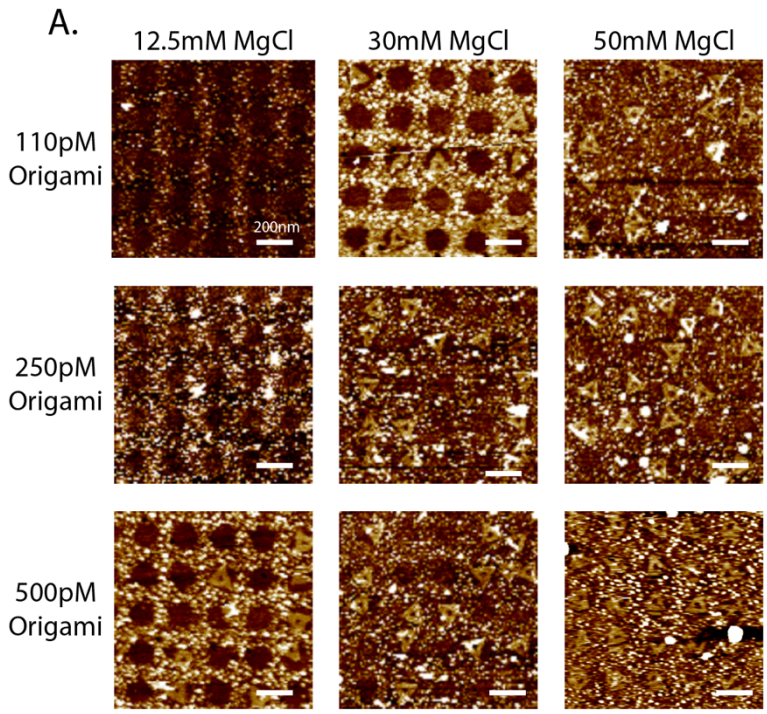

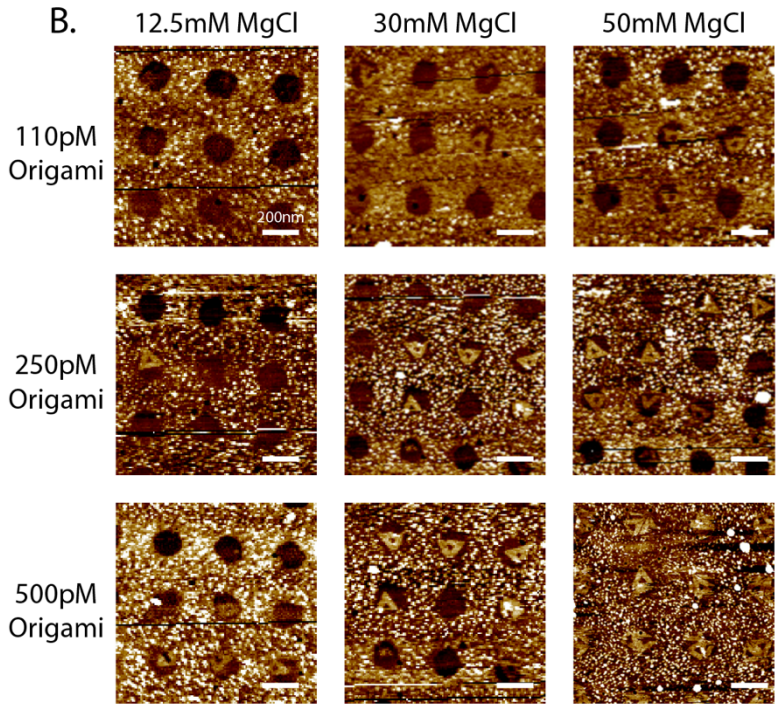

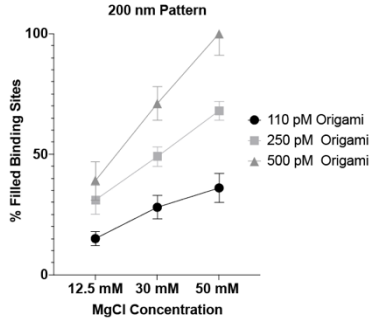

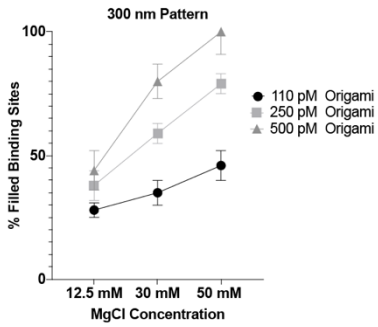

Figure 4.9. AFM characterisation of DNA origami adsorption to the nanopattern for optimisation of DNA origami placement conditions on 200 nm (A) and 300 nm (B) patterns. After optimum etching, DNA origami were incubated on the pattern for 1 hour at room temperature at three different concentrations in Tris buffer with different MgCl concentration. Both DNA origami and MgCl concentration was important for achieving a 100% placement efficiency and the optimum conditions were identified to be 500 pM DNA origami in 5 mM Tris buffer containing 50 mM MgCl. Scale bars = 200 nm.

configurations and optimum conditions were confirmed to be 500 pM DNA origami and 50 mM MgCl in 5 mM Tris at pH 8.3.

4.3.5 Covalent Cross-linking of DNA Origami to EBL Nanopatterns

The placement of DNA origami to the nanopatterned holes is dependent upon the presence of magnesium ions in the solution to provide a divalent bridge between the negatively charged silane and the negatively charged DNA. In the presence of many buffers used for tissue culture, such as PBS, DNA origami will detach form the pattern (Gopinath and Rothemund, 2014). Covalently cross-linking the patterned DNA origami to the substrate was essential to ensure the stability and reliability through several buffer washes and long term incubation and culture. After placement in optimised conditions, DNA origami were cross-linked to the glass surface via the amino modification and the carboxyl silane using an EDC/NHS reaction under the previously described optimum reaction conditions. Following overnight incubation in PBS to remove non-covalently bound DNA origami, AFM characterisation confirmed a high yield of cross-linking of without the loss of DNA origami from the nanopattern (Figure 4.10). Furthermore, this data confirms the stability of the nanopatterned DNA origami independent of Mg ion binding.

AFM characterisation of nanopatterned DNA origami revealed a discontinuous background coating of HMDS consisting of tightly packed dots, suggesting that the HMDS deposition was insufficient to achieve a smooth monolayer. Features were often higher than the DNA origami and the surface roughness (Rq) was, therefore, calculated to see if this could induce artefacts in in the cell culture assay. The EBL substrates

exhibited Rq values of 0.7 ± 0.1 nm which is not deemed sufficient to affect cell adhesion via topological effects.

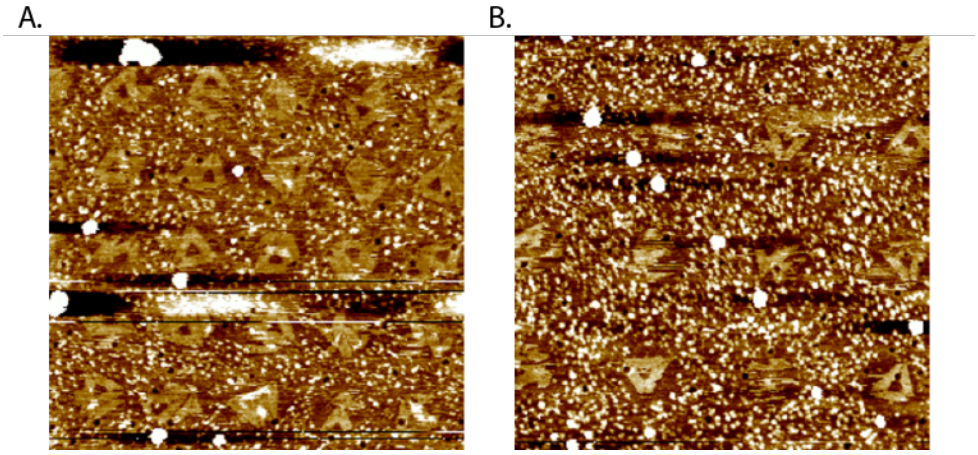

Figure 4.10. Verification of covalent bonding of DNA origami to the nanopattern and stability of patterned DNA origami in PBS. DNA origami were cast in the optimised conditions (500 pM DNA origami, 5 mM Tris, 50 mM MgCl) and bound to the surface via EDC/NHS catalysis of amino anchors and incubated in PBS overnight. AFM was used to characterise the patterned DNA origami and confirm successful patterning of DNA origami in 200 nm and 300 nm square arrays. Modified from Hawkes et al. (2019)

4.3.6 Drying of DNA Origami Nanopatterned Arrays for Long Term Storage

The successful fabrication of the pattern and covalent immobilisation of DNA origami is a complex and time consuming procedure. It would have, therefore, been advantageous to prepare the patterns in advance of the experiment and store them in a stable condition, ready for future use. Others (Gopinath and Rothemund, 2014, Gopinath et al., 2016, Shen et al., 2018b) have shown washing the substrates with ethanol solutions of increasing concentration and air drying enables stable storage at room temperature for up to 12 months.

Nanopatterned DNA origami arrays were sequentially submerged in solutions containing 50 %, 75 %, 85 % and 95 % ethanol for 10, 15, 30 and 60 seconds respectively before blow drying. AFM was used to characterise the quality of the drying. Although many good quality DNA origami were observed, a large number of DNA origami were deformed and exhibited streaking and aggregation of (presumably) salts (Figure 4.11). To avoid streaking, samples were left to air dry and while no streaks were observed, a large aggregation of salts to the holes were observed and DNA origami appeared highly distorted. Different washing steps and ethanol drying times were attempted with the same result. As the quality of the DNA origami in the dried arrays is not guaranteed, it was decided that the nanopatterned arrays would have to be made fresh for each experiment and used immediately to ensure reliability of the platform.

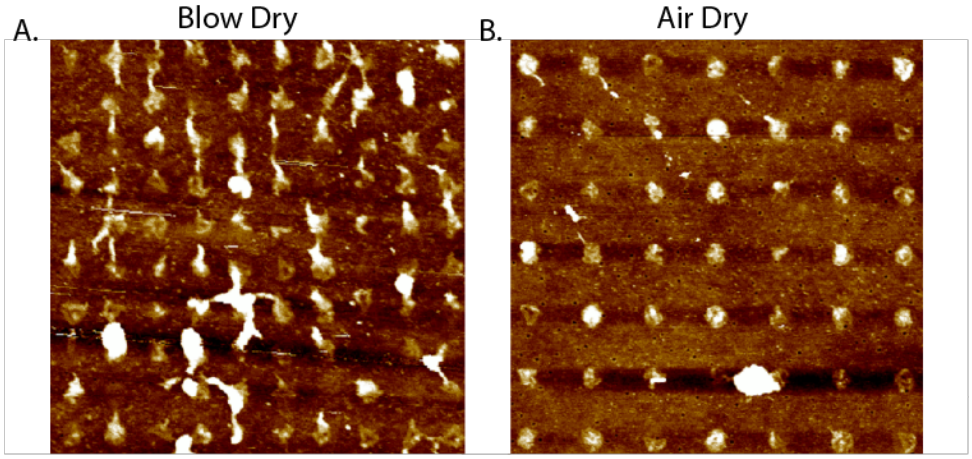

Figure 4.11. Drying of nanopatterned DNA origami covalently bound to the pattern. Samples were serially dipped in ethanol solutions of increasing strength before being blow dried (A) or air dried (B). Blow drying resulted in streaking of DNA origami while air drying resulted in aggregation of salts to the patterned features and balling up of DNA origami. Both phenomena are thought to occur due to capillary action drawing salts from the hydrophobic background towards the hydrophilic nanopatterned holes.

4.4 Peptide Modification of DNA Origami

This chapter has so far demonstrated that DNA origami can be selectively patterned and cross-linked to a substrate in stable configurations, with a precision of ~200 nm. In order to achieve control of integrin clustering with the required resolution of < 60 nm (Arnold et al., 2004), the DNA origami design was modified to present integrin selective peptides at intervals of 20 – 60 nm. In order to achieve this, specific staple strands along the outer edge of the DNA origami design were extended to present a "sticky end" sequence (AGTTGTGGATCCTACT). Sticky ends were designed to be complimentary to a single strand of ssDNA conjugated to a peptide of choice Figure 4.12.

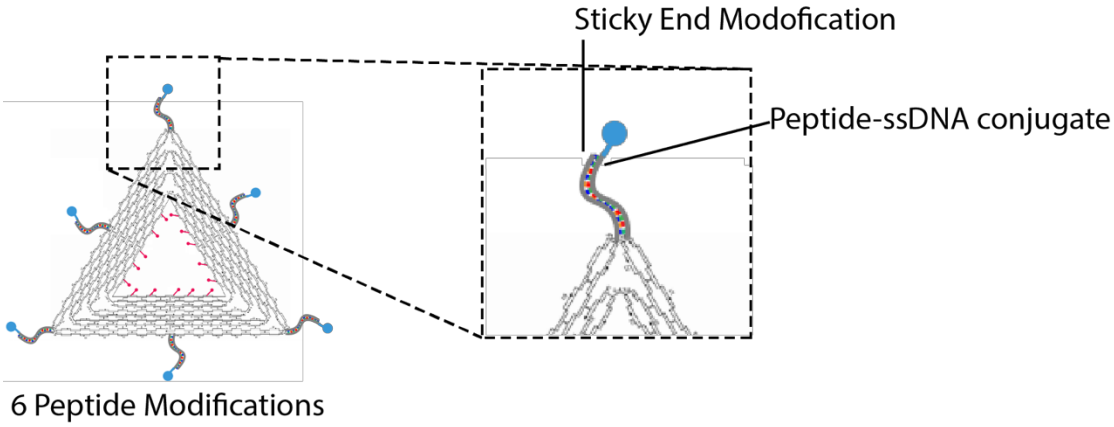

Figure 4.12. Sticky end modification for DNA origami for peptide functionalisation.

4.5 Peptides

A primary aim of the current investigation was to analyse the integrin clustering and signalling properties of fibronectin and laminin binding integrins in cardiomyocytes. It was therefore necessary to choose peptides that possess a high affinity towards the fibronectin and laminin binding integrins expressed in cardiomyocytes, which are predominantly α5β1 and α7β1 subtypes, respectively. The primary adhesion site for integrins on fibronectin is the tripeptide sequences, RGD. This sequence is located on the 10th repeat of FN-III domain. The cyclic RGD peptide (cRGD) has been reported to bind α5β1 integrins with high affinity (Pfaff et al., 1994, Kapp et al., 2017). Furthermore, cRGD peptides have been extensively utilised in previous nanopatterning work to investigate the integrin clustering dynamics of cells, such as fibroblasts, that express the fibronectin binding αvβ3 and α5β1 subtypes (Arnold et al., 2004, Cavalcanti-Adam et al., 2007, Schvartzman et al., 2011). Within cardiomyocytes, RGD peptides have been utilised with varying degrees of success and certain linear RGD have exhibited poor cell

adhesion and spreading (Boateng et al., 2005, LaNasa and Bryant, 2009). For this reason, we also sought to utilise cRGD peptides to recruit the fibronectin binding integrins expressed in cardiomyocytes. For conjugation to ssDNA, we also required our peptide of choice to contain a cysteine residue to permit thiol-ene reactions have which been highly successful in mediating conjugated products in previous work (Lowe, 2010). Therefore, we utilised the cyclic RDGfC (cRGDfC) peptide for this investigation (cyclo [Arg-Gly-Asp-D-Phe-Lys(Cys)].

Neonatal cardiomyocytes express the α7X2β1 and α6β1integrin subtypes which strongly bind to the laminin α1 chain (Nishiuchi et al., 2006, Brancaccio et al., 1998, Maitra et al., 2000). The primary integrin binding motif on the laminin α1 chain is the sequence IKVAV, which is located at the C-terminal end of the chain (Patel et al., 2019). Investigations using IKVAV peptides has been primarily focussed on neuron tissue and investigations in cardiomyocytes have not yet been carried out. Therefore, information on the affinity for laminin binding integrins for IKVAV peptides is currently unavailable. Therefore, we utilised an 18 amino acid laminin A chain peptide with a cysteine residue at the N-terminal (Cys-Ser-Arg-Ala-Arg-Lys-Gln-Ala-Ala-Ser-Ile-Lys-Val-Ala-Val-Ser-Ala-Asp-Arg), hereby referred to as the IKVAV peptide. This sequence has been previously reported to support cell adhesion and migration of neuronal cells in addition to promoting malignant behaviours in cancer cells (Sephel et al., 1989, Tashiro et al., 1989, Kikkawa et al., 2013).

4.5.1 Peptide conjugation

A significant challenge during this project has been to produce peptide conjugates in a sufficient quantity for addition to the annealing mixture, at an excess necessary to achieve efficient labelling of DNA origami structures. For example, Rothemund (2006) demonstrated that staples need to be added at a 5x excess concentration to that of the backbone. Therefore, peptide-ssDNA conjugates are required to added at a 5x excess to the concentration of sticky ends. For example, using the backbone at 40 nM requires 200 nM of staple strands /sticky ends, which 1 μM of peptide-ssDNA conjugates per each sticky end included within the design. Therefore, it was necessary to implement a peptide/ss-DNA conjugation reaction capable of producing yields in the micro- to milli-molar range.

4.5.1.1 Maleimide Conjugation

Previous work from the Palma lab has demonstrated that a thiol-ene reaction between ssDNA modified with a maleimide and a thiol group (cysteine) on a peptide (Figure 4.13), can be achieved with yields of 63% (Huang et al., 2019). Thiol-ene reactions occur via hydrothiolation of carbon-carbon (ene) bonds and have been recognised for their "click" like properties, in enabling modular reaction with many reagents, under mild conditions (Lowe, 2010). We therefore sought to replicate this reaction chemistry with the RGDfC and IKVAV peptides and ssDNA modified with a maleimide group (Figure 10A). The maleimide-ssDNA was deprotected using toluene washing and evaporation and then incubated with the peptide for 30-60 minutes (Huang et al., 2019). However, Reverse-Phase High Performance Liquid Chromatography (RP-HPLC) was unable to observe an emergence of a second peak, or a change in the column retention time was the unconjugated ssDNA (Figure 4.13). Therefore, it appeared that in this case, the maleimide-ssDNA reaction was unsuccessful. The reason for this is currently unclear but it may be, in part, due to low reactivity of the maleimide ene group compared to other

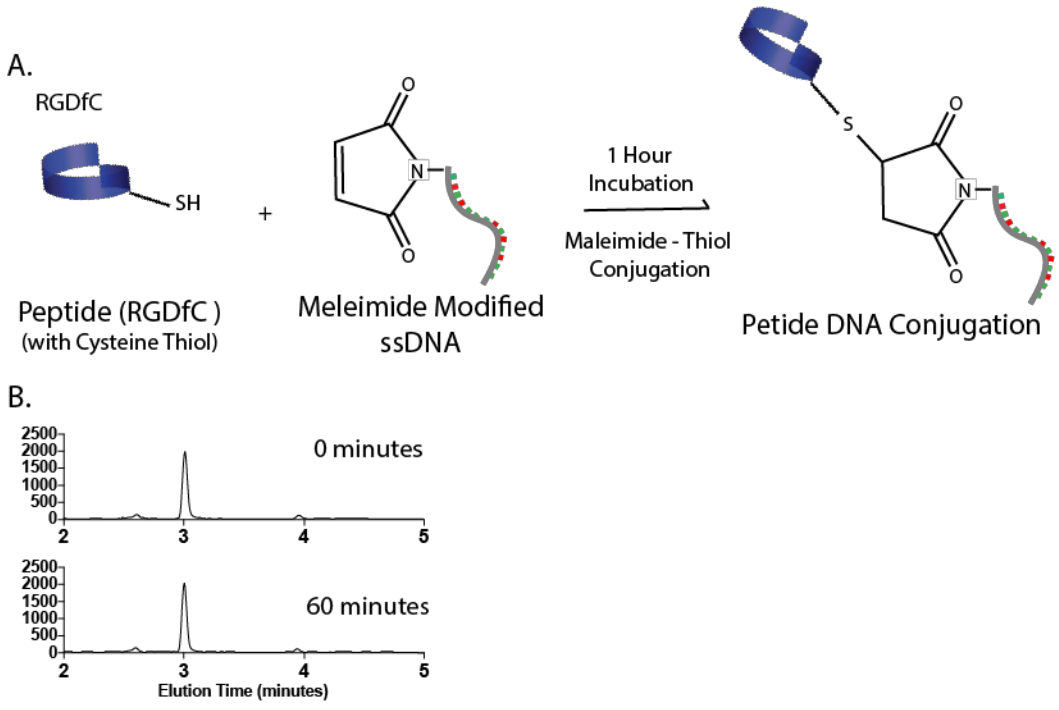

Figure 4.13. Maleimide Conjugation. A) Schematic of the maleimide-thiol conjugation. Peptides and maleimide-ssDNA are incubated together for 60 minutes in PBS. B) RP-HPLC validation of unsuccessful conjugation showing no change in unconjugated DNA peak and no emergence of a new conjugate peak. Modified from Hawkes et al. (2019).

ene-presenting molecules and the absence of a radical catalyst in the reaction which is often used for thiol-ene reactions (Lowe, 2010).

4.5.1.2 Acrydite Conjugation

The second conjugation approach utilised a UV mediated thiol-ene reaction (Figure 10C) between the peptides and acrydite modified ssDNA (Torres-Kolbus et al., 2014). The reaction occurs via an alkene group on the acrydite which demonstrates greater reactivity with thiols compared to maleimide. RGDfC peptide were firstly incubated with TCEP to reduce disulphide bonds and make the thiol groups available for conjugation. RGDfC peptides were then incubated with the acrydite modified ssDNA in the presence of the photoinitiator 2-hydroxy-4′-(2-hydroxyethoxy)-2-methylpropiophenone (which acts as a radical catalyst for the reaction) and exposed to 260 nm UV light for 5-20 minutes. RP-HPLC (260 nm absorption spectra) verified successful conjugation between cRGDfC and the ssDNA via the emergence of a new peak, which increased in magnitude with increasing reaction time, and a decrease in the intensity of the unconjugated ssDNA peak (Figure 4.14). Neither the RGD or IKVAV peptides had a specific absorption peak at 260 nm and therefore only the DNA would be detected. Furthermore, samples were filtered with a 3 kDa spin column to remove unconjugated peptides and the photoinitiator, leaving only the conjugated and unconjugated DNA products. Control experiments of the reaction mix without UV exposure, the reaction mix without the peptides but with UV exposure or the reaction mix without the ssDNA did not show the emergence of any additional peaks, suggesting that this emerging peak is the conjugated product. The successful conjugation was then confirmed for the IKVAV peptide (Figure 4.14). Peptide-ssDNA conjugates were purified using HPLC to collect only the conjugate peak and remove unconjugated ssDNA from the solution. Purified samples were freeze dried to remove solvents used in HPLC and samples were resuspended in H_2O. Additional validation of the experiment and quantification of the yield was obtained using a microvolume spectrophotometer (see methods).

4.5.2 Verifying the Efficient Functionalisation of DNA origami via Sticky-End Strands

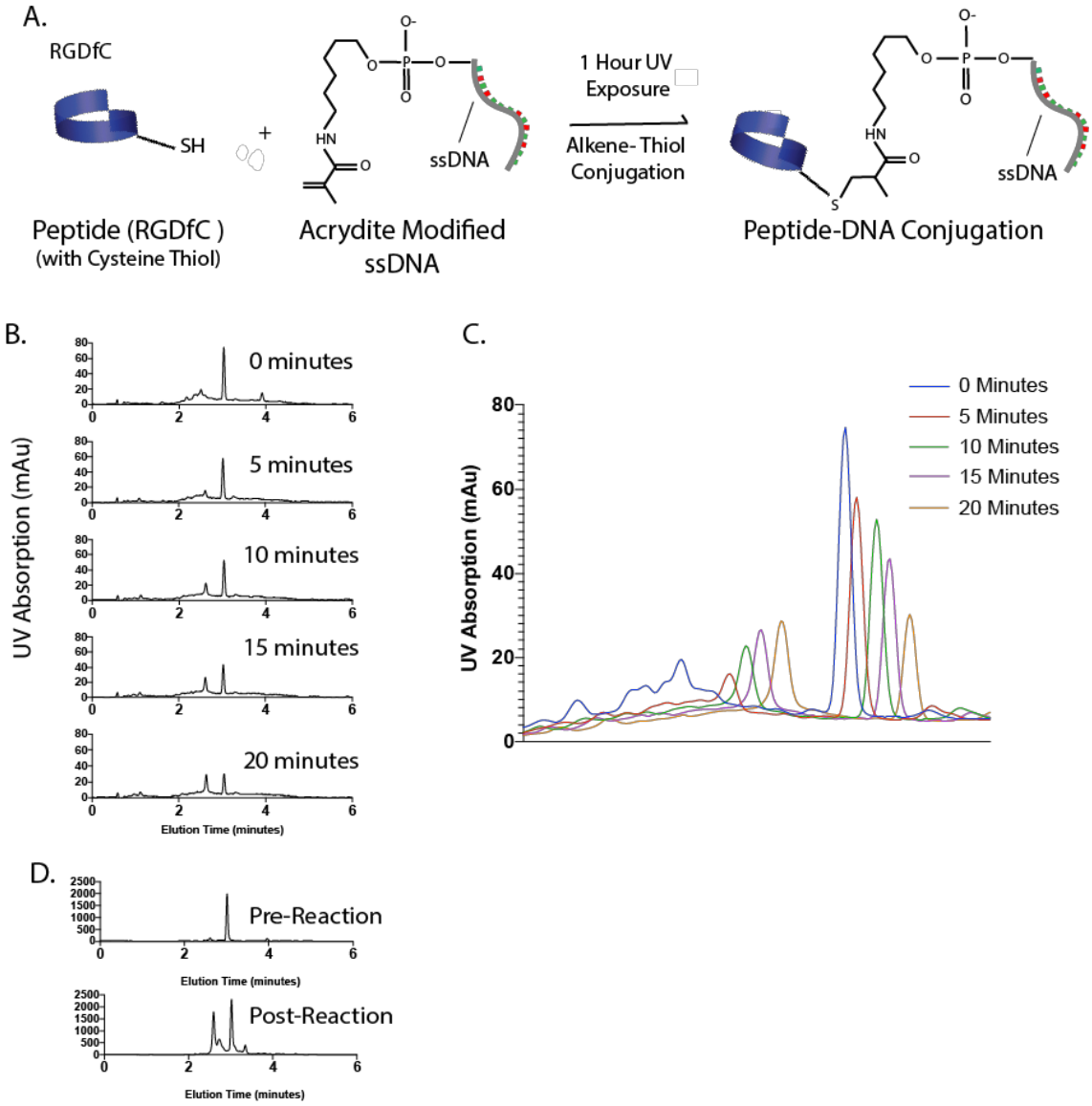

Figure 4.14. Acrydite conjugation. A. Schematic of the acrydite-thiol conjugation. B) HPLC analysis of successful conjugation between RGDfC and ssDNA, as evidenced by the decrease in the magnitude of unconjugated ssDNA relative to an increase in magnitude of an emerging peak. C) HPLC traces from 35B plotted relative to one another. Peaks have been shifted to the right for easier comparison. D) HPLC analysis confirming conjugation between IKVAV peptide and ssDNA. Modified from Hawkes et al., 2018.

Before annealing, peptide conjugates were added to the origami solution at a 10 X excess to the amount of sticky-ends available on each design. To verify if a 10X excess was sufficient to functionalise the DNA origami with high efficiency and to validate the sticky-end approach, DNA origami were labelled with fluorescent peptide conjugates for

photobleaching experiments. To achieve this, ssDNA (complimentary to sticky-ends) modified with Alexa-647 fluorophore were purchased from IDT and hybridised to DNA origami presenting 6, 12 or 18 sticky ends (Figure 12 A). To evaluate the number of fluorophores present on the 6, 12 and 18 designs, labelled DNA origami were cast at low density onto glass bottomed dishes and loaded into a confocal microscope (Zeiss Elyra) for photobleaching experiments using a 100X objective. The number of fluorescent probes on an individual origami was calculated by the total signal at the start of bleaching (minus the baseline) divided by the average signal drop of one bleaching event. The average loss of signal from 1 bleaching event was calculated from 50 observations of DNA origami presenting 6 fluorophores. The results found an average of 6.1 ± 1.4, 11.0 ± 2.2 and 19.0 ± 2.6 bleaching events for the 6, 12 and 18 fluorophore designs respectively (Figure 12). This result suggests that efficient functionalisation of DNA origami can be achieved by adding modifications at a 10 fold excess.

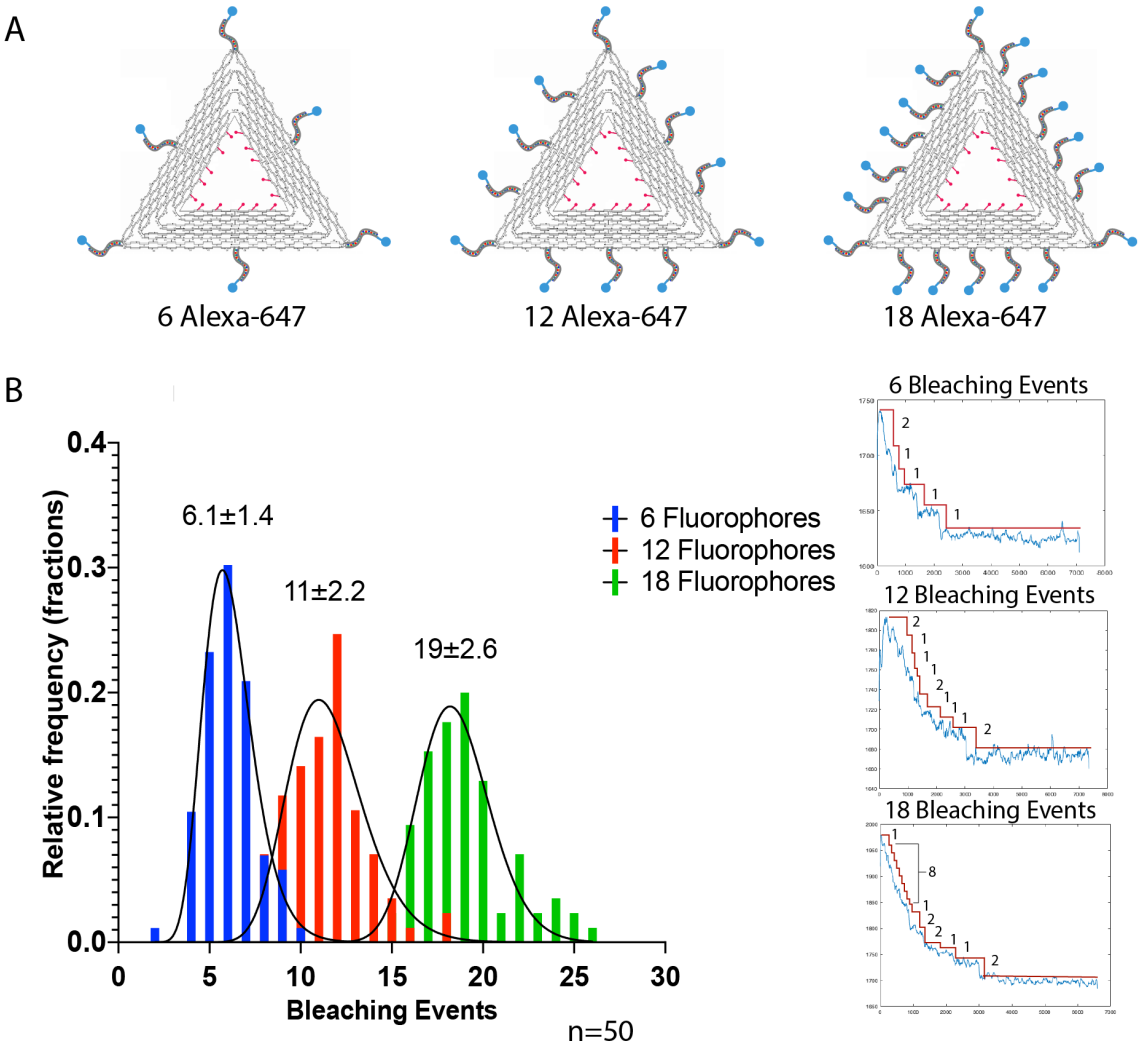

Figure 4.15. Validation of the peptide attachment approach using photobleaching of DNA origami labelled with Alexa-647 fluorophores. A) DNA origami were labelled with 6, 12 or 18 Alexa-647 fluorophores and cast onto glass bottomed dishes, loaded onto a confocal microscope and photobleached. B) A histogram of the number of bleaching events revealed an average of 6, 11 and 19 fluorophores in the 6, 12 and 18 fluorophore conditions. Bleaching events were counted by calculating the difference between the maximum signal and the background baseline by the average signal decrease from 1 bleaching event. N = 50 DNA origami per condition. The average signal decrease from 1 bleaching event was derived from 50 individual bleaching events. Frame rate = 140 pfs

4.5.3 Verifying Functionalisation of DNA Origami with Conjugated Products

4.5.3.1 Verification of cell adhesion and spreading on randomly positioned DNA Origami

Prior to carrying out investigations with the EBL nanopatterning platform, it was necessary to validate the RGD and IKVAV functionalised DNA origami for cell adhesion studies. For initial validation, readily available mouse embryonic fibroblasts (MEF) were used to prevent the unnecessary wastage of primary cells and EBL substrates. These cells express αvβ3 integrin subtypes which demonstrate a high affinity for the RGDfC peptides utilised here (Kapp et al., 2017). Initial validation studies were carried out using DNA origami which were cast randomly on glass coverslips; this approach was also chosen as randomly positioned origami arrays can be readily produced, making them suitable for any necessary optimisation.

DNA origami were fabricated with 0, 6, 12 or 18 RGDfC peptides for initial studies. As a starting point, origami functionalised with 6xRGDfC peptides were chosen to achieve an inter-ligand spacing of ~ 65 nm which is known to be the minimum required for efficient cell spreading (Arnold et al., 2004, Cavalcanti-Adam et al., 2007). 16 mm glass coverslips were prepared and silanised with carboxyethylsilanetriol (CTES) (-COOH) and DNA origami were cast randomly onto the surface at a concentration of 2 nM, achieving an average density of 10 ± 3 origami per μm^2, which was similar to the nanopattern. DNA origami were covalently cross-linked to substrates using EDC / NHS catalysis and the surface was blocked against non-specific adhesion using 5% bovine serum albumin (BSA). MEF cells were allowed to spread on the random origami

substrates for 90 minutes, in serum free medium. After fixation, the degree of cell spreading was quantified by visualising F-actin and calculating cell area.

Initial findings revealed that cells were attaching and spreading on 0 peptide controls substrates, indicating a large amount of non-specific adhesion (Figure 4.16B). To improve background passivation and prevent non-specific adhesion, methoxypolyethylene glycol amine (mPEG) was covalently cross-linked to the background using an EDC/NHS reaction to couple the amine group of the mPEG to the COOH silane (Figure 4.16C). Individual PEG molecules group together on the surface to form polymer brushes that effectively block against non-specific adhesion while exhibiting low cytotoxicity (Cai & Wind, 2016). Surface passivation took place after covalent cross-linking of the DNA origami to the surface. With mPEG surface passivation, non-specific adhesion to control substrates was dramatically reduced (Figure 4.16).

The experiment was then repeated, with mPEG passivation, using randomly cast origami presenting 6 peptides, achieving a mean ± SD density of ~60 ± 18 ligands per μm^2. Compared to controls, Cells showed clear signs of spreading and rigidity sensing such as the formation of lamellipodia and the assembly of stress fibres. Furthermore, the addition of 12 or 18 RGDfC peptides to the origami (~120 ± 36 and 120 ± 54 ligands per μm^2 respectively) resulted in an additional, significant, increase in cell spreading compared to 6 RGDfC (Figure 4.16). These results demonstrate that the RGDfC functionalised DNA origami can successfully mediate cell spreading, with low non-specific adhesion. Furthermore, additional increases in spreading on 12 and 18 peptides also provides further validation of successful fabrication of the origami design.

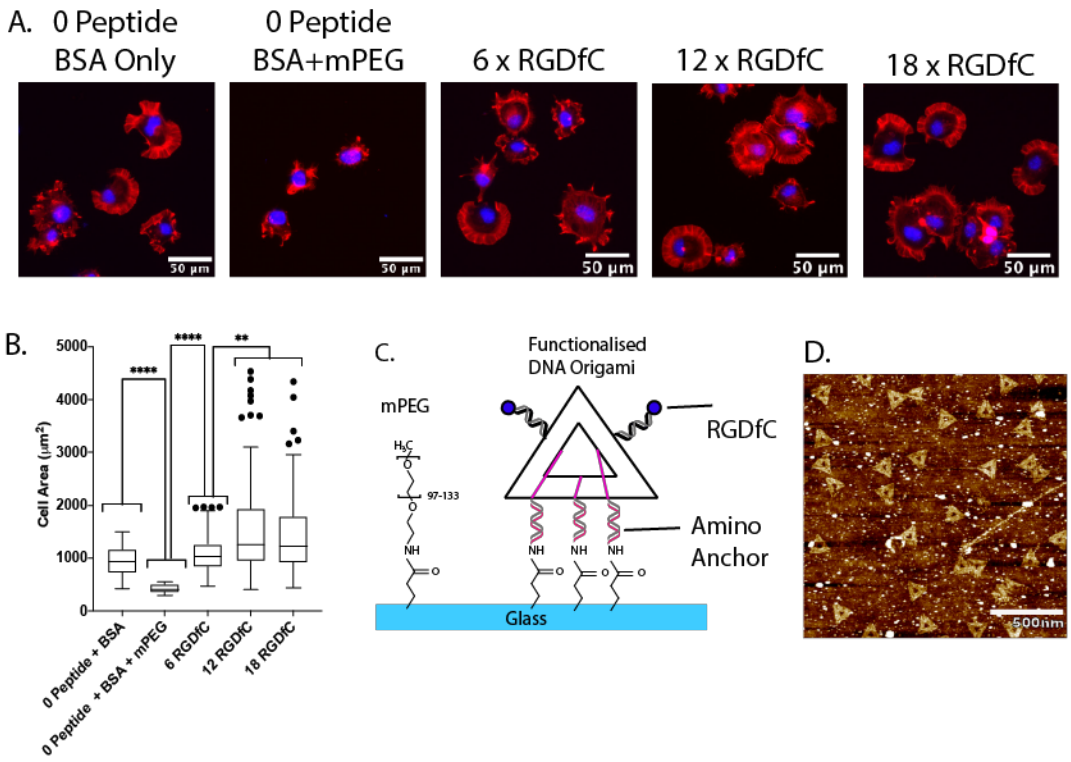

*Figure 4.16. Optimisation of blocking conditions using mouse embryonic fibroblasts cultured on random DNA origami arrays. A) mPEG was required to prevent non-specific adhesion to the background on DNA origami functionalised with 0, 6, 12 or 18 RGDfC. B) Quantification of spreading my measuring cell area, data from three independent repeats, One-way ANOVA with Tukey correction for multiple comparisons, ** = p<0.01, **** = p<0.0001. C) Schematic of mPEG passivation and covalent immobilisation of DNA origami. D) Representative AFM image of randomly positioned DNA origami. N = > 100 cells per condition.*

4.5.3.2 Verification of Peptide Functionalisation on Nanopatterned DNA Origami

To verify the successful functionalisation of DNA origami structures with conjugated products, the acrydite peptide conjugation approach was extended to fluorescently labelled peptides. RGDfC peptides labelled with an Alexa-647 dye were purchased and conjugated to acrydite modified ssDNA. Alexa-647 dyes were chosen to minimise photobleaching from the UV light and the duration of the reaction was also minimised and. TCEP concentration was also reduced from 100X to 20X as this reagent been suggested to accelerate photobleaching (Tyagarajan et al., 2003). 647-cRGDf ssDNA conjugates were verified and purified using HPLC and DNA origami were then functionalised with 12 fluorescent peptide conjugates and cross-linked onto EBL

nanopatterned substrates under optimised conditions. Furthermore, to further verify successful origami cross-linking and functionalisation with fluorescent peptides, and MEF cells were cultured on the substrates for 1 hour. Fluorescent signal was observed from the patterned areas (Figure 11 C) but the signal was very low due to photobleaching during peptide conjugation. However, cells attached and spread over the nanopatterned areas and had significantly greater cell area compared to cells that remained attached to the background after fixation (Figure 11 D). This confirms successful conjugation, origami functionalisation and nanopatterning but due to significant photobleaching, even under optimised conditions, we were unable to quantify the efficiency of origami functionalisation with this approach.

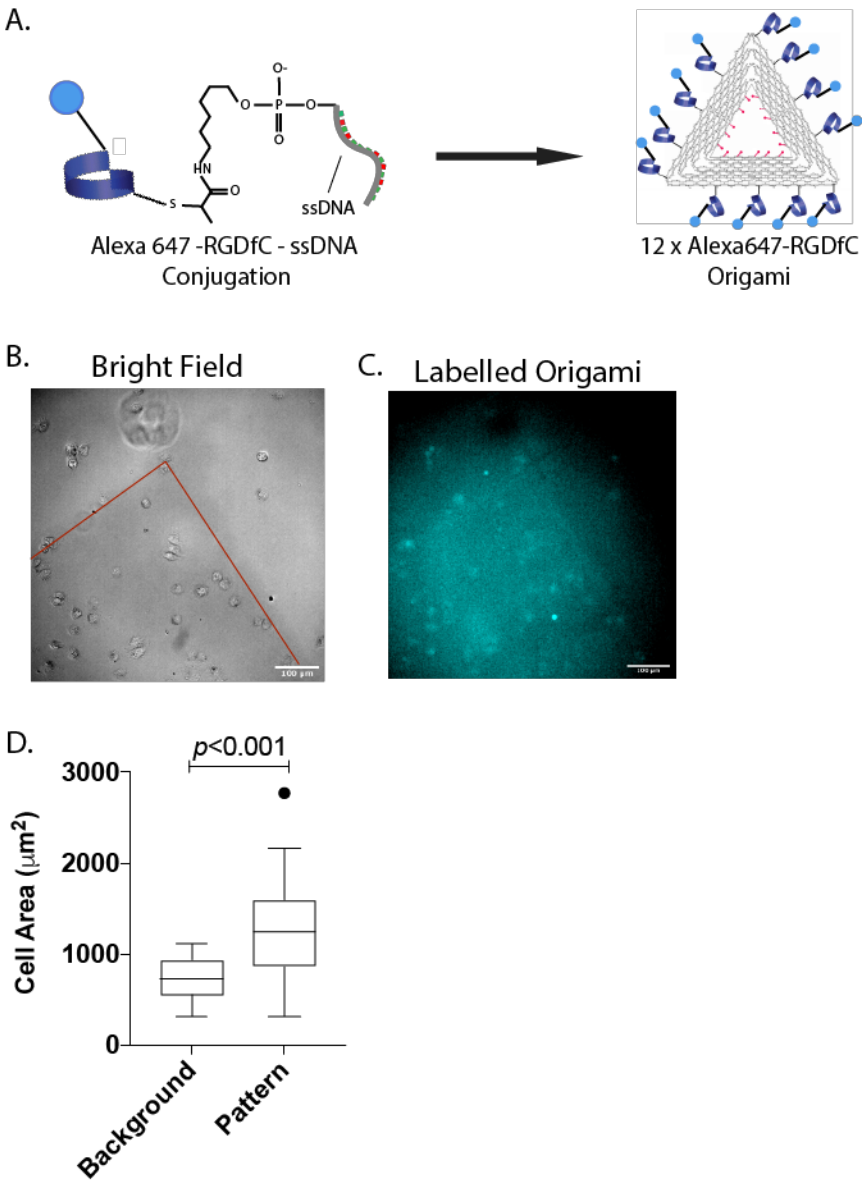

Figure 4.17. Functionalisation of DNA origami with 12 x Alexa 647-RGDfC peptides. Fluorescent peptides were conjugated to acrydte modified ssDNA and DNA origami functionalised with fluorescent RGDfC were fabricated (A). Fluorescent functionalised DNA origami were cross-linked to the nanopattern and mouse embryonic fibroblasts were cultured on the nanopattern for 1 hour before fixation. Cell area was quantified with phase contrast microscopy (B) and fluoescent nanopatternred DNA origami were visualised with an epifluorescence microscope (C). Cells spread more on the 12xAlexa647-RGDfC nanopattern than on the background (D). Student's t-test. Red line in B indicates the edge of the nanopattern.

4.5.3.3 Verification of Nanopatterned DNA Origami Arrays – Recapitulation of Previous Literature

The results from the previous chapter show that by combining e-beam lithography and DNA origami, we can fabricate ECM mimicking substrates with precise control over the concentration, composition and geometry of ligands in the ECM. However, this platform has not yet been validated against other ligand nanopatterning platforms reported in the literature.

The vast majority of the previous work on single molecule ligand nanopatterning platforms was carried out with cells expressing αvβ3 integrin subtypes (Arnold et al., 2004, Cavalcanti-Adam et al., 2007, Huang et al., 2009). These investigations reported that cells will only spread on cyclic RGD peptides when individual integrins are clustered <60 nm apart. Furthermore, studies investigating the effect of ligand geometry also reported that clusters of 4 or more ligands can be spaced 200 – 300 nm apart, with negligible effects on cell spreading (Schvartzman et al., 2011). In the light of this previous work, it was important to test the performance of the origami platform in a similar cell type. Mouse embryonic fibroblasts (MEFs) express αvβ3 integrin subtypes which have a high affinity for the RGDfC peptide (Kapp et al., 2017), and were therefore employed for initial investigations.

Previous work has demonstrated that adequate integrin clustering facilitates spreading and stable adhesion formation via the ability to exert traction forces through adhesions (Liu et al., 2014). To investigate whether increased integrin clustering would also result in increased adhesion forces, RPTP$\alpha^{(+/+)}$ MEFs were transiently transfected with a talin molecular tension sensor (Talin TS). This tension sensor contains an insert between the talin head and tail domains, which consists of two fluorophores connected via a flexible linker. The fluorophores undergo Forster Resonance Energy Transfer in absence of force (FRET). Talin provides the mechanical link between integrin β1 tails and actin, loading of talin during rigidity sensing stretches the flexible linker and pulls the two fluorophores apart, decreasing FRET. With increasing tension, the two fluorophores are pulled further apart, enabling direct evaluation of the molecular tension, of up to 5 pN, across talin at focal adhesions, via changes in FRET efficiency (Austen et al., 2015). These cells were also homozygous negative for talin (talin1 and 2, talin DKO), enabling direct evaluation of talin tension without artefact introduced by endogenous talin. Due to equipment problems, however, it was not possible to carry out the appropriate data collection of the FRET tension sensor at this time. However, the primary aim of this experiment was to

validate the integrin clustering and cell spreading behaviours of fibroblasts on the DNA origami ligand nanopatterning platform. This could still be achieved via the quantification of cell area and cell spreading. Molecular tension of talin as a consequence of integrin clustering will be analysed and presented elsewhere in future investigations.

The DNA origami nanopattern was evaluated against findings from other ligand nanopatterning platforms. Firstly, ligand spacing of <60 nm is required to initiate cell spreading (Cavalcanti-Adam et al., 2007) via the adequate distribution of force across an appropriate number of integrins, on rigid substrates (Huang et al., 2009, Oria et al., 2017). Secondly, efficient cell spreading is unaffected when individual clusters are spaced at 200 or 300 nm intervals (Schvartzman et al., 2012). Origami nanopatterns were therefore fabricated with 3, 6 or 12 RGDfC peptides (~130, ~60 and ~30 nm spacing, respectively), with inter cluster spacing of 200nm or 300nm, to test whether previous findings could be recapitulated here. All results from this experiment can be seen in Figure 4.18.

Talin DKO MEFs transiently transfected with talin TS were seeded at a concentration of 10,000 cells/ml on the nanopattern and cultured for 1.5 hours before fixation for analysis of cell attachment and spreading. On 0 peptide controls, a small number of cells adhered to the nanopattern (mean ± SD, 6 ± 5 % and 8 ± 5 % on 200 and 300 nm arrays), but were unable to spread (Cells were defined as spread if lamellipodial protrusions could be observed.) The cells on control substrates were rounded up and very small in size (86 ± 54 μm^2 and 129 ±42 μm^2, on 200 and 300 nm arrays, respectively), demonstrating that the array does not mediate non-specific cell spreading in a meaningful way.

The addition of 3, 6 or 12 peptides to the nanopattern resulted in dramatic increases in cell spreading. With 3 x RGDfC peptides (~130nm spacing), an increase in the number of spread cells (34 ± 12 % and 31 ± 12 % of cells were spread on 200 and 300nm arrays, respectively) and cell area (213 ± 60 μm^2 and 181 ± 54 μm^2 on 200 & 300 nm arrays, respectively) was observed (Figure 4.18). With 6 x RGDfC per origami, achieving the 60 nm spacing threshold, a further increase in cell spreading (61 ± 9 % and 58 ± 8 % cells spread on 200 nm and 300 nm arrays, respectively) and cell area (428 ± 150 μm^2 and 385 ± 119 μm^2 for the 200 nm and 300 nm arrays, respectively) was observed (Figure 4.18). In this condition, cells exhibited a stronger spreading phenotype, forming larger lamellipodial protrusions. Further increasing the number of peptides per origami to 12 (~30 nm spacing), did not result in a meaningful increase in the cell spreading (66.5 ± 8 % and 66.8 ± 11 % of cells were spread on 200 & 300 nm arrays, respectively) or area

(462 ± 172 μm^2 and 525 ± 229 μm^2 on 200 & 300 nm arrays, respectively), compared to 6 RGDfC.

Talin DKO MEFs without the transfected talin TS are a nonadherent cell line. The degree of cell attachment and spreading on the nanopattern would, therefore, be dependent upon the efficiency the transfection and corresponding expression of the construct. To check if the results of this experiment were confounded by transfection efficiency, all cells used during this experiment were transfected in the same T25 flask. Nevertheless, the degree of transfection efficiency between individual cells within the same flask will vary on a cell to cell basis. To check whether the differences observed in spreading on 3, 6 or 12 RGDfC peptide arrays were due to the different peptide configurations and not due to differences in transfection efficiency, the GFP signal intensity of the talin tension sensor was plotted against cell area. Figure 4.18D shows a linear relationship between talin TS expression (GFP Intensity) and cell area, demonstrating that the degree of cell spreading is dependent upon transfection efficiency, as expected. However, increasing the number of peptides (especially from 3 to 6, or 3 to 12) results in an additional increase in cell area, demonstrating an additional effect of peptide clustering on cell spreading.

These results demonstrate that using the origami nanopattern, we can recapitulate the 60 nm ligand threshold observed in $\alpha v\beta 3$ integrin rich cells from other ligand nanopatterning platforms (Arnold et al., 2004, Cavalcanti-Adam et al., 2007, Huang et al., 2009, Oria et al., 2017). Furthermore, consistent with observations by others (Schvartzman et al., 2011) no significant differences in adhesion and spreading were observed between the 200 nm and 300 nm configurations, providing further validation of the origami nanopattern.

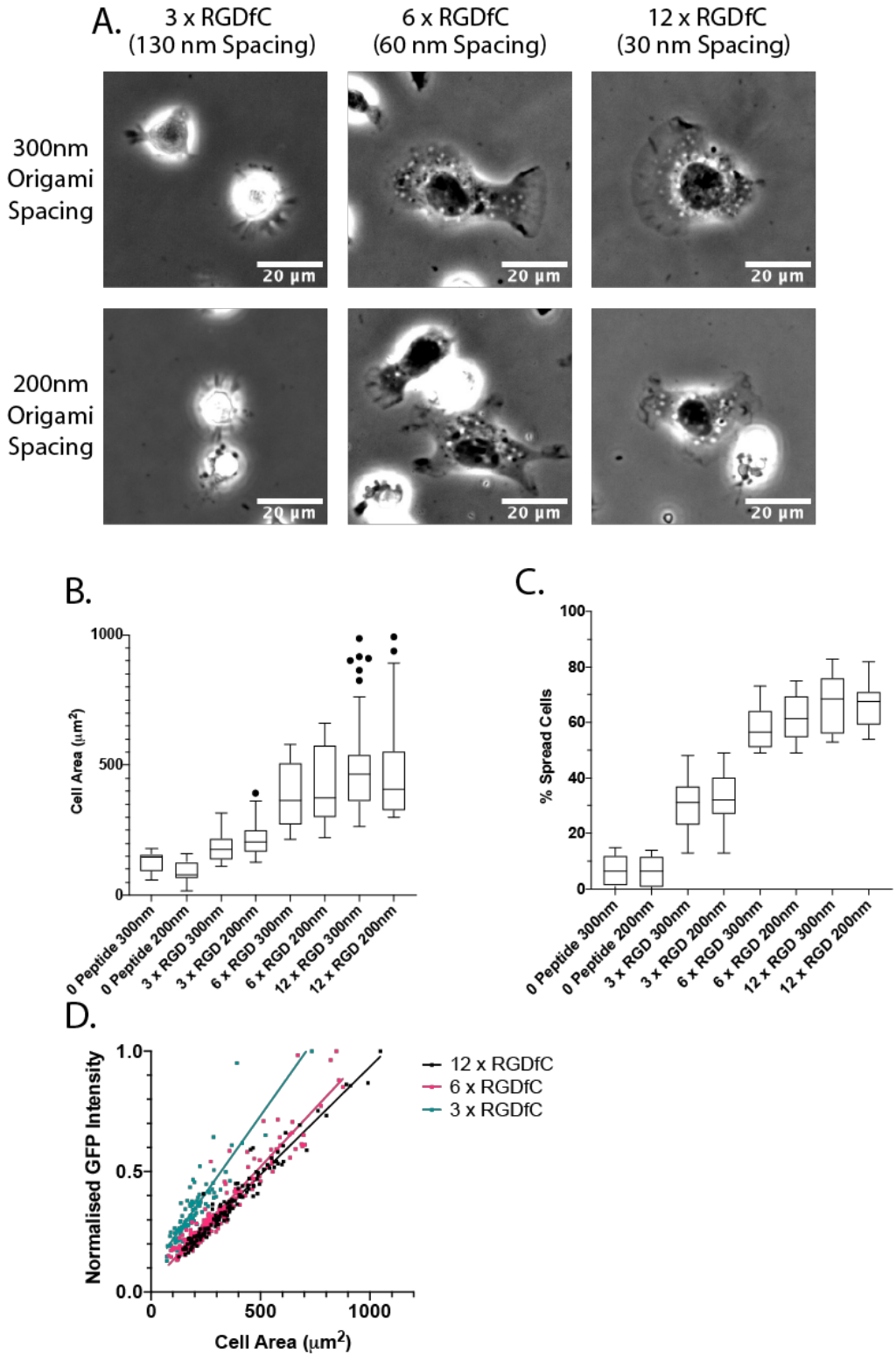
A.
3 x RGDfC
(130 nm Spacing)
6 x RGDfC
(60 nm Spacing)
12 x RGDfC
(30 nm Spacing)
300nm
Origami
Spacing
200nm
Origami
Spacing
20 µm
B.
Cell Area (µm²)
1000
500
0
0 Peptide 300nm
0 Peptide 200nm
3 x RGD 300nm
3 x RGD 200nm
6 x RGD 300nm
6 x RGD 200nm
12 x RGD 300nm
12 x RGD 200nm
C.
% Spread Cells
100
80
60
40
20
0
D.
Normalised GFP Intensity
1.0
0.5
0.0
0
500
1000
Cell Area (µm²)
12 x RGDfC
6 x RGDfC
3 x RGDfC

Figure 4.18. Validation of the DNA origami nanopatterning platform using talin double knock-out MEFs, transiently expressed with a talin tension sensor. A) representative images of cells spread on the different nanopattern configurations. B) Quantitative measurement of cell area. C) Quantitative evaluation of the number of spread cells. Cells were deemed to be spread or spreading if stable lamellipodial protrusions could be observed. D) Plot of talin TS expression (quantified by GFP intensity) against cell area to demonstrate effects of the nanopattern, independent from effects of transfection efficiency.

4.6 Discussion

Discussion points:

In summary, this chapter presented the fabrication and optimisation of a DNA origami, single molecule nanopatterning platform. By combining DNA origami with EBL, a powerful tool for the investigation of integrin signalling, in any cell type, has been presented. Millions of functional DNA origami nanostructures can be selectively positioned with high at a resolution of 300 nm or 200 nm. Furthermore, single molecule functionalisation of the origami nanoarray enables quantitative evaluation got the integrin clustering requirement of fibronectin an laminin integrin subtypes. This approach provides absolute control over the composition, concentration and geometry of integrin specific ligands to compare and contrast the clustering requirements, of different integrin subtypes, for the initiation of rigidity sensing and cell spreading. Specifically, this platform has been designed to investigate the integrin clustering dynamics of cardiomyocytes expressing fibronectin and laminin bindings integrin subtypes. The following chapter will present and discuss findings from the use of this platform to investigate the clustering and downstream signalling consequences of different integrin subtypes in cardiomyocytes.

Lithographic nanopatterning of DNA origami was originally pioneered by the Rothemund lab, who have clearly demonstrated the ability to position individual DNA nanostructures in arbitrary and precise configurations (Kershner et al., 2009, Gopinath and Rothemund, 2014, Gopinath et al., 2016). Specifically, Kershner et al. (2009) were the first to demonstrate that the pointed triangle design DNA origami could be selectively positioned

on lithographically nanopatterned surfaces, with relatively precise control over the orientation of individual DNA origami's. Gopinath and Rothemund (2014) took this work a step further by characterising the adsorption and immobilisation characteristics of the pointed triangle DNA origami, on lithographically nanopatterned surfaces. The Rothemund group has gone on to replicate their own work in subsequent publications (Gopinath et al., 2016) which has been replicated in this thesis. The current investigation, through a collaboration with the Gadegaard lab, has successfully demonstrated the ability fabricate lithographically nanopatterned DNA origami. However, the current investigation was unable to replicate previous work, under the same conditions, during the placement of DNA origami demonstrating the precarious nature of DNA origami nanopatterning. This was believed to be primarily due to differences in the surface silanisation used here, while others have also demonstrated vastly different origami placement conditions on nanopatterns of similar dimensions (Brassat et al., 2018, Gopinath and Rothemund, 2014, Huang et al., 2019). These contrasting reports highlight a potential issue with reproducibility of these nanoscale designs between laboratories and should be carefully considered when interpreting these findings. These considerations are especially important when DNA origami is being considered in the manufacturing of nanoscale plasmonic (Gopinath et al., 2016) or photoelectric (Huang et al., 2017) devices.

While the Rothemund group have been pioneers in developing and expanding lithographic DNA origami nanopatterning methodologies, the Palma group have brought this approach into the ligand nanopatterning and cell receptor signalling domain by utilising the versatility of DNA origami with DNA-peptide conjugation strategies. Previous work from the lab has demonstrated the synergistic roles of integrins and endothelial growth factor receptors in the spreading and adhesion of cancer cells (Huang et al., 2019). This thesis has advanced the previous work of the Palma lab by extending the design of the pointed triangle DNA origami to accommodate up to 18 peptides, achieving an inter-peptides spacing of <20 nm. Furthermore, the successful covalent nanopatterning of the 3, 6, 12 and 18 peptides designs has brought the capabilities of this technology in line with the capabilities of other ligand nanopatterning technologies such as the gold nano-island platform pioneered by Jochim Spatz (Arnold et al., 2004, Cavalcanti-Adam et al., 2007, Arnold et al., 2009, Huang et al., 2009, Rahmouni et al., 2013, Liu et al., 2014, Guasch et al., 2015, Schaufler et al., 2016, Kapp et al., 2017, Zarka et al., 2019a). This achievement offers great potential for this DNA origami platform in

the investigation of adhesion receptor clustering, especially with the multi-valent capabilities of DNA origami, as demonstrated by the Palma lab (Huang et al., 2019).

A significant challenge in the development of this work was the successful conjugation of peptides to ssDNA staples for hybridisation to the DNA origami structures. Previous work as demonstrated the used of thiol-maleimide reactions (Huang et al., 2019, Franquelim et al., 2018) for linking cysteine tagged peptides to ene-presenting ssDNA. The current investigation failed to replicate maleimide based conjugates for currently unknown reasons. However, this thesis has presented the successful fabrication and purification of acrydite conjugates which have the advantages of high stability prior to the reaction, highly efficient conjugation in aqueous solutions with neutral pH and high post-reaction carbon-carbon bond stability (Lutolf and Hubbell, 2003, Lowe, 2010). These acrydite conjugate were successfully hybridised to DNA origami structures and immobilised on the nanopatterned arrays, completing the platform design. However, others have also had success in implementing conjugate products more classically observed in molecular biology, such as NHS-esters (van der Velde et al., 2016), histidine tags (Shen et al., 2009), biotin-streptavidin (Huang et al., 2019) and antibody-antigen (Cremers et al., 2019). Therefore, future investigations could look to these technologies when seeking to improve upon the conjugation approach presented here. Furthermore, approaches offer tremendous opportunity when looking to design multi-valent DNA origami structures and future work would certainly benefit from a systematic evaluation of the efficacy of these approaches.

A key strength of the current chapter is the use of the DNA origami nanopatterning platform to recapitulate integrin clustering dynamics previously reported by others, using different platform. Previous work using micellular co-block polymer arrays has consistently demonstrated that αvβ3 expressing cell lines require RGD peptide spacing of <60 nm for adequate integrin clustering and cell spreading (Arnold et al., 2004, Cavalcanti-Adam et al., 2007, Huang et al., 2009, Schvartzman et al., 2011, Schaufler et al., 2016, Oria et al., 2017). To validate whether the same results could be observed on the DNA origami nanopattern immortalised MEF cells were cultured on nanopatterned RGDfC ligands at 130 nm, 60 nm and 30 nm ligand spacings with 200 nm and 300 nm. The MEF cells were highly sensitive to inter ligand spacing and only spread consistently on 60 nm and 30 nm configurations, successfully demonstrating the 60 nm threshold. No differences were observed between 200 nm and 300 nm configurations which was also consistent with the work of others (Schvartzman et al., 2011), providing further

confirmation of successful fabrication of the DNA origami design and validation of our approach to use this platform to investigate integrin clustering dynamics in a different cell type. Asa result, this investigation was able to proceed onto culturing of neonatal rat cardiomyocytes with confidence in the validity and reliability of the DNA origami nanopatterning platform.

5 NANOSCALE INTEGRIN CLUSTERING IN CARDIOMYOCYTES

5.1 Introduction

The cardiac ECM is a highly dynamic and complex structure that plays a key role in healthy functioning, development and disease (Buyandelger et al., 2011, Ward and Iskratsch, 2019). Chapter 3 presented findings that demonstrate unique spreading, traction forces and adhesion composition in NRCs when cultured on fibronectin compared to laminin. It was hypothesised that these underlying differences may initially occur at the level of the integrin adhesion. Indeed, investigations have shown key differences in activation energy (Li and Springer, 2017) and clustering (Schaufler et al., 2016) of different integrin subtypes, and it is important to understand the relevance of this within cardiomyocytes. In Chapter 4, a nanopatterning platform was developed to control the clustering of active, ligand bound integrins. Using this platform, the following chapter will present findings on the spreading and adhesion behaviours of cardiomyocytes in response to nanopatterning of fibronectin and laminin peptidomimetic ligands.

5.2 Initial Validation of Cardiomyocyte spreading and adhesion on surfaces functionalised with random DNA Origami

It was then necessary to validate the origami for integrin clustering investigations with cardiomyocytes. DNA Origami presenting 0, 6, 12 or 18 RGDfC or IKVAV peptides were cast randomly on glass coverslips at a concentration of 2 nM, followed by cross-linking of origami to the surface, passivation of the surface with mPEG and additional blocking with 5% BSA. NRCs were isolated and cultured in serum free media on the random arrays for 24 hours before fixation and quantification of cell spreading by calculation of cell area. Previous work culturing NRCs on peptides functionalised substrates has reported impeded cell spreading and severe disruption to the cytoskeleton, with an inability to assemble sarcomeres (Boateng et al., 2005, LaNasa and Bryant, 2009).

Therefore, cytoskeletal maturity was also qualitatively evaluated by calculation of α-actinin intensity and morphology, which localises to the z-line (Pandey et al., 2018). Three phenotypes of α-actinin localisation were used to assess cytoskeletal maturity; (1) localisation to stress fibre like structures (SFLS), (2) mixed localisation to SFLS and striated myofibrils and (3) predominant localisation to mature myofibrils which also demonstrate consistent alignment. All results of NRC spreading and myofibril maturity on random origami arrays can be seen in Figure 5.1.

On zero peptide controls, NRCs were rounded up and unable to spread, confirming that non-specific adhesion was minimal. Upon presentation of 6 peptides per origami (~60 ligands per μm^2), NRCs started to spread on both RGDfC and IKVAV, with no significant differences observed between the two peptides (240 ± 107 and 252 ± 76 μm^2 for RGDfC and IKVAV respectively). In general, NRCs were small on 6 RGD and IKVAV arrays and the increase in cell area did not constitute a strong spreading phenotype (Figure 5.1 A & B). Evaluation of α-actinin localisation demonstrated that most NRC exhibited SFLS with few striations or a mixed phenotype (Figure 5.1E).

On 12 peptide random arrays (~120 ligands per μm^2), NRCs spread significantly more on RGDfC and IKVAV compared to 6 peptide random arrays with an average area of 313 ± 69 μm^2 and 368 ± 157 μm^2, (respectively) with no significant difference between RGDfC and IKVAV (Figure 5.1). Localisation of α-actinin transitioned from predominantly SFLSs on 6 peptides to predominantly a mixed myofibril and SLFS phenotype on 12 peptides which occurred with a corresponding increase in α-actinin density. Furthermore, NRCs on 12 RGDfC had significantly greater actinin density than 12 IKVAV, which is suggestive of subtle differences in cytoskeletal content.

On 18 peptide random arrays (~120 ligands per μm^2), further cell spreading was only observed on RGDfC, where cell area increased to 405 ± 135 μm^2 which was significantly more than both 12 RGDfC and 18 IKVAV (346 ± 96 μm^2). Evaluation of cytoskeletal maturity revealed that more NRCs exhibited a mature, or mixed phenotype. No significant differences were observed in α-actinin content between 18 RGDfC and 18 IKVAV, as measured by α-actinin density or manual classification Figure 5.1. These findings clearly demonstrate that both RGDfC and IKVAV functionalised DNA origami facilitate NRC

spreading and cytoskeletal maturation, in a dose dependent manner. Furthermore, evaluation of cytoskeletal maturity has shown that the peptides utilised do not inhibit

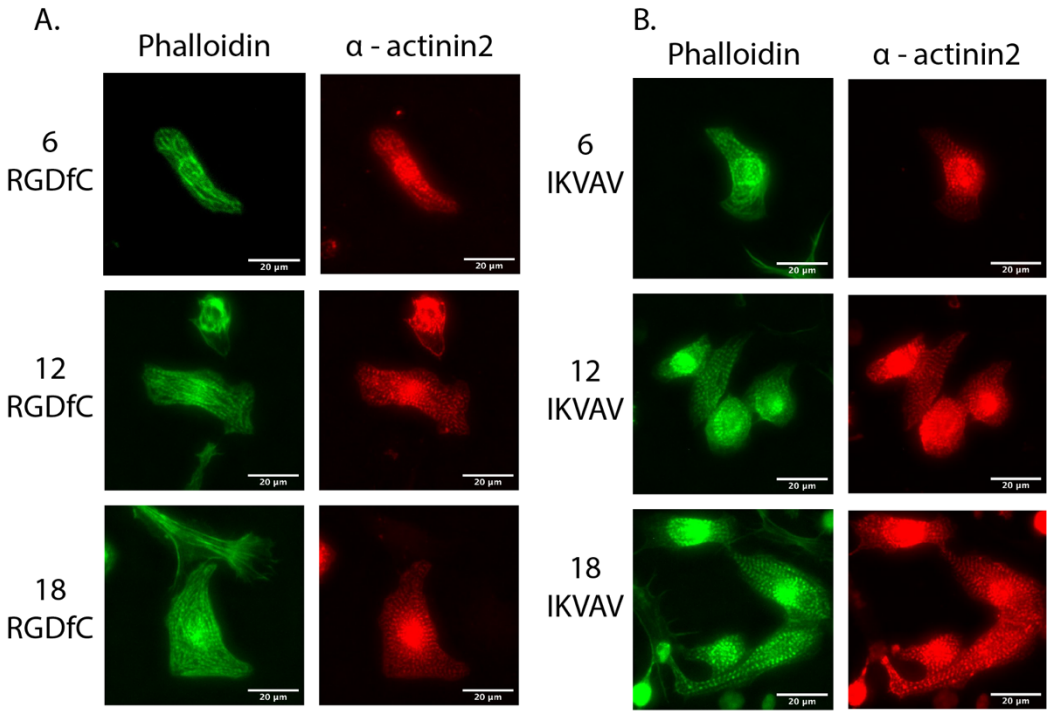

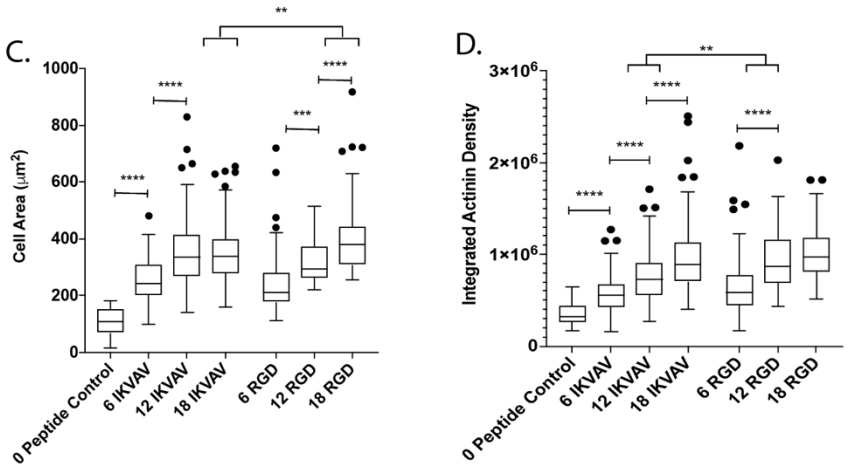

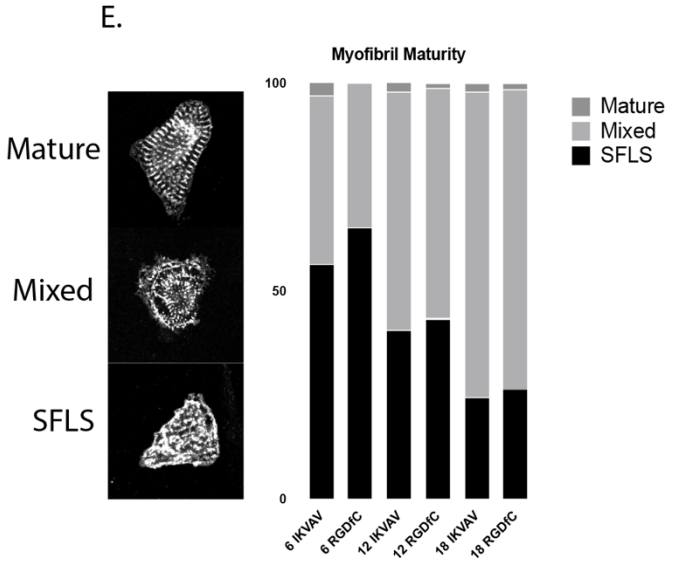

*Figure 5.1. Validation of NRC spreading and sarcomere assembly on random DNA origami arrays. NRCs were cultured on 6, 12 or 18 RGD (A) or IKVAV (B). C & D) Quantification of cell area and actinin content in each condition. E) Qualitative evaluation of myofibril maturity. Values represent the % of cells with predominantly SFLS, mixed or mature phenotype. N = > 80 cells per condition from three biological repeats. One-way ANOVA was used to compare differences within each peptide, Tukey correction for post-hoc comparison, student's t-test was used to compare differences between peptides, ** = p<0.01, **** = p<0.0001.*

myofibril assembly as reported by others (Boateng et al., 2005; LaNasa & Bryant, 2009).

5.3 Nanoscale Integrin Clustering and Spreading Properties of Cardiomyocytes

Preliminary investigations culturing NRCs on randomly positioned DNA origami functionalised with RGDfC or IKVAV demonstrated that this platform can mediate NRC spreading and adhesion. However, the random arrays can only provide information on integrin clustering relative to the area of a single origami structure (~85 nm^2) with no control over the global positioning of the origami. The DNA origami nanopatterning platform overcomes these limitations by providing precise control of the global and local integrin clustering dynamics, which are key to cell adhesion and spreading (Arnold et al., 2004, Cavalcanti-Adam et al., 2007, Oria et al., 2017).

To compare and contrast the clustering dynamics of different integrin subtypes and their effect on NRC spreading and adhesion, nanopatterned DNA origami substrates were fabricated with 6, 12 or 18 RGDfC or IKVAV peptides in 200 nm or 300 nm arrays. Table 5.1 summarises the local and global ligand properties of each nanopattern configuration. Nanopatterned DNA origami arrays with zero peptides were employed as negative controls. Substrates were passivated with mPEG and 5% BSA, to minimise nonspecific adhesion, before culturing freshly isolated neonatal cardiomyocytes for 24 hours. All results can be seen in Figure 5.2. The degree of cell spreading and cytoskeletal maturity were measured by F-actin area, intensity and circularity from two independent experiments. On zero peptide controls, few cells adhered to the substrates, suggesting a low level of non-specific adhesion. The addition of 6 RGDfC peptides (~60 nm spacing) resulted in an increase in cell attachment and initiated spreading only with 200 nm cluster spacing (150 peptides / μm^2) and not with 300 nm cluster spacing (54 peptides / μm^2).

Cell area was significantly greater than controls at (mean ± SD) 398 ± 141 μm^2 with 200 nm cluster spacing, compared to 237 ± 128 μm^2, with 300 nm cluster spacing. For cells on 6 IKVAV nanopatterns, few cells were spread on either 200 nm and 300 nm arrays suggesting insufficient integrin clustering to support spreading.

Table 5.1. Local and global parameter of the different nanopattern configurations. Inter peptide distances represent the distance between modification sites on the design of the pointed triangle DNA origami. As the orientation of each DNA origami on the nanopattern was not controlled, a precise characterisation of the nanopattern configurations is not possible and the listed values represent the closest approximation based on the known geometry of the EBL pattern and the DNA origami dimensions.

Local Ligand Density (peptides / DNA origami)	Inter Peptide Distance (nm)	DNA origami Spacing (nm)	Global Ligand Density (peptides / μm²)
6	65	300	54
6	65	200	150
12	33	300	108
12	33	200	300
18	21	300	162
18	21	200	450

Increasing the number of peptides on each DNA origami to 12 (decreasing inter ligand spacing to ~30 nm) resulted in a significant increase in cell area on both RGDfC and IKVAV peptides. Interestingly, NRCs cell area on 12 RGDfC 300 nm (108 peptides / μm^2) was comparable to cells on the 6 RGDfC 200 nm (150 peptides / μm^2) nanopattern (398 ± 141 μm^2 vs 431 ± 202 μm^2 on 6 RGDfC 200 nm and 12 RGDfC 300 nm, respectively, $p > 0.05$). A significant increase in cell area was only observed on 12 RGDfC 200 nm (300 peptides / μm^2) arrays where NRCs spread to 625 ± 191 μm^2. On 12 IKVAV arrays, initiation of spreading was observed on 200 nm cluster spacing configurations only, although the degree of spreading was not as pronounced as initiation

of spreading on RGDfC. On 12 IKVAV 200 nm configurations, NRC cell area was 285 ± 122 μm^2 with 200 nm cluster spacing where a number of cells began to form stable protrusions, compared to 205 ± 74 μm^2 with 300 nm cluster spacing.

Increasing the number of peptides on each DNA origami to 18 (decreasing inter-ligand distance to 20 nm) resulted in another significant change in spreading on both RGDfC and IKVAV. On nanopatterned RGDfC ligands, NRCs on both 200 nm (450 peptides / μm^2) and 300 nm (162 peptides / μm^2) arrays exhibited significantly less spreading (204 ± 89 and 233 ± 107, 200 nm and 300 nm arrays respectively) than cells on the 12 and 6 peptide arrays. This result may be due to excessive ligand density and substrate stiffness (Engler et al., 2004). On the other hand, increasing the number of IKVAV peptides to 18 did support further spreading in NRCs, resulting in a significant increase in spreading on the 200 nm array only, compared to 12 IKVAV configurations; Cell area on 18 IKVAV 200 nm arrays increased to 410 ± 191 μm^2, compared to 346 ± 152 on 18 IKVAV 300 nm arrays. Notably, cells cultured on 18 IKVAV 300 nm arrays did not spread more than cells on 12 IKVAV 200 nm arrays (162 peptides / μm^2 vs 300 peptides / μm^2, respectively).

In all experiments, NRCs spreading on RGDfC had significantly greater cell area than comparable conditions on IKVAV. Important differences were also observed in NRC cell morphology when spreading on RGDfC or IKVAV. In general, NRCs on RGDfC had a less circular morphology than those on IKVAV (Figure 4D) suggesting differences in adhesion formation and rigidity sensing (Wolfenson, Yang & Sheetz, 2019). To further understand these differences, F-actin content was quantified by calculating the integrated F-actin intensity. NRCs on RGDfC nanopatterns exhibited increases in F-actin content (as measured by F-actin integrated density) with increasing global ligand density, up to an extent. In almost all conditions, excluding 18 peptides, NRC cultured on RGDfC ligands had significantly greater F-actin content (Figure 4E), suggesting an important relationship between integrin clustering, cytoskeletal assembly and spreading. Interestingly, NRCs cultured on IKVAV did not exhibit the same relationship between cytoskeletal content, spreading and integrin clustering. On 18 IKVAV nanopatterns, where a stronger spreading phenotype was observed, F-actin content actually decreased suggesting impaired F-actin assembly. Together, these results suggest that $\alpha 5\beta 1$ integrin adhesions are more stable and require fewer ligand to initiate spreading on NRCs compared to $\alpha 7\beta 1$ integrin adhesions (Oria et al., 2017).

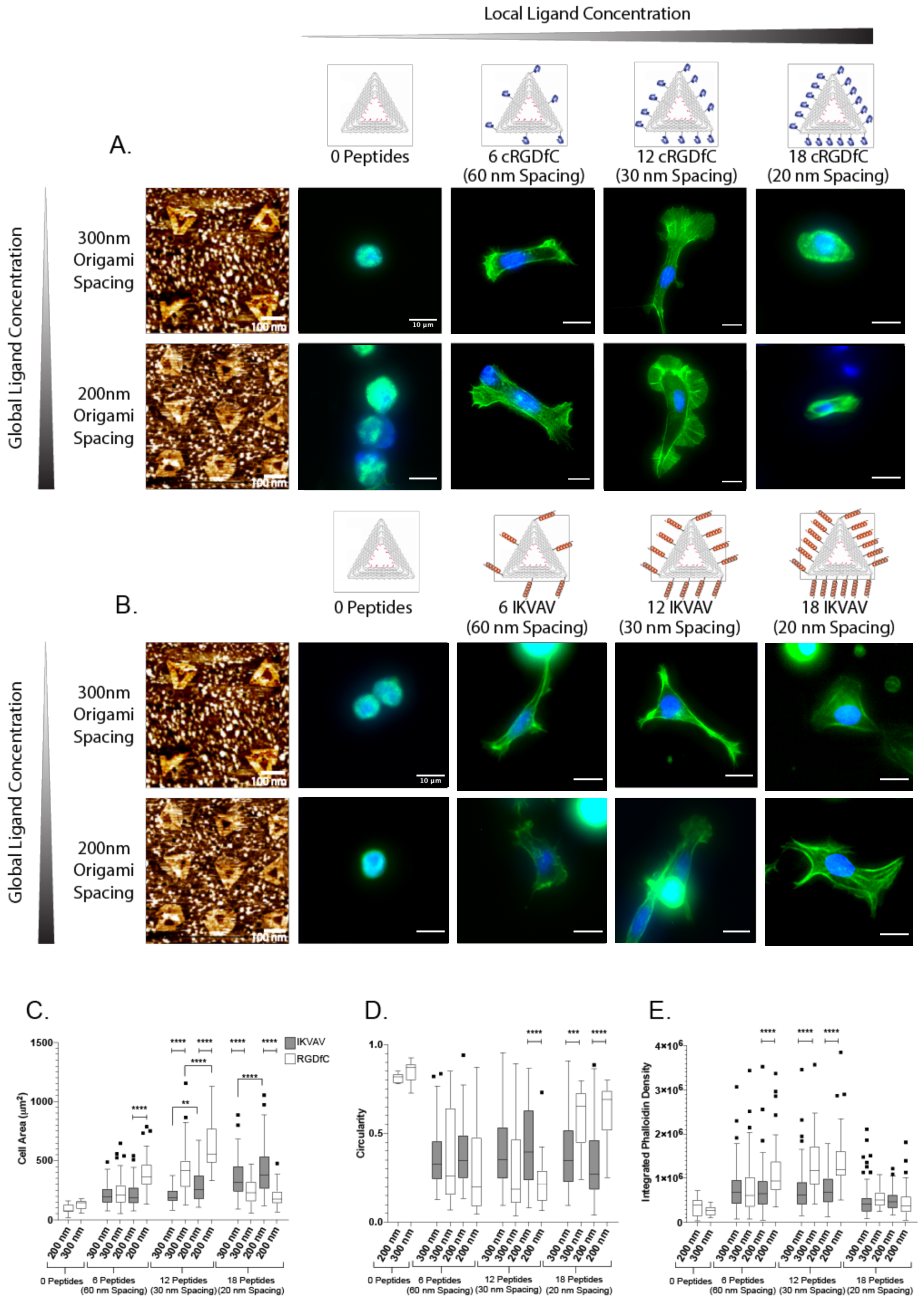
Local Ligand Concentration
A.
0 Peptides
6 cRGDfC
(60 nm Spacing)
12 cRGDfC
(30 nm Spacing)
18 cRGDfC
(20 nm Spacing)
Global Ligand Concentration
300nm
Origami
Spacing
200nm
Origami
Spacing
B.
0 Peptides
6 IKVAV
(60 nm Spacing)
12 IKVAV
(30 nm Spacing)
18 IKVAV
(20 nm Spacing)
Global Ligand Concentration
300nm
Origami
Spacing
200nm
Origami
Spacing
C.
IKVAV
RGDfC
Cell Area (μm²)
D.
Circularity
E.
Integrated Phalloidin Density
0 Peptides
6 Peptides
(60 nm Spacing)
12 Peptides
(30 nm Spacing)
18 Peptides
(20 nm Spacing)

*Figure 5.2. NRCs were cultured on RGDfC or IKVAV functionalised nanopatterns for 24 hours. A & B) Representative images of NRCs spreading on the RGDfC (A) and IKVAV (B) nanopatterns. Spreading and morphology was quantified by measuring cell area (C), circularity (D) and Integrated phalloidin density (E). Differences between peptide numbers and DNA origami spacing were evaluated with a Two-way ANOVA with Tukey corrections for multiple comparisons, ** = p<0.01, *** = p<0.001, **** = p<0.0001. Data from 2 independent experiments. N = >50 cells per condition from 2 biological repeats. Modified from Hawkes et al. 2019.*

5.4 Regulation of NRC spreading on RGDfC and IKVAV

The ability of cells to apply local contractions through integrin clusters would be dependent upon stability of integrin adhesion under force. The molecular clutch model predicts that cell adhesions require an optimum number of integrins to adequately distribute forces during rigidity sensing (Elosegui-Artola et al., 2014, Elosegui-Artola et al.., 2016, Oria et al., 2017). The model predicts that adhesions with an insufficient number of integrins yield under high force while too many integrin adhesions results in excessive distribution of force and mechanotransduction cannot occur. The current investigation has demonstrated that NRCs spreading on IKVAV require more ligands per cluster for stable adhesion and spreading compared to cells cultured on RGDfC ligands. Furthermore, upon the initiation of spreading, NRCs on RGDfC exhibit a less circular morphology, with increased F-actin content, suggesting greater contractility. Coupled with findings that NRCs on RGDfC have greater traction, it was necessary to further the role of cytoskeletal contractility in rigidity sensing and spreading on the different ligands.

Recent work from our lab has demonstrated that downstream of PKC activation, Src is activated at integrin adhesions where it regulates rigidity sensing via non-myofibrillar contractility (non-muscle myosin) and the actin assembly protein, FHOD1 (Pandey et al., 2018). To investigate Src localisation on RGDfC and IKVAV, NRCs were cultured on nanopatterned arrays with DNA origami presenting 6, 12 or 18 RGDfC or IKVAV peptides at 300 nm and 200 nm intervals. Src localisation was visualised using a validated antibody (Figure 5.3A) targeting active (phosphorylated) Src. On 6 RGDfC 300 nm arrays, cells had weak Src staining with no localisation towards the cell edge or at adhesion like structures. When cells start to spread on 6 RGDfC 200 nm arrays, evidence

of Src clustering at the cell edge was observed, which also showed partial co-localisation with α-actinin and F-actin (Figure 5.3C), consistent with its role in integrin adhesion signalling. On IKVAV nanopatterned arrays however, there was little evidence of Src clustering or localisation at the cell edge, on 12 IKVAV 200 nm (where cells begin to spread) or on 18 IKVAV 200 configurations Figure 5.3D. This could indicate differential integrin signalling mechanisms when spreading on different integrin isoforms. The data at this point is purely qualitative and future investigations will investigate the nanoclustering activity of pSrc using super resolution microscopy.

To further investigate the role of Src in NRC rigidity sensing, we returned to experiments on random DNA origami arrays. While these arrays do not provide control over inter-cluster spacing, NRCs on 18 RGDfC or IKVAV still exhibit significant differences in spreading under comparable conditions. Furthermore, unlike the nanopattern, NRCs spreading on random 18 RGCfC and IKVAV have a more mature cytoskeletal structure, and Src may be playing a stronger role in contractility. Thus, NRCs spreading on random 18 RGDfC or 18 IKVAV arrays were treated with 10 μm of the Src inhibitor PP2 for 3 hours and the corresponding change in cell area was calculated. After PP2 treatment, subtle differences were observed in spreading where cells on RGDfC had a slight significant decrease in cell area and cells on IKVAV had a slight, but significant increase. Previous work has demonstrated that contractility inhibition can promote or inhibit spreading depending on the stability of integrin-ECM bonds (Oria et al., 2017). To further test if the differential response to Src inhibition was specific for Src inhibition or due to differences in the inter-ligand bonds, NRCs on random 18 RGDfC and IKVAV arrays were treated with a range of drugs to inhibit or promote cytoskeletal contractility. To inhibit contractility, NRCs were treated with the myosin II inhibitor blebbistatin, the muscle myosin inhibitor verapamil, PP2 and the ROCK inhibitor Y-27632. To compare whether promotion of cytoskeletal contractility has the opposite effect to inhibition, cells

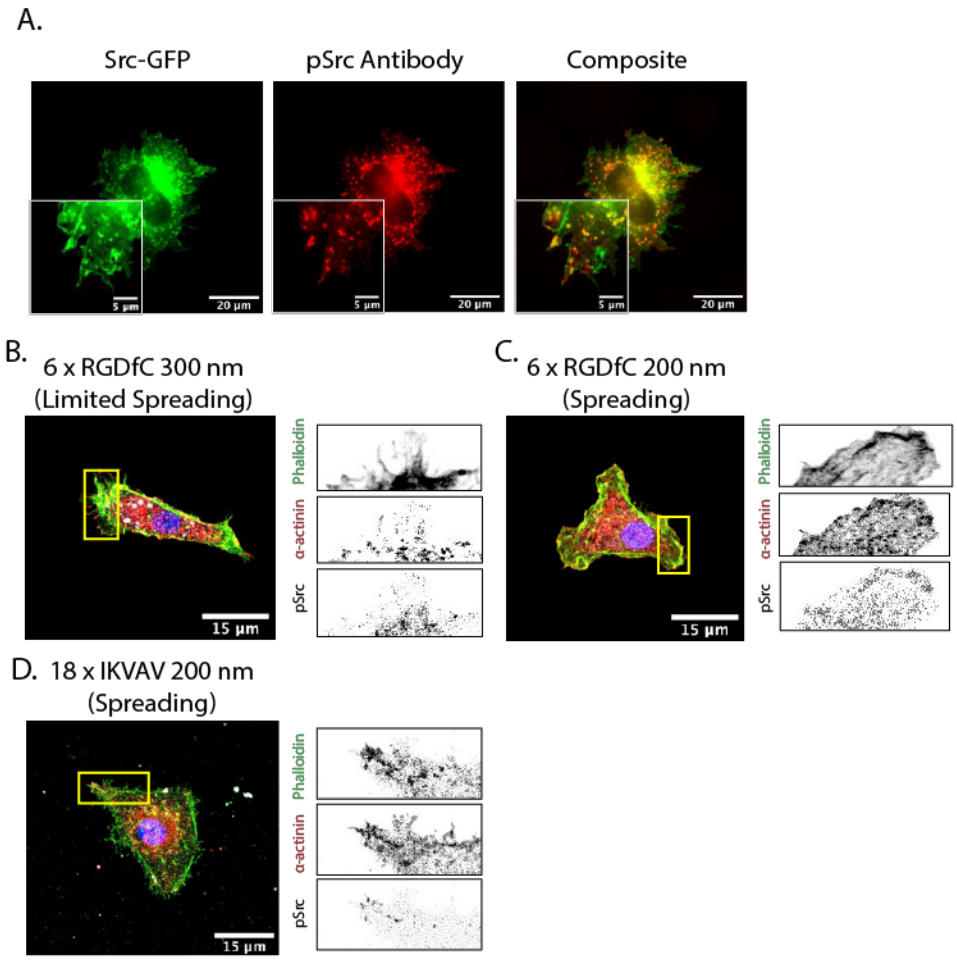

Figure 5.3. Active Src localisation on RGDfC and IKVAV Nanopatterns. A) pSrc antibody validation showing co-localisation between transfected GFP-Src and pSrc antibody. NRCs were cultured on 6 x RGDfC 300nm (B), 6 x RGDfC 200nm (C) and 18 IKVAV 200nm (D) arrays and immunostained for pSrc, α-actinin and phalloidin.

were also treated with the cardiac myosin activator omecamtiv mercabil (OM) and the myosin activator calyculin A. Finally, to investigate the role of formins in NRCs spreading on cRGDfC and IKVAV, cells were also treated with the pan formin inhibitor, smiFH2. On 18 IKVAV, inhibiting contractility resulted in a slight but significant increase in cell area in all cases, suggesting that reduced contractility may act to stabilise adhesion and facilitate spreading. On 18 RGDfC, only PP2 resulted in a significant change in cell area, suggesting that Src plays a key role in spreading and rigidity sensing. Drugs promoting contractility resulted in a significant decrease in cell area for 18 IKVAV with OM treatment only and on RGDfC, cells exhibited a significant decrease in cell area with OM and calyculin-A treatment. Upon treatment with any drug, all cells exhibited a

more circular morphology, consistent with a decrease in cytoskeletal tension. These results suggest that on RGDfC, Src plays a key role in NRC spreading and that

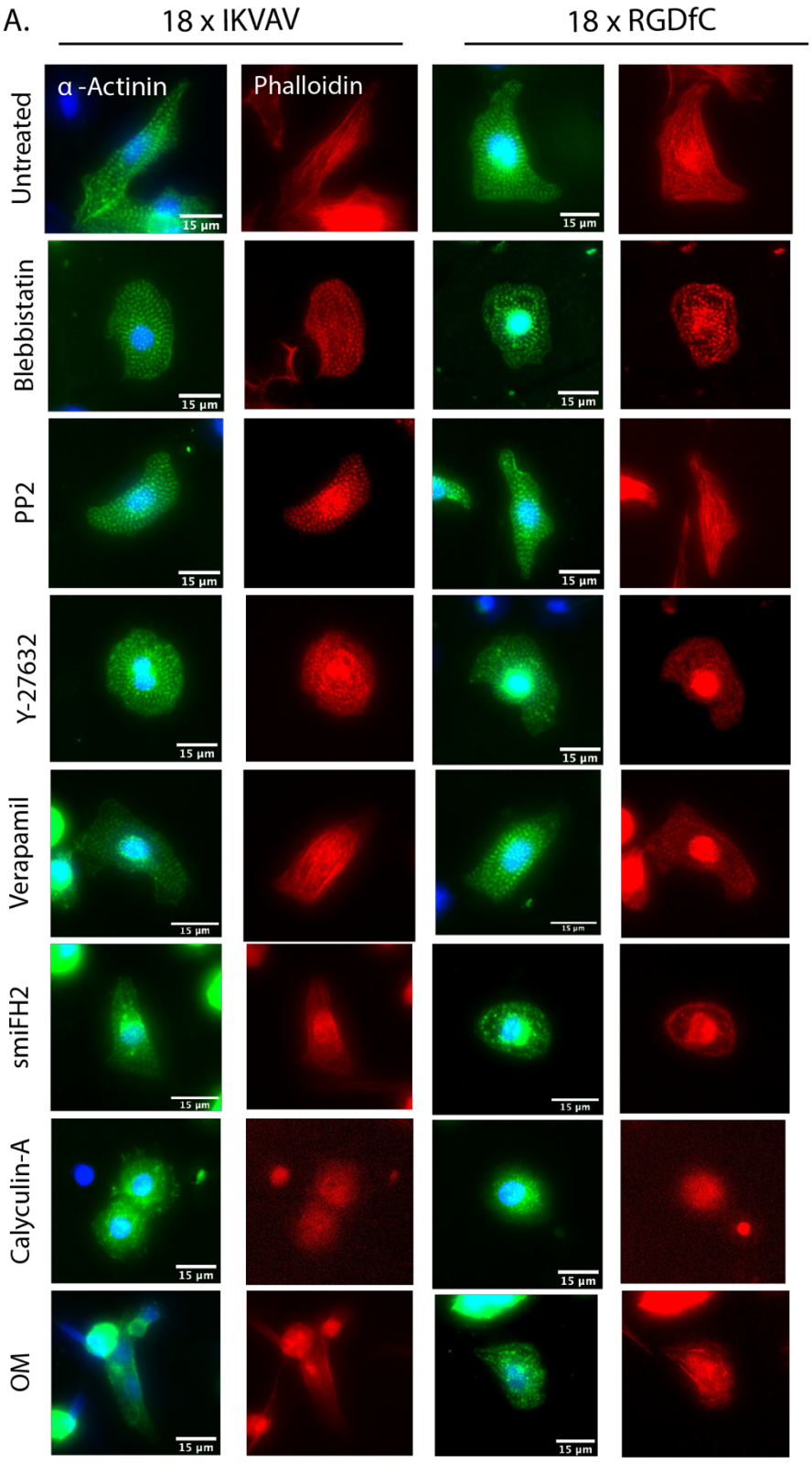

Figure 5.4. Representative images of NRCs spreading on random DNA origami presenting 18 RGD or 18 IKVAV peptides. NRCs were treated with drugs to inhibit (Blebbistatin, PP2, Y-27632 or Verapamil) or enhance Calyculin-A, OM) contractility. Cells were also treated with the formin inhibitor smiFH2. The cytoskeleton was visualised by immunostaining for α-actinin (green) or F-actin (red). Cells were spread for 19 hours after plating before being treated with drugs for 3 hours followed by fixation.

cytoskeletal contractility may play different roles in cell spreading depending on the integrin subtype.

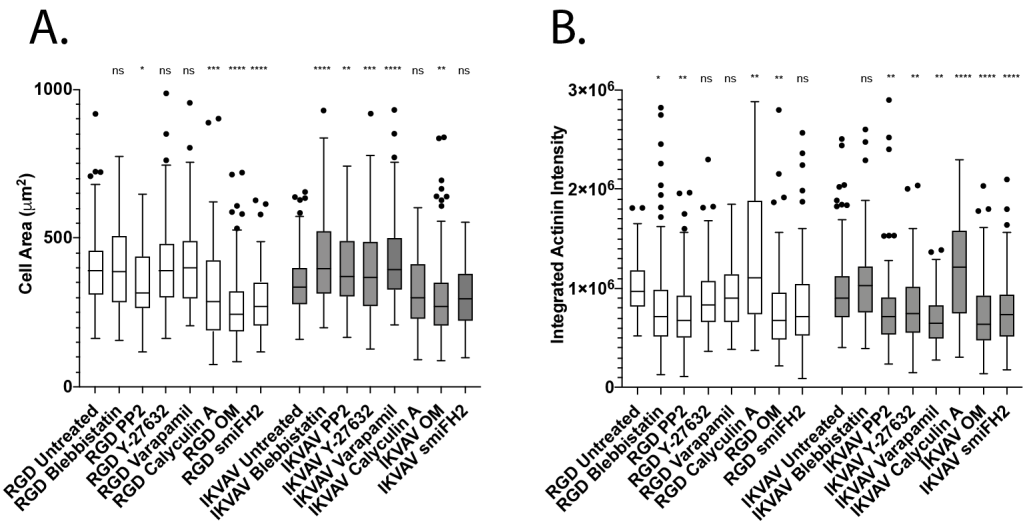

*Figure 5.5. Quantification of NRC cell area and α-actinin intensity after contractility inhibition or enhancement and formin inhibition. One-way ANOVA with Dunnets correction for multiple comparison, * = p<0.05, *=p<0.01, ***=p<0.001, ****=p<0.0001. N= 3 biological repeats.*

5.5 Discussion

This chapter has presented investigations on the nanoscale integrin clustering and cell spreading properties of α5β1 and α7β1 integrin subtypes in NRCs. The results demonstrate that fibronectin binding integrins require fewer integrin adhesions to initiate spreading than laminin binding integrins in NRCs. In comparable conditions, NRCs spreading on fibronectin mimetic peptides exhibited a more active spreading phenotype, with significantly greater cell area and cytoskeletal content after 24 hours in culture. Thus,

these findings show that fibronectin and laminin binding integrins differ in their clustering dynamics for cellular adhesion and integrin signalling. Furthermore, this investigation has also observed important effects of inter-cluster spacing or global ligand density suggesting that, unlike other cell types (Schvartzman et al., 2009, Schvartzman et al., 2011), NRCs are highly sensitive to the nanoscale organisation of their ECM.

This investigation has been the first to quantitatively compare the clustering dynamics of α5β1 and α7β1 integrins in cardiomyocytes and analyse the resulting effect on cell spreading and morphology. On RGDfC, spreading was initiated in NRCs when individual integrins where spaced ~60 nm apart but only when clusters were also spaced 200 nm apart, whereas spreading wasn't initiated on IKVAV until integrins were ~30 nm apart at 200 nm cluster spacings. On both RGDfC and IKVAV, NRCs were sensitive to the inter cluster spacing and the overall global ligand density, requiring 108 – 150 and 162 – 300 ligands per μm^2 on RGDfC and IKVAV nanopatterns, respectively. While the functional implications of these clustering differences remain unclear, these results highlight the importance of understanding the importance of ECM regulation of integrin signalling. Others have previously observed that cells utilise different integrin subtypes to enact specific behavioural phenotypes, such as migration, rigidity sensing, spreading and integrin signalling (Elosegui-Artola et al., 2014, Bharadwaj et al., 2017, Schaufler et al., 2016, Lerche et al., Preprint). The differences in integrin clustering and cell spreading between RGDfC and IKVAV binding integrins may also suggest that cardiomyocytes modulate integrin expression to regulate integrin signalling. This would be in line with the changing integrin expression observe during key developmental and pathological situations (Brancaccio et al., 1998, Nawata et al., 1999, Maitra et al., 2000, Burgess et al., 2001). Further investigation is therefore required to understand the functional impact of differential integrin expression in cardiomyocytes. The rapidly developing molecular clutch model may offer some useful insights to understand the functional importance of the results observed in the current investigation.

An important consideration from the literature is the complementary role of integrin subtypes that bind to the same ECM ligand. As demonstrated by Schaufler et al. (2016) and Bharadwaj et al. (2017), α5β1 and αvβ3 integrin subtypes exhibit functionally distinct roles at the focal adhesion, even though they both bind to the RGD motif of fibronectin. The current investigation has demonstrated that under various micro and nanopatterning configurations, RGD binding integrins appear to stimulate a stronger spreading phenotype than IKVAV binding subtypes. However, it is likely that different

RGD and IKVAV binding subtypes are present in neonatal rat cardiomyocytes, as demonstrated by micro RNA data in chapter 1. Indeed, various papers have also demonstrated a highly diverse integrin expression profile in cardiomyocytes during development and disease (Brancaccio et al., 1998, Maitra et al., 2000, Burgess et al., 2001, Willey, 2003) Therefore, future work should attempt to characterise the contribution of different integrin subtypes to adhesion, spreading and mechanotransduction in cardiomyocytes. This could be achieved via siRNA mediated knock down of integrin subtypes or through the use of integrin specific antibodies to block subtype activity during spreading. Combining this approach with the nanopatterning platform presented here would provide key information subtype specific nano-clustering and help elucidate their roles in specific cardiomyocyte behaviours, such as the hypertrophic response. Furthermore, as discussed previously, the regulation of integrin subtype activity may be dependent upon substrate rigidity (Lerche et al., Preprint, Elosegui-Artola et al., 2014, Oria et al., 2017). Therefore, future work could combine integrin subtype knockdown/blocking techniques with ligand nanopatterning on different substrate rigidities to investigate integrin subtype behaviours at functionally relevant stiffnesses.

Recent work has provided strong evidence that a molecular clutch mechanism determines the 60 nm requirement for adequate integrin clustering (Oria et al., 2017). An optimum integrin cluster density is required to withstand traction forces and engage mechanically sensitive integrin adaptor proteins during rigidity sensing; insufficient or excessive clustering results in over- or under-loading of the adhesion, respectively. Results from the nanopatterning of RGDfC and IKVAV, in addition to the work of others (Schaufler et al., 2016, Lerche et al., Preprint), suggests that different integrin subtypes have unique clustering requirements to engage the molecular clutch and initiate spreading. One possible explanation for this could be that different integrin subtypes have different bond dynamics under force. The molecular clutch model demonstrates that rigidity sensing occurs via the application of forces through integrins and their adaptor proteins and thus, stability of the integrin-ECM bond is central for efficient mechanotransduction (Elosegui-Artola et al., 2016). Integrin bond stability is highly dependent upon substrate rigidity and recent insights have identified that different subtypes are most stable at specific substrate rigidities, with collagen binding integrins ($\alpha 11\beta 1$) being most stable on soft rigidities and fibronectin binding subtypes ($\alpha 5\beta 1$ and $\alpha v\beta 6$) being most stable at higher rigidities (Elosegui-Artola et al., 2014, Oria et al., 2017, Lerche et al., Preprint). Therefore, the requirement for increased integrin clustering in NRCs cultured on IKVAV nanopatterns

suggests that α7β1 integrins are less stable under force on highly rigid glass substrates. Because integrin clustering is dependent upon substrate rigidity, it is of great interest to further development this DNA origami nanopatterning platform to substrates with tuneable stiffness to evaluate integrin clustering within more physiological contexts.

A central component of the molecular clutch model is the application of force upon integrin adhesions to engage mechanosensitive proteins involved in rigidity sensing. Actin flow and the contractile action of myosin machinery act as the primary force producers within the model. Within cardiomyocytes, rigidity sensing occurs through a unique combination of myofibrillar and non-myofibrillar contractility, with actin flow taking a less important role (Pandey et al., 2018). Inhibition of cytoskeletal contractility resulted in different effects on NRC spreading depending on whether cells were cultured on RGDfC or IKVAV peptides. NRCs spreading on RGDfC demonstrated a significant decrease in cell area and α-actinin content under Src inhibition which is consistent with previous work (Pandey et al., 2018). Furthermore, this result is also consistent with observation of Src clustering at the cell edge upon the initiation of spreading on nanopatterned RGDfC, providing further evidence of an important role for Src in fibronectin mediated spreading. However, other contractility inhibitors (blebbistatin, Y-27632 & Verapamil) did not result in significant changes in cell area or α-actinin content (with the exception of blebbistatin) on RGDfC. However, NRCs spreading on IKVAV demonstrated a general increase in cell area under all treatments for contractility inhibition. These results suggest that adhesion stability and spreading is enhanced under lower force conditions on IKVAV but not on RGDfC. On the other hand, NRCs on RGDfC and IKVAV exhibited a general decrease in cell area and disruption to α-actinin content upon stimulation of cytoskeletal contractility, suggesting that adhesion stability can be equally compromised under higher force conditions.

The nanopatterning platform presented here represents a quantitative way to compare the clustering activity of different integrin subtypes. However, this oversimplified model of the ECM ignores any cooperative effect of different integrin subtypes (Miao et al., 2002, Schiller et al., 2013, Bharadwaj et al., 2017) or that of other receptors such as the dystroglycan complex which has recently been demonstrated to possess mechanosignalling properties (Allikian et al., 2004, Morikawa et al., 2017). Furthermore, full length fibronectin contains a synergistic domain that greatly enhances integrin binding and adhesion (Benito-Jardon et al., 2017) and may play an important role in integrin signalling. An example of the effect of the simplified ECM is demonstrated by

the small cell size observed after 24 hours spreading. At 300 – 500 μm^2, these cells spread about half as much as they do on full length fibronectin and laminin. Another potential reason for this could, in part, be due to the RGDfC and IKVAV peptides chosen. The affinity of integrins for peptide ligands can be highly affected by confirmation (cyclic or linear) and sequence (RGD vs GRGDS), especially in the case of $\alpha5\beta1$ subtypes (Kapp et al., 2017). Furthermore, IKVAV peptides are found on laminin $\alpha1$ chains which primarily recruit $\alpha7X2\beta1$ integrins and within this study, the roles of other $\alpha7X\beta1$ and $\alpha3\beta1$ integrins, which bind laminin $\alpha5$chains, remains unclear. Future investigations should test the effect of different RGD and laminin peptides to further understand and validate the current results. Furthermore, the ability of DNA origami to present different peptides on the same structures also provides the opportunity to investigate the complementary role of different integrin subtypes in NRC spreading and adhesion.

The use of peptides for culturing cardiomyocytes and the investigation of their integrin signalling properties has remained limited to date. Numerous studies have reported that peptides such as RGD and YIGSR severely disrupt cell spreading, integrin signalling and cytoskeletal maturation (Boateng et al., 2005, LaNasa and Bryant, 2009). Our results also demonstrated that NRCs have reduced spreading and sarcomeric assembly when cultured on RGDfC and IKVAV nanopatterns. However, culturing of NRCs on disorganised random DNA origami arrays clearly demonstrated that, under currently unknown conditions, cells are able to assemble mature sarcomeric like structures. These findings, again, demonstrate the sensitivity of NRCs to the properties of the ECM and also suggest an important relationship between integrin clustering and cytoskeletal/sarcomeric assembly, as hypothesised by others (Sparrow and Schöck, 2009).

An unexpected result from this investigation was the inability of NRCs to spread on the 18 RGDfC nanopattern arrays. This result was observed in 4 independent repeats and was always carried out in parallel with 18 RGDfC random DNA origami arrays, which invariably enabled spreading. To the best of our knowledge, nobody has investigated the effect of integrin cluster spacing at 20 nm intervals and so, it is difficult to make comparisons within the literature. Previous work has investigated 36 nm ligand spacing in $\alpha5\beta1$ subtypes (Schaufler et al., 2016) and 30 nm spacing in $\alpha v\beta3$ subtypes (Oria et al., 2017), which facilitated greater spreading than 60 nm arrays, as seen in the present study. However, these investigations immobilise individual ligands across entire surfaces and achieve a higher ligand density of ~400 ligands per μm^2 at 60 nm spacing, compared

to 150 ligands per μm^2 on the 6 peptide, 200 nm configuration used here, making comparison difficult. Furthermore, in contrast to what others have reported in adherent cells expressing $\alpha v\beta 3$ integrins (Schvartzman et al., 2009), DNA origami nanopatterning has demonstrated that on both RGDfC and IKVAV, the spacing between clusters is very important for NRC spreading. These results again demonstrate that findings from different cell and integrin subtypes are not universally applicable and more work is required in NRCs to understand the observations made here. On a final note, it is possible that on 18 RGDfC arrays, NRC exceed their maximum ligand density on such stiff substrates. Previous work with smooth muscle cells on collagen substrates demonstrates a decline in cell area with excessive substrate stiffness and ligand density (Engler et al., 2004), providing a possible explanation for the resulted presented here.

In summary, this chapter has presented the first investigation to quantitatively evaluate and compare the integrin clustering dynamics of $\alpha 5\beta 1$ and $\alpha 7\beta 1$ integrin subtypes in NRCs. We observed that on RGDfC ligands, fewer ligands were required to initiate spreading compared to IKVAV and in all conditions, cells on RGDfC had greater cell area, more cytoskeletal enrichment and were less circular in morphology. This suggests that RGDfC and IKVAV integrin receptors differ dramatically in their clustering requirements to initiate spreading and rigidity sensing. Furthermore, manipulation of cytoskeletal contractility revealed an essential role of Src in NRC spreading on RGDfC ligands (in agreement with previous work (Pandey et al., 2018)) and also suggested that RGDfC adhesions are more mechanically stable that IKVAV adhesions. In other cell types, differential clustering of integrin subtypes has been found to reflect functional differences in their roles during spreading and adhesion (Elosegui-Artola et al., 2014, Schaufler et al., 2016, Lerche et al., Preprint). Therefore, future work should aim to investigate the differential cardiomyocyte integrin signalling dynamics occurring downstream of $\alpha 5\beta 1$ and $\alpha 7\beta 1$ integrin adhesion. Furthermore, understanding how $\alpha 5\beta 1$ and $\alpha 7\beta 1$ integrin-ECM bond kinetics differ will likely elucidate the underlying differences in clustering observed here.

6 DISCUSSION, CONCLUSIONS & FUTURE DIRECTIONS

During development and disease, cardiomyocyte integrin expression favours fibronectin binding subtypes, while laminin binding integrins are the dominant subtypes in healthy adult cardiomyocytes (Brancaccio et al., 1998, Maitra et al., 2000). Previous work has clearly demonstrated that different integrin subtypes have unique rigidity sensing properties, but the consequences of dynamic integrin expression in cardiomyocytes is not well understood (Kong et al., 2009, Chen et al., 2017, Elosegui-Artola et al., 2014, Bharadwaj et al., 2017, Schaufler et al., 2016, Ward and Iskratsch, 2019). The current investigation has taken a highly interdisciplinary approach to conduct a comparative analysis of cardiomyocyte spreading and integrin clustering on fibronectin and laminin functionalised substrates. Early results demonstrated that cardiomyocytes cultured on fibronectin exhibit stronger spreading, contractility and vinculin enrichment compared to cells cultured on laminin. It was hypothesised that these differences could arise due to differential integrin clustering. Particular focus has been given to the development and implementation of a single molecule ligand nanopatterning platform to perform a quantitative analysis of integrin clustering on fibronectin and laminin receptors. The results suggest that cardiomyocytes spreading on $\alpha 7\beta 1$ integrins require more concentrated integrin clusters to initiate spreading compared to $\alpha 5\beta 1$ integrins. Follow up investigations suggested that these differences could be driven by the ability of either subtype to respond to cytoskeletal contractility. Together these results suggest that the switch in cardiomyocyte integrin expression has important implications for integrin signalling and mechanotransduction. Furthermore, this work clearly identifies a need for further investigation into subtype specific integrin signalling in cardiomyocytes.

6.1 The Cardiac ECM – The Functional Role of Cues from The Basement Membrane

The cardiac ECM contains a diverse mixture of matrix proteins and sugars which can be classified into glycoproteins, glycosaminoglycans and proteoglycans (Rienks et al., 2014). The glycoproteins collagen, fibronectin and laminin are core elements of the basement membrane (the inner most layer) within the cardiac ECM, that provide structural rigidity and cell-receptor binding domains for the adhesion receptors, integrins. As a result, cardiomyocytes express a range of integrin subtypes, with specific affinity for collagen, fibronectin and laminin. Cardiomyocyte integrin expression is highly regulated, and specific expression profiles are activated during developmental, neonatal, healthy adult and diseased states (Belkin et al., 1997, Brancaccio et al., 1998, Nawata et al., 1999, Maitra et al., 2000, Burgess et al., 2001). Specifically, the fibronectin binding $\alpha5\beta1$ integrins are the predominant subtype during developmental and diseased states (Brancaccio et al., 1998, Nawata et al., 1999). The laminin binding $\alpha7\beta1$ integrin subtype becomes the primary receptor after downregulation of $\alpha5\beta1$ receptors in neonates, which remains steady into adulthood (Brancaccio et al., 1998, Maitra et al., 2000). Importantly, the expression of integrin subtypes closely matches the presence of glycoproteins within the ECM. For example, $\alpha5\beta1$ expression is strongly upregulated after MI, as cardiac fibroblasts rapidly deposit fibronectin around the infarcted area, in a process called fibrosis (Burgess et al., 2001, Valiente-Alandi et al., 2018). Furthermore, $\alpha7\beta1$ expression also matches the increased deposition of laminin during neonatal development (Burgess et al., 2001, Yang et al., 2015). Thus, cardiomyocytes actively utilise integrins to detect dynamic cues from the ECM.

Changes in integrin expression are strongly related to specific behaviours observed in cardiomyocytes. This has been demonstrated most convincingly in models of hypertrophy, where $\alpha5\beta1$ integrins are upregulated to detect both chemical and mechanical signals to activate compensatory hypertrophic signalling pathways such as ERK, AKT1, JNK or NFκB (Ogawa et al., 2000, Balasubramanian and Kuppuswamy, 2003, Israeli-Rosenberg et al., 2014, Pandey et al., 2018). In contrast, the neonatal increase in $\alpha7\beta1$ integrin expression also coincides with an important developmental period where cardiomyocytes lose their ability to proliferate and continued heart growth must occur via hypertrophy. However, the role $\alpha7\beta1$ integrin signalling in post-natal development is not well understood, even though laminin ligands have been reported to stimulate hypertrophic markers to a similar extent (Ogawa et al., 2000). Importantly, the

physiological hypertrophy observed in neonatal development differs dramatically to pathological hypertrophy, which results in excessive heart wall thickness and a decrease in chamber volume (Nakamura and Sadoshima, 2018). Therefore, α7β1 and α5β1 integrins may engage differential signalling regimes that contribute toward physiological and pathological hypertrophy. Thus, the lack of knowledge on the independent roles of fibronectin and laminin integrins in cardiomyocyte mechanotransduction represents a significant gap in the literature that warrants further investigation.

Chapter 3 of this thesis presented preliminary investigations into the differential behaviours of cardiomyocytes cultured on fibronectin and laminin coated substrates. The results consistently demonstrated that NRCs on fibronectin have enhanced spreading than cells cultured on laminin, at physiological and fibrotic stiffness. Cell spreading is closely regulated by the assembly of a contractile cytoskeleton, which associates with integrin adhesions to apply traction forces onto the ECM (Schwarz and Gardel, 2012, Iskratsch et al., 2014). Therefore, nanopillar arrays were employed to analyse the tractions forces in NRCs cultured on fibronectin or laminin. The results demonstrated that NRCs cultured on fibronectin exhibit greater traction forces than cells cultured on nanopillars coated with laminin. Propagation of traction forces through adhesions acts to stabilise mechanosensitive proteins such as talin, which reveal cryptic binding sites for proteins such as vinculin to reinforce actin association with the adhesion(del Rio et al., 2009). Micropatterning arrays revealed greater vinculin enrichment to fibronectin adhesions, suggesting altered rigidity sensing and mechanotransduction. Importantly, differences in cell spreading and vinculin enrichment to fibronectin adhesions were more pronounced at fibrotic stiffnesses (130 kPa), with laminin adhesions playing a more significant role at physiological stiffness (20 kPa). However, at both stiffnesses, fibronectin adhesions remained dominant with greater spreading and vinculin enrichment. These results suggest that fibronectin and laminin adhesions possess unique integrin signalling and mechanotransduction properties at fibronectin and laminin adhesions. Indeed, fibronectin adhesions have been suggested to play an enhanced role in hypertrophic signalling (Balasubramanian and Kuppuswamy, 2003, Johnston et al., 2009), but the differential role of fibronectin and laminin integrins remains poorly understood.

While the functional implications of differential integrin expression in cardiomyocytes are poorly understood, we can look towards work in other cell types that modulate integrin expression for functional purposes. Fibroblasts and other migratory cell types (e.g. U2OS) express α5β1 and αvβ3 integrin subtypes, which both bind to fibronectin. Recent

developments have established that these two subtypes possess functionally distinct roles. Owing to greater adhesion force and turnover, αvβ3 outcompete α5β1 subtypes for available adaptor proteins and initially activate rigidity sensing via RhoA/ROCK and Arp2/3 pathways. The initiation of rigidity sensing and traction forces then signals the clustering of α5β1 subtypes to further strengthen the adhesion (Bharadwaj et al., 2017, Schaufler et al., 2016). In line with their role as mechanosensors, other cell types have also been shown to exploit the enhanced adhesion kinetics of different integrin subtypes, which possess unique properties at different substrate rigidities (e.g. α5β1 vs αvβ6, (Elosegui-Artola et al., 2014)). For example, mammary gland fibroblasts assemble larger, more stable adhesions via the collagen binding α11β1 integrin subtype at low substrate rigidity (2 kPa) while fibronectin integrins become dominant at higher rigidities (Lerche et al., Preprint). Furthermore, in breast myoepithelial cells, α5β1 integrins are able to generate greater traction forces at lower tissue stiffnesses (1-10 kPa) whereas αvβ6 integrins are more suitable at higher rigidities (Elosegui-Artola et al., 2014). Within these experiments, cells were utilising differential integrin expression to perform specific behaviours (e.g. migration, adhesion formation) at specific substrate rigidities (Elosegui-Artola et al., 2018). This is hypothesised to be due to unique integrin-ECM bond dynamics (e.g. binding/unbinding rates & catch/slip bond behaviour) which are highly sensitive to force, contractility and substrate rigidity (Elosegui-Artola et al., 2018). Therefore, cardiomyocyte integrin expression may also reflect a similar requirement, as cardiac tissue stiffness changes during development and disease. The upregulation of fibronectin binding integrin subtypes may specifically promote enhanced integrin signalling through greater cytoskeletal contractility which may, in turn, favour hypertrophy during development or pathology. However, it is unclear whether the differences between fibronectin and laminin occur according to substrate rigidity. At 6 kPa (embryonic/neonatal stiffness), we observe similar spreading and α-actinin content on fibronectin and laminin adhesions but at 10 kPa, traction forces are greater in cells cultured on fibronectin. Further investigation is required to understand whether differences in rigidity sensing determine the functional role of dynamic integrin expression in cardiomyocyte or whether changes occur as a result of other factors, such as adhesome/costamere composition or integrin bond dynamics.

6.2 The Nanoscale Cytoarchitecture of Fibronectin and Laminin Adhesions in Cardiomyocytes.

A recent study has demonstrated that key differences in the functional roles in different integrin subtypes could be underpinned by their clustering properties (Schaufler et al., 2016). Work in migratory cell lines has demonstrated that on stiff (1 GPa) substrates, individual α5β1 integrin-ligand adhesions are required to be spaced < 60 nm apart to initiate stable adhesion formation (Schaufler et al., 2016, Oria et al., 2017), which is the same recorded in αvβ3 expressing cells (Arnold et al., 2004, Cavalcanti-Adam et al., 2007, Huang et al., 2009). This 60 nm clustering threshold appears to be consistent in cell types that specialise in migratory phenotypes which require strong adhesion kinetics, such as myoepithelial cells, platelets, carcinoma cells and fibroblasts (Oria et al., 2017, Huang et al., 2019, Zarka et al., 2019b). However, under comparable clustering conditions, cells cultured on α5β1 adhesions spread far more rapidly and to a greater extent than cells cultured on αvβ3 adhesions(Schaufler et al., 2016). Currently, little is known about the clustering behaviours of fibronectin and laminin integrin subtypes in cardiomyocytes. This investigation has focussed on the role of α5β1 and α7β1 subtypes which have a high affinity for fibronectin and laminin, respectively (Nishiuchi et al., 2006, Kapp et al., 2017). The current investigation has also observed the same 60 nm threshold for α5β1 subtypes within cardiomyocytes. However, unlike observations in fibroblasts on αvβ3 integrin subtypes in the current investigation (Chapter 5.3) and in previous work by others (Schvartzman et al., 2011), cardiomyocytes spreading on α5β1 subtypes were unable to spread on 60 nm configurations when individual clusters were spaced at 300 nm intervals. This result suggests that observations in others cell types on different integrin subtypes are not universally applicable. Furthermore, this finding provides further evidence that integrin subtypes do not play redundant roles in integrin signalling, consistent with previous work (Schaufler et al., 2016, Bharadwaj et al., 2017).

Another novel observation from this study is that the laminin binding α7β1 integrins require much closer clustering of ~30 nm to initiate spreading (12 peptides per cluster) than fibronectin binding α5β1 integrins (6 peptides per cluster). This is the first investigation to analyse the clustering dynamics of α7β1 in cardiomyocytes and previous work on developing the molecular clutch model can help to explain the differences in integrin clustering observed between α7β1 and α5β1 subtypes. The model predicts that integrin clustering directly modulates the forces experienced by components of the FA; a

greater number of actively engaged integrins enables distribution of traction forces among more proteins, resulting in less force being sensed by individual integrins and adaptors (Elosegui-Artola et al., 2018). Integrin clustering is an active part of maintaining protein turnover by modulating molecular tension to extend (in the case of catch bonds) or reduce (in the case of slip bonds) bond lifetime. Therefore, the increased clustering requirement for α7β1 ligands suggest that more adhesions are required for stable adhesion formation. Pharmacological inhibition of cytoskeletal contractility resulted in an increase in NRC spreading on α7β1 integrins, further suggesting that α7β1 integrin adhesions may be less stable under high forces. This would also agree with observations of decreased cytoskeletal content, traction forces and spreading in cells cultured on laminin in Chapter 3. Together, these results suggest that fibronectin adhesions mediate stronger spreading, contractility and integrin adaptor enrichment phenotypes via and enhanced stability of individual adhesions. Furthermore, this finding suggests that a transition in integrin expression to favour fibronectin binding subtypes may also favour the activation of integrin signalling and mechanotransduction pathways, as is observed during hypertrophy (Balasubramanian and Kuppuswamy, 2003, Johnston et al., 2009, Valiente-Alandi et al., 2018).

6.3 Potential Physiological Relevance of the Results Presented this Thesis

This investigation has consistently observed enhanced cardiomyocyte spreading, traction forces and adhesion enrichment when spreading over fibronectin or RGD. These behaviours were particularly prominent at higher substrate stiffness. Fibronectin binding integrins have been shown to play a key role in key behaviours observed in the failing heart, especially in cases of cardiac fibrosis or hypertension where physiological changes are observed in the myocardium (Nawata et al., 1999, Ogawa et al., 2000, Balasubramanian and Kuppuswamy, 2003, Johnston et al., 2009). Fibronectin integrins exhibit a sharp increase in expression after cardiac injury and beta 3 integrins (which bind strongly to fibronectin) have been found to have a key role in hypertrophic signalling (Ogawa et al., 2000). Indeed, recent work from the Iskratsch lab has begun to elucidate some of the molecular pathways involved in mediating such as responses and has identified Src as a key player in the mechanosensitive hypertrophic response (Pandey et al., 2018). The current investigation has presented preliminary results that suggest Src localisation to nanopatterned adhesions is greater on RGD than IKVAV. Future work

could investigate Src localisation and enrichment at fibronectin and laminin adhesion to evaluate if this hypothesis holds any water.

Another phenomenon particularly relevant to the results in this thesis is the downregulation of fibronectin binding integrin subtypes during post-natal development and the consequent upregulation of laminin binding subtypes (Brancaccio et al., 1998, Maitra et al., 2000, Burgess et al., 2001). Little is known about the signalling consequences of this behaviour. The results in this thesis suggest that this switch in integrin expression may result in a less mechanosensitive costamere. It could be hypothesised that this may help stimulate a transition to signalling from the ICD, but evidence of this does not currently exist. Another intriguing hypothesis could be that the switch to laminin binding subtypes may result in a different hypertrophic response. Fibronectin binding integrins are well documented to play key roles in pathological hypertrophy. However, there is a clear distinction between pathological and physiological hypertrophy, which result in different morphological and signalling phenotypes (Nakamura and Sadoshima, 2018). Indeed, many of the classic markers of cardiomyocyte hypertrophy, which are commonly investigated in-vitro on fibronectin coated substrates, such as JNK and p38 are considered parts of the pathological hypertrophy pathway (Nakamura and Sadoshima, 2018). On the other hand, to observe this at the level of integrins is too narrow when considering different types of hypertrophy. The DNA origami platform presented in this thesis offers a unique opportunity to investigate the role of integrin signalling alongside other important signalling receptors such as angiotensin and natriuretic peptides receptors. This could be achieved by functionalising DNA nanostructures with integrin, angiotensin and/or natriuretic peptide ligands which could subsequently be combined with nanopatterning or magnetic tweezers to investigate the corresponding signalling pathways in the presence of hypertrophic stimuli.

6.4 Summary and Conclusions

This investigation has adopted a highly interdisciplinary approach to investigate the integrin signalling behaviours of cardiomyocytes cultured on fibronectin and laminin ligands. The results have consistently demonstrated that at the level of the single cell, down to the level of integrin-ligand clusters, cardiomyocytes behave differently depending on the predominant integrin subtype. These findings are in line with work reporting differential signalling behaviours of integrin subtypes (Elosegui-Artola et al.,

2014, Schaufler et al., 2016, Bharadwaj et al., 2017, Lerche et al., Preprint). Cardiomyocyte integrin adhesions to RGDfC peptides required fewer integrins per cluster for stable adhesion which, according to the molecular clutch model (Elosegui-Artola et al., 2018), suggests that adaptor proteins may be under greater stress resulting in the activation of signalling pathways. This observation appears to be consistent with results from Chapter 3 where cardiomyocytes spreading on full length fibronectin which demonstrated greater spreading and contractility, compared to laminin. Furthermore, cardiomyocytes exhibited preferential alignment and stronger vinculin enrichment to fibronectin adhesions. Together these results suggest that differential integrin signalling regimes may be activated through fibronectin and laminin adhesions and that changes in integrin expression has important implications for cardiomyocyte behaviour.

The finding that fibronectin adhesions facilitate greater contractility and spreading via greater adhesion stability under force is a surprising one. From embryonic and neonatal development through to adulthood, laminin integrins become the dominant subtype as the myocardium stiffens from 1 – 10 kPa to 10 – 20 kPa, respectively (Ward and Iskratsch, 2019). It is not currently clear why cardiomyocytes would preferentially change integrin expression to favour subtypes which are less mechanically stable under force. It could be that cardiomyocytes utilise a range of fibronectin ($\alpha5\beta1$, $\alpha v\beta3$ and $\alpha8\beta1$) or laminin ($\alpha7\beta1$, $\alpha3\beta1$ and $\alpha6\beta1$) binding integrin subtypes, all of which may have unique characteristics that contribute towards costameric integrin signalling. On the other hand, transition of the predominant integrin to a subtype with less mechanical stability may facilitate the redirection of forces from cell-ECM to cell-cell contacts. Thus, further investigation is required to understand the cross-talk between integrin subtypes, which has been demonstrated to play a key role in cell spreading and integrin signalling (Rahmouni et al., 2013, Schaufler et al., 2016, Bharadwaj et al., 2017), and to understand their specific role in cardiomyocyte development or disease. Furthermore, other components of the costamere such as the desmin cytoskeleton and DGC may also contribute towards mechanosignaling (Morikawa et al., 2017, Ward and Iskratsch, 2019). As discussed in the future directions section, the DNA origami platform presented in this thesis provides a powerful platform to investigate the roles of different components of the costamere and cell membrane receptors, including different integrin subtypes. Therefore, the work presented in this thesis offers several opportunities to provide further clarity on the results presented.

This investigation has conducted a comparative analysis of cardiomyocyte adhesion, spreading and integrin clustering on fibronectin and laminin receptors. The results have demonstrated that NRCs cultured on fibronectin exhibit behaviours that suggest a stronger spreading and contractile phenotype, when compared to cells cultured on laminin. These differences are likely to occur due to the underlying differences in the integrin adhesion properties of $\alpha7\beta1$ and $\alpha5\beta1$ integrin subtypes, as evidenced by differences in integrin clustering and differential responses to cytoskeletal contractility. Thus, these results provide novel insights into the molecular underpinnings of cardiomyocyte integrin signalling and further our understanding of their roles in development and disease.

This thesis has also presented the optimisation and implementation of a DNA origami nanopatterning platform for the investigations of integrin adhesion and clustering behaviours in cardiomyocytes. This platform offers a highly versatile setup for the investigation of numerous additional properties of cardiomyocyte integrin signalling such as ECM composition, geometry and stoichiometry. Therefore, this platform provides many opportunities for future investigations to further understand the integrin signalling regimes of fibronectin and laminin binding integrin subtypes.

6.5 Future Directions

Recent work from the Iskratsch lab had reported that NRCs sense the rigidity of their environment through a combination of muscle and non-muscle myosin contractions. The non-receptor tyrosine kinase Src was found to play a key role in coordinating non-myofibrillar rigidity sensing through recruitment and activation of FHOD1 and non-muscle myosin. Results from nanopillars and ligand micropatterning suggest that fibronectin and laminin receptors respond differently at physiological and fibrotic stiffnesses. This may suggest the activation of a different signalling regime and that results from previous work using fibronectin substrates may not be applicable to laminin substrates. Therefore, future work could aim to evaluate whether the observed differences occur through a different pathways or due to lower Src activity.

This investigation has also presented the development of a platform to quantitatively evaluate the integrin clustering behaviours of different integrin subtypes and adhesion receptors. This platform offers the ability to evaluate the downstream signalling consequences of different integrin/ligand cluster interactions. As a result, the work carried

out here could be extended to other techniques to provide further data on the differential integrin signalling activity of fibronectin and laminin subtypes.

The observation that laminin adhesions require more ligands per cluster for stable adhesion and spreading, may suggest that they are less stable under force (Elosegui-Artola et al., 2014, Oria et al., 2017). This would be a surprising result as cardiomyocytes preferentially express laminin integrin subtypes in the adult heart, where they are required to resist higher forces, compared to developmental and neonatal stages. To further understand fibronectin vs laminin adhesion stability, magnetic tweezers could be employed to evaluate the bond strength of integrin subtypes under various force regimes. Importantly, the DNA origami platform could be extended to magnetic bead studies, by covalent attachment of peptide functionalised DNA origami to the beads themselves. This would enable the evaluation of integrin bond characteristics relative to integrin cluster size (6 – 18 peptides) and force loading regime, which dictates bond association dissociation rates (Elosegui-Artola et al., 2018). Uncovering the adhesion kinetics of fibronectin and laminin integrins in cardiomyocytes would help to provide stronger evidence of functionally distinct roles of either subtype. Furthermore, this data would also compliment the work presented in this thesis.

To further understand how fibronectin and laminin integrins alter rigidity sensing, the nanopatterned DNA origami arrays could be utilised to evaluate protein turnover (using fluorescence recovery after photobleaching) and molecular tension across mechanosensitive proteins such as talin (using FRET tension sensors). This would provide further clarity of the relationship between integrin clustering for adhesion reinforcement and the corresponding activity of key mechanotransduction proteins such as talin in response to the differential clustering regimes. This data would also compliment previous work which has demonstrated that integrin clustering enables force transmission through adhesions (Liu et al., 2014), and may provide further clarification on the integrin clustering results obtained here.

Another promising line of investigation with the DNA origami platform, is the opportunity for multivalent investigations. Recent work from the Palma lab (Huang et al., 2019) has demonstrated the power of DNA origami for the nanopatterning of more than one ligand of interest, to look at the cooperative effect of different receptors. In-vivo, cardiomyocytes express a combination of integrin receptors, which likely cooperate for various functions. Multivalent investigations offer the ability to quantitatively analyse the cooperative effects of fibronectin and laminin adhesions within the same clusters. Indeed,

previous work has demonstrated functionally distinct roles of different integrin subtypes within the same adhesions (Schaufler et al., 2016, Bharadwaj et al., 2017). Multivalent investigations also open up the possibilities to investigate the effect of integrin cluster composition on the turnover and lifetime of various proteins to evaluate how integrin expression can be modulated to fine tune the composition and corresponding mechanosignalling at the costamere. Thus, the DNA origami platform developed here provides a highly dynamic and effective platform to understand the role of different integrin subtypes in costameric signalling.

A recent study has demonstrated that the requirement for integrin clustering in FAs is dependent upon substrate stiffness (Oria et al., 2017). The results show that at physiological stiffnesses of 20 – 30 kPa, integrin clusters are required to be dramatically less dense (100-200 nm integrin spacing) than at fibrotic stiffnesses (30-60 nm integrin spacing). Therefore, the 30-60 nm clustering requirements observed are likely to overestimate the integrin clustering dynamics at physiologically relevant stiffnesses. Future investigations should aim to combine the nanopatterning capabilities of DNA DNA origami with PDMS or acrylamide substrates, to evaluate how integrin clustering dynamics change with substrate rigidity. This would further help to uncover the functional roles of fibronectin and laminin binding integrins in embryonic, healthy and diseased states.

7 REFERENCES

AL HAJ, A., MAZUR, A. J., RADASZKIEWICZ, K., RADASZKIEWICZ, T., MAKOWIECKA, A., STOPSCHINSKI, B. E., SCHONICHEN, A., GEYER, M. & MANNHERZ, H. G. 2015. Distribution of formins in cardiac muscle: FHOD1 is a component of intercalated discs and costameres. *Eur J Cell Biol,* 94**,** 101-13.

ALLIKIAN, M. J., HACK, A. A., MEWBORN, S., MAYER, U. & MCNALLY, E. M. 2004. Genetic compensation for sarcoglycan loss by integrin alpha7beta1 in muscle. *J Cell Sci,* 117**,** 3821-30.

ANTHIS, N. J., WEGENER, K. L., CRITCHLEY, D. R. & CAMPBELL, I. D. 2010. Structural diversity in integrin/talin interactions. *Structure,* 18**,** 1654-66.

ARNOLD, M., CAVALCANTI-ADAM, E. A., GLASS, R., BLÜMMEL, J., ECK, W., KANTLEHNER, M., KESSLER, H. & SPATZ, J. P. 2004. Activation of Integrin Function by Nanopatterned Adhesive Interfaces. *ChemPhysChem,* 5**,** 383-388.

ARNOLD, M., SCHWIEDER, M., BLUMMEL, J., CAVALCANTI-ADAM, E. A., LOPEZ-GARCIA, M., KESSLER, H., GEIGER, B. & SPATZ, J. P. 2009. Cell interactions with hierarchically structured nano-patterned adhesive surfaces. *Soft Matter,* 5**,** 72-77.

ATHERTON, P., LAUSECKER, F., CARISEY, A., GILMORE, A., CRITCHLEY, D., BARSUKOV, I. & BALLESTREM, C. Preprint. Force-independent interactions of talin and vinculin govern integrin-mediated mechanotransduction. *bioRxiv***,** 629683.

AUSTEN, K., RINGER, P., MEHLICH, A., CHROSTEK-GRASHOFF, A., KLUGER, C., KLINGNER, C., SABASS, B., ZENT, R., RIEF, M. & GRASHOFF, C. 2015. Extracellular rigidity sensing by talin isoform-specific mechanical linkages. *Nat Cell Biol,* 17**,** 1597-606.

BABBITT, C. J., SHAI, S. Y., HARPF, A. E., PHAM, C. G. & ROSS, R. S. 2002. Modulation of integrins and integrin signaling molecules in the pressure-loaded murine ventricle. *Histochem Cell Biol,* 118**,** 431-9.

BACHMANN, M., KUKKURAINEN, S., HYTONEN, V. P. & WEHRLE-HALLER, B. 2019. Cell Adhesion by Integrins. *Physiol Rev,* 99**,** 1655-1699.

BALASUBRAMANIAN, S. & KUPPUSWAMY, D. 2003. RGD-containing peptides activate S6K1 through beta3 integrin in adult cardiac muscle cells. *J Biol Chem,* 278**,** 42214-24.

BELKIN, A. M., ORNATSKY, O. I., KABAKOV, A. E., GLUKHOVA, M. A. & KOTELIANSKY, V. E. 1988. Diversity of vinculin/meta-vinculin in human tissues and cultivated cells. Expression of muscle specific variants of vinculin in human aorta smooth muscle cells. *J Biol Chem,* 263**,** 6631-5.

BELKIN, A. M., RETTA, S. F., PLETJUSHKINA, O. Y., BALZAC, F., SILENGO, L., FASSLER, R., KOTELIANSKY, V. E., BURRIDGE, K. & TARONE, G. 1997. Muscle beta1D integrin reinforces the cytoskeleton-matrix link: modulation of integrin adhesive function by alternative splicing. *J Cell Biol,* 139**,** 1583-95.

BENITO-JARDON, M., KLAPPROTH, S., GIMENO, L. I., PETZOLD, T., BHARADWAJ, M., MULLER, D. J., ZUCHTRIEGEL, G., REICHEL, C. A. & COSTELL, M. 2017. The fibronectin synergy site re-enforces cell adhesion and mediates a crosstalk between integrin classes. *Elife,* 6.

BHARADWAJ, M., STROHMEYER, N., COLO, G. P., HELENIUS, J., BEERENWINKEL, N., SCHILLER, H. B., FASSLER, R. & MULLER, D. J. 2017. alphaV-class integrins exert dual roles on alpha5beta1 integrins to strengthen adhesion to fibronectin. *Nat Commun,* 8**,** 14348.

BOATENG, S. Y., LATEEF, S. S., MOSLEY, W., HARTMAN, T. J., HANLEY, L. & RUSSELL, B. 2005. RGD and YIGSR synthetic peptides facilitate cellular adhesion identical to that of laminin and fibronectin but alter the physiology of neonatal cardiac myocytes. *Am J Physiol Cell Physiol,* 288**,** C30-8.

BOGATAN, S., CEVIK, D., DEMIDOV, V., VANDERPLOEG, J., PANCHBHAYA, A., VITKIN, A. & JACOBS, J. R. 2015. Talin Is Required Continuously for Cardiomyocyte Remodeling during Heart Growth in Drosophila. *PLoS One,* 10**,** e0131238.

BORG, T. K., RUBIN, K., LUNDGREN, E., BORG, K. & OBRINK, B. 1984. Recognition of extracellular matrix components by neonatal and adult cardiac myocytes. *Dev Biol,* 104**,** 86-96.

BRANCACCIO, M., CABODI, S., BELKIN, A. M., COLLO, G., TOMATIS, D., ALTRUDA, F., SILENGO, L. & TARONE, G. 1998. Differential Onset of

Expression of α7 and β1D Integrins During Mouse Heart and Skeletal Muscle Development. *Cell Adhesion and Communication,* 5**,** 193-205.

BRASSAT, K., RAMAKRISHNAN, S., BÜRGER, J., HANKE, M., DOOSTDAR, M., LINDNER, J. K. N., GRUNDMEIER, G. & KELLER, A. 2018. On the Adsorption of DNA Origami Nanostructures in Nanohole Arrays. *Langmuir,* 34**,** 14757-14765.

BURGESS, M. L., MCCREA, J. C. & HEDRICK, H. L. 2001. Age-associated changes in cardiac matrix and integrins. *Mech Ageing Dev,* 122**,** 1739-56.

BUYANDELGER, B., NG, K.-E., MIOCIC, S., GUNKEL, S., PIOTROWSKA, I., KU, C.-H. & KNÖLL, R. 2011. Genetics of mechanosensation in the heart. *Journal of cardiovascular translational research,* 4**,** 238-244.

CACHACO, A. S., CHUVA DE SOUSA LOPES, S. M., KUIKMAN, I., BAJANCA, F., ABE, K., BAUDOIN, C., SONNENBERG, A., MUMMERY, C. L. & THORSTEINSDOTTIR, S. 2003. Knock-in of integrin beta 1D affects primary but not secondary myogenesis in mice. *Development,* 130**,** 1659-71.

CALDERWOOD, D. A., FUJIOKA, Y., DE PEREDA, J. M., GARCIA-ALVAREZ, B., NAKAMOTO, T., MARGOLIS, B., MCGLADE, C. J., LIDDINGTON, R. C. & GINSBERG, M. H. 2003. Integrin beta cytoplasmic domain interactions with phosphotyrosine-binding domains: a structural prototype for diversity in integrin signaling. *Proc Natl Acad Sci U S A,* 100**,** 2272-7.

CALDERWOOD, D. A., ZENT, R., GRANT, R., REES, D. J. G., HYNES, R. O. & GINSBERG, M. H. 1999. The Talin Head Domain Binds to Integrin β Subunit Cytoplasmic Tails and Regulates Integrin Activation. *Journal of Biological Chemistry,* 274**,** 28071-28074.

CAVALCANTI-ADAM, E. A., VOLBERG, T., MICOULET, A., KESSLER, H., GEIGER, B. & SPATZ, J. P. 2007. Cell spreading and focal adhesion dynamics are regulated by spacing of integrin ligands. *Biophys J,* 92**,** 2964-74.

CHANGEDE, R., XU, X., MARGADANT, F. & SHEETZ, M. P. 2015. Nascent Integrin Adhesions Form on All Matrix Rigidities after Integrin Activation. *Dev Cell,* 35**,** 614-621.

CHEN, Y., DEFFENBAUGH, N. C., ANDERSON, C. T. & HANCOCK, W. O. 2014. Molecular counting by photobleaching in protein complexes with many subunits: best practices and application to the cellulose synthesis complex. *Molecular biology of the cell,* 25**,** 3630-3642.

CHEN, Y., LEE, H., TONG, H., SCHWARTZ, M. & ZHU, C. 2017. Force regulated conformational change of integrin alphaVbeta3. *Matrix Biol,* 60-61**,** 70-85.

CHEREAU, D., BOCZKOWSKA, M., SKWAREK-MARUSZEWSKA, A., FUJIWARA, I., HAYES, D. B., REBOWSKI, G., LAPPALAINEN, P., POLLARD, T. D. & DOMINGUEZ, R. 2008. Leiomodin is an actin filament nucleator in muscle cells. *Science,* 320**,** 239-43.

CIUBA, K., HAWKES, W., TOJKANDER, S., KOGAN, K., ENGEL, U., ISKRATSCH, T. & LAPPALAINEN, P. 2018. Calponin-3 is critical for coordinated contractility of actin stress fibers. *Sci Rep,* 8**,** 17670.

CLARK, P., CONNOLLY P FAU - MOORES, G. R. & MOORES, G. R. 1992. Cell guidance by micropatterned adhesiveness in vitro.

COX, S., ROSTEN, E., MONYPENNY, J., JOVANOVIC-TALISMAN, T., BURNETTE, D. T., LIPPINCOTT-SCHWARTZ, J., JONES, G. E. & HEINTZMANN, R. 2011. Bayesian localization microscopy reveals nanoscale podosome dynamics. *Nat Methods,* 9**,** 195-200.

CREMERS, G. A. O., ROSIER, B. J. H. M., RIERA BRILLAS, R., ALBERTAZZI, L. & DE GREEF, T. F. A. 2019. Efficient Small-Scale Conjugation of DNA to Primary Antibodies for Multiplexed Cellular Targeting. *Bioconjugate Chemistry,* 30**,** 2384-2392.

DANOWSKI, B. A., IMANAKA-YOSHIDA, K., SANGER, J. M. & SANGER, J. W. 1992. Costameres are sites of force transmission to the substratum in adult rat cardiomyocytes. *The Journal of Cell Biology,* 118**,** 1411-1420.

DEL RIO, A., PEREZ-JIMENEZ, R., LIU, R., ROCA-CUSACHS, P., FERNANDEZ, J. M. & SHEETZ, M. P. 2009. Stretching single talin rod molecules activates vinculin binding. *Science,* 323**,** 638-41.

DIMICHELE, L. A., DOHERTY, J. T., ROJAS, M., BEGGS, H. E., REICHARDT, L. F., MACK, C. P. & TAYLOR, J. M. 2006. Myocyte-Restricted Focal Adhesion Kinase Deletion Attenuates Pressure Overload–Induced Hypertrophy. *Circulation Research,* 99**,** 636-645.

DIMICHELE, L. A., HAKIM, Z. S., SAYERS, R. L., ROJAS, M., SCHWARTZ, R. J., MACK, C. P. & TAYLOR, J. M. 2009. Transient Expression of FRNK Reveals Stage-Specific Requirement for Focal Adhesion Kinase Activity in Cardiac Growth. *Circulation Research,* 104**,** 1201-1208.

DOWLING, J. J., GIBBS, E., RUSSELL, M., GOLDMAN, D., MINARCIK, J., GOLDEN, J. A. & FELDMAN, E. L. 2008. Kindlin-2 is an essential component of intercalated discs and is required for vertebrate cardiac structure and function. *Circ Res,* 102**,** 423-31.

DWYER, J., PLUESS, M., ISKRATSCH, T., DOS REMEDIOS, C. G. & EHLER, E. 2014. The formin FHOD1 in cardiomyocytes. *Anat Rec (Hoboken),* 297**,** 1560-70.

EHLER, E., FOWLER, V. M. & PERRIARD, J. C. 2004. Myofibrillogenesis in the developing chicken heart: role of actin isoforms and of the pointed end actin capping protein tropomodulin during thin filament assembly. *Dev Dyn,* 229**,** 745-55.

EHLER, E., MOORE-MORRIS, T. & LANGE, S. 2013. Isolation and Culture of Neonatal Mouse Cardiomyocytes. *JoVE***,** e50154.

EHLER, E. A.-O. H. O. O. 2018. Actin-associated proteins and cardiomyopathy-the 'unknown' beyond troponin and tropomyosin.

ELLIOTT, P. R., GOULT, B. T., KOPP, P. M., BATE, N., GROSSMANN, J. G., ROBERTS, G. C., CRITCHLEY, D. R. & BARSUKOV, I. L. 2010. The Structure of the talin head reveals a novel extended conformation of the FERM domain. *Structure,* 18**,** 1289-99.

ELOSEGUI-ARTOLA, A., BAZELLIERES, E., ALLEN, M. D., ANDREU, I., ORIA, R., SUNYER, R., GOMM, J. J., MARSHALL, J. F., JONES, J. L., TREPAT, X. & ROCA-CUSACHS, P. 2014. Rigidity sensing and adaptation through regulation of integrin types. *Nat Mater,* 13**,** 631-7.

ELOSEGUI-ARTOLA, A., TREPAT, X. & ROCA-CUSACHS, P. 2018. Control of Mechanotransduction by Molecular Clutch Dynamics. *Trends Cell Biol,* 28**,** 356-367.

ENGLER, A., BACAKOVA, L., NEWMAN, C., HATEGAN, A., GRIFFIN, M. & DISCHER, D. 2004. Substrate Compliance versus Ligand Density in Cell on Gel Responses. *Biophysical Journal,* 86**,** 617-628.

ENGLER, A. J., CARAG-KRIEGER, C., JOHNSON, C. P., RAAB, M., TANG, H. Y., SPEICHER, D. W., SANGER, J. W., SANGER, J. M. & DISCHER, D. E. 2008. Embryonic cardiomyocytes beat best on a matrix with heart-like elasticity: scar-like rigidity inhibits beating. *J Cell Sci,* 121**,** 3794-802.

ERVASTI, J. M. 2003. Costameres: the Achilles' heel of Herculean muscle. *J Biol Chem,* 278**,** 13591-4.

ESTIGOY, C. B., PONTÉN, F., ODEBERG, J., HERBERT, B., GUILHAUS, M., CHARLESTON, M., HO, J. W. K., CAMERON, D. & DOS REMEDIOS, C. G. 2009. Intercalated discs: multiple proteins perform multiple functions in non-failing and failing human hearts. *Biophysical reviews,* 1**,** 43-43.

FERREIRA-CORNWELL, M. C., LUO, Y., NARULA, N., LENOX, J. M., LIEBERMAN, M. & RADICE, G. L. 2002. Remodeling the intercalated disc leads to cardiomyopathy in mice misexpressing cadherins in the heart. *Journal of Cell Science,* 115**,** 1623.

FRAME, M. C., PATEL, H., SERRELS, B., LIETHA, D. & ECK, M. J. 2010. The FERM domain: organizing the structure and function of FAK. *Nat Rev Mol Cell Biol,* 11**,** 802-14.

FRANQUELIM, H. G., KHMELINSKAIA, A., SOBCZAK, J.-P., DIETZ, H. & SCHWILLE, P. 2018. Membrane sculpting by curved DNA origami scaffolds. *Nature Communications,* 9**,** 811.

GAHMBERG, C. G., FAGERHOLM, S. C., NURMI, S. M., CHAVAKIS, T., MARCHESAN, S. & GRONHOLM, M. 2009. Regulation of integrin activity and signalling. *Biochim Biophys Acta,* 1790**,** 431-44.

GARROD, D. R., BERIKA, M. Y., BARDSLEY, W. F., HOLMES, D. & TABERNERO, L. 2005. Hyper-adhesion in desmosomes: its regulation in wound healing and possible relationship to cadherin crystal structure. *Journal of Cell Science,* 118**,** 5743.

GHASSEMI, S., MEACCI, G., LIU, S., GONDARENKO, A. A., MATHUR, A., ROCA-CUSACHS, P., SHEETZ, M. P. & HONE, J. 2012. Cells test substrate rigidity by local contractions on submicrometer pillars. *Proc Natl Acad Sci U S A,* 109**,** 5328-33.

GLATZ, B. A. & FERY, A. 2019. The influence of plasma treatment on the elasticity of the in situ oxidized gradient layer in PDMS: towards crack-free wrinkling. *Soft Matter,* 15**,** 65-72.

GOPINATH, A., MIYAZONO, E., FARAON, A. & ROTHEMUND, P. W. K. 2016. Engineering and mapping nanocavity emission via precision placement of DNA origami. *Nature,* 535**,** 401.

GOPINATH, A. & ROTHEMUND, P. W. 2014. Optimized assembly and covalent coupling of single-molecule DNA origami nanoarrays. *ACS Nano,* 8**,** 12030-40.

GRIMES, K. M., PRASAD, V. & MCNAMARA, J. W. 2019. Supporting the heart: Functions of the cardiomyocyte's non-sarcomeric cytoskeleton. *Journal of Molecular and Cellular Cardiology,* 131**,** 187-196.

GUASCH, J., CONINGS, B., NEUBAUER, S., RECHENMACHER, F., ENDE, K., ROLLI, C. G., KAPPEL, C., SCHAUFLER, V., MICOULET, A., KESSLER, H., BOYEN, H. G., CAVALCANTI-ADAM, E. A. & SPATZ, J. P. 2015. Segregation versus colocalization: orthogonally functionalized binary micropatterned substrates regulate the molecular distribution in focal adhesions. *Adv Mater,* 27**,** 3737-47.

HANNEMANN, S., MADRID, R., STASTNA, J., KITZING, T., GASTEIER, J., SCHONICHEN, A., BOUCHET, J., JIMENEZ, A., GEYER, M., GROSSE, R., BENICHOU, S. & FACKLER, O. T. 2008. The Diaphanous-related Formin FHOD1 associates with ROCK1 and promotes Src-dependent plasma membrane blebbing. *J Biol Chem,* 283**,** 27891-903.

HAWKES, W., HUANG, D., REYNOLDS, P., HAMMOND, L., WARD, M., GADEGAARD, N., MARSHALL, J. F., ISKRATSCH, T. & PALMA, M. 2019. Probing the nanoscale organisation and multivalency of cell surface receptors: DNA origami nanoarrays for cellular studies with single-molecule control. *Faraday Discussions,* 219**,** 203-219.

HERSCH, N., WOLTERS, B., DREISSEN, G., SPRINGER, R., KIRCHGESSNER, N., MERKEL, R. & HOFFMANN, B. 2013. The constant beat: cardiomyocytes adapt their forces by equal contraction upon environmental stiffening. *Biol Open,* 2**,** 351-61.

HIRTH, S., BUHLER, A., BUHRDEL, J. B., RUDECK, S., DAHME, T., ROTTBAUER, W. & JUST, S. 2016. Paxillin and Focal Adhesion Kinase (FAK) Regulate Cardiac Contractility in the Zebrafish Heart. *PLoS One,* 11**,** e0150323.

HUANG, D., FREELEY, M. & PALMA, M. 2017. DNA-Mediated Patterning of Single Quantum Dot Nanoarrays: A Reusable Platform for Single-Molecule Control. *Sci Rep,* 7**,** 45591.

HUANG, D., PATEL, K., PEREZ-GARRIDO, S., MARSHALL, J. F. & PALMA, M. 2019. DNA Origami Nanoarrays for Multivalent Investigations of Cancer Cell

Spreading with Nanoscale Spatial Resolution and Single-Molecule Control. *ACS Nano,* 13**,** 728-736.

HUANG, J., GRATER, S. V., CORBELLINI, F., RINCK, S., BOCK, E., KEMKEMER, R., KESSLER, H., DING, J. & SPATZ, J. P. 2009. Impact of order and disorder in RGD nanopatterns on cell adhesion. *Nano Lett,* 9**,** 1111-6.

HUGHES, C. J. R. & JACOBS, J. R. 2017. Dissecting the Role of the Extracellular Matrix in Heart Disease: Lessons from the Drosophila Genetic Model. *Vet Sci,* 4.

HUMPHRIES, J. D., BYRON, A. & HUMPHRIES, M. J. 2006. Integrin ligands at a glance. *J Cell Sci,* 119**,** 3901-3.

HUMPHRIES, J. D., WANG, P., STREULI, C., GEIGER, B., HUMPHRIES, M. J. & BALLESTREM, C. 2007. Vinculin controls focal adhesion formation by direct interactions with talin and actin. *J Cell Biol,* 179**,** 1043-57.

HUXLEY, A. F. & NIEDERGERKE, R. 1954. Structural Changes in Muscle During Contraction: Interference Microscopy of Living Muscle Fibres. *Nature,* 173**,** 971-973.

HUXLEY, H. & HANSON, J. 1954. Changes in the Cross-Striations of Muscle during Contraction and Stretch and their Structural Interpretation. *Nature,* 173**,** 973-976.

ISKRATSCH, T., WOLFENSON, H. & SHEETZ, M. P. 2014. Appreciating force and shape-the rise of mechanotransduction in cell biology. *Nat Rev Mol Cell Biol,* 15**,** 825-33.

ISKRATSCH, T., YU, C. H., MATHUR, A., LIU, S., STEVENIN, V., DWYER, J., HONE, J., EHLER, E. & SHEETZ, M. 2013. FHOD1 is needed for directed forces and adhesion maturation during cell spreading and migration. *Dev Cell,* 27**,** 545-59.

ISRAELI-ROSENBERG, S., MANSO, A. M., OKADA, H. & ROSS, R. S. 2014. Integrins and integrin-associated proteins in the cardiac myocyte. *Circ Res,* 114**,** 572-586.

JAKA, O., CASAS-FRAILE, L., LOPEZ DE MUNAIN, A. & SAENZ, A. 2015. Costamere proteins and their involvement in myopathic processes. *Expert Rev Mol Med,* 17**,** e12.

JIANG, G., GIANNONE, G., CRITCHLEY, D. R., FUKUMOTO, E. & SHEETZ, M. P. 2003. Two-piconewton slip bond between fibronectin and the cytoskeleton depends on talin. *Nature,* 424**,** 334-337.

JOHNSTON, R. K., BALASUBRAMANIAN, S., KASIGANESAN, H., BAICU, C. F., ZILE, M. R. & KUPPUSWAMY, D. 2009. Beta3 integrin-mediated ubiquitination activates survival signaling during myocardial hypertrophy. *FASEB J,* 23**,** 2759-71.

KAGIYAMA, S., EGUCHI, S., FRANK, G. D., INAGAMI, T., ZHANG, Y. C. & PHILLIPS, M. I. 2002. Angiotensin II-induced cardiac hypertrophy and hypertension are attenuated by epidermal growth factor receptor antisense. *Circulation,* 106**,** 909-12.

KAPP, T. G., RECHENMACHER, F., NEUBAUER, S., MALTSEV, O. V., CAVALCANTI-ADAM, E. A., ZARKA, R., REUNING, U., NOTNI, J., WESTER, H. J., MAS-MORUNO, C., SPATZ, J., GEIGER, B. & KESSLER, H. 2017. A Comprehensive Evaluation of the Activity and Selectivity Profile of Ligands for RGD-binding Integrins. *Sci Rep,* 7**,** 39805.

KERSHNER, R. J., BOZANO, L. D., MICHEEL, C. M., HUNG, A. M., FORNOF, A. R., CHA, J. N., RETTNER, C. T., BERSANI, M., FROMMER, J., ROTHEMUND, P. W. & WALLRAFF, G. M. 2009. Placement and orientation of individual DNA shapes on lithographically patterned surfaces. *Nat Nanotechnol,* 4**,** 557-61.

KIKKAWA, Y., HOZUMI, K., KATAGIRI, F., NOMIZU, M., KLEINMAN, H. K. & KOBLINSKI, J. E. 2013. Laminin-111-derived peptides and cancer. *Cell Adhesion & Migration,* 7**,** 150-159.

KIM, C., YE, F., HU, X. & GINSBERG, M. H. 2012. Talin activates integrins by altering the topology of the beta transmembrane domain. *J Cell Biol,* 197**,** 605-11.

KIM, H.-D., SIK YOON, C., KIM, H. & RAH, B.-J. 1999. Expression of Extracellular Matrix Components Fibronectin and Laminin in the Human Fetal Heart. *Cell Structure and Function,* 24**,** 19-26.

KLAPHOLZ, B. & BROWN, N. H. 2017. Talin - the master of integrin adhesions. *J Cell Sci,* 130**,** 2435-2446.

KONG, F., GARCIA, A. J., MOULD, A. P., HUMPHRIES, M. J. & ZHU, C. 2009. Demonstration of catch bonds between an integrin and its ligand. *J Cell Biol,* 185**,** 1275-84.

KUO, P. L., LEE, H., BRAY, M. A., GEISSE, N. A., HUANG, Y. T., ADAMS, W. J., SHEEHY, S. P. & PARKER, K. K. 2012. Myocyte shape regulates lateral registry of sarcomeres and contractility. *Am J Pathol,* 181**,** 2030-7.

LAL, H., VERMA, S. K., SMITH, M., GULERIA, R. S., LU, G., FOSTER, D. M. & DOSTAL, D. E. 2007. Stretch-induced MAP kinase activation in cardiac myocytes: differential regulation through beta1-integrin and focal adhesion kinase. *J Mol Cell Cardiol,* 43**,** 137-47.

LANASA, S. M. & BRYANT, S. J. 2009. Influence of ECM proteins and their analogs on cells cultured on 2-D hydrogels for cardiac muscle tissue engineering. *Acta Biomater,* 5**,** 2929-38.

LEGATE, K. R. & FASSLER, R. 2009. Mechanisms that regulate adaptor binding to beta-integrin cytoplasmic tails. *J Cell Sci,* 122**,** 187-98.

LEGATE, K. R., MONTANEZ, E., KUDLACEK, O. & FASSLER, R. 2006. ILK, PINCH and parvin: the tIPP of integrin signalling. *Nat Rev Mol Cell Biol,* 7**,** 20-31.

LERCHE, M., ELOSEGUI-ARTOLA, A., GUZMÁN, C., GEORGIADOU, M., KECHAGIA, J. Z., GULLBERG, D., ROCA-CUSACHS, P., PEUHU, E. & IVASKA, J. Preprint. Integrin binding dynamics modulate ligand-specific mechanosensing in mammary gland fibroblasts. *bioRxiv***,** 570721.

LI, B., XIE, L., STARR, Z. C., YANG, Z., LIN, J.-S. & WANG, J. H. C. 2007. Development of micropost force sensor array with culture experiments for determination of cell traction forces. *Cell Motility,* 64**,** 509-518.

LI, H., DENG, Y., SUN, K., YANG, H., LIU, J., WANG, M., ZHANG, Z., LIN, J., WU, C., WEI, Z. & YU, C. 2017. Structural basis of kindlin-mediated integrin recognition and activation. *Proc Natl Acad Sci U S A,* 114**,** 9349-9354.

LI, J. & SPRINGER, T. A. 2017. Energy landscape differences among integrins establish the framework for understanding activation. *J Cell Biol,* 217**,** 397-412.

LIANG, X., SUN, Y., YE, M., SCIMIA, M. C., CHENG, H., MARTIN, J., WANG, G., REARDEN, A., WU, C., PETERSON, K. L., POWELL, H. C., EVANS, S. M. & CHEN, J. 2009. Targeted ablation of PINCH1 and PINCH2 from murine

myocardium results in dilated cardiomyopathy and early postnatal lethality. *Circulation,* 120**,** 568-76.

LIU, Y., MEDDA, R., LIU, Z., GALIOR, K., YEHL, K., SPATZ, J. P., CAVALCANTI-ADAM, E. A. & SALAITA, K. 2014. Nanoparticle tension probes patterned at the nanoscale: impact of integrin clustering on force transmission. *Nano Lett,* 14**,** 5539-46.

LOCKHART, M., WIRRIG, E., PHELPS, A. & WESSELS, A. 2011. Extracellular matrix and heart development. *Birth Defects Res A Clin Mol Teratol,* 91**,** 535-50.

LOWE, A. B. 2010. Thiol-ene "click" reactions and recent applications in polymer and materials synthesis. *Polymer Chemistry,* 1**,** 17-36.

LUTOLF, M. P. & HUBBELL, J. A. 2003. Synthesis and Physicochemical Characterization of End-Linked Poly(ethylene glycol)-co-peptide Hydrogels Formed by Michael-Type Addition. *Biomacromolecules,* 4**,** 713-722.

LYON, R. C., ZANELLA, F., OMENS, J. H. & SHEIKH, F. 2015. Mechanotransduction in cardiac hypertrophy and failure. *Circ Res,* 116**,** 1462-1476.

MAITRA, N., FLINK, I. L., BAHL, J. J. & MORKIN, E. 2000. Expression of α and β integrins during terminal differentiation of cardiomyocytes. *Cardiovascular Research,* 47**,** 715-725.

MAMUYA, W. S. & BRECHER, P. 1992. Fibronectin expression in the normal and hypertrophic rat heart. *The Journal of Clinical Investigation,* 89**,** 392-401.

MANSO, A. M., LI, R., MONKLEY, S. J., CRUZ, N. M., ONG, S., LAO, D. H., KOSHMAN, Y. E., GU, Y., PETERSON, K. L., CHEN, J., ABEL, E. D., SAMAREL, A. M., CRITCHLEY, D. R. & ROSS, R. S. 2013. Talin1 has unique expression versus talin 2 in the heart and modifies the hypertrophic response to pressure overload. *J Biol Chem,* 288**,** 4252-64.

MANSO, A. M., OKADA, H., SAKAMOTO, F. M., MORENO, E., MONKLEY, S. J., LI, R., CRITCHLEY, D. R. & ROSS, R. S. 2017. Loss of mouse cardiomyocyte talin-1 and talin-2 leads to beta-1 integrin reduction, costameric instability, and dilated cardiomyopathy. *Proc Natl Acad Sci U S A,* 114**,** E6250-E6259.

MANSOUR, H., DE TOMBE, P. P., SAMAREL, A. M. & RUSSELL, B. 2004. Restoration of resting sarcomere length after uniaxial static strain is regulated by protein kinase Cepsilon and focal adhesion kinase. *Circ Res,* 94**,** 642-9.

MCCAIN, M. L., YUAN, H., PASQUALINI, F. S., CAMPBELL, P. H. & PARKER, K. K. 2014. Matrix elasticity regulates the optimal cardiac myocyte shape for contractility. *Am J Physiol Heart Circ Physiol,* 306**,** H1525-39.

MEDER, B., HUTTNER, I. G., SEDAGHAT-HAMEDANI, F., JUST, S., DAHME, T., FRESE, K. S., VOGEL, B., KOHLER, D., KLOOS, W., RUDLOFF, J., MARQUART, S., KATUS, H. A. & ROTTBAUER, W. 2011. PINCH proteins regulate cardiac contractility by modulating integrin-linked kinase-protein kinase B signaling. *Mol Cell Biol,* 31**,** 3424-35.

MIAO, H., LI, S., HU, Y. L., YUAN, S., ZHAO, Y., CHEN, B. P., PUZON-MCLAUGHLIN, W., TARUI, T., SHYY, J. Y., TAKADA, Y., USAMI, S. & CHIEN, S. 2002. Differential regulation of Rho GTPases by beta1 and beta3 integrins: the role of an extracellular domain of integrin in intracellular signaling. *J Cell Sci,* 115**,** 2199-206.

MINER, J. H., PATTON, B. L., LENTZ, S. I., GILBERT, D. J., SNIDER, W. D., JENKINS, N. A., COPELAND, N. G. & SANES, J. R. 1997. The laminin alpha chains: expression, developmental transitions, and chromosomal locations of alpha1-5, identification of heterotrimeric laminins 8-11, and cloning of a novel alpha3 isoform. *J Cell Biol,* 137**,** 685-701.

MITRA, S. K., HANSON, D. A. & SCHLAEPFER, D. D. 2005. Focal adhesion kinase: in command and control of cell motility. *Nat Rev Mol Cell Biol,* 6**,** 56-68.

MONDELLO, M. R., BRAMANTI, P., CUTRONEO, G., SANTORO, G., DI MAURO, D. & ANASTASI, G. 1996. Immunolocalization of the costameres in human skeletal muscle fibers: Confocal scanning laser microscope investigations. *The Anatomical Record,* 245**,** 481-487.

MONTANEZ, E., USSAR, S., SCHIFFERER, M., BOSL, M., ZENT, R., MOSER, M. & FASSLER, R. 2008. Kindlin-2 controls bidirectional signaling of integrins. *Genes Dev,* 22**,** 1325-30.

MORIKAWA, Y., HEALLEN, T., LEACH, J., XIAO, Y. & MARTIN, J. F. 2017. Dystrophin-glycoprotein complex sequesters Yap to inhibit cardiomyocyte proliferation. *Nature,* 547**,** 227-231.

MORSE, E. M., BRAHME, N. N. & CALDERWOOD, D. A. 2014. Integrin cytoplasmic tail interactions. *Biochemistry,* 53**,** 810-20.

MUMMERY, C. L. 2018. Perspectives on the Use of Human Induced Pluripotent Stem Cell-Derived Cardiomyocytes in Biomedical Research. *Stem cell reports,* 11**,** 1306-1311.

NAKAMURA, M. & SADOSHIMA, J. 2018. Mechanisms of physiological and pathological cardiac hypertrophy. *Nat Rev Cardiol,* 15**,** 387-407.

NAWATA, J., OHNO, I., ISOYAMA, S., SUZUKI, J., MIURA, S., IKEDA, J. & SHIRATO, K. 1999. Differential expression of alpha 1, alpha 3 and alpha 5 integrin subunits in acute and chronic stages of myocardial infarction in rats. *Cardiovasc Res,* 43**,** 371-81.

NISHIUCHI, R., TAKAGI, J., HAYASHI, M., IDO, H., YAGI, Y., SANZEN, N., TSUJI, T., YAMADA, M. & SEKIGUCHI, K. 2006. Ligand-binding specificities of laminin-binding integrins: a comprehensive survey of laminin-integrin interactions using recombinant alpha3beta1, alpha6beta1, alpha7beta1 and alpha6beta4 integrins. *Matrix Biol,* 25**,** 189-97.

OGAWA, E., SAITO, Y., HARADA, M., KAMITANI, S., KUWAHARA, K., MIYAMOTO, Y., ISHIKAWA, M., HAMANAKA, I., KAJIYAMA, N., TAKAHASHI, N., NAKAGAWA, O., MASUDA, I., KISHIMOTO, I. & NAKAO, K. 2000. Outside-in signalling of fibronectin stimulates cardiomyocyte hypertrophy in cultured neonatal rat ventricular myocytes. *J Mol Cell Cardiol,* 32**,** 765-76.

OLIVIÉRO, P., CHASSAGNE, C., SALICHON, N., CORBIER, A., HAMON, G., MAROTTE, F., CHARLEMAGNE, D., RAPPAPORT, L. & SAMUEL, J.-L. 2000. Expression of laminin α2 chain during normal and pathological growth of myocardium in rat and human. *Cardiovascular Research,* 46**,** 346-355.

OLSON, T. M., ILLENBERGER, S., KISHIMOTO, N. Y., HUTTELMAIER, S., KEATING, M. T. & JOCKUSCH, B. M. 2002. Metavinculin mutations alter actin interaction in dilated cardiomyopathy. *Circulation,* 105**,** 431-7.

ORIA, R., WIEGAND, T., ESCRIBANO, J., ELOSEGUI-ARTOLA, A., URIARTE, J. J., MORENO-PULIDO, C., PLATZMAN, I., DELCANALE, P., ALBERTAZZI, L., NAVAJAS, D., TREPAT, X., GARCIA-AZNAR, J. M., CAVALCANTI-ADAM, E. A. & ROCA-CUSACHS, P. 2017. Force loading explains spatial sensing of ligands by cells. *Nature,* 552**,** 219-224.

OYUNBAATAR, N. E., LEE, D. H., PATIL, S. J., KIM, E. S. & LEE, D. W. 2016. Biomechanical Characterization of Cardiomyocyte Using PDMS Pillar with Microgrooves. *Sensors (Basel),* 16.

PALMA, M., ABRAMSON, J. J., GORODETSKY, A. A., NUCKOLLS, C., SHEETZ, M. P., WIND, S. J. & HONE, J. 2011. Controlled Confinement of DNA at the Nanoscale: Nanofabrication and Surface Bio-Functionalization. *In:* ZUCCHERI, G. & SAMORÌ, B. (eds.) *DNA Nanotechnology: Methods and Protocols.* Totowa, NJ: Humana Press.

PANDEY, P., HAWKES, W., HU, J., MEGONE, W. V., GAUTROT, J., ANILKUMAR, N., ZHANG, M., HIRVONEN, L., COX, S., EHLER, E., HONE, J., SHEETZ, M. & ISKRATSCH, T. 2018. Cardiomyocytes Sense Matrix Rigidity through a Combination of Muscle and Non-muscle Myosin Contractions. *Dev Cell,* 44**,** 326-336 e3.

PARDO, J. V., SILICIANO, J. D. & CRAIG, S. W. 1983. Vinculin is a component of an extensive network of myofibril-sarcolemma attachment regions in cardiac muscle fibers. *J Cell Biol,* 97**,** 1081-8.

PASAPERA, A. M., SCHNEIDER, I. C., RERICHA, E., SCHLAEPFER, D. D. & WATERMAN, C. M. 2010. Myosin II activity regulates vinculin recruitment to focal adhesions through FAK-mediated paxillin phosphorylation. *The Journal of Cell Biology,* 188**,** 877-890.

PATEL, A. A., OZTUG DURER, Z. A., VAN LOON, A. P., BREMER, K. V. & QUINLAN, M. E. 2018. Drosophila and human FHOD family formin proteins nucleate actin filaments. *J Biol Chem,* 293**,** 532-540.

PATEL, R., SANTHOSH, M., DASH, J. K., KARPOORMATH, R., JHA, A., KWAK, J., PATEL, M. & KIM, J. H. 2019. Ile-Lys-Val-ala-Val (IKVAV) peptide for neuronal tissue engineering. *Polymers for Advanced Technologies,* 30**,** 4-12.

PENG, X., KRAUS, M. S., WEI, H., SHEN, T. L., PARIAUT, R., ALCARAZ, A., JI, G., CHENG, L., YANG, Q., KOTLIKOFF, M. I., CHEN, J., CHIEN, K., GU, H. & GUAN, J. L. 2006. Inactivation of focal adhesion kinase in cardiomyocytes promotes eccentric cardiac hypertrophy and fibrosis in mice. *J Clin Invest,* 116**,** 217-27.

PENG, X., WU, X., DRUSO, J. E., WEI, H., PARK, A. Y., KRAUS, M. S., ALCARAZ, A., CHEN, J., CHIEN, S., CERIONE, R. A. & GUAN, J. L. 2008. Cardiac developmental defects and eccentric right ventricular hypertrophy in

cardiomyocyte focal adhesion kinase (FAK) conditional knockout mice. *Proc Natl Acad Sci U S A,* 105**,** 6638-43.

PFAFF, M., TANGEMANN, K., MÜLLER, B., GURRATH, M., MÜLLER, G., KESSLER, H., TIMPL, R. & ENGEL, J. 1994. Selective recognition of cyclic RGD peptides of NMR defined conformation by alpha IIb beta 3, alpha V beta 3, and alpha 5 beta 1 integrins. *Journal of Biological Chemistry,* 269**,** 20233-8.

QI, L., JAFARI, N., LI, X., CHEN, Z., LI, L., HYTONEN, V. P., GOULT, B. T., ZHAN, C. G. & HUANG, C. 2016. Talin2-mediated traction force drives matrix degradation and cell invasion. *J Cell Sci,* 129**,** 3661-3674.

QI, L., YU, Y., CHI, X., XU, W., LU, D., SONG, Y., ZHANG, Y. & ZHANG, H. 2015. Kindlin-2 interacts with alpha-actinin-2 and beta1 integrin to maintain the integrity of the Z-disc in cardiac muscles. *FEBS Lett,* 589**,** 2155-62.

QIN, D., XIA, Y. & WHITESIDES, G. M. 2010. Soft lithography for micro- and nanoscale patterning. *Nature Protocols,* 5**,** 491-502.

RAFIQ, N. B. M., NISHIMURA, Y., PLOTNIKOV, S. V., THIAGARAJAN, V., ZHANG, Z., SHI, S., NATARAJAN, M., VIASNOFF, V., KANCHANAWONG, P., JONES, G. E. & BERSHADSKY, A. D. 2019. A mechano-signalling network linking microtubules, myosin IIA filaments and integrin-based adhesions. *Nat Mater,* 18**,** 638-649.

RAHMOUNI, S., LINDNER, A., RECHENMACHER, F., NEUBAUER, S., SOBAHI, T. R., KESSLER, H., CAVALCANTI-ADAM, E. A. & SPATZ, J. P. 2013. Hydrogel micropillars with integrin selective peptidomimetic functionalized nanopatterned tops: a new tool for the measurement of cell traction forces transmitted through alphavbeta3- or alpha5beta1-integrins. *Adv Mater,* 25**,** 5869-74.

RANDALL, T. S. & EHLER, E. 2014. A formin-g role during development and disease. *Eur J Cell Biol,* 93**,** 205-11.

RANGARAJAN, E. S., LEE, J. H., YOGESHA, S. D. & IZARD, T. 2010. A helix replacement mechanism directs metavinculin functions. *PLoS One,* 5**,** e10679.

RIENKS, M., PAPAGEORGIOU, A. P., FRANGOGIANNIS, N. G. & HEYMANS, S. 2014. Myocardial extracellular matrix: an ever-changing and diverse entity. *Circ Res,* 114**,** 872-88.

RINGELMANN, B., RÖDER, C., HALLMANN, R., MALEY, M., DAVIES, M., GROUNDS, M. & SOROKIN, L. 1999. Expression of Laminin α1, α2, α4, and

α5 Chains, Fibronectin, and Tenascin-C in Skeletal Muscle of Dystrophic 129ReJdy/dyMice. *Experimental Cell Research,* 246**,** 165-182.

RODRIGUEZ, A. G., HAN, S. J., REGNIER, M. & SNIADECKI, N. J. 2011. Substrate stiffness increases twitch power of neonatal cardiomyocytes in correlation with changes in myofibril structure and intracellular calcium. *Biophys J,* 101**,** 2455-64.

ROG-ZIELINSKA, E. A., NORRIS, R. A., KOHL, P. & MARKWALD, R. 2016. The Living Scar--Cardiac Fibroblasts and the Injured Heart. *Trends in molecular medicine,* 22**,** 99-114.

ROSS, R. S., PHAM, C., SHAI, S. Y., GOLDHABER, J. I., FENCZIK, C., GLEMBOTSKI, C. C., GINSBERG, M. H. & LOFTUS, J. C. 1998. Beta1 integrins participate in the hypertrophic response of rat ventricular myocytes. *Circ Res,* 82**,** 1160-72.

ROTHEMUND, P. W. 2006. Folding DNA to create nanoscale shapes and patterns. *Nature,* 440**,** 297-302.

RUDIGER, M., KORNEEVA, N., SCHWIENBACHER, C., WEISS, E. E. & JOCKUSCH, B. M. 1998. Differential actin organization by vinculin isoforms: implications for cell type-specific microfilament anchorage. *FEBS Lett,* 431**,** 49-54.

SAMAREL, A. M. 2005. Costameres, focal adhesions, and cardiomyocyte mechanotransduction. *Am J Physiol Heart Circ Physiol,* 289**,** H2291-301.

SAMAREL, A. M. 2014. Focal adhesion signaling in heart failure. *Pflugers Arch,* 466**,** 1101-11.

SANEMATSU, F., KANAI, A., USHIJIMA, T., SHIRAISHI, A., ABE, T., KAGE, Y., SUMIMOTO, H. & TAKEYA, R. 2019. Fhod1, an actin-organizing formin family protein, is dispensable for cardiac development and function in mice. *Cytoskeleton (Hoboken),* 76**,** 219-229.

SCHAUFLER, V., CZICHOS-MEDDA, H., HIRSCHFELD-WARNECKEN, V., NEUBAUER, S., RECHENMACHER, F., MEDDA, R., KESSLER, H., GEIGER, B., SPATZ, J. P. & CAVALCANTI-ADAM, E. A. 2016. Selective binding and lateral clustering of alpha5beta1 and alphavbeta3 integrins: Unraveling the spatial requirements for cell spreading and focal adhesion assembly. *Cell Adh Migr,* 10**,** 505-515.

SCHILLER, H. B., HERMANN, M. R., POLLEUX, J., VIGNAUD, T., ZANIVAN, S., FRIEDEL, C. C., SUN, Z., RADUCANU, A., GOTTSCHALK, K. E., THERY, M., MANN, M. & FASSLER, R. 2013. beta1- and alphav-class integrins cooperate to regulate myosin II during rigidity sensing of fibronectin-based microenvironments. *Nat Cell Biol,* 15**,** 625-36.

SCHNEIDER, C. A., RASBAND, W. S. & ELICEIRI, K. W. 2012. NIH Image to ImageJ: 25 years of image analysis. *Nature Methods,* 9**,** 671-675.

SCHOEN, I., HU, W., KLOTZSCH, E. & VOGEL, V. 2010. Probing cellular traction forces by micropillar arrays: contribution of substrate warping to pillar deflection. *Nano Lett,* 10**,** 1823-30.

SCHONICHEN, A. & GEYER, M. 2010. Fifteen formins for an actin filament: a molecular view on the regulation of human formins. *Biochim Biophys Acta,* 1803**,** 152-63.

SCHONICHEN, A., MANNHERZ, H. G., BEHRMANN, E., MAZUR, A. J., KUHN, S., SILVAN, U., SCHOENENBERGER, C. A., FACKLER, O. T., RAUNSER, S., DEHMELT, L. & GEYER, M. 2013. FHOD1 is a combined actin filament capping and bundling factor that selectively associates with actin arcs and stress fibers. *J Cell Sci,* 126**,** 1891-901.

SCHULZE, N., GRAESSL, M., BLANCKE SOARES, A., GEYER, M., DEHMELT, L. & NALBANT, P. 2014. FHOD1 regulates stress fiber organization by controlling the dynamics of transverse arcs and dorsal fibers. *J Cell Sci,* 127**,** 1379-93.

SCHVARTZMAN, M., NGUYEN, K., PALMA, M., ABRAMSON, J., SABLE, J., HONE, J., SHEETZ, M. P. & WIND, S. J. 2009. Fabrication of Nanoscale Bioarrays for the Study of Cytoskeletal Protein Binding Interactions Using Nanoimprint Lithography. *J Vac Sci Technol B Microelectron Nanometer Struct Process Meas Phenom,* 27**,** 61-65.

SCHVARTZMAN, M., PALMA, M., SABLE, J., ABRAMSON, J., HU, X., SHEETZ, M. P. & WIND, S. J. 2011. Nanolithographic control of the spatial organization of cellular adhesion receptors at the single-molecule level. *Nano Lett,* 11**,** 1306-12.

SCHWARZ, U. S. & GARDEL, M. L. 2012. United we stand: integrating the actin cytoskeleton and cell-matrix adhesions in cellular mechanotransduction. *J Cell Sci,* 125**,** 3051-60.

SEPHEL, G. C., TASHIRO, K. I., SASAKI, M., GREATOREX, D., MARTIN, G. R., YAMADA, Y. & KLEINMAN, H. K. 1989. Laminin a chain synthetic peptide which supports neurite outgrowth. *Biochemical and Biophysical Research Communications,* 162**,** 821-829.

SHEN, B., KOSTIAINEN, M. A. & LINKO, V. 2018a. DNA Origami Nanophotonics and Plasmonics at Interfaces. *Langmuir,* 34**,** 14911-14920.

SHEN, B. X., LINKO, V., TAPIO, K., PIKKER, S., LEMMA, T., GOPINATH, A., GOTHELF, K. V., KOSTIAINEN, M. A. & TOPPARI, J. J. 2018b. Plasmonic nanostructures through DNA-assisted lithography. *Science Advances,* 4.

SHEN, W., ZHONG, H., NEFF, D. & NORTON, M. L. 2009. NTA Directed Protein Nanopatterning on DNA Origami Nanoconstructs. *Journal of the American Chemical Society,* 131**,** 6660-6661.

SIT, B., GUTMANN, D. & ISKRATSCH, T. 2019. Costameres, dense plaques and podosomes: the cell matrix adhesions in cardiovascular mechanosensing. *J Muscle Res Cell Motil,* 40**,** 197-209.

SKWAREK-MARUSZEWSKA, A., HOTULAINEN, P., MATTILA, P. K. & LAPPALAINEN, P. 2009. Contractility-dependent actin dynamics in cardiomyocyte sarcomeres. *J Cell Sci,* 122**,** 2119-26.

SPARROW, J. C. & SCHÖCK, F. 2009. The initial steps of myofibril assembly: integrins pave the way. *Nat Rev Mol Cell Biol,* 10**,** 293-8.

SURYAKUMAR, G., KASIGANESAN, H., BALASUBRAMANIAN, S. & KUPPUSWAMY, D. 2010. Lack of beta3 integrin signaling contributes to calpain-mediated myocardial cell loss in pressure-overloaded myocardium. *J Cardiovasc Pharmacol,* 55**,** 567-73.

SWERYDA-KRAWIEC, B., DEVARAJ, H., JACOB, G. & HICKMAN, J. J. 2004. A New Interpretation of Serum Albumin Surface Passivation. *Langmuir,* 20**,** 2054-2056.

TABDANOV, E., GONDARENKO, S., KUMARI, S., LIAPIS, A., DUSTIN, M. L., SHEETZ, M. P., KAM, L. C. & ISKRATSCH, T. 2015. Micropatterning of TCR and LFA-1 ligands reveals complementary effects on cytoskeleton mechanics in T cells. *Integrative Biology,* 7**,** 1272-1284.

TABDANOV, E. D., PURAM, V., ZHOVMER, A. & PROVENZANO, P. P. 2018. Microtubule-Actomyosin Mechanical Cooperation during Contact Guidance Sensing. *Cell Rep,* 25**,** 328-338 e5.

TANGNEY, J. R., CHUANG, J. S., JANSSEN, M. S., KRISHNAMURTHY, A., LIAO, P., HOSHIJIMA, M., WU, X., MEININGER, G. A., MUTHUCHAMY, M., ZEMLJIC-HARPF, A., ROSS, R. S., FRANK, L. R., MCCULLOCH, A. D. & OMENS, J. H. 2013. Novel role for vinculin in ventricular myocyte mechanics and dysfunction. *Biophys J,* 104**,** 1623-33.

TASHIRO, K., SEPHEL, G. C., WEEKS, B., SASAKI, M., MARTIN, G. R., KLEINMAN, H. K. & YAMADA, Y. 1989. A synthetic peptide containing the IKVAV sequence from the A chain of laminin mediates cell attachment, migration, and neurite outgrowth. *J Biol Chem,* 264**,** 16174-82.

TAYLOR, J. M., ROVIN, J. D. & PARSONS, J. T. 2000. A role for focal adhesion kinase in phenylephrine-induced hypertrophy of rat ventricular cardiomyocytes. *J Biol Chem,* 275**,** 19250-7.

THEODOSIOU, M., WIDMAIER, M., BOTTCHER, R. T., ROGNONI, E., VEELDERS, M., BHARADWAJ, M., LAMBACHER, A., AUSTEN, K., MULLER, D. J., ZENT, R. & FASSLER, R. 2016. Kindlin-2 cooperates with talin to activate integrins and induces cell spreading by directly binding paxillin. *Elife,* 5**,** e10130.

TORRES-KOLBUS, J., CHOU, C., LIU, J. & DEITERS, A. 2014. Synthesis of non-linear protein dimers through a genetically encoded Thiol-ene reaction. *PLoS One,* 9**,** e105467.

TORSONI, A. S., CONSTANCIO, S. S., NADRUZ, W., JR., HANKS, S. K. & FRANCHINI, K. G. 2003. Focal adhesion kinase is activated and mediates the early hypertrophic response to stretch in cardiac myocytes. *Circ Res,* 93**,** 140-7.

TYAGARAJAN, K., PRETZER, E. & WIKTOROWICZ, J. E. 2003. Thiol-reactive dyes for fluorescence labeling of proteomic samples. *Electrophoresis,* 24**,** 2348-58.

VAKALOGLOU, K. M., CHOUNTALA, M. & ZERVAS, C. G. 2012. Functional analysis of parvin and different modes of IPP-complex assembly at integrin sites during Drosophila development. *J Cell Sci,* 125**,** 3221-32.

VAKALOGLOU, K. M., CHRYSANTHIS, G., RAPSOMANIKI, M. A., LYGEROU, Z. & ZERVAS, C. G. 2016. IPP Complex Reinforces Adhesion by Relaying Tension-Dependent Signals to Inhibit Integrin Turnover. *Cell Rep,* 14**,** 2668-82.

VALIENTE-ALANDI, I., POTTER, S. J., SALVADOR, A. M., SCHAFER, A. E., SCHIPS, T., CARRILLO-SALINAS, F., GIBSON, A. M., NIEMAN, M. L.,

PERKINS, C., SARGENT, M. A., HUO, J., LORENZ, J. N., DEFALCO, T., MOLKENTIN, J. D., ALCAIDE, P. & BLAXALL, B. C. 2018. Inhibiting Fibronectin Attenuates Fibrosis and Improves Cardiac Function in a Model of Heart Failure. *Circulation,* 138**,** 1236-1252.

VAN DER VELDE, J. H. M., OELERICH, J., HUANG, J., SMIT, J. H., AMINIAN JAZI, A., GALIANI, S., KOLMAKOV, K., GOURIDIS, G., EGGELING, C., HERRMANN, A., ROELFES, G. & CORDES, T. 2016. A simple and versatile design concept for fluorophore derivatives with intramolecular photostabilization. *Nature Communications,* 7**,** 10144.

VAN DER VELDEN, H. M. W. & JONGSMA, H. J. 2002. Cardiac gap junctions and connexins: their role in atrial fibrillation and potential as therapeutic targets. *Cardiovascular Research,* 54**,** 270-279.

VASILE, V. C., WILL, M. L., OMMEN, S. R., EDWARDS, W. D., OLSON, T. M. & ACKERMAN, M. J. 2006. Identification of a metavinculin missense mutation, R975W, associated with both hypertrophic and dilated cardiomyopathy. *Mol Genet Metab,* 87**,** 169-74.

WARD, M. & ISKRATSCH, T. 2019. Mix and (mis-)match - The mechanosensing machinery in the changing environment of the developing, healthy adult and diseased heart. *Biochim Biophys Acta Mol Cell Res*.

WHITE, E. S., BARALLE, F. E. & MURO, A. F. 2008. New insights into form and function of fibronectin splice variants. *J Pathol,* 216**,** 1-14.

WICKSTROM, S. A., LANGE, A., MONTANEZ, E. & FASSLER, R. 2010. The ILK/PINCH/parvin complex: the kinase is dead, long live the pseudokinase! *EMBO J,* 29**,** 281-91.

WILLEY, C. 2003. Focal complex formation in adult cardiomyocytes is accompanied by the activation of β3 integrin and c-Src. *Journal of Molecular and Cellular Cardiology,* 35**,** 671-683.

WILLIAMS, C., QUINN, K. P., GEORGAKOUDI, I. & BLACK, L. D., 3RD 2014. Young developmental age cardiac extracellular matrix promotes the expansion of neonatal cardiomyocytes in vitro. *Acta Biomater,* 10**,** 194-204.

WOLFENSON, H., YANG, B. & SHEETZ, M. P. 2019. Steps in Mechanotransduction Pathways that Control Cell Morphology. *Annual Review of Physiology,* 81**,** 585-605.

WOO, S. & ROTHEMUND, P. W. K. 2014. Self-assembly of two-dimensional DNA origami lattices using cation-controlled surface diffusion. *Nature Communications,* 5**,** 4889.

WU, Q., ZHANG, J., KOH, W., YU, Q., ZHU, X., AMSTERDAM, A., DAVIS, G. E., ARNAOUT, M. A. & XIONG, J.-W. 2015. Talin1 is required for cardiac Z-disk stabilization and endothelial integrity in zebrafish. *The FASEB Journal,* 29**,** 4989-5005.

YANG, B., LIEU, Z. Z., WOLFENSON, H., HAMEED, F. M., BERSHADSKY, A. D. & SHEETZ, M. P. 2016. Mechanosensing Controlled Directly by Tyrosine Kinases. *Nano Lett,* 16**,** 5951-61.

YANG, H., BORG, T. K., LIU, H. & GAO, B. Z. 2015. Interactive relationship between basement-membrane development and sarcomerogenesis in single cardiomyocytes. *Exp Cell Res,* 330**,** 222-32.

YAO, M., GOULT, B. T., KLAPHOLZ, B., HU, X., TOSELAND, C. P., GUO, Y., CONG, P., SHEETZ, M. P. & YAN, J. 2016. The mechanical response of talin. *Nat Commun,* 7**,** 11966.

YUAN, H., MARZBAN, B. & KIT PARKER, K. 2017. Myofibrils in Cardiomyocytes Tend to Assemble Along the Maximal Principle Stress Directions. *J Biomech Eng,* 139.

ZARKA, R., HOREV, M., VOLBERG, T., NEUBAUER, S., KESSLER, H., SPATZ, J. & GEIGER, B. 2019a. Differential modulation of platelet adhesion and spreading by adhesive ligand density. *Nano Letters,* in press.

ZARKA, R., HOREV, M. B., VOLBERG, T., NEUBAUER, S., KESSLER, H., SPATZ, J. P. & GEIGER, B. 2019b. Differential Modulation of Platelet Adhesion and Spreading by Adhesive Ligand Density. *Nano Lett,* 19**,** 1418-1427.

ZEMLJIC-HARPF, A. E., MILLER, J. C., HENDERSON, S. A., WRIGHT, A. T., MANSO, A. M., ELSHERIF, L., DALTON, N. D., THOR, A. K., PERKINS, G. A., MCCULLOCH, A. D. & ROSS, R. S. 2007. Cardiac-myocyte-specific excision of the vinculin gene disrupts cellular junctions, causing sudden death or dilated cardiomyopathy. *Mol Cell Biol,* 27**,** 7522-37.

ZHOU, L., MA, B. & HAN, X. 2016. The role of autophagy in angiotensin II-induced pathological cardiac hypertrophy. *J Mol Endocrinol,* 57**,** R143-R152.

ZIEGLER, W. H., LIDDINGTON, R. C. & CRITCHLEY, D. R. 2006. The structure and regulation of vinculin. *Trends Cell Biol,* 16**,** 453-60.

8 APPENDICES

MODIFIED STRANDS OF TRIANGULAR DNA ORIGAMI – PEPTIDE MODIFICATION:

Map Location	Modified Sequence
B32	AATACTGCGGAATCGTAGGGGGTAATAGTAAAATGTTTAGACT AGTTGTGGATCCTACT
C32	TCTTTGATTAGTAATAGTCTGTCCATCACGCAAATTAACCGTTA GTTGTGGATCCTACT
B12	AACTCCAAGATTGCATCAAAAAGATAATGCAGATACATAAAGT TGTGGATCCTACT
A12	CATTCAACAAACGCAAAGACACCAGAACACCCTGAACAAAAGT TGTGGATCCTACT
B20	TAATTGCTTTACCCTGACTATTATGAGGCATAGTAAGAGCAGTT GTGGATCCTACT
A20	TTGACGGAAATACATACATAAAGGGCGCTAATATCAGAGAAGT TGTGGATCCTACT
B30	TGCTGTAGATCCCCCTCAAATGCTGCGAGAGGCTTTTGCAAGTT GTGGATCCTACT
A32	CAGAAGGAAACCGAGGTTTTTAAGAAAAGTAAGCAGATAGCCG AGTTGTGGATCCTACT
B26	CGGATGGCACGAGAATGACCATAATCGTTTACCAGACGACAGT TGTGGATCCTACT
A26	CACCGTCACCTTATTACGCAGTATTGAGTTAAGCCCAATAAGTT GTGGATCCTACT
C30	TAAAACATTAGAAGAACTCAAACTTTTTATAATCAGTGAGAGTT GTGGATCCTACT
C12	AGAGATAGTTTGACGCTCAATCGTACGTGCTTTCCTCGTTAGTT GTGGATCCTACT
C20	GAATACGTAACAGGAAAAACGCTCCTAAACAGGAGGCCGAAGT TGTGGATCCTACT

C26	CTATTAGTATATCCAGAACAATATCAGGAACGGTACGCCAAGTTGTGGATCCTACT
A37	AGAGAATAACATAAAAACAGGGAAGCGCATTAAGTTGTGGATCCTACT
B37	ACAGGTAGAAAGATTCATCAGTTGAGATTTAGAGTTGTGGATCCTACT
A30	GAGCCAGCGAATACCCAAAAGAACATGAAATAGCAATAGCAGTTGTGGATCCTACT
C37	CGAGAAAGGAAGGGAAGCGTACTATGGTTGCTAGTTGTGGATCCTACT
C56	TTAATGAAGTTTGATGGTGGTTCCGAGGTGCCGTAAAGCAAGTTGTGGATCCTACT
C61	TTCCAGTCCTTATAAATCAAAAGAGAACCATCACCCAAATAGTTGTGGATCCTACT
B64	ACCAACCTAAAAAATCAACGTAACAAATAAATTGGGCTTGAGAAGTTGTGGATCCTACT
C64	AACTCACATTATTGAGTGTTGTTCCAGAAACCGTCTATCAGGGAGTTGTGGATCCTACT
C49	GTTTGCGTCACGCTGGTTTGCCCCAAGGGAGCCCCCGATTAGTTGTGGATCCTACT
A64	ACGACAATAAATCCCGACTTGCGGGAGATCCTGAATCTTACCAAGTTGTGGATCCTACT
A56	ACAAGAAAGCAAGCAAATCAGATAACAGCCATATTATTTAAGTTGTGGATCCTACT
B65	AGTTGTGGATCCTACTCCTGACGAGAAACACCAGAACGAGTAGGCTGCTCATTCAGTGA
C65	AGTTGTGGATCCTACTACGTGGACTCCAACGTCAAAGGGCGAATTTGGAACAAGAGTCC

B41	CGACCTGCGGTCAATCATAAGGGAACGGAACAACATTATTAGTTGTGGATCCTACT
C41	TTTCACCAGCCTGGCCCTGAGAGAAAGCCGGCGAACGTGGAGTTGTGGATCCTACT
A41	TTTCCTTAGCACTCATCGAGAACAATAGCAGCCTTTACAGAGTTGTGGATCCTACT
B56	CCAAGCGCAGGCGCATAGGCTGGCAGAACTGGCTCATTATAGTTGTGGATCCTACT
A65	AGTTGTGGATCCTACTTGCTATTTTGCACCCAGCTACAATTTTGTTTTGAAGCCTTAAA
B49	TATCATCGTTGAAAGAGGACAGATGGAAGAAAAATCTACGAGTTGTGGATCCTACT
A49	AGCATGTATTTCATCGTAGGAATCAAACGATTTTTTGTTTAGTTGTGGATCCTACT
B61	AAAACACTTAATCTTGACAAGAACTTAATCATTGTGAATTAGTTGTGGATCCTACT
A61	GCGCCTGTTATTCTAAGAACGCGATTCCAGAGCCTAATTTAGTTGTGGATCCTACT

MODIFIED STRANDS OF TRIANGULAR DNA ORIGAMI – AMINO ANCHORS

Map Location	Modified Sequence
A05	TTTGATGATTAAGAGGCTGAGACTTGCTCAGTACCAGGCGTTTTTTTTTTTTTTTTT
A13	TTTAACGGTTCGGAACCTATTATTAGGGTTGATATAAGTATTTTTTTTTTTTTTTTTT
A33	CCTTTTTTCATTTAACAATTTCATAGGATTAGTTTTTTTTTTTTTTTTTT
A42	AGAGTCAAAAATCAATATATGTGATGAAACAAACATCAAGTTTTTTTTTTTTTTTTTT
A50	ACATAGCGCTGTAAATCGTCGCTATTCATTTCAATTACCTTTTTTTTTTTTTTTTTT
B05	ACAGTCAAAGAGAATCGATGAACGACCCCGGTTGATAATCTTTTTTTTTTTTTTTTTT
B13	CGTTCTAGTCAGGTCATTGCCTGACAGGAAGATTGTATAATTTTTTTTTTTTTTTTTT
B33	AGGGATAGCTCAGAGCCACCACCCCATGTCAATTTTTTTTTTTTTTTTTT
B42	AGACGTTACCATGTACCGTAACACCCCTCAGAACCGCCACTTTTTTTTTTTTTTTTTT
B50	AGCGTAACTACAAACTACAACGCCTATCACCGTACTCAGGTTTTTTTTTTTTTTTTTT
C05	TGGCAATTTTTAACGTCAGATGAAAACAATAACGGATTCGTTTTTTTTTTTTTTTTTT
C13	GATTATACACAGAAATAAAGAAATACCAAGTTACAAAATCTTTTTTTTTTTTTTTTTT

C33	CGCGTCTGATAGGAACGCCATCAACTTTTACATTTTTTTTTTTTTTTTTT
C42	GTAACCGTCTTTCATCAACATTAAAATTTTTGTTAAATCATTTTTTTTTTTTTTTTTTTT
C50	GGATAGGTACCCGTCGGATTCTCCTAAACGTTAATATTTTTTTTTTTTTTTTTTTTTTTT

UNMODIFIED SSDNA STRANDS OF TRIANGULAR DNA ORIGAMI

Map Location	Sequence
A01	CGGGGTTTCCTCAAGAGAAGGATTTTGAATTA
A02	AGCGTCATGTCTCTGAATTTACCGACTACCTT
A03	TTCATAATCCCCTTATTAGCGTTTTTCTTACC
A04	ATGGTTTATGTCACAATCAATAGATATTAAAC
A05	TTTGATGATTAAGAGGCTGAGACTTGCTCAGTACCAGGCG
A06	CCGGAACCCAGAATGGAAAGCGCAACATGGCT
A07	AAAGACAACATTTTCGGTCATAGCCAAAATCA
A08	GACGGGAGAATTAACTCGGAATAAGTTTATTTCCAGCGCC
A09	GATAAGTGCCGTCGAGCTGAAACATGAAAGTATACAGGAG
A10	TGTACTGGAAATCCTCATTAAAGCAGAGCCAC
A11	CACCGGAAAGCGCGTTTTCATCGGAAGGGCGA
A12	CATTCAACAAACGCAAAGACACCAGAACACCCTGAACAAA
A13	TTTAACGGTTCGGAACCTATTATTAGGGTTGATATAAGTA
A14	CTCAGAGCATATTCACAAACAAATTAATAAGT
A15	GGAGGGAATTTAGCGTCAGACTGTCCGCCTCC
A16	GTCAGAGGGTAATTGATGGCAACATATAAAAGCGATTGAG
A17	TAGCCCGGAATAGGTGAATGCCCCCTGCCTATGGTCAGTG
A18	CCTTGAGTCAGACGATTGGCCTTGCGCCACCC
A19	TCAGAACCCAGAATCAAGTTTGCCGGTAAATA
A20	TTGACGGAAATACATACATAAAGGGCGCTAATATCAGAGA
A21	CAGAGCCAGGAGGTTGAGGCAGGTAACAGTGCCCG
A22	ATTAAAGGCCGTAATCAGTAGCGAGCCACCCT
A23	GATAACCCACAAGAATGTTAGCAAACGTAGAAAATTATTC
A24	GCCGCCAGCATTGACACCACCCTC

A25	AGAGCCGCACCATCGATAGCAGCATGAATTAT
A26	CACCGTCACCTTATTACGCAGTATTGAGTTAAGCCCAATA
A27	AGCCATTTAAACGTCACCAATGAACACCAGAACCA
A28	ATAAGAGCAAGAAACATGGCATGATTAAGACTCCGACTTG
A29	CCATTAGCAAGGCCGGGGGAATTA
A30	GAGCCAGCGAATACCCAAAAGAACATGAAATAGCAATAGC
A31	TATCTTACCGAAGCCCAAACGCAATAATAACGAAAATCACCAG
A32	CAGAAGGAAACCGAGGTTTTTAAGAAAAGTAAGCAGATAGCCG
A33	CCTTTTTTCATTTAACAATTTCATAGGATTAG
A34	TTTAACCTATCATAGGTCTGAGAGTTCCAGTA
A35	AGTATAAAATATGCGTTATACAAAGCCATCTT
A36	CAAGTACCTCATTCCAAGAACGGGAAATTCAT
A37	AGAGAATAACATAAAAACAGGGAAGCGCATTA
A38	AAAACAAAATTAATTAAATGGAAACAGTACATTAGTGAAT
A39	TTATCAAACCGGCTTAGGTTGGGTAAGCCTGT
A40	TTAGTATCGCCAACGCTCAACAGTCGGCTGTC
A41	TTTCCTTAGCACTCATCGAGAACAATAGCAGCCTTTACAG
A42	AGAGTCAAAAATCAATATATGTGATGAAACAAACATCAAG
A43	ACTAGAAATATATAACTATATGTACGCTGAGA
A44	TCAATAATAGGGCTTAATTGAGAATCATAATT
A45	AACGTCAAAAATGAAAAGCAAGCCGTTTTTATGAAACCAA
A46	GAGCAAAAGAAGATGAGTGAATAACCTTGCTTATAGCTTA
A47	GATTAAGAAATGCTGATGCAAATCAGAATAAA
A48	CACCGGAATCGCCATATTTAACAAAATTTACG
A49	AGCATGTATTTCATCGTAGGAATCAAACGATTTTTTGTTT

A50	ACATAGCGCTGTAAATCGTCGCTATTCATTTCAATTACCT
A51	GTTAAATACAATCGCAAGACAAAGCCTTGAAA
A52	CCCATCCTCGCCAACATGTAATTTAATAAGGC
A53	TCCCAATCCAAATAAGATTACCGCGCCCAATAAATAATAT
A54	TCCCTTAGAATAACGCGAGAAAACTTTTACCGACC
A55	GTGTGATAAGGCAGAGGCATTTTCAGTCCTGA
A56	ACAAGAAAGCAAGCAAATCAGATAACAGCCATATTATTTA
A57	GTTTGAAATTCAAATATATTTTAG
A58	AATAGATAGAGCCAGTAATAAGAGATTTAATG
A59	GCCAGTTACAAAATAATAGAAGGCTTATCCGGTTATCAAC
A60	TTCTGACCTAAAATATAAAGTACCGACTGCAGAAC
A61	GCGCCTGTTATTCTAAGAACGCGATTCCAGAGCCTAATTT
A62	TCAGCTAAAAAAGGTAAAGTAATT
A63	ACGCTAACGAGCGTCTGGCGTTTTAGCGAACCCAACATGT
A64	ACGACAATAAATCCCGACTTGCGGGAGATCCTGAATCTTACCA
A65	TGCTATTTTGCACCCAGCTACAATTTTGTTTTGAAGCCTTAAA
B01	TCATATGTGTAATCGTAAAACTAGTCATTTTC
B02	GTGAGAAAATGTGTAGGTAAAGATACAACTTT
B03	GGCATCAAATTTGGGGCGCGAGCTAGTTAAAG
B04	TTCGAGCTAAGACTTCAAATATCGGGAACGAG
B05	ACAGTCAAAGAGAATCGATGAACGACCCCGGTTGATAATC
B06	ATAGTAGTATGCAATGCCTGAGTAGGCCGGAG
B07	AACCAGACGTTTAGCTATATTTTCTTCTACTA
B08	GAATACCACATTCAACTTAAGAGGAAGCCCGATCAAAGCG
B09	AGAAAAGCCCCAAAAAGAGTCTGGAGCAAACAATCACCAT

B10	CAATATGACCCTCATATATTTTAAAGCATTAA
B11	CATCCAATAAATGGTCAATAACCTCGGAAGCA
B12	AACTCCAAGATTGCATCAAAAAGATAATGCAGATACATAA
B13	CGTTCTAGTCAGGTCATTGCCTGACAGGAAGATTGTATAA
B14	CAGGCAAGATAAAAATTTTTAGAATATTCAAC
B15	GATTAGAGATTAGATACATTTCGCAAATCATA
B16	CGCCAAAAGGAATTACAGTCAGAAGCAAAGCGCAGGTCAG
B17	GCAAATATTTAAATTGAGATCTACAAAGGCTACTGATAAA
B18	TTAATGCCTTATTTCAACGCAAGGGCAAAGAA
B19	TTAGCAAATAGATTTAGTTTGACCAGTACCTT
B20	TAATTGCTTTACCCTGACTATTATGAGGCATAGTAAGAGC
B21	ATAAAGCCTTTGCGGGAGAAGCCTGGAGAGGGTAG
B22	TAAGAGGTCAATTCTGCGAACGAGATTAAGCA
B23	AACACTATCATAACCCATCAAAAATCAGGTCTCCTTTTGA
B24	ATGACCCTGTAATACTTCAGAGCA
B25	TAAAGCTATATAACAGTTGATTCCCATTTTTG
B26	CGGATGGCACGAGAATGACCATAATCGTTTACCAGACGAC
B27	TAATTGCTTGGAAGTTTCATTCCAAATCGGTTGTA
B28	GATAAAAACCAAAATATTAAACAGTTCAGAAATTAGAGCT
B29	ACTAAAGTACGGTGTCGAATATAA
B30	TGCTGTAGATCCCCCTCAAATGCTGCGAGAGGCTTTTGCA
B31	AAAGAAGTTTTGCCAGCATAAATATTCATTGACTCAACATG TT
B32	AATACTGCGGAATCGTAGGGGGTAATAGTAAAATGTTTAGA CT
B33	AGGGATAGCTCAGAGCCACCACCCCATGTCAA
B34	CAACAGTTTATGGGATTTTGCTAATCAAAAGG

B35	GCCGCTTTGCTGAGGCTTGCAGGGGAAAAGGT
B36	GCGCAGACTCCATGTTACTTAGCCCGTTTTAA
B37	ACAGGTAGAAAGATTCATCAGTTGAGATTTAG
B38	CCTCAGAACCGCCACCCAAGCCCAATAGGAACGTAAATGA
B39	ATTTTCTGTCAGCGGAGTGAGAATACCGATAT
B40	ATTCGGTCTGCGGGATCGTCACCCGAAATCCG
B41	CGACCTGCGGTCAATCATAAGGGAACGGAACAACATTATT
B42	AGACGTTACCATGTACCGTAACACCCCTCAGAACCGCCAC
B43	CACGCATAAGAAAGGAACAACTAAGTCTTTCC
B44	ATTGTGTCTCAGCAGCGAAAGACACCATCGCC
B45	TTAATAAAACGAACTAACCGAACTGACCAACTCCTGATAA
B46	AGGTTTAGTACCGCCATGAGTTTCGTCACCAGGATCTAAA
B47	GTTTTGTCAGGAATTGCGAATAATCCGACAAT
B48	GACAACAAGCATCGGAACGAGGGTGAGATTTG
B49	TATCATCGTTGAAAGAGGACAGATGGAAGAAAAATCTACG
B50	AGCGTAACTACAAACTACAACGCCTATCACCGTACTCAGG
B51	TAGTTGCGAATTTTTTCACGTTGATCATAGTT
B52	GTACAACGAGCAACGGCTACAGAGGATACCGA
B53	ACCAGTCAGGACGTTGGAACGGTGTACAGACCGAAACAAA
B54	ACAGACAGCCCAAATCTCCAAAAAAAAATTTCTTA
B55	AACAGCTTGCTTTGAGGACTAAAGCGATTATA
B56	CCAAGCGCAGGCGCATAGGCTGGCAGAACTGGCTCATTAT
B57	CGAGGTGAGGCTCCAAAAGGAGCC
B58	ACCCCCAGACTTTTTCATGAGGAACTTGCTTT
B59	ACCTTATGCGATTTTATGACCTTCATCAAGAGCATCTTTG
B60	CGGTTTATCAGGTTTCCATTAAACGGGAATACACT

B61	AAAACACTTAATCTTGACAAGAACTTAATCATTGTGAATT
B62	GGCAAAAGTAAAATACGTAATGCC
B63	TGGTTTAATTTCAACTCGGATATTCATTACCCACGAAAGA
B64	ACCAACCTAAAAAATCAACGTAACAAATAAATTGGGCTTGAGA
B65	CCTGACGAGAAACACCAGAACGAGTAGGCTGCTCATTCAGTGA
C01	TCGGGAGATATACAGTAACAGTACAAATAATT
C02	CCTGATTAAAGGAGCGGAATTATCTCGGCCTC
C03	GCAAATCACCTCAATCAATATCTGCAGGTCGA
C04	CGACCAGTACATTGGCAGATTCACCTGATTGC
C05	TGGCAATTTTTAACGTCAGATGAAAACAATAACGGATTCG
C06	AAGGAATTACAAAGAAACCACCAGTCAGATGA
C07	GGACATTCACCTCAAATATCAAACACAGTTGA
C08	TTGACGAGCACGTATACTGAAATGGATTATTTAATAAAAG
C09	CCTGATTGCTTTGAATTGCGTAGATTTTCAGGCATCAATA
C10	TAATCCTGATTATCATTTTGCGGAGAGGAAGG
C11	TTATCTAAAGCATCACCTTGCTGATGGCCAAC
C12	AGAGATAGTTTGACGCTCAATCGTACGTGCTTTCCTCGTT
C13	GATTATACACAGAAATAAAGAAATACCAAGTTACAAAATC
C14	TAGGAGCATAAAAGTTTGAGTAACATTGTTTG
C15	TGACCTGACAAATGAAAAATCTAAAATATCTT
C16	AGAATCAGAGCGGGAGATGGAAATACCTACATAACCCTTC
C17	GCGCAGAGGCGAATTAATTATTTGCACGTAAATTCTGAAT
C18	AATGGAAGCGAACGTTATTAATTTCTAACAAC
C19	TAATAGATCGCTGAGAGCCAGCAGAAGCGTAA
C20	GAATACGTAACAGGAAAAACGCTCCTAAACAGGAGGCCGA

C21	TCAATAGATATTAAATCCTTTGCCGGTTAGAACCT
C22	CAATATTTGCCTGCAACAGTGCCATAGAGCCG
C23	TTAAAGGGATTTTAGATACCGCCAGCCATTGCGGCACAGA
C24	ACAATTCGACAACTCGTAATACAT
C25	TTGAGGATGGTCAGTATTAACACCTTGAATGG
C26	CTATTAGTATATCCAGAACAATATCAGGAACGGTACGCCA
C27	CGCGAACTAAAACAGAGGTGAGGCTTAGAAGTATT
C28	GAATCCTGAGAAGTGTATCGGCCTTGCTGGTACTTTAATG
C29	ACCACCAGCAGAAGATGATAGCCC
C30	TAAAACATTAGAAGAACTCAAACTTTTTATAATCAGTGAG
C31	GCCACCGAGTAAAAGAACATCACTTGCCTGAGCGCCATTAAAA
C32	TCTTTGATTAGTAATAGTCTGTCCATCACGCAAATTAACCGTT
C33	CGCGTCTGATAGGAACGCCATCAACTTTTACA
C34	AGGAAGATGGGGACGACGACAGTAATCATATT
C35	CTCTAGAGCAAGCTTGCATGCCTGGTCAGTTG
C36	CCTTCACCGTGAGACGGGCAACAGCAGTCACA
C37	CGAGAAAGGAAGGGAAGCGTACTATGGTTGCT
C38	GCTCATTTTTTAACCAGCCTTCCTGTAGCCAGGCATCTGC
C39	CAGTTTGACGCACTCCAGCCAGCTAAACGACG
C40	GCCAGTGCGATCCCCGGGTACCGAGTTTTTCT
C41	TTTCACCAGCCTGGCCCTGAGAGAAAGCCGGCGAACGTGG
C43	ACGTTGTATTCCGGCACCGCTTCTGGCGCATC
C44	CCAGGGTGGCTCGAATTCGTAATCCAGTCACG
C45	TAGAGCTTGACGGGGAGTTGCAGCAAGCGGTCATTGGGCG
C46	GTTAAAATTCGCATTAATGTGAGCGAGTAACACACGTTGG

C47	TGTAGATGGGTGCCGGAAACCAGGAACGCCAG
C48	GGTTTTCCATGGTCATAGCTGTTTGAGAGGCG
C49	GTTTGCGTCACGCTGGTTTGCCCCAAGGGAGCCCCCGATT
C50	GGATAGGTACCCGTCGGATTCTCCTAAACGTTAATATTTT
C51	AGTTGGGTCAAAGCGCCATTCGCCCCGTAATG
C52	CGCGCGGGCCTGTGTGAAATTGTTGGCGATTA
C53	CTAAATCGGAACCCTAAGCAGGCGAAAATCCTTCGGCCAA
C54	CGGCGGATTGAATTCAGGCTGCGCAACGGGGGATG
C55	TGCTGCAAATCCGCTCACAATTCCCAGCTGCA
C56	TTAATGAAGTTTGATGGTGGTTCCGAGGTGCCGTAAAGCA
C57	TGGCGAAATGTTGGGAAGGGCGAT
C58	TGTCGTGCACACAACATACGAGCCACGCCAGC
C59	CAAGTTTTTTGGGGTCGAAATCGGCAAAATCCGGGAAACC
C60	TCTTCGCTATTGGAAGCATAAAGTGTATGCCCGCT
C61	TTCCAGTCCTTATAAATCAAAAGAGAACCATCACCCAAAT
C62	GCGCTCACAAGCCTGGGGTGCCTA
C63	CGATGGCCCACTACGTATAGCCCGAGATAGGGATTGCGTT
C64	AACTCACATTATTGAGTGTTGTTCCAGAAACCGTCTATCAGGG
C65	ACGTGGACTCCAACGTCAAAGGGCGAATTTGGAACAAGAGTCC
Link-A1C	TTAATTAATTTTTTACCATATCAAA
Link-A2C	TTAATTTCATCTTAGACTTTACAA
Link-A3C	CTGTCCAGACGTATACCGAACGA
Link-A4C	TCAAGATTAGTGTAGCAATACT
Link-B1A	TGTAGCATTCCTTTTATAAACAGTT
Link-B2A	TTTAATTGTATTTCCACCAGAGCC

Link-B3A	ACTACGAAGGCTTAGCACCATTA
Link-B4A	ATAAGGCTTGCAACAAAGTTAC
Link-C1B	GTGGGAACAAATTTCTATTTTTGAG
Link-C2B	CGGTGCGGGCCTTCCAAAAACATT
Link-C3B	ATGAGTGAGCTTTTAAATATGCA
Link-C4B	ACTATTAAAGAGGATAGCGTCC
Loop	GCGCTTAATGCGCCGCTACAGGGC
C42	GTAACCGTCTTTCATCAACATTAAAATTTTTGTTAAATCA

STUDIES USED IN INTEGRIN EXPRESSION MINI META-ANALYSIS

Neonatal Ventricular Cardiomyocytes

Study 1: Geo Page , PubMed, Anand et al., 2013 Doi 10.1016/j.cell.2013.07.013

Genevestigator Experiment ID: RN-00210

Title : BET Bromodomains Mediate Transcriptional Pause Release in Heart Failure [NRVM Expression]

Method: Cells were harvested from 2 day old Sprague-Dawley Rats and maintained in serum free medium for 48 hours. For cellular samples, total RNA from NRVM was isolated using the High Pure RNA isolation kit (Roche #11828665001) with on-column DNAase treatment according to manufacturer's directions. Purified RNA was reverse transcribed to complementary DNA using the iScriptTM RT Supermix (Biorad #170-8841) following manufacturer's protocol.

Data taken from three independent repeats of control samples treated with DMSO for 90 minutes

Log2 Values for ITGa5: 9.26, 9.21, 9.23

Log2 Values for ITGa7: 13.9, 13.79, 13.87

Log2 Values for ITGa6: 12.86, 12.82, 12.68

Log2 Values for ITGa3: 12.78, 12.72, 12.72

Log2 Values for ITGb1: 16.37, 16.28, 16.33

Log2 Values for ITGa8: 11.41, 11.42, 11.4

Log2 Values for ITGav: 12.31, 12.25, 12.14

Log2 Values for ITGb3: 10.62, 10.66, 10.69

Study 2 : Array Express Page, PubMed , Marshall et al., 2010 Doi: 10.1371/journal.pone.0010027

Genevestigator Experiment ID: RN-00294

Title: ERK1/2 Signaling Dominates Over RhoA Signaling in Regulating Early Changes in RNA Expression Induced by Endothelin-1 in Neonatal Rat Cardiomyocytes

Method: Neonatal ventricular cardiomyocytes derived from Sprague Dawley rats. Cardiomyocytes were isolated from ventricles of 2-day-old neonatal Sprague Dawley rats, and propagated in 80% DMEM/20% MEM. RNA from three individual experiments was pooled and analyzed as a single sample set. Total RNA was taken from cells after 42-48 hours in culture.

Log2 Values for ITGa5: 11.79, 11.75, 11.42, 11.38, 11.69, 11.39, 11.48, 11.47

Log2 Values for ITGa7: 12.87, 12.99, 12.92, 12.87, 12.73, 12.92, 12.90, 12.91

Log2 Values for ITGa6: 11.69, 11.55, 11.55, 11.36, 11.54, 11.30, 11.72, 11.60

Log2 Values for ITGa3: 12.00, 11.95, 12.02, 11.86, 11.95, 11.95, 11.91, 11.95

Log2 Values for ITGb1: 15.55, 15.23, 15.20, 15.31, 15.53, 15.05, 15.21, 15.38

Log2 Values for ITGa8: 11.15, 11.31, 11.42, 11.09, 11.11, 11.37, 11.45, 11.14

Log2 Values for ITGav: 10.86, 10.99, 11.11, 11.11, 10.91, 11.04, 11.5, 11.16

Log2 Values for ITGb3: 10.96, 11.48, 11.82, 11.86, 11.06, 11.53, 12.05, 12.1

Study 3: Array Express, Pubmed, Markou et al., 2010 DOI: 10.1186/1471-2164-11-343

Genevestigator Experiment ID: RN-00297

Title: Regulation of the cardiomyocyte transcriptome vs translatome by endothelin-1 and insulin: translational regulation of 5' terminal oligopyrimidine tract (TOP) mRNAs by insulin.

Method: Neonatal ventricular cardiomyocytes isolated from ventricles of 1-3-day-old Sprague Dawley rats. Cardiomyocytes were cultured in 68% Dulbecco's modified Eagele's medium, 17% M199, 15% fetal calf serum, and 100 units/ml penicillin and

streptomycin for 18 h. Serum was withdrawn and cells cultured in 80% DMEM/20%MEM for 24 h. Total RNA was used for the analysis.

Log2 Values for ITGa5: 11.86, 12.27, 12.19, 11.69

Log2 Values for ITGa7: 13.08, 13.11, 13.32, 13.20

Log2 Values for ITGa6: 11.70, 11.97, 11.70, 11.79

Log2 Values for ITGa3: 12.46, 12.27, 12.42, 12.26

Log2 Values for ITGb1: 15.50, 15.30, 15.42, 15.57

Log2 Values for ITGa8: 11.64, 11.63, 11.31, 11.72

Log2 Values for ITGav: 11.32, 11.35, 11.18, 11.11

Log2 Values for ITGb3: 11.34, 11.6, 11.74, 11.41

Study 4: GEO, PubMed, Yoshikawa et al., 2009 Doi: 10.1152/ajpendo.90767.2008.

Genevestigator Experiment ID: RN-00298

Title: Ligand-based gene expression profiling reveals novel roles of glucocorticoid receptor in cardiac metabolism.

Method: Neonatal ventricular cardiomyocytes derived from Wistar rats treated with vehicle (ethanol) for 3h. Cardiomyocytes were isolated from ventricles of 1-day-old neonatal Wistar rats. Primary cultures of cardiomyocytes were grown in OPTI-MEM for 24 h, and then treated with ethanol for 3h. Pooled RNA samples were used from three independent experiments.

Log2 Values for ITGa5: 10.77, 11.64

Log2 Values for ITGa7: 13.00, 12.86

Log2 Values for ITGa6: 12.48, 11.77

Log2 Values for ITGa3: 12.79, 13.13

Log2 Values for ITGb1:15.32, 15.06

Log2 Values for ITGa8: 11.07, 10.10

Log2 Values for ITGav: 10.58, 9.62

Log2 Values for ITGb3: 12.32, 11.16

ANTIBODIES TESTED BUT FOUND TO BE OF INSUFFICIENT QUALITY

Daam1 (Rabbit) – Protientec – 20466 – used at 1:200

mDia1 (Rabbit) – Abcam – Ab11173 – used at 1:200

FMNL1 (Rabbit) – Abcam – Ab97456 – used at 1:200

FMNL3 – (Goat) – Santa Cruz – sc66770 – used at 1:200